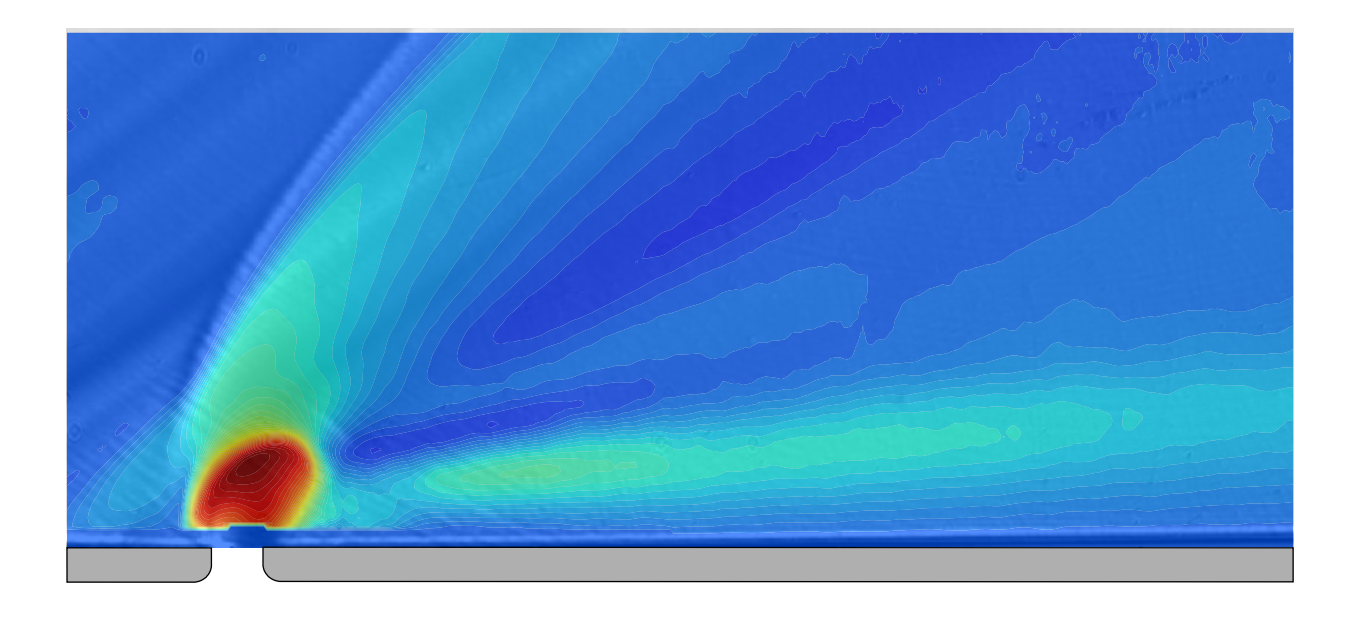
Experimental Investigation of Transverse Jet Injection into Supersonic Crossflow

Ventsislav Viktorov Pazhev

November 6, 2020







Experimental Investigation of Transverse Jet Injection into Supersonic Crossflow

MASTER OF SCIENCE THESIS

For obtaining the degree of Master of Science in Aerospace Engineering at Delft University of Technology

Ventsislav Viktorov Pazhev

November 6, 2020



Copyright \odot Ventsislav Viktorov Pazhev All rights reserved.

DELFT UNIVERSITY OF TECHNOLOGY DEPARTMENT OF AERODYNAMICS, WIND ENERGY, FLIGHT PERFORMANCE & PROPULSION (AWEP)

The undersigned hereby certify that they have read and recommend to the Faculty of Aerospace Engineering for acceptance a thesis entitled "Experimental Investigation of Transverse Jet Injection into Supersonic Crossflow" by Ventsislav Viktorov Pazhev in partial fulfillment of the requirements for the degree of Master of Science.

	Dated: November 6, 2020
Committee chair:	Dr.ir. B.W. van Oudheusder
Thesis supervisor:	Dr.ir. F.F.J. Schrije
Examiner:	Dr. A. Gangoli Rac
Examiner:	Dr.ir. W.J. Baars

Abstract

This MSc thesis deals with the behaviour of jets injected transversely into supersonic crossflow for variable flow field control variables. The understanding of the jet trajectory and the formation and behaviour of the large-scale structures associated with such flow fields is paramount for aerospace applications such as fuel injection in Supersonic Combustion Ramjet (SCRamjet) engines and reaction-jet-based attitude control systems. Contemporary research on the topic has dealt extensively with defining jet trajectory correlations and obtaining flow field visualisations and numerical simulation data in the near-and far-field of the interaction. Quantitative full-field measurements of the far-field have also been performed. However, there is a scarcity of full-field quantitative experimental data in the near field of the injection.

The study addresses this issue by performing near and mid-field experimental measurements of the of transverse jets injected into a Mach 2 supersonic crossflow via Schlieren imaging and Particle Image Velocimetry (PIV). The data was obtained for $x/d_j < 17$. Three different jet Mach numbers were tested with Schlieren imaging, $M_j = 1, 1.5$ and 2 and two for PIV, $M_j = 1$ and 2. The jet-to-crossflow momentum flux ratio J was varied between 0.6 and 2.0. The ratio between the crossflow boundary layer thickness and the jet injection diameter was kept constant at $\delta/d_j = 1.25$.

Imaging data from the Schlieren campaign was processed in order to obtain time-averaged visualisations and use the latter to extract the main geometric parameters of the shock system. The visualisations displayed the characteristic interaction bow and separation shock and jet barrel shock and Mach disc. The combination of a thick boundary layer with the crossflow Mach number yielded a situation where the bow shock penetrates deep into the boundary layer, and the barrel shock is turned in the direction of the crossflow. The separation shock wave manifested only for $M_j = 2$ injection. For the other injection cases, compression waves were observed. The Mach disc height and thus the near field flow obstruction was found to increase with J. The more extensive blockage leads to increased separation length, bow shock stand-off and angle. The increase of the jet Mach number was found to have the opposite effect. This difference can be related to the jet pressurisation and operational regime. Sensor measurement data combined with the use of semi-empirical relations suggest that the $M_j = 2$ jet operates in overexpanded condition, whilst the other injections are underexpanded.

Two-dimensional mid-plane PIV instantaneous velocity profiles were processed in order to obtain mean flow velocity fields and mean turbulence parameters. Mean velocity fields were further used to extract velocity deficit and vertical velocity profiles at several locations downstream of vi

the injection. The mean flow data displayed clearly the thickening of the boundary layer in front of the jet, the above-discussed shock structures and indicated the location and strength of the jet wake and the characteristic Counter-Rotating Vortex Pair (CVP), formed downstream of the injection. Increase in J led to an increase of the jet wake and CVP strength, penetration into the crossflow and width. Increasing the M_j led to similar transverse penetration but at reduced strength and width of the structures. Furthermore, for the overexpanded supersonic injection, in contrast to the underexpanded sonic one, a large area of downwash was observed downstream of the injection point. For those cases, the upwash related to the CVP does not appear until about 10 jet diameters. The jet wake is also not clearly visible until about $5d_j$.

The mean turbulence parameters were used to extract Turbulence Intensity (TI) and Reynolds shear stress R_{xy} contours. Three areas of higher turbulence were observed - two at the bow and barrel shock and one related to the formation and propagation of the CVP, located just aft of the barrel shock and extending streamwise. The extend of high turbulence associated with the CVP was found to be directly proportional to J and inversely proportional to M_j . Furthermore, despite issues with particle slip and resolution at the shock locations, two patches of opposite R_{xy} could be indicated windward of the injection. The latter may be related to the formation of shear layer vortices.

Trajectory fits based on loci of maximum velocity deficit and vertical velocity showed the jet is quickly aligned with the crossflow. Although trends are similar to those of previously developed formulas, the experimental data lies beneath the empirical correlation trajectories as the latter is based on the upper edge of the jet. The trajectory-based on velocity deficit was found to penetrate higher as compared to the one based on vertical velocity.

Preface and Acknowledgements

The moment has finally come for the completion of this thesis and my Master studies in Aerospace engineering. This brings such strong and overwhelming feelings. I cannot help but remember the lyrics of the song by Rod Stewart, Faith of the Heart:

"It's been a long road,
To get from there to here.
It's been a long time,
But my time is finally here.
And I can feel a change in the wind right now.
Nothing's in my way.
And they're not gonna hold me down no more.
No they're not gonna hold me down.
Cause I've got faith of the heart.
I'm going where my heart will take me.
I've got faith to believe.
I can do anything.
I've got strength of the soul.
And no one's going to bend or break me.

I can reach any star..."

When I was a child, I used to listen to that song when it played with the introductory credits of the series "Star Trek: Enterprise". The short cinematic showed the technological progress of mankind - the journey from the sailboat through the space shuttle and to faster than light transport. But what really stood in the base of all of this was the innate drive of humanity for adventure and exploration - one of the many things that drove me to endeavour on my journey.

And I was not alone on this road. I have been aided and, in a way, shaped by very many people, which I would like to acknowledge here.

First of all, I would like to thank my supervisors, Dr.ir. F.F.J. Schrijer and Dr.ir. B.W. van Oudheusden, who have been with me through my intricate road to this degree. I remember the

first time we were discussing possible thesis topic and how one phrase, jet in crossflow, started this project. I chose this topic due to my interest in high-speed aerodynamics and the impression you left in me during our lectures. I am grateful for you for your patience and understanding. Thank you for our discussions, your guidance and help and for offering me this thesis project.

Of course, I would also like to thank the technical personnel of the high-speed lab: Dennis, Nico, Frits and Peter. You all contributed to various critical aspects of my thesis - drawings, manufacturing, purchase, server help, or simply being bugged multiple times a day to run the wind tunnel. Besides the technical personnel, I was also helped by dr. Haohua Zhong and Arti, who gave me a crash course on Particle Image Velocimetry during their experimental campaigns. Thank you!

Besides my family, on the first line during the last weeks were some people very dear to me. Ana, Javi Fatou Gomez and Javi Berzosa Molina, Maria, Lucas, Tim and Mauricio. Thank you for your support and for proof-reading some of my works at short notice. Your support has been invaluable. Ana, thank you for being by me in my worst. I cannot wait to continue my travels with you.

Of course, I would also like to express my gratitude to the students who used to occupy the high-speed lab basement. Without them, a thesis in aerodynamics is not the same. I already miss all of you - Javi, Niels, Jaime, Dorian, Francesco, Luigi, Blanca, Arun and all others. I would always remember the evening dinners with Javi late in the lab and our fruitful discussions. I am happy we remained friends and shared so many memories, starting with salsa.

Besides my friends form the aerodynamics lab, I must also not forget Ashu, Marina, Miriam and Dimitrios. You supported me over a very turbulent year, and we had so many good memories. It seems destiny put us back together, and I am looking forward to meeting you again.

I must note, that my path would not be the same if not for my experience during my Bachelor studies and the many amazing people I met, some of which remain incredibly close to me even to this day. Timo, Valeria and Calin - you are likely some of my oldest friends. Thank you for your support over the years. I cannot count the number of crazy memories we made together. Furthermore, my great friend Mauricio cannot remain unmentioned. Even with great distance, your mentorship and friendship warm my heart. The Force is strong with you... Always!

And at last, my family. Well, I have two. Two loving and supporting families and two amazing and smart brothers, alphabetically, Nikola and Viktor! I love you very much and cherish every moment with you. I do not doubt the fact that soon you will be the one who will embark on writing a thesis of your own. Aim high and never, ever stop, whist remembering to live all moments to the fullest. Dear family, parents and step-parents, you have been my steadfast moral and mental support over the years. I wish to see you more often and spend more time with you for you to bring real joy in my life. It is you who gave me the wings to embark on this long journey. My loving mother, Elka, was always willing to do everything to ensure I will achieve my dreams. My father, Viktor, was always supporting me and consistently tried to bring the rational engineer in me, a rather dreamy person. Hopefully, I achieved my balance. Finally, my late grandparents were not able to see the completion of this work. But they live in my memory and all they did and are will always guide me in acts.

One journey ends, and a new one starts. What is more important, the journey or the destination?

Delft, The Netherlands November 6, 2020 Ventsislav Viktorov Pazhev

Contents

A	Abstract			
P	refac	e and Acknowledgements	vii	
A	crony	yms	vii	
N	omei	nclature	xix	
1	Inti	roduction	1	
	1.1	Background and motivation	1	
	1.2	Research objectives	4	
	1.3	Scope and methodology	6	
		1.3.1 Scope	6	
		1.3.2 Methodology	6	
	1.4	Contribution	7	
	1.5	Outline	7	
2	Lite	erature Review	9	
	2.1	General characteristics of the compressible jet injection flowfield	9	
	2.2	Free jet gas dynamics	12	
	2.3	Gas dynamics of compressible jets in crossflow	14	
		2.3.1 Exhaust plume for jet in crossflow	16	
		2.3.2 Nozzle Backpressure models	18	
	2.4	Jet trajectory	20	
		2.4.1 Analytical model by Zukoski and Spaid	21	
		2.4.2 Semi-analytical model by Orth	22	
		2.4.3 Compressible vortex pair model	25	
		2.4.4 Empirical trajectory correlations	26	

xii Contents

		2.4.5	Portz correlation	
		2.4.6	Trajectory parametric analysis	
	2.5		scale structures and mixing	
		2.5.1	Incompressible jets-in-crossflow flow topology	
		2.5.2	Compressible jets flow topology	
		2.5.3	Low momentum ratio jets	1
		2.5.4	Mixing	4
		2.5.5	Control parameters effect on large-scale structures and mixing 4	3
		2.5.6	Conclusions	9
3	Inje	ction	System Design 5:	1
	3.1	ST-15	Supersonic wind tunnel	1
		3.1.1	Typical section conditions	3
		3.1.2	ST-15 test parameters and sensors	3
		3.1.3	ST-15 modification	4
	3.2	Exper	imental requirements	5
		3.2.1	Experimental test cases	5
		3.2.2	Reverse calculation of required pressures	5
		3.2.3	Mass flow study	6
		3.2.4	Effective backpressure and nozzle choking	8
	3.3		nozzle design	
		3.3.1	Settling chamber	
		3.3.2	Nozzle converging subsection	
		3.3.3	Nozzle dimensions	
	3.4		sonic nozzle design	
		3.4.1	Nozzle throat diameter	4
		3.4.2	Inviscid flow considerations	
		3.4.3	Friction losses	4
		3.4.4	Flow separation	6
		3.4.5	Nozzle contours	3
	3.5	System	n concept and performance	3
		3.5.1	System concept and implementation	3
		3.5.2	System performance	5
4	Exp	erime	ntal Techniques 7'	7
	4.1		ren imaging	7
		4.1.1	Governing principle	
		4.1.2	Schlieren configuration for transverse injection into supersonic crossflow . 8:	
	4.2		le Image Velocimetry	
		4.2.1	Governing principle	
		4.2.2	Flow seeding	
				J

Contents

		4.2.3 Illumination and light-sheet optics	7
		4.2.4 Acquisition and imaging optics	9
		4.2.5 PIV configuration for transverse injection into supersonic crossflow 9	1
		4.2.6 PIV data processing	3
	4.3	Conclusions	4
5	Res	alts And Discussion 9	5
	5.1	Shock structure analysis	5
	5.2	Mean velocity field analysis	0
		5.2.1 Velocity contours	1
		5.2.2 Velocity profiles	6
	5.3	Turbulence analysis	9
	5.4	Jet trajectory analysis	2
		5.4.1 Experimental trajectory fits	2
		5.4.2 Comparison with empirical trajectory correlations	3
		5.4.3 Approximate momentum flux	4
	5.5	Summary	6
6	Con	clusions and Recommendations 11	9
	6.1	Conclusions and Contribution	9
		6.1.1 Engineering contribution	9
		6.1.2 Scientific contribution	
		6.1.3 Main question	
	6.2	Recommendations	3
A	_	plementary Equations and Theory 13	
	A.1	General relations	
		A.1.1 Nozzle operational regimes	
	A.2	Heister and Karagozian summarized backpressure prediction	
	A.3	Analytical interaction shock shape prediction	
	A.4	Heister and Karagozian Compressible vortex pair trajectory model	
	A.5	Parametric analysis of compressible jet in crossflow	2
В	Sen	or Data 14	
	B.1	Section Schlieren test matrix and control settings	
	B.2	PIV test matrix and control settings	7
\mathbf{C}	Exp	erimental Procedures 14	
	C.1	Run procedures PIV	9
	C.2	Nozzle exchange procedure	9

		\sim		
\mathbf{X}	IV	Con	ten	C.S

D	Supplemen	ntary Figures		151
	D.1 PIV ve	elocity fields	 	. 151
	D.2 Schlier	ren images	 	. 160
\mathbf{E}	Drawings			161
	E.1 Wind t	tunnel Mach 2 nozzle block cut-out drawings	 	. 161
	E.2 Injection	on system drawings	 	. 165

xvi

Acronyms

```
CCD Charge Coupled Device. 89
CVP Counter-Rotating Vortex Pair. vi, 10, 32, 36–41, 43–45, 47–50, 91, 95, 101–103, 107–109,
     112, 113, 116, 117, 121–123, 141
DEHS Di-Ethyl-Hexyl-Sebacat. 73, 85, 86, 92, 120
DES Detached Eddy Simulation. 41, 42
DNS Direct Numerical Simulation. xxii, 36, 37, 41, 42
FOV Field of View. xxiv, 77, 83, 84, 89, 90, 94, 120
HSL High-Speed Lab. 51, 54, 119
HWA Hot Wire Anemometry. 83
LDV Laser Doppler Velocimetry. 21, 29, 41, 45, 83
LES Large Eddy Simulation. 16, 21, 29, 30, 32, 41, 49
Nd:YAG solid-state frequency-doubled Neodymium-Doped Yttrium Aluminium Garnet laser.
NPLS Nanoparticle-Based Planar Laser Scattering. 28, 113
NS Normal Shock Wave. xxviii, 100, 106, 115
OS Oblique Shock Wave. xxviii, 100, 106, 115
PIV Particle Image Velocimetry. v, xxiii, xxiv, xxviii, 5-7, 16, 21, 30, 32, 41, 52, 53, 55, 56,
     73, 77, 81, 83–95, 100, 101, 106, 107, 112, 116, 117, 120–122, 124, 147, 148
```

xviii Acronyms

PLIF Planar Laser-Induced Fluorescence. 26, 32, 38, 44

 ${\bf RANS}$ Reynolds-Averaged Navier-Stokes. 20, 21, 41

SCRamjet Supersonic Combustion Ramjet. v, 3, 6, 10, 42, 44, 46

STI Shock-Turbulence Interaction. 41

SWBLI Shock Wave/Boundary-Layer Interaction. 9, 22, 109, 122

TI Turbulence Intensity. vi, xxiv, xxv, 5, 95, 109, 110, 117, 121, 122, 157–159

Nomenclature

Greek Symbols

 α conical nozzle half angle

 β shock angle

 γ specific heats ratio

 λ nozzle divergence factor

 μ viscosity

 ν kinematic viscosity

 ρ density

 ρ_0 stagnation density Θ jet inclination angle

k Specific reaction-rate constant

Latin Symbols

 \mathcal{M} molecular mass

J jet-to-crossflow momentum flux ratio

M Mach number p static pressure p_0 total pressure

 $p_{b_{eff}}$ nozzle effective backpressure

 $egin{array}{ll} A & & {
m surface \ area} \\ c & & {
m speed \ of \ light} \\ d & & {
m diameter} \\ \end{array}$

 D_h hydraulic diameter d_z laser sheet thickness

f friction factor f optics focal length

Nomenclature Nomenclature

$f_{\#}$	aperture
l	length
p_b	nozzle backpressure
Re	Reynolds number
t_{ign}	Ignition delay time
t_r	Burning time
u	horizontal velocity component
v	vertical velocity component
x	streamwise direction
y	vertical direction
∞	crossflow fluid property
j	jet fluid property

List of Figures

1.1	Schematic of transverse injection into crossflow. Adapted from Mahesh (2013)	1
1.2	Examples of smoke plumes in crossflow	2
1.3	Examples of compressible jet-in-crossflow applications	3
2.1	Characteristic flow topology for transverse injection into supersonic crossflow $$. $$	10
2.2	Underexpanded jet issuing in ambient conditions	12
2.3	Laval nozzle schematic with introduction of the notations at the main stations along the nozzle. Adapted from Anderson Jr (1991)	13
2.4	Schematic of the idealised free jet plume of an overexpanded Laval nozzle with Mach reflection reflection. Adapted from Zucker and Biblarz (2012) using theory from Wang and Yu (2015), Hadjadj et al. (2004) and Ben-Dor (2007)	14
2.5	Schematic of the idealised free jet plume of a highly underexpanded Laval nozzle with regular reflection. Adapted from Kieffer (1981) using theory from Wang and Yu (2015), Hadjadj et al. (2004) and Ben-Dor (2007)	14
2.6	Schematic of the flow field around an axisymmetric body with transversely injected jet into supersonic crossflow. The schematic is created by Morkovin et al. (1952) and modified by Mahesh (2013)	15
2.7	Typical operational regimes for compressible jets in crossflow at different jet total pressure p_{0_j} , boundary boundary layer thickness δ and separation height b . (Based on figures and interpretations from Portz (2005) and Orth et al. (1969))	17
2.8	Schematic of a simplified jet in supersonic crossflow flow field based on Papamoschou and Hubbard (1993). The flow is inviscid and the jet is assumed to be perfectly expanded	19
2.9	Schematic drawing of the analytical model of Zukoski and Spaid (1964)	22
2.10	Centreline trajectory of the model by Orth et al. (1969)	23

xxii List of Figures

2.11	Mach disc distance Orth et al. (1969)	24
2.12	Comparison of different correlations for $J=2.9$ as presented by Gruber et al. (1997)	27
2.13	Transverse penetration comparison of different correlations with the data obtained from the experiments by Ben-Yakar et al. (2006) at $J=1.5$	28
2.14	Transverse penetration comparison of different correlations with the data obtained from the experiments by Sun et al. (2013) and the modified correlation of Rothstein and Wantuck (1992) at different jet-to-crossflow momentum flux ratios	29
2.15	Comparison of jet trajectories, as presented by Chai et al. (2015) $\dots \dots$	30
2.16	Jet trajectories found as loci of peak velocity locations; dark lines, trajectories derived from the streamwise velocity deficit and grey lines, trajectories from vertical velocity component. As presented by Beresh et al. (2005a)	33
2.17	General-to-effective jet-to-crossflow momentum flux ratio based on simplified normal shock calculations versus crossflow Mach number. As presented by Portz (2005) .	34
2.18	Trajectories of Helium and Argon jets with $J=8.3$ and $M_{\infty}=2$. As presented by Papamoschou and Hubbard (1993)	34
2.19	Effect of the boundary layer thickness on the jet penetration as presented by Portz (2005)	35
2.20	Incompressible transverse injection flow topology	37
2.21	Incompressible transverse jet horseshoe vortex system	38
2.22	Flow structures encountered in high momentum jet injection	39
2.23	Schlieren of hydrogen and ethylene in supersonic crossflow. Exposure time of 200 $[ns], J=1.4, M_{\infty}=3.38$. Obtained from Ben-Yakar et al. (2006)	40
2.24	Instantaneous cross-planes images at three locations for circular injection of air and helium. $J=2.90,M_{\infty}=1.98$ Obtained from Gruber et al. (2000)	40
2.25	Jet vortical structures from Direct Numerical Simulation (DNS) results. Obtained from Sun and Hu (2018)	42
2.26	Hairpin vortices encountered at low momentum injection for low velocity jets. Obtained from Sau and Mahesh (2008)	42
2.27	Mach contours at the injection mid-plane in the near field of jet system. Obtained from You et al. (2013)	43
2.28	Impression of the structures encountered in low momentum jet injection. The image is based on analysis of plots of iso-surfaces of a positive value of the Q criterion. Obtained from You et al. (2013)	43
2.29	Concentration measurements with helium injection from Zukoski and Spaid (1964)	45
2.30	Classification of time scales in chemically reacting flows. Presented by Warnatz et al. (2006)	47
2.31	Effect of the jet-to-crossflow momentum flux ratio on the vortical structures in the far field.	49

List of Figures xxiii

3.1	ST-15 schematics: 1-Settling chamber; 2-de Laval nozzle; 3-Test section; 4-Supersonic diffuser Sun (2014)	52
3.2	ST-15 supersonic wind tunnel with PIV set-up and Schlieren illumination optics visible. The image was obtained after the experiments related to this thesis were completed	52
3.3	Isometric preview of the new lower part of the ST-15 Mach 2 de Laval nozzle block and test section	54
3.4	Pressure measurement equipment	57
3.5	Schematic of the sonic nozzle	60
3.6	Nozzle contour	62
3.7	Nozzle schematic for general nozzle; flow left to right	63
3.8	Nozzle geometrical efficiency	64
3.9	Local Reynolds number $Re_d(x)$ along the supersonic portion of the nozzle	65
3.10	Minimum half angle α_{min} for given wall roughness	66
3.11	Free shock separation (FSS) schematics and pressure distribution Östlund (2002)	67
3.12	FSS Romine (1998)	68
3.13	Nozzle wall pressure normalized with the ambient pressure for different half angles $-15^{\circ},10^{\circ},5^{\circ}$; white circles denote wall static pressure measurements and the solid lines denote the semi-empirical model results Malik and Tagirov (1987)	69
3.14	Pressure in overexpanded nozzle $A_e/A_t = 10$, $\alpha = 10^{\circ}$ Fostrer and Cowles (1949)	70
	Pressure ratio over the separation zone as function of M_i for different half angle α	70
3.16	Nozzle contours	73
3.17	Injection system schematics	74
3.18	Injection system	74
	Pressure drop over the system for two injection Mach numbers	75
4.1	Visual interpretation of light deflection according to Snell's Law. The incoming light is approximated to consist of plain waves. Using point-source approximation the deflected light ray can be constructed with by parallel waves formed tangent to the point source waves	79
4.2	Basic system schematics of a Schlieren arrangement with extended light source, lenses and no collimator lens and pinhole at the source. Taken from Settles and Covert (2002)	80
4.3	Schlieren configuration for transverse injection into supersonic crossflow	82
4.4	Basic PIV measurement system. Obtained from Raffel et al. (2007)	83
4.5	Schematic of the generic PIV processing routine. Obtained from Scarano (2013)	84
4.6	Laskin-nozzle based seeding generator Raffel et al. (2007)	86

xxiv List of Figures

4.7	Laser pulse separation and and pulse pair separation	87
4.8	Components of the laser sheet formation optics used for the experiments	88
4.9	Image of the laser optics of the PIV set-up with laser light on	88
4.10	Generic PIV imaging optics. Taken from Scarano (2013)	89
4.11	Field of View (FOV) for PIV with camera overlap Pazhev et al. (2019)	90
4.12	Dual PIV camera configuration	91
4.13	Experimental set-up for the PIV experiments	92
4.14	Visualisation of the PIV image processing algorithm	94
5.1	Schlieren imaging of the jet in supersonic crossflow	96
5.2	Variation of the mean oblique shock wave angle approximation β with J and M_j . Lines are plotted for $M_j = 1$ (\bullet), $M_j = 1.5$ (\blacktriangle) and $M_j = 2$ (\blacksquare). Error bars representing measurement standard deviation of $1 \times \sigma$ are also included	97
5.3	Shock system geometric characteristics as measured from averaged Schlieren images. Lines are plotted for $M_j=1$ (\bullet), $M_j=1.5$ (\blacktriangle) and $M_j=2$ (\blacksquare). Error bars representing measurement standard deviation of $1\times\sigma$ are also included	98
5.4	Schematic of the proposed operational regime for a compressible jet in crossflow with thick boundary layer δ penetrated by the bow shock. It should be noted that, depending on the injection parameters, the separation shock may be replaced by a compression fan. Indicated are the free stream Mach number M_{∞} , the separation shock height b and the Mach disc height b , and the jet exit properties, b and	99
5.5	Streamwise horizontal velocity contours for variable momentum flux ratio for the Mach 1 injection at the midplane $y/h=0$ of the test section, designated as $z/d_j=0$	102
5.6	Vertical velocity contours for variable momentum flux ratio for the Mach 1 injection at the midplane $y/h=0$ of the test section, designated as $z/d_j=0$	103
5.7	Streamwise horizontal velocity contours for variable jet Mach number and momentum flux ratio injection at the midplane $y/h=0$ of the test section, designated as $z/d_j=0$	104
5.8	Vertical velocity contours for variable jet Mach number and momentum flux ratio injection at the midplane $y/h=0$ of the test section, designated as $z/d_j=0$	105
5.9	Streamwise velocity deficit, u_{deff} , profiles at the midplane $y/h=0$. Lines are plotted for $J=0.6$ (·····), $J=1$ (-···), $J=2$ (—)	107
5.10	Vertical velocity profiles at the midplane $y/h = 0$.Lines are plotted for $J = 0.6$ (·····), $J = 1$ (····), $J = 1.5$ (····), $J = 2$ (····).	108
5.11	TI contours for variable jet Mach number and momentum flux ratio injection at the midplane $y/h=0$ of the test section, designated as $z/d_j=0$	110
5.12	Reynolds shear stress R_{xy} contours for variable jet Mach number and momentum flux ratio injection at the midplane $y/h = 0$ of the test section, designated as $z/d_j = 0 \dots \dots$	111

List of Figures xxv

5.13	Experimental trajectories based on velocity maxima for variable momentum flux ratio J at jet Mach number M_j . $(M_j = 1: J = 0.6 (\cdots), J = 1 (), J = 1.5 (), J = 2 (); M_j = 2: J = 0.6 (\cdots), J = 1 (), J = 1.5 (), J = 2 ().$	112
5.14	Comparison between the trajectories based on velocity loci - $((U_{inf}-u)/U_{inf})_{max}$ sonic (—), v_{max} sonic (), $((U_{inf}-u)/U_{inf})_{max}$ supersonic (—), v_{max} supersonic () and fits based on the experimental studies by Gruber et al. (1994) (—), Sun et al. (2013) (), Papamoschou and Hubbard (1993) () and Portz	111
L 1 L		114
5.15	Estimated effective momentum flux ratios at two flow positions behind a normal and oblique shock wave for $M_j = 1(\bullet)$, $M_j = 1.5$ (\blacktriangle) and $M_j = 2$ (\blacksquare)	115
A.1	Operational conditions and regimes for de Laval nozzle. Adapted from Wang and Yu (2015)	135
A.2	Characteristic shock shape and displacement correlation. As presented by Orth et al. (1969)	138
A.3	Schematic of the perfectly expanded jet in inviscid supersonic crossflow model developed by Heister and Karagozian (1990)	140
D.1	Streamwise velocity contours	151
D.1	Streamwise velocity contours	152
D.2	Streamwise velocity contours	153
D.3	Vertical velocity contours	154
D.3	Vertical velocity contours	155
D.4	Vertical velocity contours	156
D.5	TI contours	157
D.5	TI contours	158
D.6	TI contours	159
D.7	Time average Schlieren images of the jet in supersonic crossflow	160
E.1	Back insert lower. Unless otherwise stated all dimensions are in millimetres. The drawing Title block was omitted per request from the technical personnel. Author: FDD/ V.Pazhev	161
E.2	Back insert upper. Unless otherwise stated all dimensions are in millimetres. The drawing Title block was omitted per request from the technical personnel. Author: FDD/ V.Pazhev	162
E.3	Cap plate. Unless otherwise stated all dimensions are in millimetres. The drawing Title block was omitted per request from the technical personnel. Author: FDD/V.Pazhev	163
E.4	Clamp piece. Unless otherwise stated all dimensions are in millimetres. The drawing Title block was omitted per request from the technical personnel. Author: FDD/ V.Pazhev	163

xxvi List of Figures

E.5	$M_j = 1.0$ injection nozzle. Unless otherwise stated all dimensions are in millimetres. The drawing Title block was omitted per request from the technical personnel. Author: V.Pazhev	165
E.6	$M_j=1.5$ injection nozzle. Unless otherwise stated all dimensions are in millimetres. The drawing Title block was omitted per request from the technical personnel. Author: V.Pazhev	165
E.7	$M_j=2.0$ injection nozzle. Unless otherwise stated all dimensions are in millimetres. The drawing Title block was omitted per request from the technical personnel. Author: V.Pazhev	166
E.8	$M_j=1.0$ injection assembly. Nozzle and fitting. Unless otherwise stated all dimensions are in millimetres. The drawing Title block was omitted per request from the technical personnel. Author: V.Pazhev	166
E.9	$M_j=1.5$ injection assembly. Nozzle and fitting. Unless otherwise stated all dimensions are in millimetres. The drawing Title block was omitted per request from the technical personnel. Author: V.Pazhev	167
E.10	$M_j = 2.0$ injection assembly. Nozzle and fitting. Unless otherwise stated all dimensions are in millimetres. The drawing Title block was omitted per request from the technical personnel. Author: V.Pazhev	167

List of Tables

2.1	Compilation of empirical trajectory relations	26
2.2	Compilation of empirical trajectory relations	31
3.1	ST-15 wind tunnel inflow parameters	53
3.2	Experimental test matrix; Note: $J=0$ stands for crossflow (free stream) measurement required for analysis of the data	55
3.3	Jet pressure array $p_j[kPa]$	55
3.4	Jet pressure array $p_{0_j}[kPa]$	56
3.5	Tube diameters and gage Mach number	57
3.6	Experimental results	58
3.7	Pressure matching $\frac{p_j}{p_{b_{eff}}}$	58
3.8	Nozzle pressure ratio $\frac{p_{b_{eff}}}{p_{0_{j}}}$	58
3.9	Pressure ratios for shock at the nozzle end and isentropic expansion	59
3.10	Summary of major sonic nozzle dimensions	63
3.11	Divergent subsection preliminary sizing	64
3.12	Separation location according to Schilling Romine (1998) $\frac{x}{l_{n_d}}$	71
3.13	Separation location according to Schmucker Schmucker (1984) $\frac{x}{l_{n_d}}$	71
3.14	Separation location based on pressure raise in the separated zone predicted by Kudryavtsev and pressure raise in the interaction zone predicted by Zukovsky. Information obtained from Östlund (2002)	72
3.15	Separation location based on pressure raise in the separated zone predicted by stlund and pressure raise in the interaction zone predicted by Zukovsky. Information obtained from Östlund (2002)	72

xxviii List of Tables

4.1	Properties of PIV seeding used in supersonic nows based on Ragni et al. (2011) and Scarano (2013). The S_k is estimated based on the τ_s results presented by Ragni et al. (2011) and the τ_f based on the boundary layer thickness as seen in Equation 4.12 and the date presented in Table 3.1	86
4.2	Particle image velocimetry experimental parameters summary	92
5.1	Pressure matching $p_j/p_{b_{eff}}$ for the jet plume at the jet exit and after the Mach disc for the case of Normal Shock Wave (NS) and Oblique Shock Wave (OS) approximation based on sensor data and information extracted from Schlieren images	100
5.2	Pressure matching for the jet plume at the jet exit and after the Mach disc for the case of NS and OS approximation based on sensor data and information extracted from Schlieren images	115
B.1	Test matrix and injection parameters for the Schlieren campaign	146
B.2	Free stream (crossflow) parameters for the Schlieren campaign	146
B.3	Test matrix and injection parameters for the PIV campaign	147
B.4	Free stream (crossflow) parameters for the PIV campaign	148

Chapter 1

Introduction

This thesis work in the field of Supersonic Aerodynamics deals with the study of the interaction of two flows of fluid. In this first chapter, the background and motivation of the research are presented. Based on this, the main goals, scope are defined, and the contribution of the work is presented. Finally, an outline of the report is provided to the reader.

1.1 Background and motivation

Transverse jet injection refers to a particular case of interaction between two flows where a jet of fluid, regarded as the main flow, is injected at a right angle into another fluid, regarded as the crossflow. The configuration is shown in Figure 1.1. A short retrospective on the historical observations of the phenomenon is presented in the following paragraphs. It will provide some background on the topic and its general significance for scientific research.

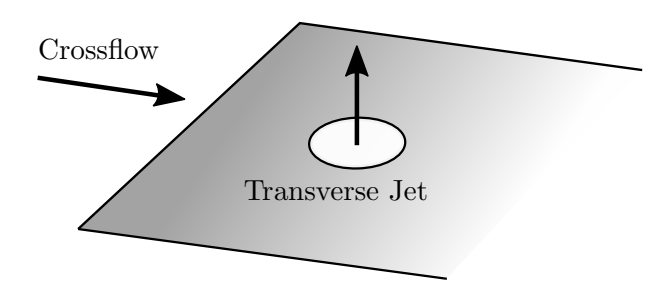


Figure 1.1: Schematic of transverse injection into crossflow. Adapted from Mahesh (2013)

In nature, transverse jets in crossflow are observed with phenomena where air or a smoke plume would emerge in a quiescent environment or interact with airstreams in the atmosphere. An example of this is the plumes of volcanic eruptions, such as the one presented in Figure 1.2a. After the beginning of the Industrial Revolution, due to the growing concern with dust particle propagation caused by smoke from the chimneys of industrial plants, forest fires and volcanic

2 Introduction

eruptions, meteorologists undertook a detailed analysis of the phenomenon. An example of a smoke jet in atmospheric crossflow can be seen on Figure 1.2b. As a result of this increasing concern, the initial research in the area focused on the development of the fundamental scaling laws for the jet plume trajectory and spread, as well as the decay of a scalars concentration along the jet trajectory. Subsequent studies focused more on the formation of the large-scale structures characteristic for the flow field .





(a) Plume from the Kirishima volcano in Japan on Jan- (b) Britain's industrial channels: Warwickshire around uary 26, 2011. As presented by Mahesh (2013) the 1940s and 1950s. Obtained from Hills (2012)

Figure 1.2: Examples of smoke plumes in crossflow

After the end of the Second World War, the Aerospace industry broke the sound barrier of Mach one and humanity entered the era of supersonic and, eventually, hypersonic flight. Hypersonic flight can be defined as flight where the vehicle Mach number is larger than 5. In this context, transverse injection found several applications where the jet plume would exit in a supersonic crossflow. Consequently, the previous knowledge of incompressible injection was taken and expanded into the domain of compressible flows. The current work is motivated, namely by the need for better understanding of the nature of such flow fields in order to support their utilisation.

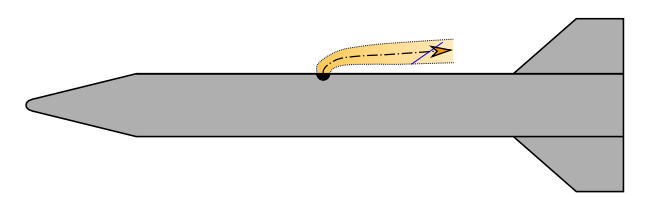
The first major application of transverse injection in compressible crossflow is as a mean of vehicle attitude control and thrust vectoring. An example of external injection is the reaction jet control for axisymmetric atmospheric vehicles, schematised in Figure 1.3a. Thrust vectoring for solid-rocket boosters, on the other hand, is achieved through internal, secondary liquid injectors. The latter would provide blockage and deflect the plume of the rocket motor.

As early as 1950, Morkovin et al. published one of the fundamental papers on the topic. Similarly to the incompressible jet research, the high-velocity jet studies focused initially on dimensional analysis and jet trajectory prediction. The primary drive was the prediction of crossflow blockage and the interaction of the jet plume with vehicle components, such as fins. Recently, more attention has been put on the analysis of the formation of the jet large-scale turbulent structures and the prediction of turbulence intensity. This knowledge would help evaluate their effect on overall vehicle performance. For example, strong vortical structures of side-control jets can harm

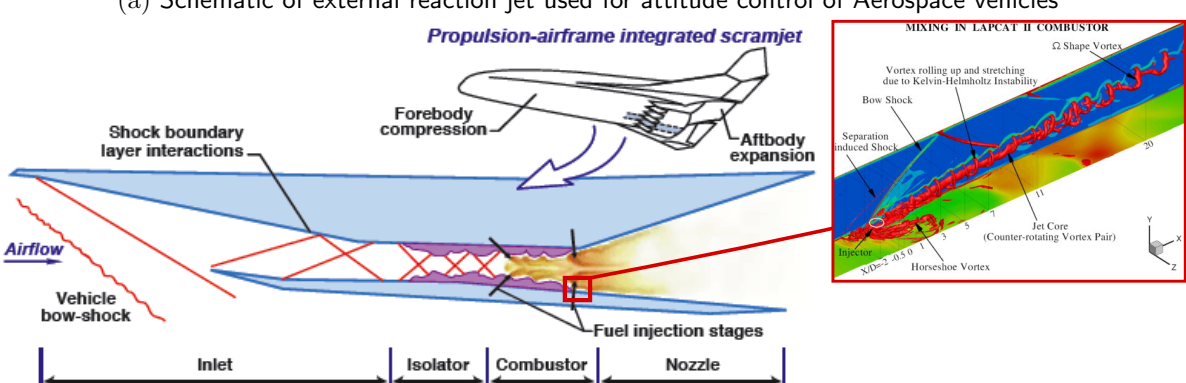
vehicle control surface performance.

The second major application utilizing the theory of transverse injection is linked to the recent interest development of air-breathing hypersonic flight vehicles. Such, vehicles, unlike rockets, mix externally obtained air from the atmosphere with a propellant, in order to achieve ignition, combustion and produce thrust. The propulsion system of those vehicles has been given the name SCRamjet. A "regular" ramjet would ingest air and compress it via generated shock waves as it "rams" through the air. The main characteristic of the SCRamjet is the fact that the ingested air remains at supersonic velocities in the combustion chamber. In his book on the topic, Segal (2009) established that SCRamjet engine propelled vehicles, such as the concept example seen on Figure 1.3b, could potentially have a have superior performance as compared to rocket motors at Mach numbers above 6. Therefore, this propulsion system is one of the promising technologies to make space travel more accessible via the development of modified launchers or even two- or single-stage horizontal take-off space planes.

In this relation, the understanding of jet injection is extremely important for the development of SCRamjet technology as it can be utilised for fuel injection. A fuel jet injected transversely into the combustion chamber would block the main flow, creating shock waves and eventually igniting due to the pressure rise. It will further turn in the flow direction and form large-scale vortical structures which, through their interaction, enhance the mixing process between air and fuel and aid combustion. Consequently, the most promising supersonic combustion fuel injection concepts use jets injected transversely or at an angle. The design of such systems brings about the need to thoroughly understand the turbulent mixing characteristics of the compressible jets and their relation to the generated large-scale and shock structures. Furthermore, the investigation of the main jet flow control parameters and the impact of their variation is critical for SCRamjet fuel injector design.



(a) Schematic of external reaction jet used for attitude control of Aerospace vehicles



(b) Schematic of hypersonic vehicle utilizing SCRamjet propulsion obtained from NASA (2006). A zoom-in on the transverse injection of fuel is also presented. The image is obtained from numerical simulation results by You et al. (2013). The jet injection image is used for illustration purposes only.

Figure 1.3: Examples of compressible jet-in-crossflow applications

4 Introduction

As seen above, current developments in the Aerospace industry drive the need for a better understanding of the behaviour compressible transverse jets and its control. It is namely this need that motivated the Aerodynamics group in TU Delft to initiate a research line and contribute to addressing the open questions concerning the flow characteristics of transverse injection for Aerospace applications. This thesis work is the pilot of this research line. The open issues of interest targeted by this study will be outlined in the following paragraphs.

Based on the consulted literature it was found that the large body of experimental research in this part of the flow domain relied on mainly flow visualisation techniques [Morkovin et al. (1952); Portz and Segal (2006); Ben-Yakar et al. (2006); Gruber et al. (1997, 2000); Sun et al. (2013)]. Quantitative full-field experimental data for varying injection parameters are only available for the far-field above 20 jet diameters. It is provided by the velocimetry measurements of Beresh et al. (2005a,b, 2006). Concerning the near field surrounding the jet and the mid-field below 20 jet diameters, the numerical and flow visualisation studies of Eberhardt and Hickel (2015); Kawai and Lele (2009); Santiago and Dutton (1997) underline the importance of the shock structures on the development of the large-scale structures and mixing. Furthermore, the correlated jet trajectories have shown a large amount of scatter and variation of accuracy. Recently, a detailed quantitative analysis of the near field has been conducted mainly using numerical methods, such as the ones by Eberhardt and Hickel (2015); Mahesh (2013); Chai et al. (2015); Kawai and Lele (2009); Muppidi and Mahesh (2007). However, conclusions of the conducted numerical simulations have limited validation data available.

Despite the importance of the near and mid-field for the mixing capabilities of the jet and as a source of the far-field structures, there is a scarcity of full-field quantitative experimental investigation data in this region. Moreover, observations on the effects of the jet control parameters on the velocity field in this region are also scarce. Jet control parameters are those that alter the behaviour of the interaction. Some of the most important parameters are the jet-to-crossflow momentum flux ratio, J, and the jet and free-stream Mach number, M_j and M_{∞} [Morkovin et al. (1952); Orth et al. (1969); Papamoschou and Hubbard (1993); Zukoski and Spaid (1964)].

As a result of this observation, this research aims to contribute to the existing research gap by attending the lack of full-field quantitative experimental data in the near field of the interaction for varying momentum flux ratio and jet Mach number. Through our experiments, we obtained data and investigated the control parameter effects on the averaged flow field in the range below twenty jet diameters.

Furthermore, as pilot research in the area for the group, during this MSc thesis, the current wind tunnel experimental equipment was also retrofitted with a test section cavity to hose the designed jet injection system.

1.2 Research objectives

Based on the discussed motivation the main goal of this thesis is stated in the following research question:

How are the averaged flow field and jet trajectory in the near and mid-field of a jet injected transversely into supersonic crossflow affected by the jet control parameters? The selected control parameters for this research are the jet-to-crossflow momentum flux ratio and the jet Mach number. The reasoning behind their selection is to be elaborated on in the next section.

The set of sub-questions required to address the main question are:

- 1. How are internal jet shock structures and interaction shock structures affected by the jet control parameter variation?
- 2. How do the jet-to-crossflow momentum flux ratio and jet Mach number affect the flow mean velocities in the near and mid-field?
- 3. How do the jet-to-crossflow momentum flux ratio and jet Mach number affect the turbulent characteristics in the near and mid-field of the injection?
- 4. Does the approximated ratio between the jet exit pressure and the ambient backpressure show any relation to flow field structures observed in the experiments?
- 5. What is the implication control parameters variation on the vortical strength and mixing potential of the jet in the near and mid-field?
- 6. How is the jet trajectory based on the averaged velocity field affected by the variation of the jet control parameters?.

The objectives to be met based on the previous questions are as follow:

- 1. Obtain instantaneous Schlieren images and process the latter in order to generate mean Schlieren visualisations in the mid-plane of jet injection.
- 2. Use the schlieren data to generate quantitative plots of the shock structure parameters for varying jet the control variables.
- 3. Process the instantaneous PIV data and obtain mean mid-plane velocity contours.
- 4. Use the instantaneous and mean velocity data to obtain turbulent characteristics in the mid-plane, such as TI and Reynolds stress.
- 5. Obtain velocity profiles and trajectory plots based on the velocity maxima of the profiles in order to conclude the jet wake and large-scale structures' penetration and trajectory.
- 6. Analyse the obtained data and make observations on the effects of the selected control parameters on the shock structures, mid-plane flow field, turbulent characteristics and jet trajectory.
- 7. Where possible, comment on the implications of the results on the jet wake development, vortical structures strength and mixing potential.

6 Introduction

1.3 Scope and methodology

1.3.1 Scope

The set of jet-in-crossflow control variables under investigation is limited based on the available lab equipment and information from the consulted literature concerning their significance. Furthermore, a maximum of two variables is selected.

Multiple studies such as the early work of Portz and Segal (2006) and the more contemporary publications of Beresh et al. (2005a, 2006) establish the jet-to-crossflow momentum flux ratio, denoted as J, as the leading flow field control variable. Designing an injection system that could alter J was feasible, and thus, is selected as the first jet control parameter.

The alteration of the second major control variable - the crossflow Mach number - was not found feasible for this study. The crossflow for the experiments will be provided by the ST-15 supersonic wind tunnel of the Faculty of Aerospace Engineering. As will be discussed later on in this report, it implements fixed metal de-Laval nozzle blocks that vary the freestream Mach number. The latter contains the test section, as well. Modification of multiple nozzle blocks was not possible. Therefore, the crossflow Mach number is set constant - $M_{\infty} = 2$. This number is of the order of magnitude of the flow encountered in SCRamjet combustion chambers, as seen in Segal (2009).

A significant secondary variable that was feasible for control and interesting for research was the jet Mach number, M_j . It could be altered by the exchange of small de-Laval nozzles mounted at the end of the jet delivery system. This has been defined as a second control parameter. Consequently, other secondary control variables such as injectant species and injector shape and configurations are not considered in this research.

Furthermore, the jet exit diameter d_j is set to 4 millimetres based on mass-flow considerations, and jet diameter ranges encountered in previous studies. The incoming boundary layer has a constant thickness of about 5 millimetres. This sets a constant ration $\delta/d_i = 1.25$.

In order to obtain quantitative data in the nearfield, the techniques of PIV and Schlieren imaging are used. The research is limited to mid-plane (jet side view) 2-dimensional vector fields. Volumetric and cross-plane (jet end view) measurements are omitted. The latter can only be performed as a proper understanding of the system is gained, and analysis of the mid-plane measurement data is conducted.

The effect of combustion is neglected as the PIV system used is not capable to properly calculating flow velocity vectors at the areas with combustion. Finally, despite the ability to provide full-field velocity measurements, the system constrains us to uncorrelated samples in the time domain due to the high velocities of the flow.

1.3.2 Methodology

As a result of the above-defined scope and objectives, the methodology for this research includes system and experimental design.

The system design includes both the jet injection system and the related modifications of the existing lab equipment. First of all, a jet injection system that is capable of delivering transverse

1.4 Contribution 7

jets into the wind tunnel test section with variable J and M_j is required. Furthermore, it should also be capable of implementing jet particle seeding in order to be able to conduct PIV experiments with seeded jet. The injection system is built in the test section wall of one of the ST-15 wind tunnel nozzle block. To be able to house the system, a cut-out in the block is made. This is designed with the capability to house various experimental equipment, such that it could also be used for future research.

Finally, measurements of the flow field and visualization of the density variation (thus shock structures) will be performed using the PIV and Schlieren imaging techniques, respectively. The latter are selected as planar (2-dimensional) PIV will yield full-field flow velocity vector maps (u, v) and - Schlieren visualization will contribute snapshots of the shock structures formed by the interaction of the two flow fields.

1.4 Contribution

This thesis aims to complement the existing research with several contributions. First of all, by investigating into the relationship between the variation of the jet control parameters and the flow structures in the mid-plane of the injection in the near and mid-field of the interaction. This is achieved through a combined analysis of full-field quantitative velocimetry data and schlieren imaging. Secondly, attending the lack of full-field quantitative experimental data in the near field of the interaction for varying momentum flux ratio by obtaining multiple sets of velocity vectors over two velocimetry campaigns. The first campaign, extensively reported here, generates velocity field data in a window of [-3:17.5] jet diameters surrounding the injection point. The second campaign focused on a zoomed-in area around the jet and is reserved for future analysis as it delivers only incremental information.

1.5 Outline

The conclusions that lead to the above-discussed research problem are based on a literature study presented in Chapter 2. The design of the injection system and the test facilities modification are detailed-out in Chapter 3. The experimental set-up and processing for the Schlieren imaging and PIV are discussed in the subsequent Chapter 4. The results are then presented and discussed in Chapter 5 and, finally, based on the made observations, conclusions and recommendations for continuation of this research are presented in Chapter 6. For further information on different topics and data processing outside of the main focus of this work, please review the Appendices belonging to this report.

8 Introduction

Chapter 2

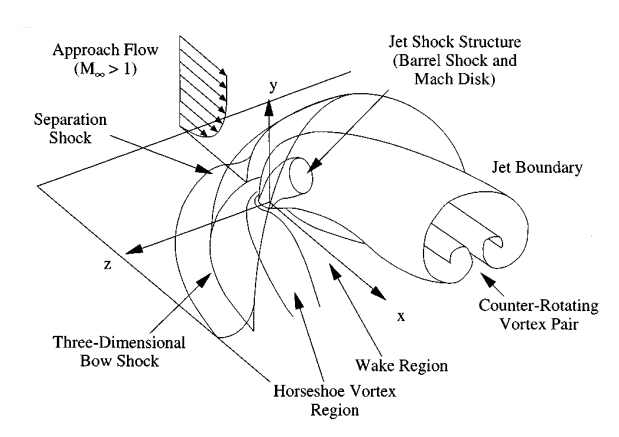
Literature Review

In the introduction the complexity of jet injection in supersonic crossflow was stressed upon. As a pilot research from our group on this topic, in order to build fundamental understanding of the flow physics, a broad literature study was conducted. This chapter summarises the observations on the contributions relevant for this thesis. Prior to venturing into a deeper dive in the scientific knowledge on the matter, a general introduction on the characteristic flow structure is made. The latter is of utmost importance for the understanding of the structure and content of the complete chapter. Subsequently, this study will dive in deeper into the theory behind the gas dynamics, jet trajectory and scaling parameters, and jet large-scale structures and mixing potential.

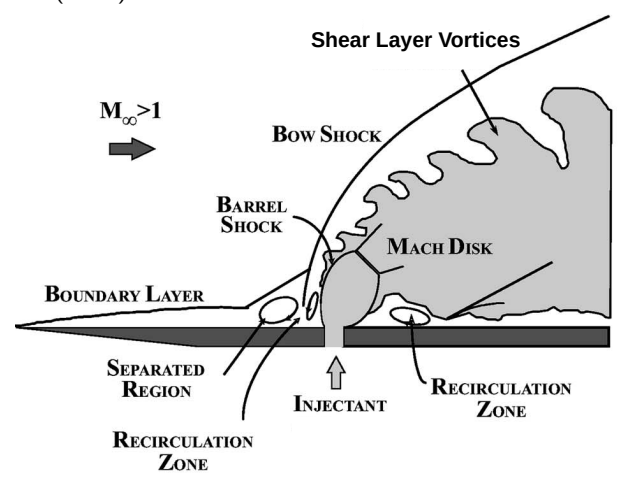
2.1 General characteristics of the compressible jet injection flowfield

From the consulted literature it can be concluded that the jet-in-crossflow flow field is characterised Shock Wave/Boundary-Layer Interaction (SWBLI) and vortex/shock interaction. As seen in Figure 2.1, upon exiting the jet injection orifice, the jet is turned sharply due to the momentum of the incoming crossflow. As discussed by Mahesh (2013) and Huang (2016), the large-scale turbulent structures of compressible jets are similar to the ones materialised by incompressible injection. However, due to the high velocity of the interacting flows, the supersonic injection flow field is also characterised by a set of flow discontinuities, shocks waves, and compression and expansion waves.

Extensive experimental and numerical data is abundant with respect to incompressible jets such as the experiments performed by Fric (1963), Kelso and Smits (1995) and Kelso et al. (1996). A solid stepping stone for the research into compressible jets, this knowledge has to be compared to turbulent flows with a significantly higher Reynolds numbers. Despite those different flow characteristics influencing the turbulent energy cascade, the large-scale and averaged flow field structures, as observed by the review on Huang (2016) and Mahesh (2013), can still be divided in the same categories. Those include the jet shear layer vortices, the horseshoe vortices, the



(a) Characteristic three-dimensional flow topology for transverse jet injection into supersonic crossflow. As presented by Gruber et al. (1997)



(b) Characteristic mid-plane^a flow topology for transverse jet injection into supersonic crossflow. As presented by Ben-Yakar et al. (2006)

Figure 2.1: Characteristic flow topology for transverse injection into supersonic crossflow

CVP and the wake vortices. The CVP and the horseshoe vortices have been well-schematised by Gruber et al. (1997) in Figure 2.1a. As will be discussed in Chapter 2.5, the CVP is formed by the turning and stretching of the shear layer of the jet and has a large influence on the mixing properties of the jet, as well as its interaction with any solid surfaces. The horseshoe vortices, on the other hand, are formed due to the obstruction and subsequent separation of the crossflow. The imprint of these vortices can be seen as the windward separation and recirculation regions in the mid-plane cross-section, presented in Figure 2.1b. The importance of these structures can be related to the flameholding capabilities of the injector in case of SCRamjet applications and to the surface pressure distribution for the thrust vectoring applications. The jet shear layer vortices can be seen in Figure 2.1b. These vortices form at the interface between the jet and crossflow fluid and have a significant role in the mixing processes in the near-field. The last type of vortical structures encountered with incompressible jets, the vertical wake vortices formed in the wake of the jet, have received less attention in compressible injection research.

^aA mid-plane is the plane along the jet propagation axis in the middle of the jet cross-section.

However, Beresh et al. (2005a) also implement it in their model of the compressible jet injection flowfield.

Besides the large-scale structures, the other characteristic trait of the compressible jet injection are the formed shock structures. Depending on the area of application, two major cases have been addressed in the literature. Research related to thrust vectoring applications has dealt with both supersonic jets and transonic and supersonic crossflow, such a the experiments performed by Beresh et al. (2003, 2005a,b, 2006). The research related to the jet applications for supersonic combustion fuel injectors are, of course, focused on supersonic crossflow, such as the research performed by Gruber et al. (1994, 1996, 1997, 2000). As will be discussed in Chapter 2.3, the shock system of the interaction can be divided in two parts: the discontinuities related to the jet compressibility and the discontinuities related to the interaction between the jet and the crossflow. As the jet emerges and is turned by the momentum of the incoming flow it creates a blockage. This blockage, similarly to the case of a blunt body in a freestream, as observed by Orth et al. (1969), goes on to create a strong bow shock. Depending on the bow shock strength, the incoming crossflow boundary layer separation length may change, causing a second, oblique or separation shock wave. Those structures are well represented in both Figure 2.1a and Figure 2.1b. The jet shock structures, on the other hand, are a direct result of the nozzle pressure ratio - the pressure difference over the jet orifice. The common jet plume state investigated by the current state-of-the-art is highly underexpanded nozzle. With such high pressurisation of the nozzle the plume expands and the expansion waves coalesce into a barrel shock, which is terminated by a quasi-normal shock called Mach disc. Finally, a second re-compression shock has also been observed following the second recirculation zone in the wake of the jet and sketched in Figure 2.1b.

As a final note of this quick introduction the main flow field control variable is presented. Parametric analysis of incompressible jets, such as the one performed by Kelso et al. (1996), established that the main flow control variable and scaling parameter for the flow field and trajectory is the jet-to-crossflow momentum flux ratio, defined as

$$J = \frac{\rho_j U_j^2}{\rho_\infty U_\infty^2},\tag{2.1}$$

where $\rho_j U_j^2$ is the dynamic pressure of the jet flow and $\rho_j U_j^2$ is the dynamic pressure of the crossflow. The dimensional analysis performed by Morkovin et al. (1952) and the later studies by Orth et al. (1969) established the same parameter as the dominant variable with supersonic jets. However, due to the compressibility of the fluids, the formula can better be expressed in terms of the jet and crossflow Mach numbers, resulting in

$$J = \frac{\gamma_j p_j M_j^2}{\gamma_\infty p_\infty M_\infty^2}. (2.2)$$

To facilitate the understanding of the discussed flow phenomena the presented review has been divided in four sections. The gas-dynamic analysis is split into two, providing also a short introduction with respect to compressible free jet flow is presented, as it is a fundamental building block to understand the complete flow topology. The rest of the sections remain as mentioned previously.

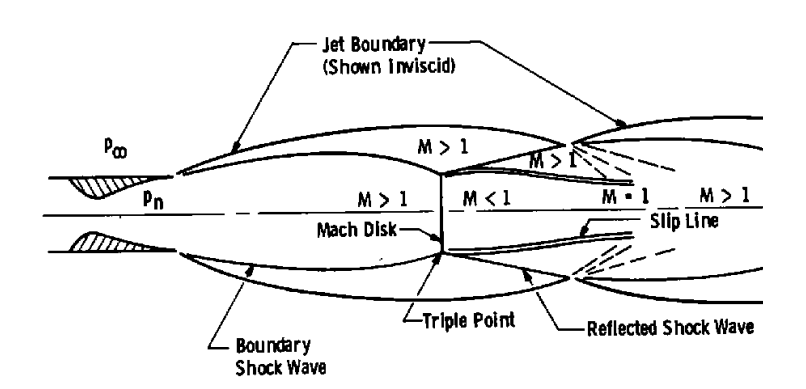
2.2 Free jet gas dynamics

To facilitate the understanding of the shock structures formed due to secondary jet injection, firstly, a jet issuing into ambient conditions is considered. Although a thorough explanation of the de Laval nozzle operational regimes will be introduced, the focus of the study will remain on underexpanded jets, such as most transverse jets and the cases presented in this work.

In practice, such flow field is encountered at the outlet nozzles of rocket motors at high altitudes where the ambient pressure is low and the jet becomes effectively underexpanded. An example is the ascent of the Saturn V rocket as seen in Figure 2.2a. At such conditions, as seen in Figure 2.2b, a characteristic shock cell structure is formed. The details of its formation are guided by the de Laval nozzle operational regime.



(a) Exhaust plume of the Saturn V vehicle during the ascend phase of the Apollo 11 mission United States Air Force (1969)



(b) Shock wave structure in plumes Peters and Phares (1976)

Figure 2.2: Underexpanded jet issuing in ambient conditions

Four nozzle operational regimes can be defined. For the purpose of this study the under-and overexpanded regimes are of great interest. At those regimes, due to the pressure difference at the nozzle exit which can be expressed as the ratio p_j/p_b , wave structures are formed at the jet exit. If the jet is overexpanded and needs to be compressed, shock waves form at the nozzle exit. If the jet is underexpanded and has to be expanded further, expansion waves form. If shocks are formed they further interact downstream, forming regular or Mach reflections, depending on the above-mentioned backpressure ratio. The definition of the conditions at the different nozzle stations will be defined according to Figure 2.3 for the remainder of this report. For more details on the nozzle operational regimes, please consult Appendix A.

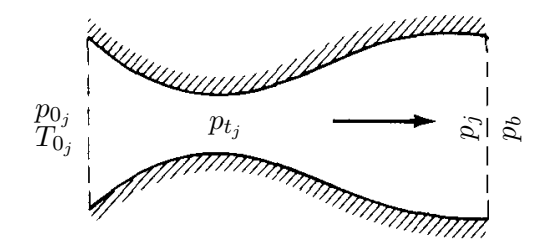


Figure 2.3: Laval nozzle schematic with introduction of the notations at the main stations along the nozzle. Adapted from Anderson Jr (1991)

As discussed earlier, the exact flow topology of the free jet after the formation of the first wave structures is dependent on the two boundary conditions that the flow has to satisfy - pressure equilibrium with the backpressure p_b and flow tangency at the centre streamline. For the purpose of this research a closer look will be taken into the waves formed in the wake of over-(Regime III) and underexpanded (Regime IV) free jets, which are the two flow regimes encountered during the operation of sonic and supersonic nozzles in transonic and supersonic crossflow, as summarized by Mahesh (2013). Furthermore, based on the observations seen in the consulted literature we will focus no the cases of Mach reflection, rather than regular reflections.

To recapitulate, the overexpanded condition occurs when $\frac{p_j}{p_b} < 1$. As a result, the jet flow has to be compressed to the value of the back pressure and oblique shocks are formed at the nozzle exit. However, due to the requirement for flow tangency at the centreline, the flow has to be directed horizontally, which is achieved through a second set of oblique shocks, reflected from the first set. As observed by Wang and Yu (2015), at high nozzle pressure ratios the Mach reflection is materialized. It is complicated due to the formation of the slipstream between the subsonic and supersonic flow after the triple point and the interaction between the slip stream and the expansion waves. A schematic of the flow field can be seen on Figure 2.4. The expansion waves emanating from the interaction between the reflected shock wave RW and the free jet boundary bends the slipstream formed at the triple point T. This creates a virtual de Laval nozzle that accelerates the subsonic flow formed after the quasi-normal shock (Mach disc) to supersonic velocity. The practical importance of this interaction, as explained by Hadjadj et al. (2004), is its influence on the size and height of the Mach disc. These parameters are controlled by the conditions at the entrance and the throat of the virtual de Laval nozzle.

As mentioned earlier, if $\frac{p_j}{p_b} > 1$, the jet nozzle flow is in underexpanded regime. Due to the high static pressure of the jet flow, it has to be expanded over the lips of the nozzle through a set of Prandtl-Meyer expansions waves. The underexpanded jet regime, however, as discussed in the detailed review on the topic by Franquet et al. (2015), can also be subdivided into three states. At lower pressures the moderately underexpanded jet with regular reflections is manifested. If the pressure ratio is increased, however, a regular reflection of the intercepting shocks is no longer possible. Consequently, a Mach reflection with a curved barrel shock manifests. As discussed by Kieffer (1981) and Franquet et al. (2015), barrel shock is formed by the curved intercepting shock waves formed due to the reflection of the expansion waves from boundary of the jet. The intercepting shocks are near parallel to the jet boundary. They physically intercept the remainder of the expansion waves emanating form the nozzle lip and terminate them. The schematic of the flow field can be seen in Figure 2.5 and 2.2b. In case the pressure is increase to large values a extremely underexpanded jet structures are formed, the Mach disc can no longer

be modelled with a normal shock and the structures terminate after the first shock cell.

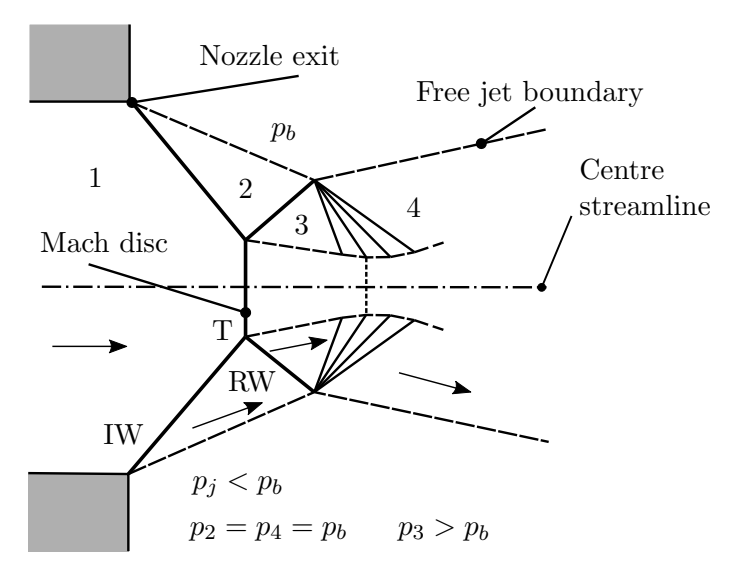


Figure 2.4: Schematic of the idealised free jet plume of an overexpanded Laval nozzle with Mach reflection reflection. Adapted from Zucker and Biblarz (2012) using theory from Wang and Yu (2015), Hadjadj et al. (2004) and Ben-Dor (2007)

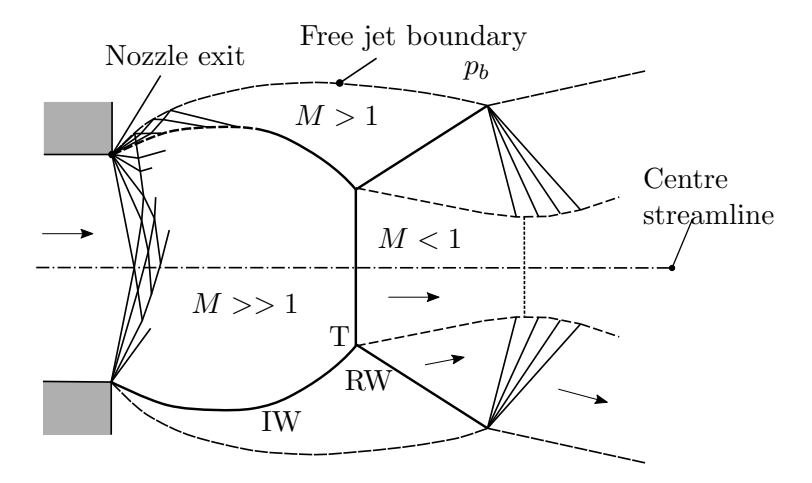


Figure 2.5: Schematic of the idealised free jet plume of a highly underexpanded Laval nozzle with regular reflection. Adapted from Kieffer (1981) using theory from Wang and Yu (2015), Hadjadj et al. (2004) and Ben-Dor (2007).

2.3 Gas dynamics of compressible jets in crossflow

The fundamental research on the gas dynamics of transverse jets in crossflow was performed by Morkovin et al. (1952), Zukoski and Spaid (1964), Hawkins et al. (1967) and Orth et al. (1969). The research was based on experimental simulations of the jet and their visualisation via Schlieren imaging and concentration measurements, in the case of Zukoski and Spaid (1964), as well as pressure measurements. Analytical or semi-analytical models for the prediction of the most prominent flow structures has also been developed.

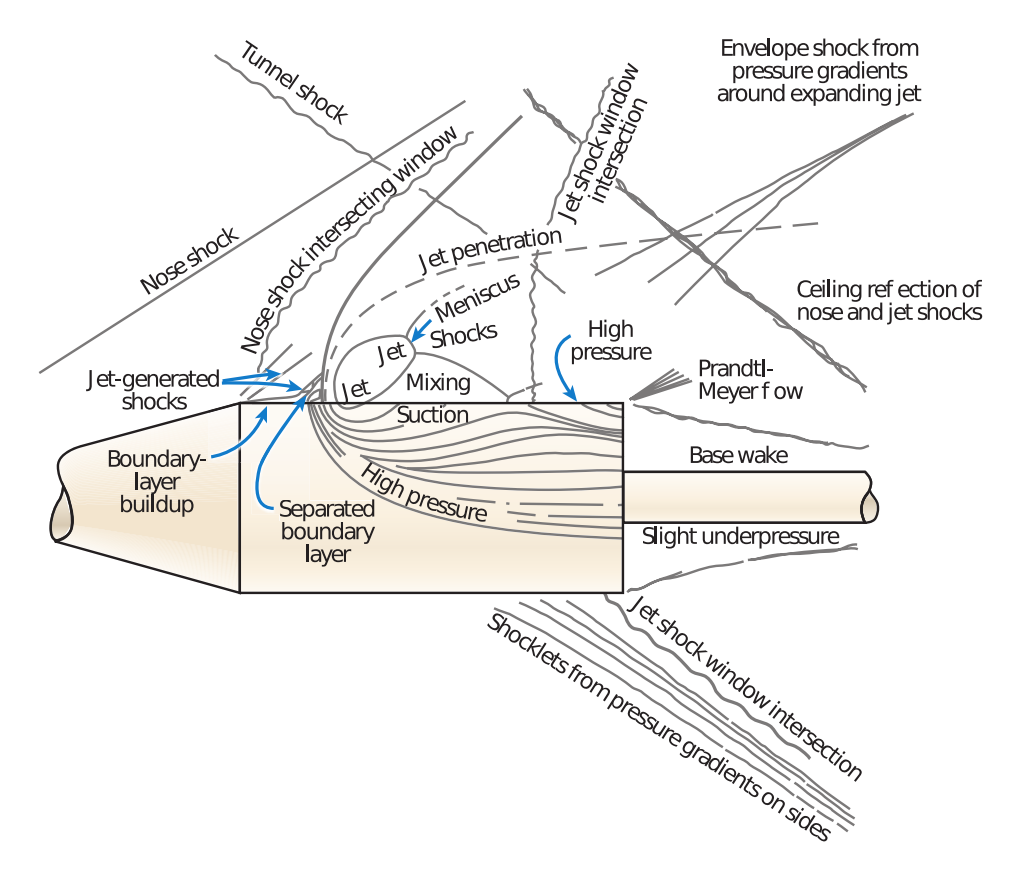


Figure 2.6: Schematic of the flow field around an axisymmetric body with transversely injected jet into supersonic crossflow. The schematic is created by Morkovin et al. (1952) and modified by Mahesh (2013)

Considering the case of underexpanded injection, if supersonic crossflow is applied, the shock structures sketched in Figure 2.1 and Figure 2.6 materialise. The surface pressure measurements around an axisymmetric body with reaction jet performed by Morkovin et al. (1952) are a good indication of the existence of the shock system and the separation regions discussed previously. As seen on the figures, the jet plume will turn sharply due to the streamwise momentum of the crossflow. As observed by Orth et al. (1969), the sharp deflection occurs directly after the normal shock. The cause for the sharp deflection is the reduced jet dynamic pressure downstream of the Mach disc Downstream of the jet, as seen in Figure 2.1, separation region is formed and the Y structure gets distorted due to the crossflow. To elaborate, one of the shock legs reaches the surface and reflects. This indicates that, due to mixing of the crossflow (defined as jet-pump effect by Morkovin et al. (1952)) and jet fluids, there is no slipstream discontinuity. Temperature and pressure measurements presented by Morkovin et al. (1952) affirm the contact of the jet fluid with the wall.

Besides the jet shock structures, due to the blockage caused by the injection, a detached bow shock wave is formed at a finite distance upstream of the injection port. Already during the first Schlieren experiments performed by Morkovin et al. (1952), a thickening of the boundary layer and its eventual separation due to the presence of the bow shock was observed. According to Orth et al. (1969), the separation occurs where the pressure rise on the surface due to the bow shock is more than 3 to 1. This, in term, leads to formation of an oblique shock at the foot of

the detached shock.

Finally a pocket of low pressure is formed behind the jet. It has been attributed to the "jet-pump effect" introduced by Morkovin et al. (1952) and discussed above. This pocket of separated flow applies suction to the crossflow circumventing the jet, which in turn would cause the streamlines of the crossflow to bent inwards, towards the jet wake as seen in Figure 2.6. This is an effect as will be observed in Chapter 2.5 is characteristic also for the suction created by the separation region behind incompressible jets.

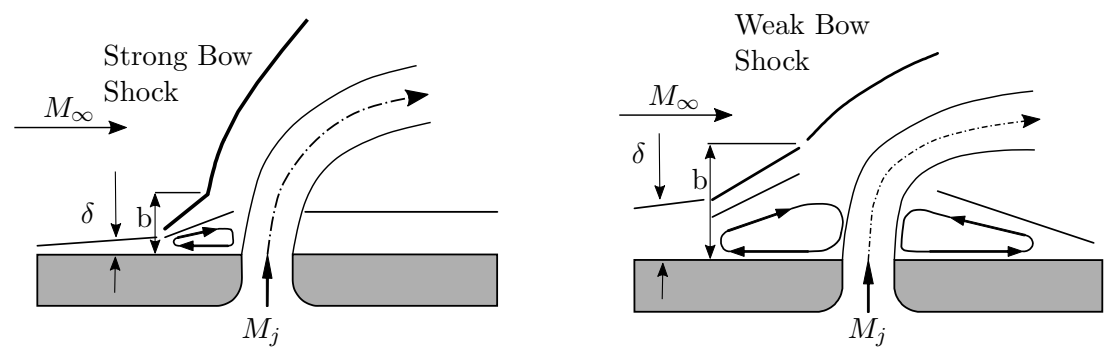
Before proceeding with the discussion, it is convenient to define a proper naming convention for the shock structures on the jet. From now on, the separation and detached bow shocks caused by the blockage of the jet will be related to as the interaction shock system. The barrel shock and Mach disc will be related to as the jet shock system. This definition is rather arbitrary, as the jet shock structure is dependent on the pressure changes over the interaction shock system, a topic discussed in the following section. However, the naming convention gives clear distinction between the systems.

2.3.1 Exhaust plume for jet in crossflow

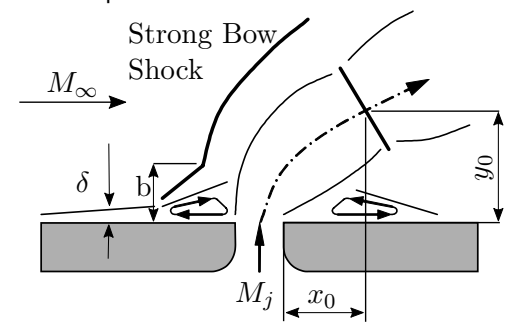
As observed by Orth et al. (1969), similarly to the case of free jets, jet shock structure in supersonic crossflow is also dependant on the ratio of the jet total pressure, p_{0_j} and the ambient pressure after the shock system, p_b . To elaborate, due to the direct relationship through the isentropic flow equation for pressure, presented in Equation A.2, the total pressure determines the jet exit pressure p_{e_j} , and thus the ratio p_{e_j}/p_b . Therefore, the operational regime of the jet in crossflow can be controlled in a similar manner to the one of free compressible jets.

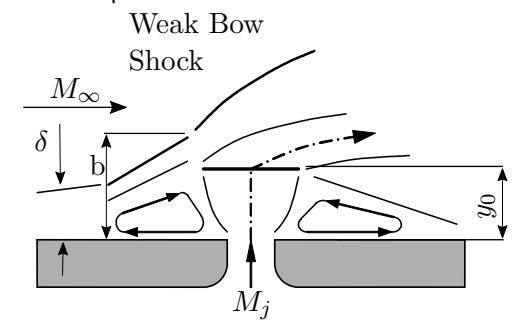
Departing from these observations, Orth et al. (1969) proposed that it should be possible to match the jet exit pressure p_{e_j} and the ambient pressure at the jet exit, such that the structures within jet are reduced to a minimum. This is the theoretical state referred to as "pressure matching". As will be discussed later, the concept of pressure matching and its effect on the jet shock structures is significant for both jet trajectory and mixing. To elaborate, according to model developed by Orth et al. (1969), the shape and the strength of the jet shock system determines the effective momentum of the jet behind the Mach disc and thus challenges the paradigm that to increase the jet penetration one could simply increase the jet total pressure p_{0_j} . To emphasise this, both Orth et al. (1969) and Heister and Karagozian (1990) suggest that the pressure-matched jet may be capable of achieving better penetration due to the loss of jet dynamic pressure as it passes through the shock systems. Furthermore, analysis of time-resolved Large Eddy Simulation (LES) results by Kawai and Lele (2009) relate the features of the jet shock structures to the formation of the jet shear layer vortices.

Compared to free jet, when crossflow is introduced to the problem of transverse injection, the flow field is further complicated due to the resulting viscous and shock interactions. Based on based on Schlieren imaging experiments, Orth et al. (1969) and Portz (2005) went on to define four typical flow fields encountered with transverse injection images. The latter are schematised in Figure 2.7. As explained by Orth et al. (1969), which flow field materializes depends on the size of the boundary layer and separation upstream of the orifice and the nozzle exit pressure ratio $\frac{p_j}{p_b}$. As seen in Figure 2.7, no flow field model is developed for overexpanded jet, such as the one encountered by Beresh et al. (2005a), who performed a far field PIV for a side force control jet.



 $\begin{array}{lll} \hbox{(a) Thin boundary layer with small separation and (b) Thick boundary layer with large separation and} \\ \hbox{matched pressure} \end{array}$





 $\begin{array}{ll} (c) \ \mbox{Thin boundary layer with small separation and un-} (d) \ \mbox{Thick boundary layer with large separation and underexpanded jet} \\ \end{array}$

Figure 2.7: Typical operational regimes for compressible jets in crossflow at different jet total pressure p_{0_j} , boundary boundary layer thickness δ and separation height b. (Based on figures and interpretations from Portz (2005) and Orth et al. (1969))

With respect to the nozzle exit pressure ratio, the mechanisms of wave formation have been discussed in the previous section. However, in the case of compressible jet in crossflow, high level of turbulence and rapid mixing exist already at the jet exit. Consequently, only the first shock cell materialises. The effect of the incoming flow properties has a significant effect on both the interaction and jet shock structures.

As discussed by Portz (2005), depending on the size of the boundary layer and the separation, cases with prominent bow shock or bow-separation shock interaction are formed. Thick boundary layer with large separation, compared to the jet penetration, and weak bow shock can be observed in Figure 2.7b and 2.7d. Thin boundary layer with small separation and strong bow shock can be observed in Figure 2.7a and 2.7c. The boundary layer separation itself however, is interrelated to boundary layer state and the adverse pressure gradient caused by the jet blockage. To elaborate, depending on the amount of blockage the detached bow shock is formed. The strength of the bow shock induces a wall pressure gradient and tends to separate the incoming boundary layer, forming the oblique shock at the foot its foot. As reported by Orth et al. (1969), the shock pressure ratio sufficient to cause separation in the flow and the advent of a oblique shock has been determined through empirical data to be around 3/1. Furthermore, as noted by Heister and Karagozian (1990), the separation occurs about 2-3 jet diameters ahead of the orifice.

Focusing on the underexpanded cases in Figure 2.7, Portz and Segal (2006) use the Mach disc

height as a measure of the boundary layer separation size in order to predict the advent of strong or weak shock formation. The results of the study shows that when the Mach disc height is larger than the separation size a strong bow shock is developed. The boundary layer separates but the separation is small compared to the penetration height. In the opposite case, where the Mach disc is of the same size or smaller that the separation region, provided that the sufficient pressure jump is achieved, a weaker, shallow bow shock is formed.

Shifting the focus on the jet shock structure itself, as discussed earlier, the jet exit pressure ratio is of paramount importance for the state of the exhaust plume. However, as observed by Orth et al. (1969) and later Papamoschou and Hubbard (1993) and Portz (2005), the ambient pressure at the injection orifice is strongly dependent on the pressure jump over the bow shock. First of all, depending on the shock strength, even when p_j is kept constant, the jet shock structure may change regime due to the backpressure enforced by the compression of the crossflow through the shock. Secondly, returning to Figure 2.7c, the large static pressure jump over the shock will bend the Mach disc in flow direction. In contrast, as seen in Figure 2.7d, the Mach disc is parallel to the wall because the static pressure jump over the weaker shock wave is smaller. However, the encountered numerical and experimental data neither proof nor disproof this concept as no horizontal Mach disc has been encountered.

Related to the above discussion, the effective jet-to-crossflow momentum flux ratio is also correlated to the shock structures. Increasing the ratio would result in deeper penetration of the jet, as observed by all consulted references, for example Gruber et al. (2000), Beresh et al. (2005b), Mahesh (2013). However, although easy to measure and well established as an important scaling parameter, the momentum ratio calculated using the crossflow values is different as compared to the one encountered by the jet itself. To elaborate, let us look at Figure 2.7a, ignoring the jet shock structures. As observed by Portz (2005), the dynamic pressure of the crossflow drops after it is compressed by the detached bow shock. As seen in Equation 2.2, the reduction in the effective dynamic pressure seen by the jet will, in fact, change the effective momentum ratio. This drop should then effectively change the jet penetration into the crossflow. A complex interrelationship, the changed penetration will alter the jet blockage, thus altering the shock strength and the effective momentum ratio. In addition, however, if now the jet shock structures are included into the analysis, as seen in Figure 2.7c the process becomes even more elaborate. As observed by Orth et al. (1969), Papamoschou and Hubbard (1993) and Portz (2005) the pressure jump after the interaction system determines the pressure field at the jet exit. This, together with the nozzle total pressure, determines the operational regime of the nozzle and affects the strength of the nozzle shock system. As a result, multiple studies have attempted to predict the pressure filed surrounding the injector port. At this point one can pose the question on the use of effective momentum flux for scaling.

2.3.2 Nozzle Backpressure models

A first order approximation of the pressure field around the injector based on surface inclination methods is proposed by Zukoski and Spaid (1964). The approximation uses modified Newtonian theory to calculate the forces exerted on the jet. However, the theory has several major limitations. First of all, Newtonian theory gives acceptable results for the pressure coefficient experienced by a solid body in hypersonic stream only when the Mach number approaches infinity and the specific heats ratio, γ approaches one. In such situation the flow deflection angle and the shock angle become equal. Furthermore, boundary layer effects and near-field mixing

between the jet and crossflow fluid have been omitted. Finally, as has been noted by Zukoski and Spaid (1964), it is expected that the theory is applicable only where the jet penetration is much larger than the boundary layer thickness and separation. In other words, in cases such as the ones seen on Figure 2.7a and 2.7c. More detailed discussion of Newtonian theory is presented in the following chapter and in Anderson Jr (2007).

Another model for the nozzle backpressure has been achieved through simplification of the interaction to a 2-dimensional model. Instead of complicated bow-separation shock system, a single bow shock with a normal shock portion in an inviscid flow is considered, conceptually shown in Figure 2.8. As a result, in this idealised model, the jet backpressure and total backpressure can be computed via the normal shock relationship for the static pressure jump over the wave and the Rayleigh Pitot formula. The relationships are derived in Zucker and Biblarz (2012) and Anderson Jr (1991) and state that:

$$\frac{p_b}{p_\infty} = \frac{2\gamma}{\gamma + 1} M_\infty^2 - \frac{\gamma - 1}{\gamma + 1} \tag{2.3}$$

and

$$\frac{p_{0_b}}{p_{\infty}} = \left[\frac{(\gamma + 1)^2 M_{\infty}^2}{4\gamma M_{\infty}^2 - 2(\gamma - 1)} \right]^{\frac{\gamma}{(\gamma - 1)}} \frac{1 - \gamma + 2\gamma M_{\infty}^2}{\gamma + 1}.$$
 (2.4)

In spite of its simplicity, as noted by Portz (2005), the complicated three-dimensional pressure field is not accurately represented by this simplistic model and an analytical approach is required. The simple shock wave model is thus either only used for analytical analysis of the dependent variables of the problem, for example Papamoschou and Hubbard (1993), or as a building block to higher-fidelity semi-analytical models.

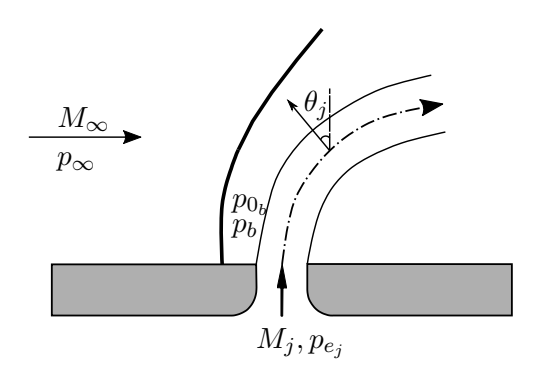


Figure 2.8: Schematic of a simplified jet in supersonic crossflow flow field based on Papamoschou and Hubbard (1993). The flow is inviscid and the jet is assumed to be perfectly expanded.

As early as 1969, a theory that provides approximation of the ambient pressure around the jet exit after the interaction shock system and its effect on the jet shock system was developed by Orth et al. (1969). The theory is based on earlier studies of free jets, where the nozzle exit pressure ratio, $\frac{p_j}{p_b}$, and the specific heats ratio, γ , is used for the determination of the jet Mach number, M_j and Mach disc vertical location, y_0 , as seen on Figure 2.7. Orth et al. (1969) modified the theory by approximating the jet as a 3-dimensional blunt body protrusion in the

flow. In the model the static pressure is expected to vary between a maximum at the stagnation point in front of the jet exit, to a minimum behind the jet. Therefore, the new "effective" backpressure, as defined by Orth et al. (1969), is expected to vary between these two values. The authors used geometrical similarity to model the jet as a cylindrical protrusion in the flow. For this particular flow case, experimental data for the average pressure field around a circular cylinder from the University of Maryland was available. According to the data the effective backpressure is approximated as:

 $p_{b_{eff_{Orth}}} = \frac{2}{3}p_{0_b},$ (2.5)

where p_{0_b} is the total pressure after a normal shock wave, as seen in Figure 2.8. The proportionality coefficient was determined via Pitot tube measurements. The total pressure is thus calculated using 2.4.

This empirical backpressure correlation was used in order to calculate the Mach disc height (see the following section) as a validation parameter for the Reynolds-Averaged Navier-Stokes (RANS) k- ω model by Viti et al. (2009) and a close match was achieved.

Finally, a higher-fidelity analytical/numerical model for the transverse jet in supersonic crossflow flow field was developed by Heister and Karagozian (1990). The model builds on the preceding works by attempting to calculate the pressure field surrounding the jet and include near-field mixing. Just as in the previous models, the boundary layer and any associated SWBLI structures are neglected. Due to the flow field complexity, Heister and Karagozian (1990) use a numerical model to calculate the pressure field surrounding the jet. For this, a first order Godunov method (Godunov et al. (1961)) is implemented. The method solves the 2-dimensional Euler equations for a number of finite cross-sectional slices of the jet. The jet is considered perfectly expanded. However, to apply the method the jet geometry has to be characterised based on the crossflow parameters. Due to the inherent bluffness of the jet cross-sectional geometry, Heister and Karagozian (1990) approximate the local equivalent cross-sectional Mach number, M_{eq} , as the Mach number occurring after a normal shock. However, due to the local inclination of the jet plume slices, the crossflow Mach number for the slice is taken as $M_{\infty} \sin \theta_j$. Details on the correlation can be found in Appendix A. According to this publication, the backpressure is approximately

$$p_{b_{eff}} = 0.5p_1 \tag{2.6}$$

in the range $M_{\infty} \in [2; 3]$, where p_1 is the static pressure after a normal shock wave.

All in all, multitude of approximations exist for the averaged pressure field surrounding the jet. However, due to the complexity of the interaction, none of the developed models accounts for the incoming boundary layer and separation. Furthermore, none of these encountered literature attempts to compare these models and/or state an equivalent local jet momentum flux ratio caused by the combination of reduced jet dynamic pressure after the disc and the interaction shock system. The correlations are simply used for the prediction of the operational regime of the jet nozzle.

2.4 Jet trajectory

The most investigated feature of the secondary injection flow field is the flow trajectory. The research on trajectory started with the first Schlieren and Shadowgraph visualisations captured

by Morkovin et al. (1952). Currently, more quantitative data is available, such as the far field planar PIV by Beresh et al. (2005a) and the near field Laser Doppler Velocimetry (LDV), performed by Santiago and Dutton (1997), providing better prediction of the actual trajectory and strength of the jet large scale structures. Furthermore, numerical studies implementing RANS, LES and hybrid methods have attempted to model the averaged and instantaneous flowfield, respectively. Despite of the difficulties of numerics with respect to simulating both flow discontinuities and resolving the turbulent structures of the flow, qualitative similarities with some experimental data has been achieved. The study of Chai et al. (2015), for example, used LES to compare time averaged results with the experiments of Santiago and Dutton (1997) and Beresh et al. (2005a).

The importance of the understanding of the jet trajectory, or, in particular, the transverse penetration and lateral spread of the jet, lies in in its importance with respect to the applications of the jet-in crossflow phenomenon. With respect to supersonic combustors, fuel penetration into the crossflow, as observed by Segal (2009), is related to the bulk transport of fuel into the air. Therefore, it is important prerequisite for mixing, facilitating quick combustion, as the residence time of the air within the combustor is of the order of milliseconds. Furthermore, as observed by Portz (2005), near-field penetration results in stronger vortex formation, known to enhance mixing. The second, major application, thrust vectoring of aerospace vehicles, requires accurate determination of the jet trajectory and spread, together with its turbulent characteristics, in order to predict the interaction with any bodies located directly after the jet, or, in the case of internal injection in rocket nozzles, to predict the effective obstruction and plume deflection for thrust vectoring.

In this section we will outline the different types of trajectory models, their major assumptions and the significance of the major parameters of the flow field on its topology.

2.4.1 Analytical model by Zukoski and Spaid

The first analytical model for the jet trajectory was developed by Zukoski and Spaid (1964). The model utilises the similarity of the injection flow field to the one produced by a blunt axisymmetric body immersed in supersonic flow. Thus, the shock structure seen in Figure 2.9 is reproduced by a quarter sphere followed by an axisymmetric body. To a acquire a functional relation for the penetration depth, Zukoski and Spaid (1964) determined the nose diameter by applying a momentum balance between the nose drag and the momentum flux of the injectant. The nose diameter of the equivalent body, in term, determines the effective vertical penetration of the jet. The functional relationship is established by making the following assumptions:

- 1. Sonic jet;
- 2. The crossflow boundary layer is neglected;
- 3. The mixing in the near-field is negligible;
- 4. The equivalent geometry is composed of the bodies described above, namely the quarter of a sphere followed by an axisymmetric body;
- 5. The separation zone behind the jet orifice lies in the equivalent body;
- 6. Pressure forces acting on the spherical nose are calculated through modified Newtonian flow;
- 7. The injected fluid expands isentropically to the ambient free stream pressure and flows tangent to it at the aft face of the spherical nose;

8. The momentum flux in out-of-plane direction (x-z plane as seen in Figure 2.9) is neglected.

To illustrate the model geometry a schematic of the control volume is presented in Figure 2.9. As seen on the schematic, θ is the local inclination of the surface tangential line with respect to the crossflow and h is the nose radius or, equivalently, the jet penetration height. The stagnation conditions after the normal shock are thus obtained when $\theta = \frac{\pi}{2}$.

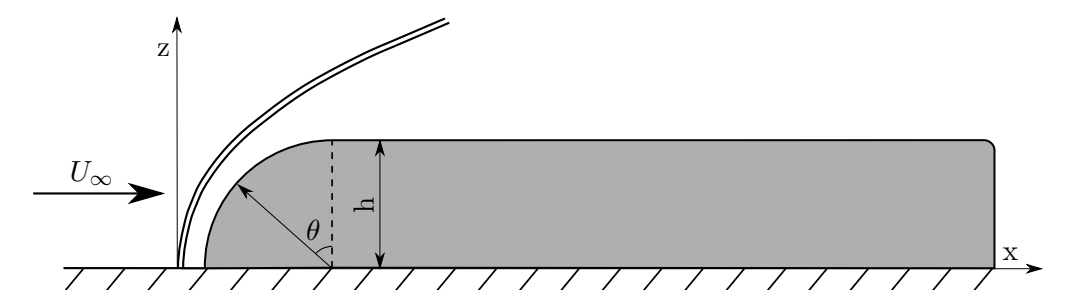


Figure 2.9: Schematic drawing of the analytical model of Zukoski and Spaid (1964)

In order to determine the radius of the equivalent body nose, the functional relationship developed by Zukoski and Spaid (1964) balances the axial forces on the outer and inner surface of the cylindrical nose. Namely,

$$F_{x_{Newton}} = F_{x_{jet}}. (2.7)$$

he pressure force excreted on the spherical outer face is obtained from the modified Newtonian theory. According to the modified theory by Lees presented by Anderson Jr (2007).

Without going into the detail of the derivation this results in the expression for the spherical nose radius or the equivalent jet disturbance heigh, defined as

$$\frac{h}{d(c^{\frac{1}{2}})} = \left(\left(\frac{1}{M_{\infty}} \right) \sqrt{\frac{p_{0_j}}{p_{\infty}}} \frac{\gamma_j}{\gamma_{\infty}} \frac{2}{C_{p_{max}}} \times \left\{ \frac{2}{\gamma_j - 1} \left(\frac{2}{\gamma_j + 1} \right)^{\frac{\gamma_j + 1}{\gamma_j - 1}} \left[1 - \left(\frac{p_{\infty}}{p_{0_j}} \right)^{\frac{\gamma_j - 1}{\gamma_j}} \right] \right\}^{\frac{1}{4}} \right). \tag{2.8}$$

The model was validated with maximum concentration profiles of argon and helium jets and showed good correspondence with the measured data. The penetration height has been show to correlate better with the line of maximum concentration rather than the jet's actual outer edge. However, due to the discovered large mixing in the near field, Zukoski and Spaid (1964) concluded that the model can only be applied in the direct vicinity of the jet exit. Finally, as previously mentioned, due to the inviscid nature of the flow and the lack of SWBLI, the model can only be used in cases in which the injectant penetration height is much larger than the boundary layer thickness.

2.4.2 Semi-analytical model by Orth

A semi-analytical model was developed by Orth et al. (1969). The model builds up on the previous correlations by introducing the additional jet penetration after the Mach disc height,

neglected in previous research. It is applicable for perfectly expanded and underexpanded jets. The model can be divided in two parts - the Mach disc heigh and angle empirical correlation, and the perfectly expanded jet solid body model. In the underexpended condition, a matched pressure jet analytical trajectory model is superimposed on the Match disc height and the initial conditions for the calculations are those past the normal shock. For the perfectly expanded case the analytical model can be used directly.

The analytical model for perfectly expanded jets is based on the following assumptions:

- 1. Two-stage hypothesis states that in the initial state of the injection the jet retains its identity while it is accelerated and turned in the crossflow direction. Therefore, near field mixing is neglected.
- 2. The second stage of injection, which is dominated by collateral turbulent mixing, is not modelled.
- 3. The modelled trajectory is a central streamline of the jet.
- 4. The plume is regarded as a solid body a series of segments of an infinite cylinder at an angle. These elements experience drag due to viscous shear and pressure caused by the interaction with the crossflow, which result in bending the plume. The drag coefficient is determined using empirical correlations defined by Horner (1965). The configuration is presented in Figure 2.10.
- 5. The cross section is approximated as an ellipse.
- 6. An empirically approximated separation heigh is subimposed on the set to account for increased penetration.
- 7. Jet mass flow remains constant, rendering the momentum balance equation along the jet axis unnecessary.
- 8. The model uses a local J_{eff} based on the pressure jump over the Mach disc.
- 9. The drag coefficient used in the model accounts for pressure jump over the shock, but the force is nondimensionalised using freestream conditions.

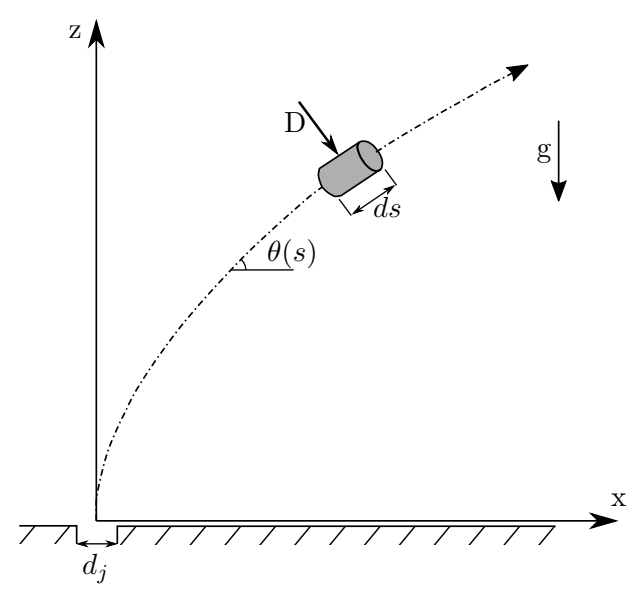


Figure 2.10: Centreline trajectory of the model by Orth et al. (1969)

Due to its later use for deriving comparison trajectory curve during the results analysis this method will be elaborated on in grater detail. Without getting into the details of the derivation of the momentum balance equation perpendicular to the jet axis, the integral form of the relation is defined as

$$0.88(2.5\pi)J\int_{\theta}^{\theta_0} \frac{d\theta'}{C_D \sin^2(\theta')} = (0.22\frac{s}{d_i} + 2.25)^4 - 2.25^4. \tag{2.9}$$

Here the integration is divided in two parts. The first starts from a lower limit, which is arbitrary, and ends at

$$\theta_1 = \sin^{-1}(M_\infty). \tag{2.10}$$

For this first integral the first part of the curved fit is used which is defined as

$$C_D = 1.2 + (M_{\infty} \sin \theta)^{7/2}.$$
 (2.11)

The second part of the integral is from θ_1 to θ_0 , which is either the incidence angle after the Mach disc or the injection angle. For this part of the integral the drag coefficient is defined as

$$C_D = 1.06 + 1.14(M_\infty \sin \theta)^{-3}.$$
 (2.12)

For the underexpended case it has been observed by Hawkins et al. (1967) that there is only weak dependence of the first Mach disc location on the separated zone. Therefore, the location of the disc is determined via the pressure matching $p_j/p_{b_{eff}}$. If no experimental data is available a fit to experimental data is developed by Orth et al. (1969), as seen in Figure 2.11. The horizontal displacement x_0 is taken as equal to the vertical displacement, based on data analysis by Orth et al. (1969).

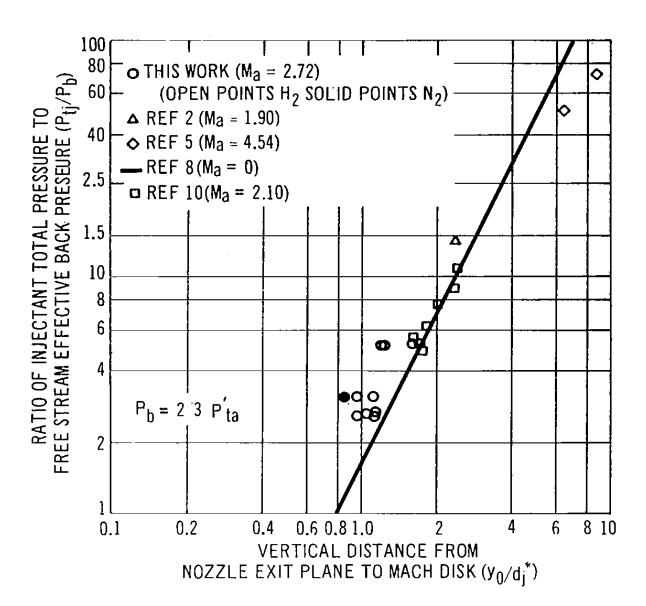


Figure 2.11: Mach disc distance Orth et al. (1969)

To superimpose the analytical trajectory correlation on top of the Mach Disc location, the initial conditions after the Mach disc are required. Looking at Equation 2.9, J, θ and C_D are required. C_D is obtained directly from the relationships defined by Horner (1965) and depend on the

crossflow Mach number and the jet incidence angle, θ . The jet incidence angle can be found using a line between the jet injection centre and the location of the Mach disc, as defined x_0 and y_0 . The only term left is the momentum ratio, J. For this, Orth et al. (1969) use an effective momentum ratio, J_{eff} , based on the Mach number after the Mach disc. However, the term in the denominator of Equation 2.2 is still based on the freestream conditions and not on effective backpressure. This term comes from the nondimensionalisation of the drag coefficient. The relation for the Mach number before the normal shock, $M_{j_{pd}}$, can be defined as

$$\frac{z}{d_j^*} = M_{j_{pd}}^{\frac{1}{\gamma_j - 1}} \sqrt{\left(\frac{\gamma_j - 1}{2}\right)^{\frac{\gamma_j}{\gamma - 1}} \frac{\gamma_j + 1}{4.8\gamma_j}},\tag{2.13}$$

where in this equation and in Figure 2.11, d_j^* is the equivalent sonic injector diameter given constant mass flow and the same exit pressure, p_j . Subsequently, the effective jet pressure and Mach number after the Mach disc, $p_{j_{eff}}$ and $M_{j_{eff}}$, can be found using the normal shock relationships defined in Anderson Jr (1991).

For the pressure matched case Orth et al. (1969) states that the pressure jump is already strong enough and boundary layer separation should occur. Consequently, an equivalence of drag between the reduced values in the separated region and the increased values above the separation has been performed for a solid cylinder. The relation shows an approximate equivalence giving a vertical displacement of the jet trajectory as calculated above in the order of $2\delta^{99}$.

Concentration measurements of cold H_2 and N_2 for both underexpanded and pressure-matched conditions (based on Equation 2.5) show slight under-prediction of the trajectory.

Furthermore, as discussed in Chapter 2.3, Orth et al. (1969) went on to postulate that the overpressurisation of the jet and the increase of the jet-to-crossflow momentum ratio does not lead to optimal penetration. To elaborate, due to the momentum loss over the Mach disc caused by the pressure mismatch, the effective momentum ratio after the the wave drops, directly reducing the penetration of the plume after the shock. This underlines the importance of the Mach disc height and strength for the penetration, which leads to the use of the effective momentum ratio, which however, still uses freestream values for the backpressure.

2.4.3 Compressible vortex pair model

Addressing the jet vortical structure and mixing with the crossflow, as well as the detailed pressure field resolution behind the detached bow shock, Heister and Karagozian (1990) developed a two-part model for the interaction with perfectly expanded jet. Due to the complexity of the interaction shock system, the crossflow is modelled numerically. The jet itself is modelled as a compressible vortex pair formed by the viscous and impulsive forces imposed on the jet boundary. The model is locally two-dimensional. The trajectory and mixing relation is formed by combining the vortex pair equations with a mass and momentum chalance between the two models along the jet axis.

As seen above, although detailed analysis of the parameters and flow field features has been performed, simple semi-analytical and numerical/analytical methods are unable to simultaneously account for all the complex parameters of the flowfield. Either near-field mixing is completely

omitted and effective backpressure is not fully implemented in the model, or the jet shock structures effect on the effective momentum of the jet after the shock system is not accounted for. In addition, configurations with overexpanded jets have not been modelled. However, the results have shown to be a good approximate of the jet penetration, within a defined margin of accuracy, for preliminary prediction of the jet trajectory. Furthermore, parametric analysis have shown the importance of the jet-to-crossflow momentum flux ratio as a main parameter.

Acknowledging the limitations of the previous methods in fully capturing the complexities of the flowfield, researchers focused on deriving empirical correlations based on experimental data and, later on, evaluating these correlations and using the data as validation for numerical simulations.

2.4.4 Empirical trajectory correlations

Due to the complexity of the flow field and the limitations of the different experimental facilities a multitude of empirical correlations for the jet trajectory exist. As observed by Mahesh (2013), most of these correlations are based on flow visualisations. Furthermore, the definition of the penetration curve has been based on multiple measurement criteria. As seen in the previous section, the Mach disc height was used by Zukoski and Spaid (1964), the concentration profiles of hydrogen have been used by Orth et al. (1969). Other studies use the visible upper edge of the plume as seen in Schlieren images, such as Ben-Yakar et al. (2006) and Papamoschou and Hubbard (1993), average intensity of 90% in the crossflow with Mie Scattering, such as Gruber et al. (1997) and visible upper edge with Planar Laser-Induced Fluorescence (PLIF) by Rothstein and Wantuck (1992).

The curve fits to experimental data, which are either logarithmic fit or power law curves.

The empirical correlations are based on scaling laws involving either the jet diameter, d_j or d_jJ as scaling parameters for the curve fits. A reference set of the most well established correlations that will be compared is presented Table 2.1. As seen in the table, the correlations are either a power law or logarithmic fits.

Paper	Experiment	Relation
Gruber et al. (1997)	Rayleigh/Mie	$\frac{y}{d_i J} = 1.20 J(\frac{x + d_j/2}{d_i J})^{0.344}$
	Scattering	, s
Rothstein and Wantuck (1992)	PLIF of OH	$\frac{y}{d_i} = 2.173 J^{0.276} (\frac{x}{d_i})^{0.281}$
		$\frac{y}{dz} = J^{0.312} \ln[4.704(\frac{x}{dz} + 0.637)]$
McDaniel and Graves (1986)	PLIF of iodine	$ \frac{y}{d_j} = 2.173 J^{0.276} \left(\frac{x}{d_j}\right)^{0.281} \frac{y}{d_j} = J^{0.312} \ln[4.704 \left(\frac{x}{d_j} + 0.637\right)] \frac{y}{d_j} = \frac{0.344}{M_{\infty}^2} \frac{p_j}{p_{\infty}} \ln[2.077 \left(\frac{x}{d_j} + 2.059\right)] \frac{y}{d_j} = 3.87 J^{0.3} \left(\frac{x}{d_j}\right)^{0.143} $
Rogers (1971)	Concentration	$\frac{y}{d_{s}} = 3.87 J^{0.3} (\frac{x}{d_{s}})^{0.143}$
	of H_2	
Lin et al. (2010)	Raman Scattering	$\frac{y}{d_j} = 1.16J^{0.72} \left(\frac{x}{d_j}\right)^{0.32} \theta^{0.11}$
	of ethylene	,
Papamoschou and Hubbard (1993)	PLIF of iodine	$\frac{y}{J} = 2.63J^{0.36}(\frac{x}{J})^{0.28}$

Table 2.1: Compilation of empirical trajectory relations

In the following paragraphs comparison of some of the correlations presented above will be made, based on experimental data and plots obtained from the consulted literature.

The first correlation in Table 2.1 is the power law fit by Gruber et al. (1997). As stated earlier, the fitting is done to the upper boundary of the plume as defined by the 90% intensity of the images obtained by the authors. Scaling is performed to d_j as, according to the observations of Gruber et al. (1997), low speed fits collapsed well using this criterion. It is important to note note that the penetration curves are only applicable for the near field of the injection, as the far-field values tend to infinity. Within the context of the experimental results of Gruber et al. (1997), good collapse between the data and the fit are achieved. As seen on Figure 2.12, the power-law correlation of Rothstein and Wantuck (1992) provides similar results, whilst the correlation of McDaniel and Graves (1986) under-predicts the penetration, compared to the other two curves.

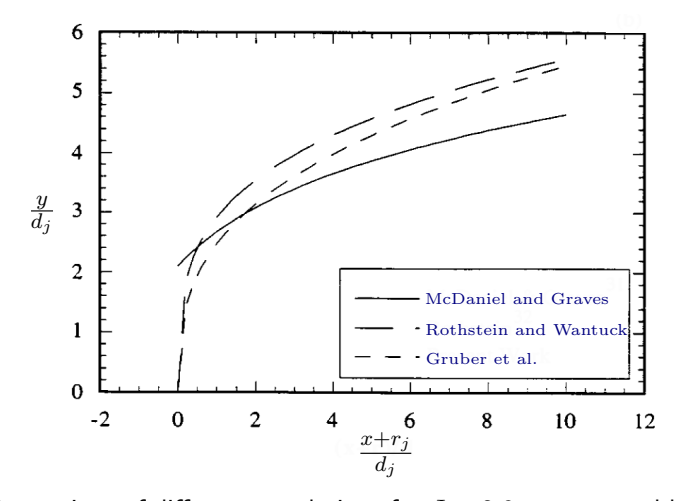


Figure 2.12: Comparison of different correlations for J=2.9 as presented by Gruber et al. (1997)

However, it is logical that a fit to a given experimental dataset would produce exceptional results for the given dataset, as compared to other data. To really validate the accuracy and limitations of a given fit, it has to be compared with results form other studies. Such a comparison of the fits included in Figure 2.12 is performed by Ben-Yakar et al. (2006) and Sun et al. (2013).

Within the framework of the experiments of Ben-Yakar et al. (2006), the penetration points are obtained manually from the visually observed upper edge of Schlieren images of hydrogen and ethylene sonic jets with nitrogen crossflow at $M_{\infty}=3.38$. The idea being, simulating the free flight conditions at M=10. According to Ben-Yakar et al. (2006), this measurement of the penetration has been shown to correspond to "about 1% concentration of molecularly mixed fluid". The measured data for 8 Schlieren images compared with the correlations from 2.12 are presented in 2.13.

As seen in the figure, the penetration as measured by Ben-Yakar et al. (2006) is higher than the one predicted with the formula of Gruber et al. (1997). A possible explanation presented by Ben-Yakar et al. (2006) is the fact that the visual observation provides information for the concentration line of 1%, whilst the study of Gruber et al. (1997) provides data for the concentration line of 10%. Better agreement is achieved with the correlation by Rothstein and Wantuck (1992). A final note, the shear layer development and the species effect on the penetration observed in Figure 2.13 will be discussed in the following sections, where analysis of the control parameters will be conducted.

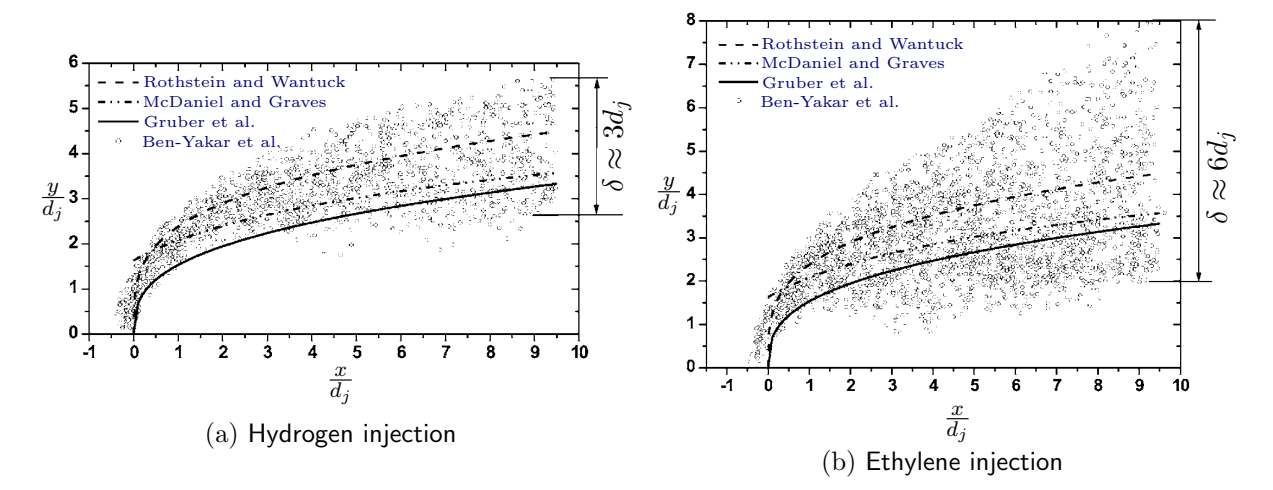


Figure 2.13: Transverse penetration comparison of different correlations with the data obtained from the experiments by Ben-Yakar et al. (2006) at J=1.5

A more recent study performed by Sun et al. (2013) used a novel visualisation technique providing higher spacial and temporal resolution for the imaging of the eddies in the mid-plane injection of Nitrogen gas - Nanoparticle-Based Planar Laser Scattering (NPLS). The technique is based on Rayleigh Scattering where nanoparticles are used instead of traditional seeding. According to Sun et al. (2013), the precision of the definition of the upper edge of the jet is thus more precise than the one of the experiments by Gruber et al. (1997)(10% concentration) and Ben-Yakar et al. (2006)(1% concentration). The comparison plots for the data obtained by the upper edge tacking (manual) for 40 instantaneous images is shown together with several trajectory correlations in Figure 2.14.

The correlation provided by Rothstein and Wantuck (1992) is based on experiments conducted with hydrogen in heated air cross-flow but, as seen above, it has been proven to show good correlation with unheated single-phase sonic injection. Furthermore, unlike the correlation of Gruber et al. (1997), a better prediction in the far-field is achieved. The trajectory overestimation is further amplified by the increase of the momentum flux ratio. Similar observation was also made by the analysis performed by Portz (2005), who, as will be discussed later, made a thorough analysis of different factors affecting the penetration and performed Schlieren experiments varying a large set of jet control variables.

Another two correlation curves are also introduced in the Figure 2.14. The correlation developed by Lin et al. (2010) is presented in Table 2.1 and is based on Raman Scattering of sonically injected ethylene in supersonic crossflow at Mach 2. The penetration height is defined as 1% of the mole fraction of ethylene. The study of Lin et al. (2010) concludes that the trajectory prediction of Gruber et al. (1997) is lower, just like the results of Ben-Yakar et al. (2006), which, again, can be explained with the different definition of the penetration height in the experiments. However, the opposite is observed in the figure above and best fit is achieved with the trajectory correlation of Rothstein and Wantuck (1992). To improve the issue with the diverging far-field prediction, Sun et al. (2013) proposes a modified trajectory correlation based on the one from Rothstein and Wantuck (1992). As seen in Figure 2.14, it indeed improves the

prediction in the far-field with the given dataset. The correlation is defines as:

$$\frac{y}{d_{\rm j}J} = \frac{2.933}{J^{0.5830}} \left(\frac{x}{d_{\rm j}J}\right)^{0.161} \tag{2.14}$$

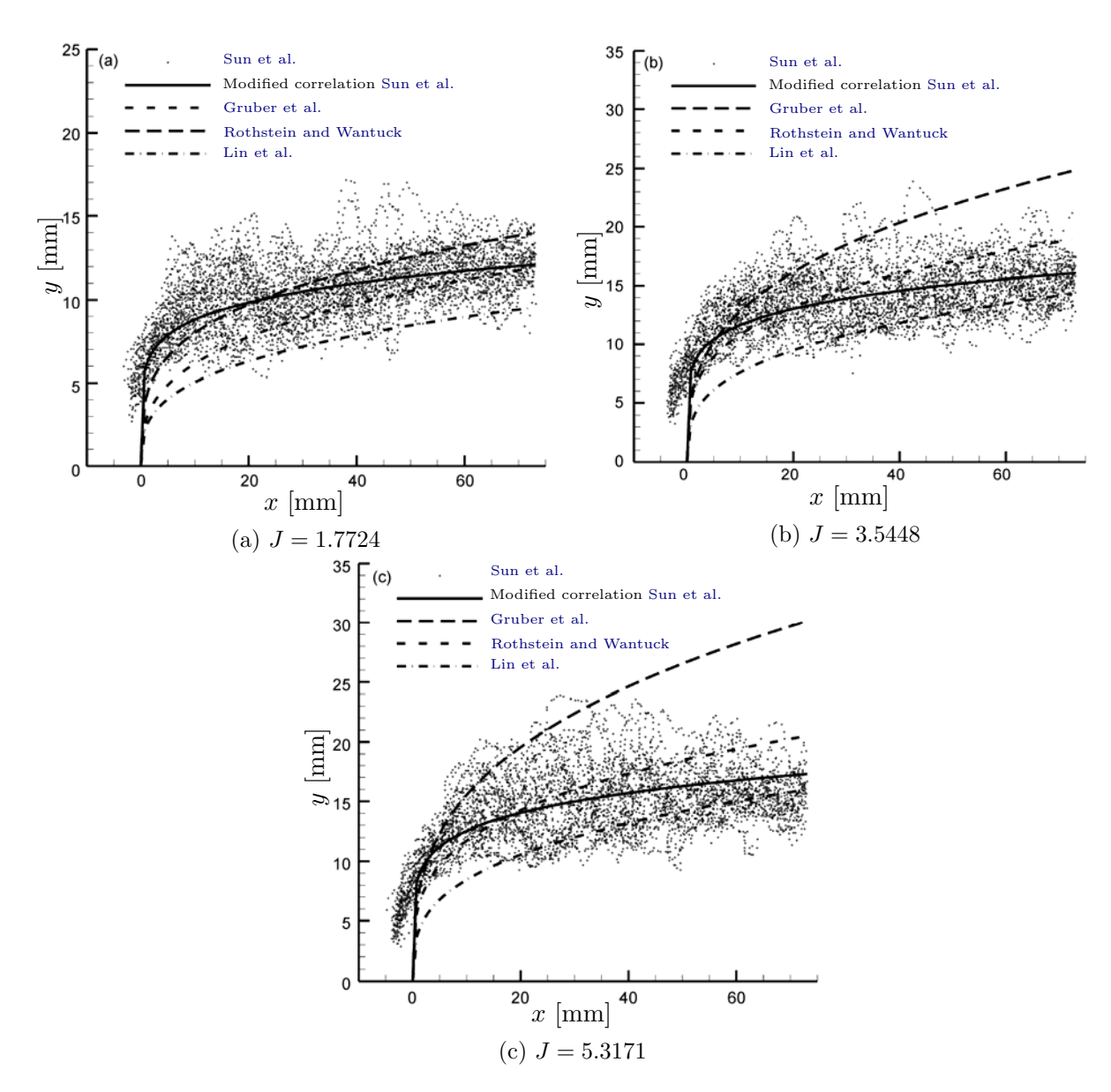


Figure 2.14: Transverse penetration comparison of different correlations with the data obtained from the experiments by Sun et al. (2013) and the modified correlation of Rothstein and Wantuck (1992) at different jet-to-crossflow momentum flux ratios

Finally, a detailed comparison of the trajectory correlations was also performed by Chai et al. (2015). Unlike the other studies analysed so far, Chai et al. (2015) performed LESs replicating the conditions of the experiments of Santiago and Dutton (1997) and Beresh et al. (2005a). Santiago and Dutton (1997) performed LDV at 4000 measurement locations for a sonic jet issuing

in Mach 1.6 crossflow at J=1.7 and $d_j=4$ [mm]. Beresh et al. (2005a) performed far-field PIV of a supersonic jet at $M_j=3.73$ into subsonic crossflow at varying jet-to-crossflow momentum flux ratios. It is important to note that, as seen previously, quantitative field measurements are relatively new tool in the research field of compressible jets in crossflow, one of the reasons being the complexity of their implementation. This underlines the importance of acquiring quantitative data for the validation of advanced numerical models, which claim to be able to simulate the flow field with sufficient accuracy to be used for design and analysis. Without going into further details in this section, the simulation results for mean velocities and turbulence intensities by Chai et al. (2015) show very good agreement with the data from Beresh et al. (2005a) and Beresh et al. (2005b). The comparison with the data for sonic jets in supersonic crossflow by Santiago and Dutton (1997) is good with respect to the mean velocity profiles, but worse considering the turbulence intensities. Chai et al. (2015) attributes these discrepancies to the lower Reynolds number of the simulations and/or the experimental uncertainties.

With the above in mind, Chai et al. (2015) compared part of the above-presented empirical correlations to LES acquired centre streamline trajectory. The comparison can be seen in Figure 2.15. According to the plot the trajectory by Gruber et al. (1997) matches most closely the one predicted with LES. However, the LES trajectory corresponds to a central streamline and the fit by Gruber et al. (1997) to 10% concentration. Furthermore the fit of Rothstein and Wantuck (1992) corresponds to 1% concentration and has been shown to predict a somewhat higher trajectory. A note has to also be taken that the scaling now also includes the momentum flux ratio and that, even when it is used as a scaling parameter, the trajectories do not collapse.

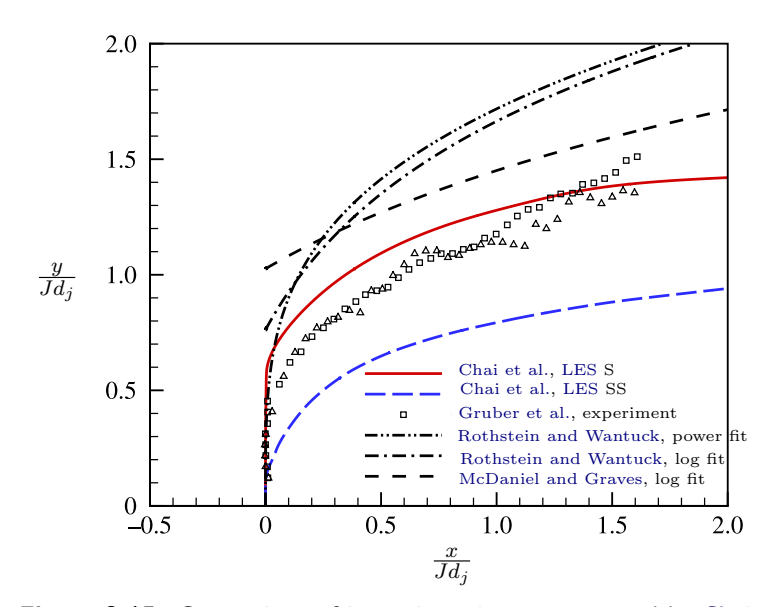


Figure 2.15: Comparison of jet trajectories, as presented by Chai et al. (2015)

As seen above, a large body of research exists on the modelling and prediction of the jet penetration and trajectory. The state of the art trajectory correlations have been compared and their derivation has also been analysed. Based on the consulted literature it can be concluded that greater accuracy has been achieved with power law curve fits. Thus, approximation of the trajectory is achieved, but there is a large scatter between the different fits. Tied with experimental visualisations, one of the immediate conclusions that can be drawn about any of the empirical correlations is that they are, in the particular, as accurate as the accuracy of the flow

measurement technique used. From the analysed trajectories, the closest one to most tested experimental sets is either the trajectory of Rothstein and Wantuck (1992), or its modification developed by Sun et al. (2013). Furthermore, the empirical correlations consider mainly the jet-to-crossflow momentum flux ratio and are developed for sonic jets. Additional, secondary effects such as the boundary layer thickness, crossflow and jet Mach number, whose importance for the shock structures has been shown in Figure 2.7, and the injectant species have not been taken into account in the discussed.

2.4.5 Portz correlation

In order to tackle all secondary effects on the trajectory and attempt to create a universal scaling law Portz and Segal (2006) conducted a parametric analysis and a large number of Schlieren experiments. The penetration was determined through visual observation aided by the difference of the refractive index between the crossflow composed of air and the injectants, including Helium, Hydrogen and Argon. The experimental variables of the experiments are summarised in Table 2.2.

Table 2.2: Compilation of empirical trajectory relations

Parameter	Range
$\overline{M_{\infty}}$	1.6, 2.5
J	0.5 - 3.0
$\frac{\delta^{99}}{d_j}$	0.8 - 3.7
Injectant gas	He, H_2, Ar

As seen above, based on the results from previous research, authors determined that the most influential parameters are the jet-to-crossflow momentum flux ratio, the boundary layer thickness and the molecular mass of the crossflow and injectant, as well as the freestream Mach number, used to determine the coefficients of the equation. One can see that the jet Mach number is excluded from the equation. Citing previous research, Portz and Segal (2006) state that the jet Mach number has little effect on the trajectory and also elaborates that most studies are done based on sonic jets. This indeed has been observed given a set J, due to close interdependency of the parameters. The correlation attempts to predict the location of the upper edge of the jet. The Reynolds effects on penetration have been found negligible.

$$\frac{y}{d_j} = AJ^B \left(\frac{x}{d_j} + C\right)^E \left(\frac{\delta^{99}}{d_j}\right)^F \left(\frac{\mathcal{M}_j}{\mathcal{M}_\infty}\right)^G \tag{2.15}$$

Where,

- $A = 1.0491 M_{\infty} 0.01924$
- $B = -0.0803M_{\infty} + 0.6145$
- $C = -2.34/M_{\infty}$
- $E = 0.406 M_{\infty}^{-0.08228}$
- $F = 0.0666M_{\infty} + 0.3252$
- G = -0.025

The above correlation showed good agreement when applied to the the experimental conditions of previous studies. The largest differences being caused by the differences in the crossflow Mach number. It is promising due to the fact that it accounts for additional control parameters, however, it should be further investigated how it compares in performance with respect to the already-established correlations and an independent dataset.

2.4.6 Trajectory parametric analysis

Due to the complexity of the flow field of the interaction there is a large domain of variables affecting both the jet trajectory and flow structures. The latter have been shown to include the free stream Mach number M_{∞} , the jet Mach number M_j , the ratio of the jet to effective backpressure $\frac{p_j}{p_{b_eff}}$, the ratio of free stream boundary layer thickness to the jet diameter $\frac{\delta^{.99}}{d_j}$, the shape of the injector port and the injection angle, and the molecular weights if the injectant species. The above statement being supported by the studies of Rothstein and Wantuck (1992), Gruber et al. (1994), Mahesh (2013) and Huang (2016). However, by far the most dominant control variable, as observed in previous research, is the jet-to-crossflow momentum flux ratio. A summarized dimensional analysis found in literature can be found in A. In this section we will observe the effects of the momentum flux ratio, jet and crossflow Mach numbers and boundary layer thickness. Given the scope of this study, the effect of injectant species and orifice shape are neglected.

Previous experimental and numerical studies have firmly established the dominant influence of the jet-to-crossflow momentum flux ratio on the jet trajectory. To elaborate, an increase in J leads to an increase in the transverse penetration, as observed by Rothstein and Wantuck (1992), Chai et al. (2015), Beresh et al. (2005a) and Portz and Segal (2006). Particularly interesting and conclusive are the results of Beresh et al. (2005a). As discussed earlier, the author performed far-field mid-plane, planar PIV. The full-field measurement provided streamwise, u, and vertical, v, velocity vector plots. Based on the vector plots the streamwise velocity deficit, $\frac{U_{\infty}(x)-u}{U_{\infty}}$, and vertical velocity, $\frac{v}{U_{\infty}}$, profiles were extracted for several horizontal positions. Subsequently, based on a least squares fit using 7 points about either the maximum deficit or vertical velocity location, the local jet penetration is established for the given location. The plot of the penetration correlations based on the flow velocities, representing the relation of the momentum ratio on the jet penetration, is presented on Figure 2.16. It can also be seen that based on streamwise velocity deficit the jet penetrates higher as compared to the trajectory based on maximum vertical velocity. Th vertical velocity being associated with an upwash imprint of the CVP, which will be analysed in more detail in Chapter 2.5.

One important aspect of the jet penetration that cannot be seen in the plots from Beresh et al. (2005a) is the difference between near- and far-field behaviour of the jet trajectory. As seen by the penetration plots presented by Portz (2005), the penetration in the near field increases rapidly with downstream distance, whilst the penetration in the far field increases gradually.

With respect to lateral spread of the jet, data is available from the early pressure measurements by Morkovin et al. (1952) as well as modern research data based on the use of flow visualisation techniques such as the Rayleigh/Mie Scattering performed by Gruber et al. (2000) and the PLIF performed by VanLerberghe et al. (2000) and full-field stereoscopic PIV performed by Beresh et al. (2006). Furthermore LES simulations data from the cases ran by Chai et al. (2015) are

also available. All of the above show that the lateral spread increases with the increase of the jet-to-crossflow momentum ratio in a similar manner as the transverse penetration.

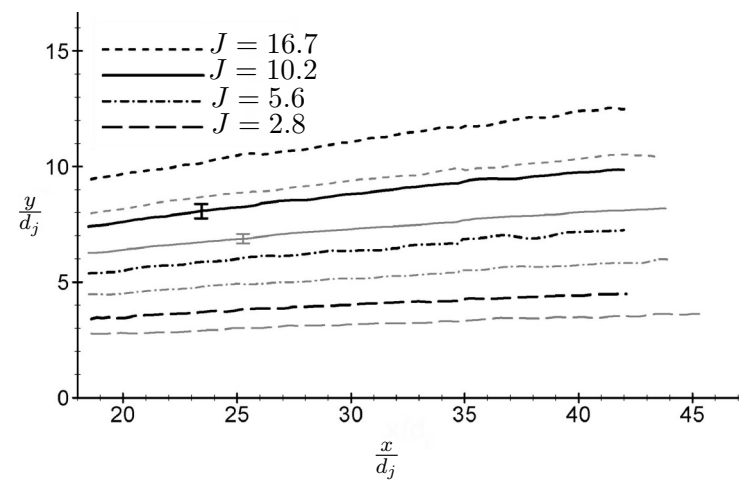


Figure 2.16: Jet trajectories found as loci of peak velocity locations; dark lines, trajectories derived from the streamwise velocity deficit and grey lines, trajectories from vertical velocity component. As presented by Beresh et al. (2005a)

As observed by Portz (2005) and Papamoschou and Hubbard (1993), the second major trajectory control parameter is the crossflow Mach number, M_{∞} . Above it was also shown, based on the derivations of Papamoschou and Hubbard (1993), that, unlike the jet Mach number, M_j , the freestream Mach number, M_{∞} can be varied rather independently form the jet-to-crossflow momentum flux ratio. The experiments of Portz and Segal (2006), Papamoschou and Hubbard (1993), Beresh et al. (2005a) and Beresh et al. (2006) show conclusively that the increase in the crossflow Mach number increases the jet transverse penetration and lateral spread. Returning to Chapter 2.3, increasing the crossflow Mach number effectively increases J by decreasing the dynamic pressure surrounding the jet exit. An exemplary functional expression for the effective jet-to-crossflow momentum ratio based on the local crossflow dynamic pressure behind a normal shock wave in the flow is developed by Portz and Segal (2006). The relationship is defined as

$$J_{eff_{M_{\infty}}} = J \frac{\gamma p_{\infty} M_{\infty}^2}{\gamma p_b M_b},\tag{2.16}$$

where p_b and M_b are the crossflow static pressure and Mach number behind the normal shock wave, respectively. The schematic of the simplified flow field that corresponds to this model was presented in Figure 2.8. For the $M_{\infty}=1.6$ experiments by Portz and Segal (2006), this led to $J_{eff_{M_{\infty}}}=2J$, increasing both transverse penetration and lateral spread in the same manner as J discussed in the previous section. However, as discussed in Chapter 2.3, empirical conditions for determining the conditions behind the interaction shock system will be more appropriate for the calculation of the effective jet-to-crossflow momentum flux ratio due to the complexity of the interaction.

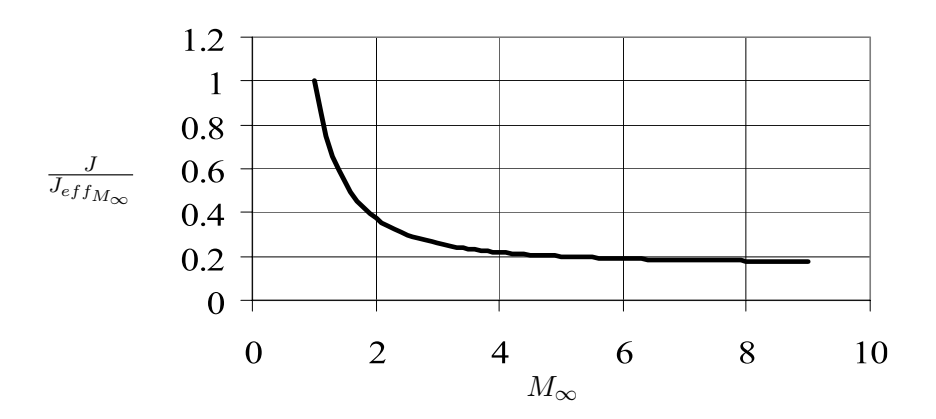


Figure 2.17: General-to-effective jet-to-crossflow momentum flux ratio based on simplified normal shock calculations versus crossflow Mach number. As presented by Portz (2005).

A more complicated topic with respect to jet trajectory is the effect of M_j . As observed by Papamoschou and Hubbard (1993), the jet Mach number, as well as the nozzle backpressure ratio, $\frac{p_j}{p_{b_{eff}}}$ are directly related to the jet-to-crossflow momentum flux ratio. Furthermore, due to the square in the relation, the jet Mach number and J are very strongly related. Consequently, from pure analytical observations, given a fixed J and M_{∞} , and thus $p_{b_{eff}}$, the change in jet Mach number will simply alter the pressurisation of the nozzle. Therefore, it should theoretically be able to alter the jet shock structures and the nozzle operational regime.

The trajectory results for variable M_j and constant J obtained by Papamoschou and Hubbard (1993) are presented in Figure 2.18. As seen in the figure, when the jet-to-crossflow momentum flux ratio is fixed, the variation in the jet Mach number provides no difference in the penetration.

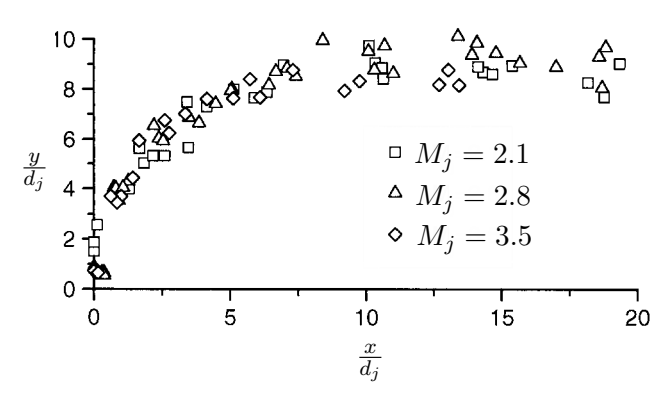


Figure 2.18: Trajectories of Helium and Argon jets with J=8.3 and $M_{\infty}=2$. As presented by Papamoschou and Hubbard (1993).

If J is not kept constant, given a sonic injection, over pressurising the jet, or, in other words, increasing $\frac{p_j}{p_{b_eff}}$, will increase the penetration, as J will increase, following Equation A.39. However, through concentration measurements, Orth et al. (1969) observed that the effects are not large for overexpanded and small for underexpanded jets. As discussed earlier, this is

caused by the losses over the jet shock structures. Returning to Equation A.39, to increase the jet-to crossflow momentum flux ratio one can then change the jet Mach number. It was thus observed by Papamoschou and Hubbard (1993) that the highly overexpanded jets have similar penetration to pressure-matched jets, allowing to reach similar penetration with lower backpressure and minimal jet structures.

Orth et al. (1969) performed experiments with constant mass flow and total pressure, showing an increase of penetration up to an optimum at around $M_j = 2.2$. However at these settings, the outlet diameter has to be changed, affecting yet another control parameter, $\frac{\delta^{99}}{d_j}$. Secondly, J and p_j change simultaneously, thus changing both the nozzle exit ratio and the jet-to-crossflow momentum flux ratio, not allowing to assess the effect of the nozzle overpressure itself on the penetration.

If the true local jet-to-crossflow momentum flux ratio is to be considered, firstly the effective backpressure and the Mach number behind the normal shock have to be used. Secondly, the Mach number and pressure after the Mach disc gave to be calculated. Then, a penetration based on the local J after the predicted Mach disc height can be developed.

Finally, as seen by the previous discussions, although the jet Mach number does not have any significant effect on penetration when the jet-to-crossflow momentum flux ratio is kept constant it plays an important role, together with the nozzle pressure ratio, on the jet shock structures. As observed by Santiago and Dutton (1997), this may have an important impact on the entrainment of the jet core after the Mach disc.

The different flow configurations based of the ratio $\frac{\delta^{99}}{d_j}$ and jet and interaction shock structures have already been presented in Figure 2.7. The most detailed observations of the boundary layer thickness effect on the jet trajectory have been reported by Portz (2005) and Portz and Segal (2006). As seen on Figure 2.19, the increase of the boundary layer thickness leads to increase in transverse penetration.

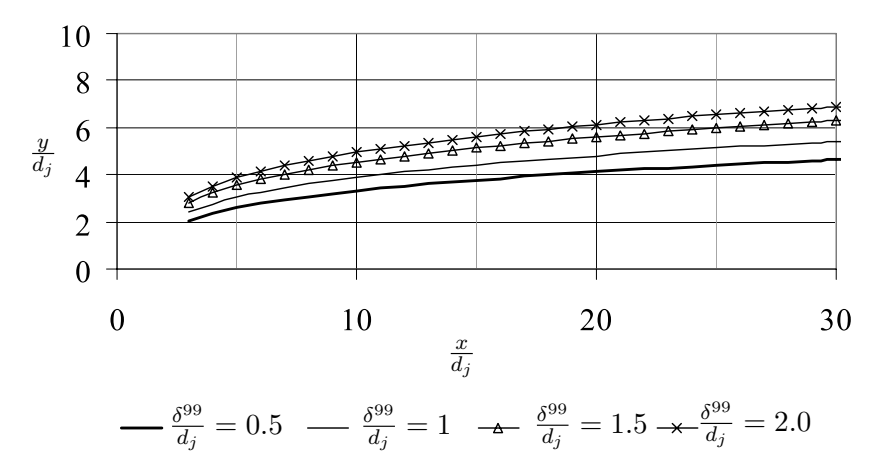


Figure 2.19: Effect of the boundary layer thickness on the jet penetration as presented by Portz (2005)

The main reason for the increased penetration is found to be the velocity reduction in the boundary layer. However, Portz (2005) also noted the dependence of the boundary layer effect on the crossflow Mach number, M_{∞} . With high supersonic Mach numbers part of the boundary layer is also supersonic. Consequently, the strong detached bow shock penetrates deeply into the

boundary layer itself, effectively reducing the dynamic pressure in the vicinity of the injector and thus increasing the local jet-to-crossflow momentum flux ratio. The higher M_{∞} , the stronger this effect and, as this mechanism for increasing the transverse penetration is more efficient, the boundary layer effect is diminished.

An additional observation on the boundary layer effect can be made by splitting the penetration into out-of-wall penetration and penetration after the boundary layer height has been reached. When the crossflow has a low Mach number and the boundary layer is thick, first of all, due to the weak bow shock the $p_{b_{eff}}$ is lower and penetration should be increased as discussed earlier. However, the effect of the thick boundary layer, as compared to the jet injection diameter, d_j , as observed by Portz and Segal (2006), is to bend the jet before it has fully penetrated the layer itself. Thus it emerges out of it already at an angle. As explained by Portz and Segal (2006), this results in weaker obliques shocks and locally produces a lowered effective jet-to-crossflow momentum flux ratio. Consequently, the penetration after the boundary layer thickness has been reached will be reduced. As will be discussed later, with the reduced obstruction.

2.5 Large-scale structures and mixing

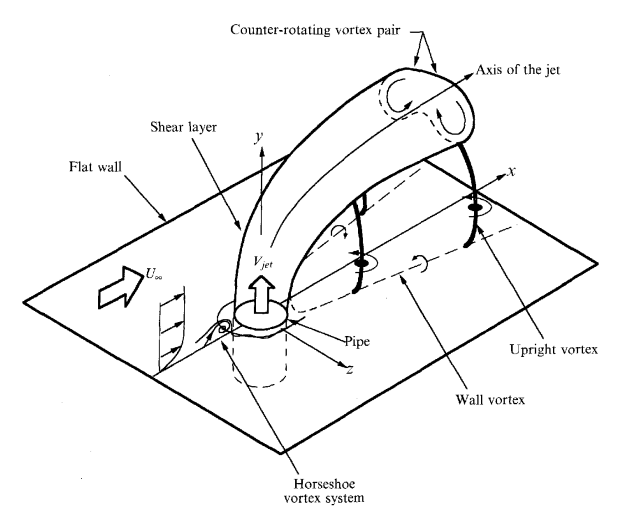
2.5.1 Incompressible jets-in-crossflow flow topology

The large-scale structures of compressible transverse jets bear many similarities with the structures observed in subsonic flows. Some of the most detailed descriptions of the incompressible jet structures have been provided by the experimental studies of Fric (1963), who used smoke-wire visualisations in combination with hot-wire measurements, Kelso and Smits (1995); Kelso et al. (1996), who used hydrogen bubble wire and smoke visualisation in combination with flying hot wire and the DNS performed by Muppidi and Mahesh (2007). The results of this research led to the categorisation of the coherent structures in four distinct groups - jet shear layer vortices, horseshoe vortices, CVP and wake vortices. The full overview of the structures is illustrated on Figure 2.20. As re-stated by Kelso et al. (1996), an important observation as to the origin of these structures was made by Fric (1990); Fric and Roshko (1994), namely: "...in a flow of uniform density, vorticity cannot be generated away from solid boundaries." Consequently, the structures should be generated by vorticity at the "...flat wall and/or nozzle boundaries."

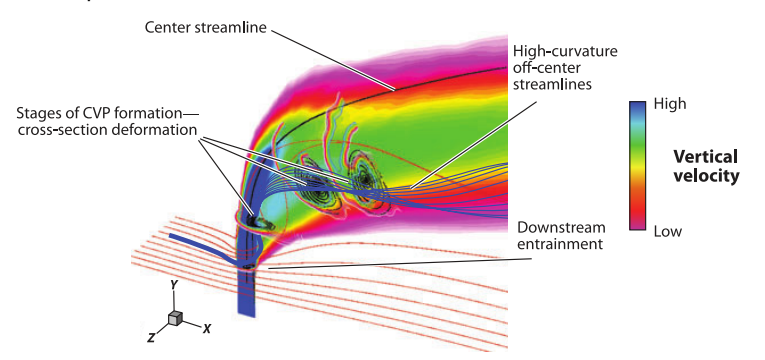
The first set of structures to discuss are the jet shear layer vortices. As observed by Kelso et al. (1996), at low Reynolds numbers a "hovering vortex" forms just above the upstream edge of the injection surface and a Kelvin-Helmholtz-like instability forms above it. With increasing Reynolds number the instability shifts towards the jet exit and periodic roll-up of the vortices is occurs. Upon exiting the orifice, as can be observed in Figure 2.21, the vortex rings are tilted clockwise, remaining parallel to the jet trajectory. Roll-up at higher Reynolds numbers occurs over the entire perimeter of the jet.

Furthermore, as stipulated by Kelso et al. (1996) based on experimental data and analysis of previous research findings, the vortex rings contribute to the formation of the second large-scale structure - the jet CVP. Upon roll-up the vortex ring folds. The conceptual interpretation of the vorticity redistribution leading to the folding of the vortex ring is presented in Figure 2.21a. To complement the CVP and shear layer roll-up formation theory, Kelso et al. make a superimposed composite of the vortex ring, tilting, stretching and folding, which can be seen in Figure 2.21b. To elaborate, the upstream segment of the vortex ring tilts and, as previously discussed, follows

the jet curvature. The downstream segment remains aligned with the jet trajectory. The edges of this downstream portion of the ring, as seen in the sectional views (A-A and B-B) in Figure 2.21a, contribute to the vorticity of the CVP. Muppidi and Mahesh (2006), on the other hand, propose a different explanation for the formation of the CVP, According to their analysis of a two-dimensional model problem developed for the study, the jet acceleration and pressure field are responsible for the formation of the CVP. Finally, as can be observed on Figure 2.20b, the CVP is located below the centre streamline of the jet and thus, the jet plume is wider on the leeward side. The CVP in turn creates upwash in the mid plane allowing to determine its location based on velocity or vorticity maxima.



(a) Flow topology for incompressible transverse jet injection. Obtained from Kelso et al. (1996). The wall and upright vortices are part of the wake vortex structure.

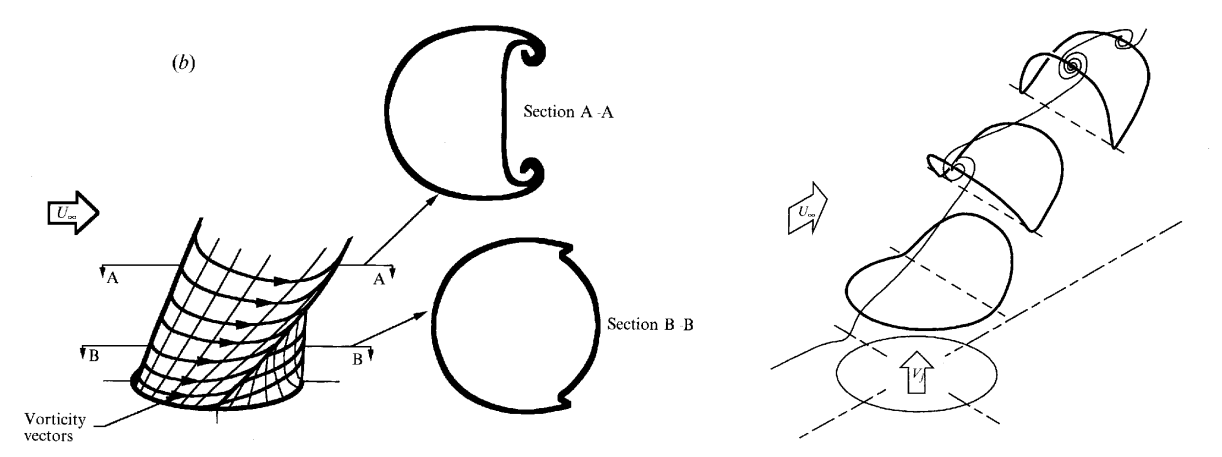


(b) Mean flow of incompressible transverse jet. Results from DNS by Muppidi and Mahesh (2007) where J=5.7 and $Re_i=5000.0$ Obtained from Mahesh (2013)

Figure 2.20: Incompressible transverse injection flow topology

The third set of structures is the horseshoe vortex system. Solid bodies are known to initiate horseshoe vortex formation due to the separation of the incoming flow caused by the blockage and the resulting pressure gradient. The blockage caused by the jet also ensues separation of the crossflow boundary layer and the formation of 3-dimensional horseshoe vortices. Furthermore, due to the formation of second separation zone behind the jet, the surrounding flow is sucked in towards the centreline. Consequently, the horseshoes are bend inwards towards the centreline as well. Finally, observed by Kelso et al. (1996), at low Reynolds numbers, the vortices with the

same vorticity sign as the crossflow boundary layer extend downstream along the wall, whilst the ones with opposite vorticity are incorporated in the jet CVP.



- of the vortex rings and, as stipulated by Kelso et al., leads to the formation of the CVP. Obtained from Kelso et al. (1996)
 - up and folding and tilting. from Kelso et al. (1996)

Figure 2.21: Incompressible transverse jet horseshoe vortex system

Finally, the observations of Kelso and Smits (1995); Kelso et al. (1996) establish that the upright wake vortices originate form the vorticity of the flat-wall boundary layer. The fluid at the wall outside the horseshoe vortices wraps around the jet due to the pressure gradient and local onset of separation combined with the upwash of the CVP, vertical boundary layer vortices are formed. The latter have been observed off the centreline and have been shown to exhibit unsteady, periodic characteristics. In addition, as discussed above, the horseshoe vortex wraps around the jet and, due to the low pressure region behind it, bends inwards and impinges on the wake vortices contributing to their vorticity.

2.5.2Compressible jets flow topology

The vortical structures of compressible transverse jets in crossflow may be, as explained by Ben-Yakar et al. (2006), "...partially extrapolated from studies of jets in subsonic flows."

Experimental research on the flow structures of compressible jets has been based mostly on mid- and cross-plane flow visualisations. The studies discussed previously provide information about the shock structures and the imprint of the vortical structures the mid-plane. Some of the most significant contributions have been made by the Schlieren and Shadowgraphy studies by Morkovin et al. (1952); Orth et al. (1969); Papamoschou and Hubbard (1993); Portz and Segal (2006); Ben-Yakar et al. (2006), the Rayleigh/Mie scattering by Gruber et al. (1997, 2000), as well as the PLIF by Hollo et al. (1992); Ben-Yakar et al. (2006)¹. With respect to large scale structures, as seen in Figure 2.22a, the mid-plane visualisations detected the separation zone related to the horseshoe vortices and the separation zone behind the jet due to the imposed

¹In fact, Ben-Yakar et al. (2006) use OH-PLIF, where OH is a naturally occurring combustion product during their experiments.

blockage, as well as the characteristic jet shear layer vortices. With respect to the origins of those structures, during their analytical research, Heister and Karagozian (1990) concluded that, similarly to the low-velocity interaction flowfield, the kidney shaped vortices are formed by the pressure field and viscous forces acting on the periphery of the jet.

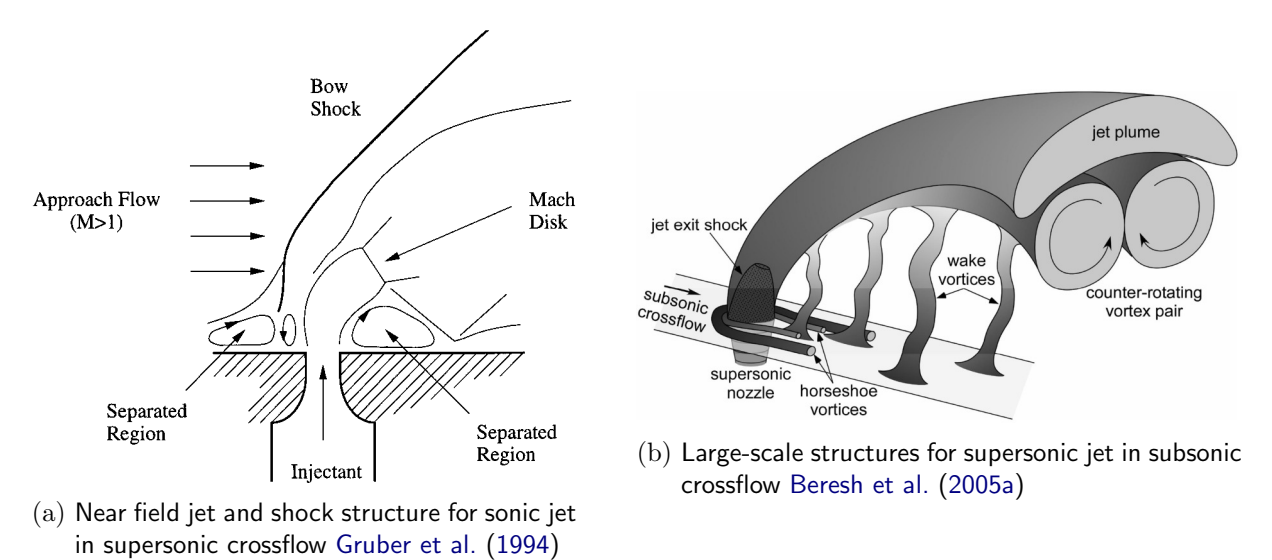
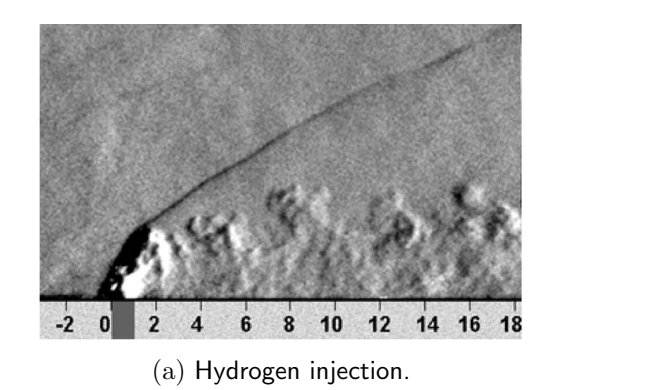


Figure 2.22: Flow structures encountered in high momentum jet injection

The dynamics of the shear layer vortices for different injectant species were analysed in detail by Gruber et al. (1997, 2000) and Ben-Yakar et al. (2006). A Schlieren visualisation of the mid-plane of the in flow field can be seen in Figure 2.23. The studies showed the shear layer vortices are generated in the near field and interact with each other. If eddies are merged they penetrate deeper into the crossflow due to the energy increase. Those eddies are then tilted along their trajectory. Depending on the velocity of the species, different velocity gradient can be established at the interface between the two fluids. When the eddies are tilted they are effectively stretched by the velocity gradient. Air and ethylene, for example, have high velocities. As seen in Figure 2.23b, as the eddies of ethylene turn, larger gaps and braid regions between the consecutive eddies form. Further stipulation by Ben-Yakar et al. (2006) is the claim that the two-dimensional shear layer vortices are actually part of circumferential rollers from hairpins. Data for high speed flows discusses this sort of structures only with very low momentum flux ratios. In addition, Ben-Yakar et al. go on to observe, similarly to Gruber et al. (1997), breakup of those structures in the mid-field, which can be clearly seen for the ethylene and air injection presented on Figure 2.23b and Figure 2.24b, respectively. The former then elaborates that this tearing is due to the arms of the vortex tubes not being able to sustain the shear stresses. Thus, Ben-Yakar et al. attributes the development mechanism for the large-scale eddies in the near field of the injection to "tilting-stretching-tearing".

Cross-plane visualisations provide information about the formation and development of the CVP, as well as the development of the shear layer eddies, seen previously. Such visualisations were performed by Gruber et al. (2000); VanLerberghe et al. (2000). To exemplify sets of instantaneous images from Gruber et al. (2000) is presented in Figure 2.24. In the first images, at $x/d_j = 0$, the jet plume, shear layer structures and the bow shock are discernible. Downstream, as the plume lift from the surface, the CVP is formed and the related upwash is observed. To

conclude, initiation of breakup of the CVP is visible at $x/d_j = 8$. Concentration measurements of jet cross-planes were also performed. For example Zukoski and Spaid (1964); Rogers (1971); Hollo et al. (1992).



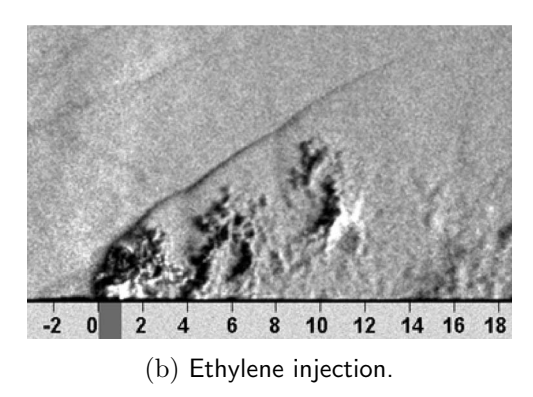
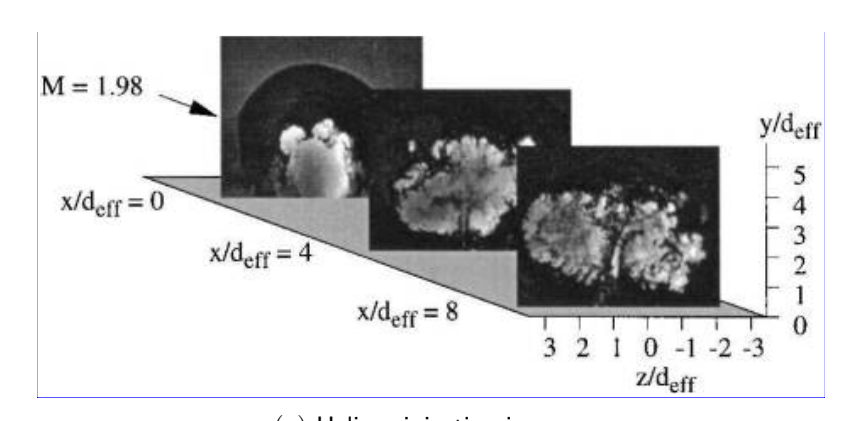


Figure 2.23: Schlieren of hydrogen and ethylene in supersonic crossflow. Exposure time of 200 [ns], J=1.4, $M_{\infty}=3.38$. Obtained from Ben-Yakar et al. (2006)



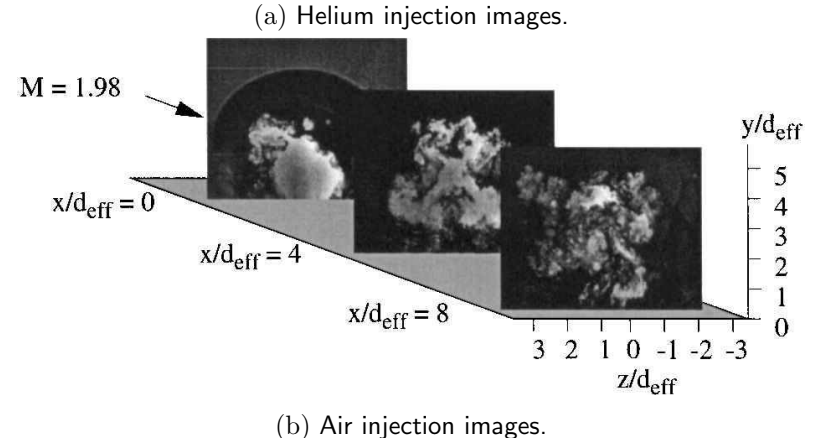


Figure 2.24: Instantaneous cross-planes images at three locations for circular injection of air and helium. $J=2.90,\,M_\infty=1.98$ Obtained from Gruber et al. (2000)

esides concentration and pressure measurements, the quantitative experimental data, and, in particular, full-field data, for compressible transverse injection is scarce. Santiago and Dutton

(1997) performed LDV for the near field of a jet in Mach 1.6 crossflow. One mid-plane and two cross-plane measurements were taken for a single momentum flux ratio of 1.6. Furthermore, far-field mid- and cross-plane PIV has been performed by Beresh et al. (2005a,b, 2006). The experiments of Beresh et al. were performed at transonic crossflows for several momentum flux ratios. As seen by the schematic on Figure 2.22b, similar structures were observed with such injection cases. Furthermore, it has been observed, as seen on Figure 2.31a, that with increasing distance from the injection orifice the CVP depart further away from the wall, thus, even in the far field the injection fluid is not parallel. Furthermore, the vortices also loose their strength and become larger as the advance in the flowfield. Beresh et al. (2005b) also used a conditional ensemble averaging procedure to produce the mean size of the shear layer vortices. It has been concluded that for lower momentum flux ratios this diameter increases and for higher J it decreases.

The numerical studies of transverse injection into supersonic crossflow utilise either RANS, LES or Detached Eddy Simulation (DES) models. As observed by Mahesh (2013), most computations are based on algebraic mixing length and eddy-viscosity models. RANS models aim at obtaining the averaged flow structures, whilst LES aims to capture the development and dynamics of the vortical systems. The use of DES is related to reducing the computational costs of LES. As mentioned previously, Kawai and Lele (2009) observed that capturing the discontinuities together with the resolving the turbulent eddy motions present a difficulty at high Reynolds number flows. The importance of the Reynolds number on the large scale structures has been underlined by Eberhardt and Hickel (2015). In particulat, it affects the separation zones and the Mach number before the Mach disc. However, several numerical LES and DES simulations show good collapse with the available experimental data. Yet, quantitative experimental data for validation at different M_j and J is not readily available. Such studies include the LES performed by Eberhardt and Hickel (2013, 2015, 2016); Chai et al. (2015); Rana et al. (2013), DES was performed by Muppidi and Mahesh (2007); Kawai and Lele (2009). As observed by Huang (2016), the latter confirm the existence of teh established canonical jet vortical structures.

However a recent DNS study performed by Sun Sun and Hu (2018). The shows that vortical structure in the compressible case may be more intricate due to the existence of extra term in the vorticity production caused by compressibility of the flow - the barcoclinic effect. This effect was also analysed by Eberhardt and Hickel (2015, 2013), but, besides alteration of the strength and size of the eddies and turbulence stresses due to the Shock-Turbulence Interaction (STI), no change in the topology was observed. Figure 2.25 presents the concepts discussed above.

2.5.3 Low momentum ratio jets

Despite the largely accepted convention of the canonical jet-in-crossflow flow topology for both compressible and incompressible jets it has been observed that different flow structures may form with cases of low J. Such observations have been done by Sau and Mahesh (2008); Mahesh (2013); You et al. (2013).

Incompressible jet studies such as the DNS performed by Sau and Mahesh (2008) for J < 2 and experimental studies reported in Mahesh (2013) for J < 1 show that no vortex rings are formed. Instead, a train of hairpins has been observed. These structures can be seen on Figure 2.26. As theorised by Mahesh, the hairpins form due to the crossflow boundary-layer vorticity overwhelming the oppositely signed jet orifice vorticity and causing shedding at the

trailing edge of the jet exit. It has also been observed that at high jet Reynolds numbers, where high is regarded mode than 300, the Ω - shaped vortices become more unsteady.

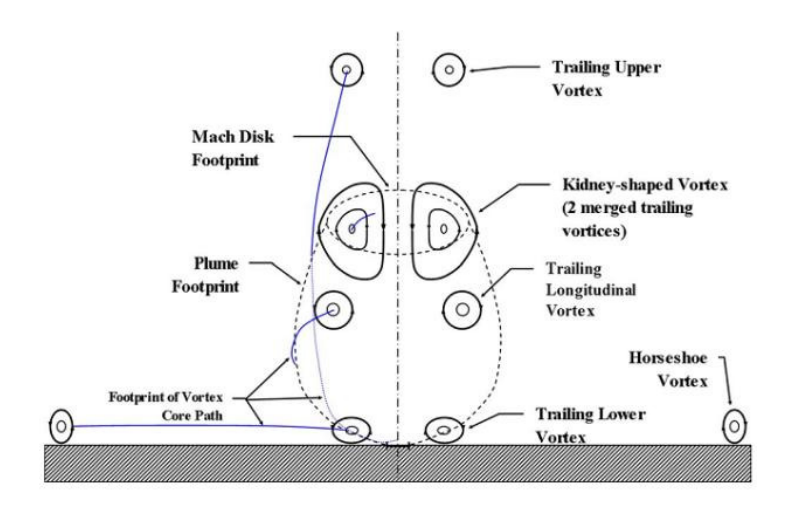


Figure 2.25: Jet vortical structures from DNS results. Obtained from Sun and Hu (2018)

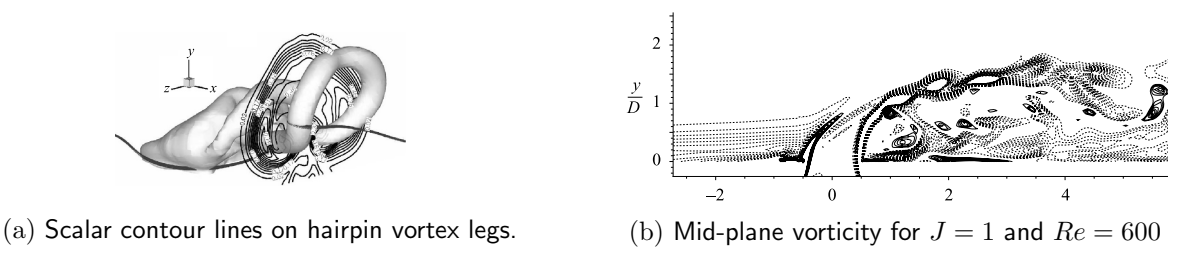


Figure 2.26: Hairpin vortices encountered at low momentum injection for low velocity jets. Obtained from Sau and Mahesh (2008)

The experimental and numerical data on the topic of low momentum flux injection for jets in supersonic crossflow has been found to be rather scarce. One such study is the DES performed by You et al. (2013). The study aimed not only at evaluating the capabilities of this combined method to resolve the turbulent structures of the flow, but also to investigate the particular case of low momentum compressible jets. This particular case represents the fuel injection in the combustor of the HyShot II SCRamjet developed at the University of Queensland. The simulation modelled a sonic Hydrogen injection at Mach 2.4 crossflow at momentum flux ratio of 0.35.

The DES results showed several major differences of the the-near field flow structures. Those include the change of the interaction and jet shock structures. A Mach contour of the near-field of the interaction is presented in Figure 2.27. Besides the formation of a hovering vortex, a non-uniform pressure forms over the nozzle in the centreline. This causes a different structure formation as compared to the simple cases of over-, under- and perfectly expanded jet. In particular, the bow shock causes a sharp pressure jump leading to the need for the formation of a detached normal shock at the windward portion of the jet orifice. The leeward portion forms the characteristic barrel shock and Mach disc. Streamlines downstream of the jet show a formation of a nodal, a similar one was also observed by Kelso et al. (1996) with low velocity

jets. Entrainment of the crossflow is also visible. To validate the results You et al. compare different numerically obtained data due to the fact that there were no quantitative experimental data available at the time.

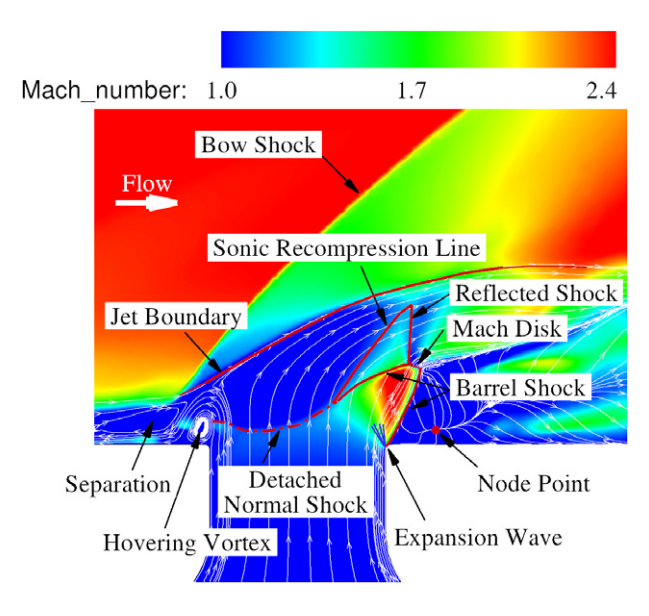


Figure 2.27: Mach contours at the injection mid-plane in the near field of jet system. Obtained from You et al. (2013)

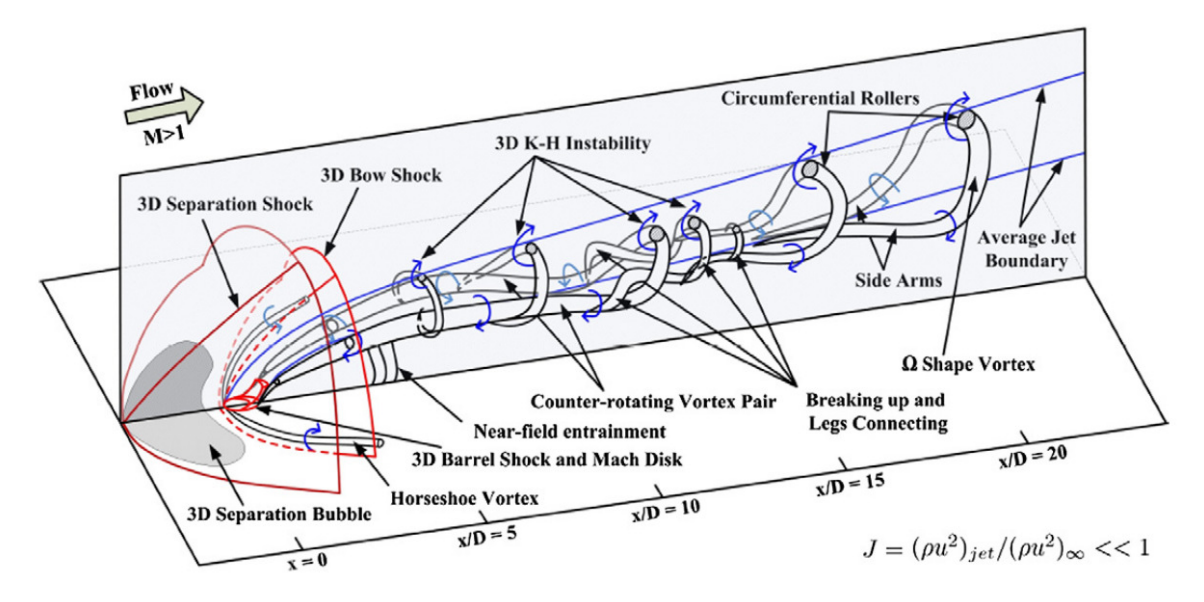


Figure 2.28: Impression of the structures encountered in low momentum jet injection. The image is based on analysis of plots of iso-surfaces of a positive value of the Q criterion. Obtained from You et al. (2013)

A composite impression of the full-field flow topology is presented in Figure 2.28. Until 5 jet diameters the characteristic topology is observed including the formation of CVP, wake vortices

44 Literature Review

and horseshoe vortices. The shear layer vortices are visible as 3-dimensional Kelvin-Helmholtz instabilities wrapping around the vortex pair. Around 10 to 15 diameters, however, the CVP starts to transform into Ω -shaped structures and breaks apart. To elaborate, as explained by You et al., initially a parallel ring structures, the Kelvin-Helmholtz instabilities tilt due to the large velocity gradient. The rings then open and the legs connect. When the CVP starts breaking down the instabilities connect with the shed vortices to form the Ω -shaped structures.

2.5.4 Mixing

As observed by Segal (2009), within a prospective operational envelope of a SCRamjet engine, around Mach 6 to 10, with the expected compression ratios of about 3 to 1, the combustor inflow Mach number ranges between 2 and 3. In order to manufacture an airframe of feasible sizes, a residence time in the order of milliseconds will be achieved. During this time the injected fuel has to penetrate the crossflow, mix with the flow from the intake and combust. The combustion is initiated due to molecular collisions, resulting in chemical reactions and the related heat release. This cannot be achieved until the species have mixed on a molecular level.

As seen in the previous paragraph, the molecular mixing proceeds any chemical reactions. According to the observations of the existing body of knowledge, Segal (2009) emphasises its significance as the longest process and thus the limiting factor in the combustion chamber.

The major mixing mechanisms for the transverse injection configuration have have been established by a multitude of experimental and numerical studies, summarized in detail by Mahesh (2013) and Huang (2016). The mixing mechanisms for the near and far field differ in their nature. In the far field the diffusion mixing is dominating. In the near field, as noted by Segal (2009), bulk mixing due to non-parallel streamlines and formation of large vortical structures is encountered. To elaborate, as discussed by Ben-Yakar et al. (2006), in the process the entrainment-stretching mixing mechanism is most significant. The latter is also supplemented by the flame holding potential of the separation induced by the detached bows shock and the related horseshoe vortex system. Hollo et al. (1992) found that the transition between the two mixing regions occurs around $10 - 20d_i$.

Near field mixing

Ben-Yakar et al. (2006), who performed Schlieren and OH-PLIF of hydrogen and ethylene, observed that the entrainment-stretching mixing in the near field is caused by the shear layer vortices. This is, indeed, one of the major, but not only mechanism for mixing in the near field. On macro scale, fluid from the free stream is engulfed within the eddies due to the velocity gradient on the fluid interface. These vortical structures also cause stretching of the interface between the two fluids and steepening of the concentration gradients at the interfaces. The OH-PLIF also suggest that, depending on the convective Mach number of the jet, mixing can either occur at the interface of the large-scale structures or penetrate deeper into the core of the jet. To complement those observations, Santiago and Dutton (1997) also observed high Reynolds shear stresses at the shear layer regions, suggesting highly correlated turbulent structures and rapid mixing.

The potential of near-field mixing for transverse jets in supersonic crossflow was already underlined by the argon and helium concentration measurements performed by Zukoski and Spaid

(1964). According their data, presented on Figure 2.29a, already at distance 2x/d, where d is the calculated penetration height using their analytical model, maximum concentration is 0.8. Consequently, Zukoski and Spaid (1964) concluded that the injectant is already substantially mixed with the crossflow. Furthermore, downstream mixing of the injectants has been concluded to be slower than the one in the near field.

To elaborate, the authors attributed the rapid mixing to the shape of the crossplane concentration profiles, as seen in Figure 2.29b. The kidney shaped pattern is the imprint of the CVP formed by the jet, the second major mixing mechanism. They further went on to recognise the upwash of gas from the wall to the centre of the vortex pair.

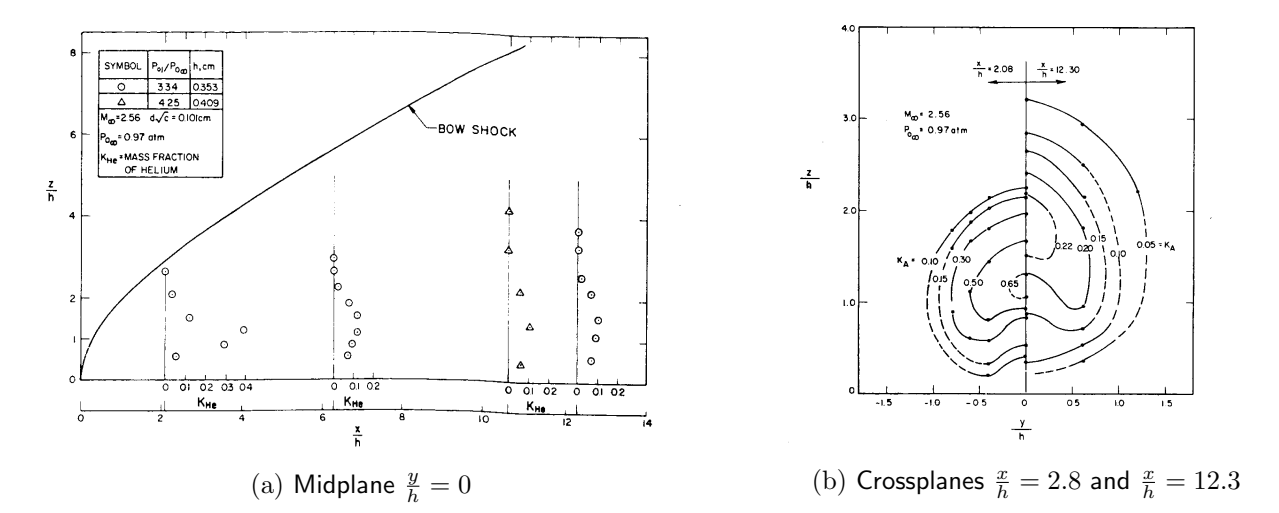


Figure 2.29: Concentration measurements with helium injection from Zukoski and Spaid (1964)

Further observations on the near-field mixing were reported by Morkovin et al. (1952) and Rogers (1971). The combination of Schlieren and Shadowgrapy visualisations and pressure measurements performed by Morkovin et al. reveal the separation zone behind the jet. It is further observed that the mixing in this region is especially violent. The potential of this separation zone behind the barrel shock was also observed by Santiago and Dutton (1997) through LDV. As suggested by Santiago and Dutton, the low Reynolds stresses and high velocity gradient cause the unmixed crossflow to wrap around the jet and and impinge on the plume. Going a step further this can be related to the upwash at the centreline observed by Zukoski and Spaid (1964); Gruber et al. (2000); Beresh et al. (2005a, 2006). This upwash has been observed to entrain the crossflow fluid, which reminds of the wake vortices occurring in low speed jets observed by Kelso et al. (1996). The influence of the barrel shock structure has also been recognised by Eberhardt and Hickel (2015). According to Eberhardt and Hickel, the injectant initially confined within the barrel shock contours becomes subsonic as it passes through the normal shock. This core is then mixed with the surrounding fluid. Therefore, observed by Eberhardt and Hickel (2015) and Santiago and Dutton (1997), the size and shape of the barrel shock can have a significant influence on the mixing characteristics in the near field.

Hydrogen mass fraction measurements performed by Rogers (1971) show that jet maximum concentration decreases to 12% in only $7d_j$. According to the author the mixing length required for stoichiometric average fuel-air ratio based on cold mixing is around 10 hydraulic diameters.

46 Literature Review

Significance of flame-holding

In the previous sections the importance of the shock induced separation in front of the jet plume, as well as the resulting 3-dimensional horseshoe vortex pair and its relation to the flameholding capabilities of the injection system were mentioned. It is only proper that we establish the importance of the flameholding itself for the SCRamjet combustion process. Not-directly-related to the mixing itself, flameholding is still a critical element of the combustion process as a whole. Based on a multitude of research papers on scramjet combustion, Segal (2009) provides an extensive explanation, shortly presented here.

As observed by Segal (2009), total combustion time for a distributed-reaction regime 2 can be divided into ignition delay time, t_{ign} , and burning time, t_r . Despite the multitude of different definitions for t_{ign} , a general definition as 5% of the equilibrium temperature can be used. The definition of the ignition time for hydrogen, however, can be based on the the specific reaction-rate constant, k, of the chemical reaction $H + O_2 \rightarrow OH + H$. Assuming mixing is not connected to mixing, Segal (2009) summarises that ignition delay time can then be defined as:

$$t_{ign} = 1/k \,[O_2]$$
 with $k = 3.52 \times 10^{16} T^{-0.7} \exp(-8580/T)$, (2.17)

where $[O_2]$ is the molar concentration of molecular oxygen. Based on flight conditions of Mach numbers between 6 and 8 Segal (2009) estimated an ignition delay time in the range of 10^{-5} [s].

The burning time can be defined as the time to reach 95% of the equilibrium temperature. The definition for hydrogen stated by Segal (2009) depends on the pressure and the total temperature and and is defined as:

$$t_r = 3.25 \times 10^{-4} p_b^{-1.6} e^{(-0.8 \cdot T_0/1000)}. \tag{2.18}$$

The total combustion time for the flight Mach range between 6 and 8 determined by Segal (2009) is then of the order of 10^{-3} [s]. This time scale can then be compared to the transport time scale presented in Figure 2.30, yielding time scales of the same magnitude. The direct conclusion of this observation is that exothermic reactions cannot be completed within the combustor unless the residence time is not increased via the implementation of a flameholding mechanism.

Near field vortex-shock interactions

The effect of the shock wave structures on the near-field mixing was already observed by Morkovin et al. (1952). Based on Schlieren and Shadowgraph images the authors conclude that the separated flow formed in front of the detached bow shock wave is being "..." pumped away" by the mixing with the boundary of the jet at the same rate as it forms."

The Mie Scattering mid-plane visualisations performed by Gruber et al. (1996) show that the large-scale structures have a significant influence on the near-wall behaviour of the detached bow-shock. It has also been observed that when with thick crossflow boundary layer, the bow shock is lifted and the injectant and crossflow fluid mix at subsonic velocities.

²At high Reynolds and moderate Damkler numbers.

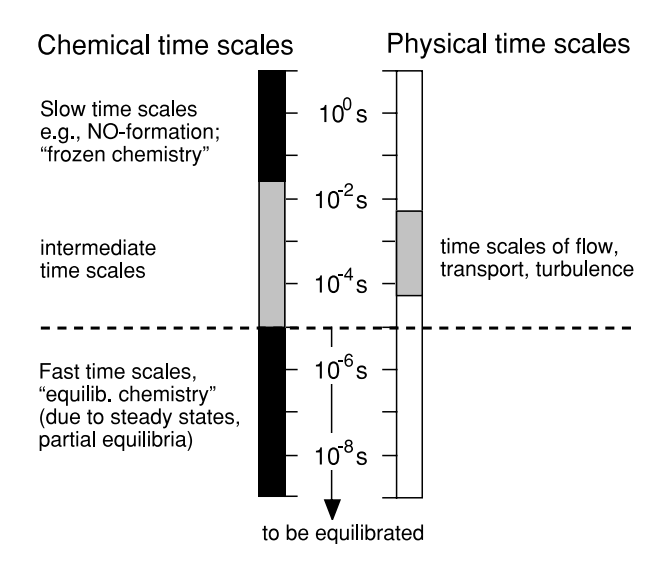


Figure 2.30: Classification of time scales in chemically reacting flows. Presented by Warnatz et al. (2006)

As investigated by Kawai and Lele (2009) in LES experiments, a detailed hypothesis on the dynamics and formation of large-scale structures and their relation to shock-structures in the near-field of interaction between sonic jets and supersonic crossflow has been established.

Kawai and Lele establish the existence of bow and separation shocks, jet barrel and normal shocks, reflected shocks from the barrel and normal shocks and a peculiar jet internal shock, which is cause by the unsteady nature of the flow field. To elaborate, the crossflow experiences blockage caused due to the emerging jet fluid. This blockage causes the formation of a bow shock at a set distance in front of the injection point. The pressure gradients imposed on the boundary layer by the bow shock result in boundary layer separation and an oblique shock wave connected to the foot of the bow shock. The emerging jet is under-expanded and thus proceeds to expand at rapid rates, increasing significantly the jet velocity. As a result of the pressure difference between the expanding fluid and the ambient environment the jet becomes engulfed by a barrel shock and a normal shock. It has been observed by Kawai and Lele (2009) that all the jet streamlines pass through these structures. Similar observation is made by Eberhardt and Hickel (2013).

In the time-averaged results, Kawai and Lele (2009) also observed the jet CVP create a suction zone causing secondary wall-bounded vortex pair similar to the one observed by Sun and Hu (2018). From the instantaneous images, however, Kawai and Lele (2009) could conclude that the CVP is formed by a multitude of u-shaped vortices similar to the hypothesis proposed by Ben-Yakar et al. (2006).

Let us return to the relation between the shock structures and the unsteady structures of the jet. In their simulations Kawai and Lele (2009) discovered a relation in the pressure of the separated zone in front of the bow shock, the dynamic behaviour of the jet shock system and the shedding of the shear layer vortices. In particular, when the pressure inside the separation zone raises, the expansion of the jet behind the barrel shock reduces, effectively retaining the pressure balance. This lesser expansion of the jet allows the shear layer to support rapid growth of instability waves and starts to oscillate. Due to this fluctuation, the jet flow is blocked by the deflected shear

48 Literature Review

layer, causing an additional shock structure inside the jet itself. The shock structure is connected via a kink to the barrel shock. Whilst this first shock translates, a second one appeared in the results of Kawai and Lele (2009), causing a tipple point. The triple point translates downstream together with the associated large-scale vortex and deflects rapidly. The formed jet shear layer mixes the jet with the crossflow, enhancing mixing, as proposed by the observations of Eberhardt and Hickel (2015) and Santiago and Dutton (1997). It must be mentioned, however, that the jet Reynolds number is $Re_i = 2.4e4$, around six times less than that observed in experiments.

2.5.5 Control parameters effect on large-scale structures and mixing

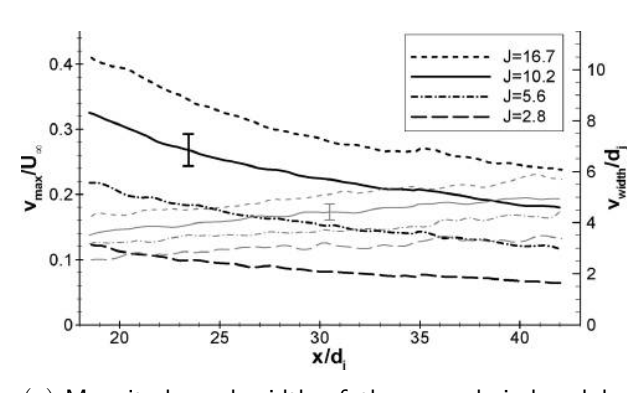
Effect of momentum ratio, crossflow and jet Mach numbers

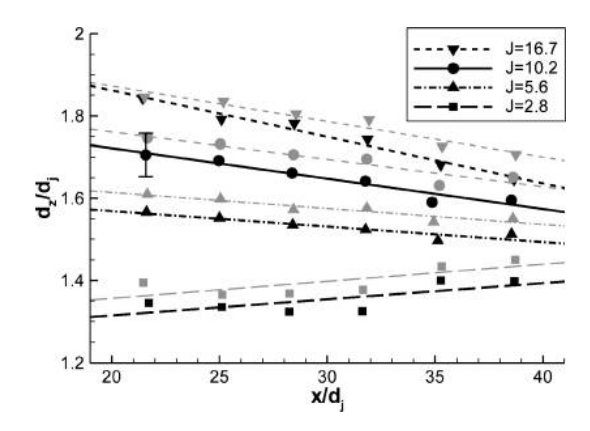
As discussed previously, the combination between the momentum flux ratio of the jet and the jet and crossflow Mach numbers control the underexpansion of the jet nozzle. It has been argued by Rogers (1971), based on results of concentration measurements, that the underexpansion is related to the degree of separation in front of the jet itself. In his research, Portz (2005) suggest that the variation of the crossflow Mach number will have similar effect on the size and strength of the large-scale structures as it has on the jet vertical and lateral trajectory. To elaborate, if the Mach number is increase, a stronger bow shock will be produced, decreasing the dynamic pressure in the vicinity of the jet. This in turn will allow the formation of larger and stronger turbulent structures. Another way to look at this phenomenon is the effective increase of the jet-to-crossflow momentum ratio, which, as already discussed above, has a direct effect on the formation of the flow structures.

Data for the effect of the jet-to-crossflow momentum flux ratio on the large-scale turbulent structures in the near-field of the interaction is more scarce, especially for experimental studies. Beresh et al. (2005a,b, 2006), however, studied the effect of J on the vertical velocity profile, turbulent stresses and the size of the shear layer vortices. As seen on Figure 2.31a, the magnitude of the vertical velocity peak, distance from the centreline, and the width of the peak itself increases with increasing J. This suggests stronger and larger CVP located further away from the wall. As seen by the previous observations, this is beneficial for the mixing characteristics of the flowfield. Furthermore, as seen in Figure 2.31b, the mean size of the shear layer eddies also increases with J.

Boundary layer effect

The boundary layer thickness expressed as the nondimensional ratio $\frac{\delta^{99}}{d_j}$ has tertiary effect on the jet trajectory and transverse penetration. With respect to this, as observed by Portz (2005), it has a direct effect on the vorticity generation as the penetration depth is directly related to the strength and size of the large-scale eddies in the flow. Therefore, an increased boundary layer thickness should have favourable effect on mixing. However, Portz (2005) observed that, despite this, at lower M_{∞} , the thicker boundary layer will lead to effectively tilted injection above the boundary layer thickness. The tilted injection will cause a diminished flow obstruction as compared to transverse injection. With the reduced obstruction, the vortex generation related to bulk mixing will also be reduced.





- (a) Magnitude and width of the upwash induced by the CVP. Dark lines - maximum vertical velocity; grey lines - width of the velocity peak. Obtained from Beresh et al. (2005a)
- (b) Mean diameter of the convected shear layer vortices. Dark lines eddies of positive vorticity; grey lines eddies of negative vorticity. Obtained from Beresh et al. (2005b)

Figure 2.31: Effect of the jet-to-crossflow momentum flux ratio on the vortical structures in the far field

2.5.6 Conclusions

As seen above, a large amount of studies have been dedicated to the formation and development of transverse jets in supersonic crossflow. The general flow topology has been established and it resembles that of incompressible jets. However, some studies suggest there is a difference in the instantaneous structures and the mean flow structures. In particular, breakup of the CVP in hairpin vortices has been suggested by Kawai and Lele (2009) and Ben-Yakar et al. (2006). Such breakup is proposed for low momentum-flux jets by You et al. (2013), which is in line with low speed jet research. Furthermore, low momentum flux jets have exhibited different barrel shock structure. However, no experimental data has been found regarding those cases for compressible jets.

Mixing in the near-field up to $10 - 20d_j$, the range being established by Eberhardt and Hickel (2015), is dominated by entrainment-stretching mixing. A rapid mixing process enhanced by the tilting-stretching-tearing of the eddies in the near field and the entrainment due to the separation behind the jet and the upwash of the CVP. The far field mixing has mostly been attributed to molecular diffusion.

The relationship between the large-scale structures and mixing with respect to the jet-to-crossflow momentum flux ratio has partially been investigates.

Experimentally, flow visualisation data is available, but quantitative measurements are scarce. It is proposed that J improves the mixing characteristics of the flow. Furthermore, the importance of the barrel shock on the mixing of the fluid passing through the Mach disc and forming a subsonic core has been emphasised by Santiago and Dutton (1997), Eberhardt and Hickel (2015) and Kawai and Lele (2009). However, this study found no quantitative experimental data able to quantify the effects of the nozzle backpressure on the turbulent stresses or velocity profiles behind the Mach disc. This, combined with the fact that different shock structures have been observed by LES performed by You et al. (2013) for low J, present an interesting gap for experimental research.

50 Literature Review

Investigation of the flow field dependence on the momentum flux ratio for the far field has been performed by Beresh et al. (2005a,b, 2006). The investigation showed increase of the strength, width and the vertical penetration of the CVP and increase of the shar layer vortices size.

Injection System Design

In the framework of this project it is required to experimentally simulate the transverse jet within the flow facilities of the High-Speed Lab (HSL). As seen in Chapter 1,the defined project scope requires the experimental simulation of cold transverse jets with variable jet-to-crossflow momentum flux ration and jet exit Mach number. The latter is implemented via the design of pressurized injection system that has to be installed in the wind tunnel facility's test section with minimal disruptions to the incoming crossflow.

The retrofitting of the experimental facilities for housing the injection system and the system design are presented in this chapter. Firstly, the selected experimental facility is introduced. Secondly, the modification of the wind tunnel test section is presented. Subsequently, the experimental test-matrix and the resulting system requirements are addressed. Based on the latter, taking into account inviscid and viscous flow considerations, the jet injection nozzles designed based on semi-empirical methods. With the design of the nozzles completed, the full injection system concept is presented and its efficiency is discussed.

3.1 ST-15 Supersonic wind tunnel

The ST-15 wind tunnel was selected for this modification as it is the only available supersonic tunnel in the HSL which can be easily modified and provide the required testing conditions.

The first supersonic wind tunnel to be operated by the Faculty of Aerospace Engineering, the ST-15 has helped contribute to the large body of research of high-speed aerodynamics for close to seventy years. The ST-15 is an intermittent, blow-down wind tunnel. As seen on Figure 3.1, it comprises of four sections: the settling chamber, the de Laval nozzle, the test section and the supersonic diffuser.

As detailed by Sun (2014), the settling chamber is supplied with dried air from a 300 m^3 reservoir at $p_{0_r} = 4000 \ kPa$. The fully loaded pressure vessel provides total running time of approximately 18 minutes at $M_{\infty} = 2$. The air from the vessel is settled through two layers of wire mesh screens. The settling chamber total conditions are listed in Table 3.1.

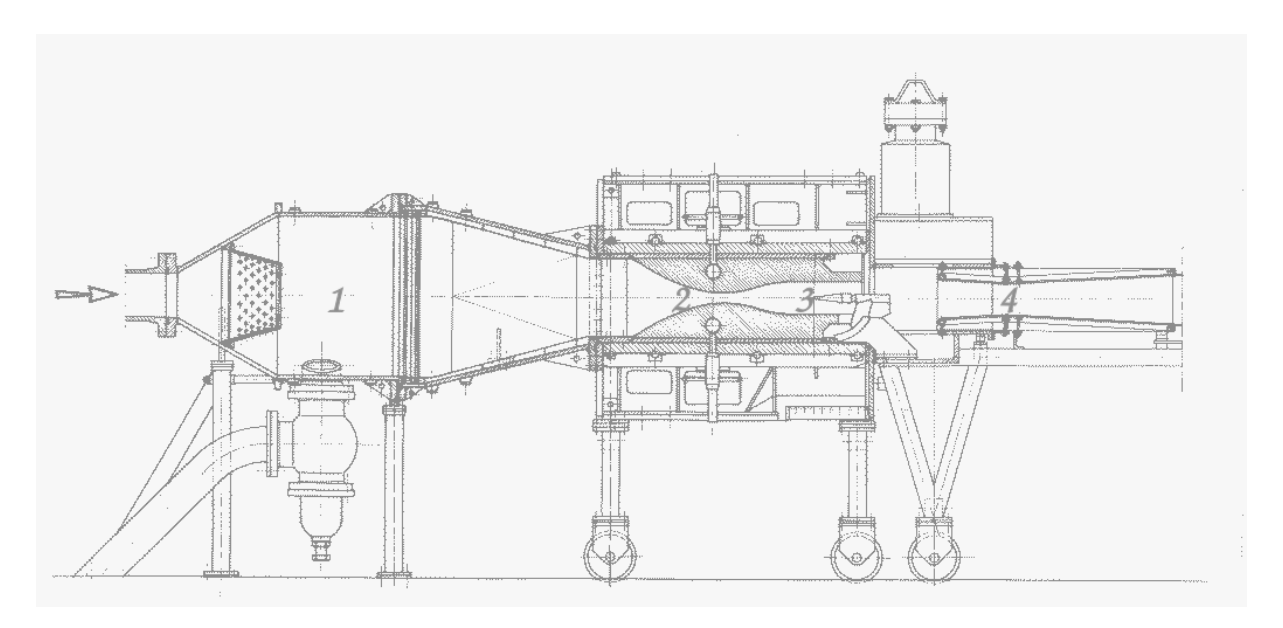


Figure 3.1: ST-15 schematics: 1-Settling chamber; 2-de Laval nozzle; 3-Test section; 4-Supersonic diffuser Sun (2014)



Figure 3.2: ST-15 supersonic wind tunnel with PIV set-up and Schlieren illumination optics visible. The image was obtained after the experiments related to this thesis were completed.

The nozzle and test section are both machined into aluminium blocks. Thus, each block provides

different nozzle geometry and different Mach number. The Mach numbers that can be currently provided are: 1.5, 2.0, 2.5 and 3.0. However, as explained previously, only the Mach 2 block is used for the current project.

Returning to Figure 3.1, the test section is located directly after the Laval nozzle. It has dimensions of $150x150 \ mm^2$. The wind tunnel test section boundary layer parameters have been measured via high-resolution PIV experiments performed by Giepman (2016). It develops along a smooth surface of about one meter under nearly adiabatic conditions. The free-stream conditions and boundary layer properties are presented in the second and third section of Table 3.1, respectively.

Finally, before the beginning of the diffuser two flanges were installed to provide horizontal and vertical optical access for a periscope probe. The probe is used for laser sheet illumination as related to PIV imaging, which will be discussed in the following chapter.

3.1.1 Typical section conditions

The static conditions in the test section have been calculated via the isentropic flow relations for air with constant $\gamma = 1.4$ [-] and R = 287.05 [J/kgK].

Parameter	Quantity	${f Units}$		
Settling	g chamber co	nditions		
$\overline{p_0}$	200	[kPa]		
T_0	290	[K]		
Free-stream conditions				
$\overline{M_{\infty}}$	2	[-]		
U_{∞}	524	[m/s]		
Calculated to	Calculated test section static conditions			
p_{∞}	25.56	[kPa]		
T_{∞}	161.11	[K]		
$ ho_{\infty}$	0.552	$[kg/m^3]$		

Table 3.1: ST-15 wind tunnel inflow parameters.

3.1.2 ST-15 test parameters and sensors

For the purposes of the research, the targeted total pressure of the wind tunnel is reduced in order to allow for reaching higher momentum flux rations at lower jet exit pressures. That is necessary due to the pressurisation limit of the seeding equipment as will be explained in the next chapter. This leads to the following wind tunnel target conditions for the experiments:

- Wind tunnel free-stream Mach number: M=2
- Settling chamber pressure: $p_{sc} = 2 \ bar$
- Settling chamber temperature $T_{sc}=285~K$

Furthermore, for all experiments the total pressure and temperature of the settling chamber and the static pressure of both sides of the test section are measured using conventional pressure ports and a thermocouple. Due to the high total pressures at the jet supply - around and exceeding 4 bar - a Honeywell SCX150AN pressure transducer is used. The latter are connected to an acquisition computer through a National Instruments CompactDAQ USB Chassis. The acquisition frequency for all sensor reading is set to 5 Hz.

3.1.3 ST-15 modification

For this research, transverse injection of sonic and supersonic jets into the test section free stream, or, as defined in this report, crossflow, needs to be implemented. In order to avoid inserts in the section, which would affect the boundary layer and/or introduce extra blockage, it has been decided to embed a supersonic injector within the bottom wall of the test section. In such a manner, the jet nozzle end is, as much as possible, manufactured and installed flush with the wall.

As explained previously, the de Laval nozzles of the ST-15 are composed of two metal Mach blocks, spanning from the settling chamber to the diffuser. Therefore, the test section is part of the actual Mach block. In order to obtain data for incoming crossflow of the magnitude of Mach 2, which is typical for supersonic combustor applications as well as supersonic aircraft reaction control, the Mach 2 nozzle block is selected as the block used for this study. Consequently, to house the injection system, the bottom Mach block is to be retrofitted with a cavity for experimental equipment.

To achieve this, in cooperation with the HSL technical personnel, a cavity in the lower Mach 2 nozzle block is designed. The dimensions of the cut-out are not limited by the system but by the maximum allowable cut-out volume. In this manner, future proof design for other experiments are delivered. The cavity is milled in the aluminium test block in-house. To close the system-off, a cap plate (simple plate) and test plates fitted with thread for the injection system are also designed. A clamping system consisting of two clamping pieces bolted from within the cavity, to avoid flow disturbance, are also manufactured. All of the components were manufactured in-house at the Mechanical Workshop at the Faculty of Aerospace Engineering. The cut-out can be seen in Figure 3.3. The major dimensions of the primary cut-out cavity are $143 \times 110 \times 80.6$ millimetres. For detailed technical drawings, please consult Appendix E.

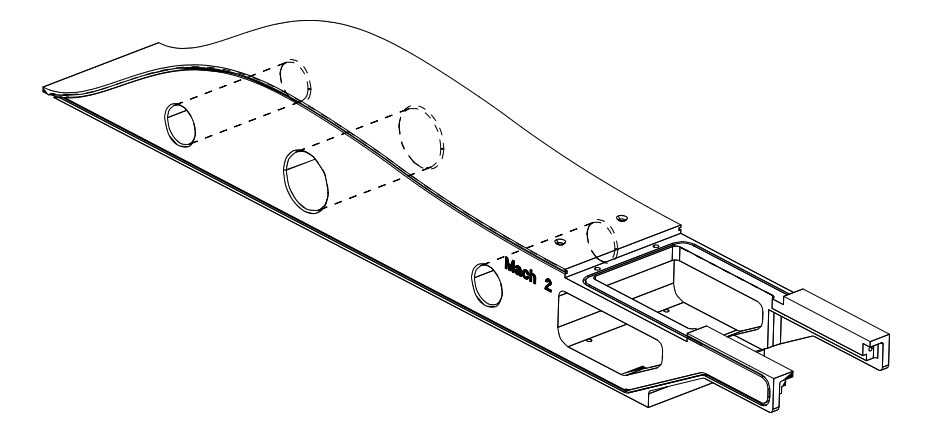


Figure 3.3: Isometric preview of the new lower part of the ST-15 Mach 2 de Laval nozzle block and test section

3.2 Experimental requirements

3.2.1 Experimental test cases

To meet the defined project scope, a test matrix with the two selected test-case variables is developed. The latter is based on typical values of the parameters for supersonic combustor injection nozzles as found by the consulted literature and limited by the available equipment.

As will be elaborated later-on in this work, due to, among others, flow domain areas with large pressure gradients, the PIV correlation quality is affected, requiring a larger population dataset for statistical correlation. Consequently, for the purposes of this research, and with respect to flow facilities test time and set-up complexity, it has been decided to reduce the test cases for PIV imaging. Furthermore, as will be elaborated on in Chapter 4, the PIV seeding generator played an important limiting role on the maximum attainable J.

The above considerations result in the test matrix presented in Table 3.2. Besides the selected test variable magnitudes used for the further design of the system, the matrix also indicates which test cases belong to the chosen experimental techniques.

Table 3.2: Experimental test matrix; Note: J=0 stands for crossflow (free stream) measurement required for analysis of the data

J/M	1.0	1.5	2.0
0.0	Schlieren/PIV	Schlieren	Schlieren/PIV
0.6	Schlieren/PIV	Schlieren	Schlieren/PIV
1.0	Schlieren/PIV	Schlieren	Schlieren/PIV
1.5	Schlieren/PIV	Schlieren	Schlieren/PIV
2.0	Schlieren/PIV	Schlieren	Schlieren/PIV

3.2.2 Reverse calculation of required pressures

From Equation 2.2 the jet static pressure can be determined as a function of the jet Mach number and the momentum ratio, resulting in

$$p_j = \frac{J\gamma_\infty p_\infty M_\infty^2}{\gamma_j M_i^2}. (3.1)$$

The calculation results in a two-dimensional array containing 12 pressure values, each corresponding to a combination between the test matrix parameters (Table 3.3). It can be seen that there is direct proportionality between the momentum ratio and jet pressure, as well as inverse proportionality between the jet Mach number and the inlet pressure.

Table 3.3: Jet pressure array $p_j[kPa]$

J/M	1.0	1.5	2.0
0.6	61	27	15
1.0	102	45	25
1.5	153	68	38
$^{2.0}$	204	91	51

Given the static pressure, using the isentropic relations from Anderson Jr (1985), the jet total conditions, as well as static temperature and density and speed of sound can be computed. However, only the required total pressure can be determined without any further assumptions. To determine the other variables of the flow another state variable is necessary. For the design computation it was assumed that the total temperature of the air provided by the wall air delivery system is the same as the one in the settling chamber of the wind tunnel. As a result, the required total pressure in the jet settling chamber is tabulated below.

Table 3.4: Jet pressure array $p_{0_i}[kPa]$

J/M	1.0	1.5	2.0
0.6	116	100	120
1.0	193	166	200
1.5	290	250	300
2.0	387	333	400

For seeding the jet and the wind tunnel with aerosol used for PIV experiments the PIVTec PivPart45 seeder with maximum backpressure of 500 kPa is used. To seed the jet, overpressure of 70 to 100 kPa is required. Consequently, the total pressure of the seeded jet can only be up to 430 kPa if it is to be seeded. Initially this was not possible as the tunnel was usually run at total pressure of 3 bars. However, it was found that the tunnel can successfully start with a lower total pressure of 2 bars, enabling the conduction of the full test matrix.

3.2.3 Mass flow study

To accelerate the flow to sonic conditions a convergent nozzle is used. In this case the throat diameter is equivalent to the jet outlet diameter. When the flow has to be accelerated to supersonic velocity a convergent-divergent nozzle is used. In this case, as stated above, the exit diameter is the same as the throat diameter for the sonic injector.

The injector throat diameter is constrained by the mass flow that can be sustained by the flow delivery system system in order to produce the desired M_j and J. This, in turn, dictates the total pressure in the jet settling chamber, which will be used as a control parameter during the experiments.

Pressure measurement

The flow feed for the settling chamber of the injector is provided by the HSL facility airflow delivery system (wall ports of the ST-15 hall). To estimate the maximum mass flow and the related total pressure that the system can provide throat diameter an experiment is conducted. Short tubes of different exit diameter are fitted onto the pressure system connection via a pressure gauge. The experimental equipment can be seen on Figure 3.4.

Due to the large pressure ratio expected and the short length of the tubes, the flow can be expected to be choked and approximated as inviscid. To assure that the measured pressure is close to the total value sufficiently high ratio between the measurement tube area and the outlet area is taken, this reducing the velocity at the measurement location. The range of

diameters selected for the experiment are based on correlations between injection diameters and total pressures found in the relevant literature Gruber et al. (1997), Gruber et al. (2000), Sun et al. (2013). The range of diameters and the resulting Mach number according to compressible, inviscid theory is presented in Table 3.5, where the gage Mach number is calculated using the Mach area relation as seen in Equation 3.2.







(b) Experimental set-up

Figure 3.4: Pressure measurement equipment

Table 3.5: Tube diameters and gage Mach number

$d_t[mm]$	$d_g[mm]$	$M_g[-]$
2	12	0.016
2.5	12	0.025
3	12	0.036
4	12	0.064
5	12	0.101

$$\left(\frac{A}{A^*}\right)^2 = \frac{1}{M^2} \left[\frac{2}{\gamma + 1} \left(1 + \frac{\gamma - 1}{2} M^2 \right) \right]^{\frac{\gamma + 1}{\gamma - 1}} \tag{3.2}$$

Maximum deliverable mass flow and total pressure

Given the large pressure difference and short length of the pipes the flow can be assumed to be choked and viscous effects can be neglected. Consequently, the mass flow can be calculated based on isentropic relations at sonic conditions. If the total temperature is assumed to be 290 [K] and the total pressure is assumed to be the one measured via the pressure gauge the mass flow equation can was derived as

$$\dot{m} = \frac{p_0 \pi d_t^2}{\sqrt{T_0 4}} \sqrt{\frac{\gamma}{R} \left(\frac{2}{\gamma + 1}\right)^{\frac{\gamma + 1}{\gamma - 1}}}.$$
(3.3)

The calculation resulted in the following table, summarizing the deliverable mass flow and total pressure:

d_t	$p_0[kPa]$	$\dot{m}[g/s]$
2	975	7.3
2.5	960	11.2
3	950	15.9
4	905	27.0
5	890	41.5

Table 3.6: Experimental results

The nozzle diameter for this study was selected to be study is 4 millilitres. The above study shows the capability of the wall pressure delivery system do deliver sufficient mass flow and sustain the required levels of total pressure for the experimental matrix.

3.2.4 Effective backpressure and nozzle choking

The effective backpressure - the ambient pressure at the jet exit- computed for the current freestream Mach number based on 2.6 is $57.02 \ kN/m^2$. The one based on 2.6 is $96.12 \ kN/m^2$. Due to the fidelity of the newer model, for the current document, $p_{b_{eff}} = 57.02 kN/m^2$ is used. This decision will be evaluated during Schlieren experiments.

Using the effective backpressure the pressure matching, $p_j/p_{b_{eff}}$, and nozzle pressure ratio, $p_{b_{eff}}/p_{0_i}$, were calculated. The results are presented in Table 3.7 and Table 3.8.

Table 3.7: Pressure matching $\frac{p_j}{p_{b_{eff}}}$

J/M	1.0	1.5	2.0
0.6	1.067	0.474	0.267
1.0	1.778	0.79	0.444
1.5	2.667	1.185	0.667
2.0	3.556	1.58	0.889

Table 3.8: Nozzle pressure ratio $\frac{p_{b_{eff}}}{p_{0_i}}$

J/M	1.0	1.5	2.0
0.6	0.495	0.575	0.479
1.0	0.297	0.345	0.288
1.5	0.198	0.23	0.192
2.0	0.149	0.172	0.144

As seen in Table 3.7 the test matrix provided cases with variable pressure matching which should, theoretically, lead to cases of underexpanded and overexpanded jet.

Furthermore, it has to be determined if with the current test matrix favourable pressure rations are achieved. To elaborate, for the sonic cases the flow should be choked at the throat. For the supersonic cases, there should be no shock wave inside the nozzle. Given $\gamma = 1.4$, the choking

pressure becomes $p^* = 0.520p_0$. For sonic injectors, chocking will occur at values below this number. As seen above all sonic injectors are below this value.

For supersonic injectors, as the pressure ratio continues to drop in the diverging subsection. A different pressure, p_{e_3} as defined by Anderson Jr (1985), which is lower than the p^* , will cause choking of the throat. However, it will not guarantee supersonic flow in the diverging portion of the nozzle. With increase of the pressures above the p_{e_3} a shock wave will travel through the nozzle. The first situation where supersonic flow is achieved in the entire nozzle according to inviscid theory is when the shock is at its exit. As for the current research, either pressure matched or under and overexpanded case are the focus of the investigation. Therefore, the pressure ratio should be such that it is lower than the pressure ratio causing normal shock at the exit, defined by Anderson Jr (1985) as p_{e_5} .

This pressure can be found by using normal shock wave relations after the prospective shock wave at the exit and multiplying the latter with the isentropic pressure ratio, resulting in

$$\frac{p_{e_5}}{p_0} = \frac{p_{e_6}}{p_0} \times \frac{p_2}{p_1}. (3.4)$$

Table 3.9: Pressure ratios for shock at the nozzle end and isentropic expansion

Ratio/M	1.5	2.0
$\frac{p_{e_5}}{p_0}$	0.670	0.575
$\frac{p_0{}_j}{p_0{}_j}$	0.272	0.128

The above results confirm that, according to inviscid theory, no subsonic flow should occur within the nozzles.

3.3 Sonic nozzle design

The injection system general layout consists of a small settling chamber and a sonic nozzle. The settling chamber is connected to the airflow delivery through a pressure regulator and the flow seeder. The total pressure is measured at the settling chamber location and the total temperature at the small seeding pot. The chamber is then connected to the test subsection via the converging duct of the nozzle. The nozzle contour, as will be discussed later, is machined/3D-printed in a threaded plug connected to the test plate. The schematic of the nomenclature for the nozzle is presented in the following rough sketch.

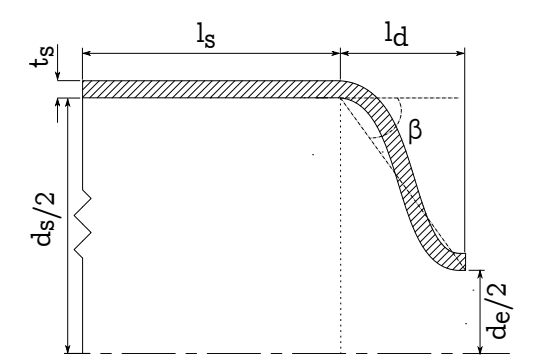


Figure 3.5: Schematic of the sonic nozzle

In the figure above, the exit diameter has previously been selected to be 4 [mm], being an optimal situation provided the amount of available overpressure and the requirements of the PIV measurement.

3.3.1 Settling chamber

The settling chamber diameter, which can be seen on Figure 3.5 can be determined using the isentropic relations as defined in Anderson Jr (1985). According to Pope and Goin (1965) the limit on the velocity in the settling should be between 3 and 30 m/s. Due to the limited amount of space below the test subsection the acceptable velocity was selected as 20 m/s. The exit diameter, as stated previously, is equal to 4 mm. This results in

$$d_s = 12.58[mm] (3.5)$$

The length of the settling chamber is based on the computational results presented in Ho and Emanuel (2000). The authors developed a converging nozzle design methodology based on steady, inviscid, axisymmetric perfect gas model aimed at uniform sonic conditions at the outlet. The method was validated using a numerical approach based on the NASA NPARC code. The results shown suggest that, if the non-dimensional length $l_s/0.5d_e$ is used as a control parameter, the increase of $l_s/0.5d_e$ provides uniformity of the Mach number distribution at both the inlet and the throat. The authors concluded that ratios of around 6 provide satisfactory matching between the actual Mach distribution and a uniform distribution, as derived using simulations with NPARC. Based on the preceding discussion the settling chamber length is defined as

$$l_s = 6 \times 2 = 12[mm] \tag{3.6}$$

The chamber is designed for the maximum required total pressure $p_{0_{max}} = 10bar$. The minimum thickness can be derived from the hoop stresses of a thin walled cylinderAhlstrom and Jan (1992) with an additional safety factor sf = 2:

$$t_{s_{min}} = \frac{sf \cdot p_{0_{max}} d_s}{2\sigma_{\theta}} \tag{3.7}$$

The above equation when using steel with yield strength $\sigma_{y_{steel}} = 350MPa$ provides a value of only 0.04 [mm], rendering the material thickness uncritical for the design. Thickness of 1.5[mm] is selected.

3.3.2 Nozzle converging subsection

The converging subsection of the de Laval nozzle accelerates the flow from the settling chamber to the nozzle throat where it reaches Mach 1. Deceleration of the flow near the walls and the related increase of boundary layer thickness are common occurrence, yet they seem to be ignored by most designers Pope and Goin (1965).

Pope Pope and Goin (1965) proposed several arbitrary methods for the design of the curve of the subsection. For the dimensioning of the current nozzle, however, the design method proposed by Ho and Emanuel (2000) is used. The design method is motivated by MLN (minimum length nozzle) theory, but can be used for any convergent subsection providing choked conditions at the throat with uniform sonic velocity. The theory is applicable to inviscid, compressible flow for both 2-dimensional and asymmetric nozzles. Ho and Emanuel (2000).

The converging subsection is developed based on a analytic wall contour controlled by non-dimensional parameters. Lengths are nondimensionalised with the throat radius and the velocities with the speed of sound at the throat. The control parameters were varied and the wall shape was optimized for planar sonic surface using the NPARC code by NASA.

The function for the nondimensionalised y coordinate, y' is defined as:

$$y' = f(x'), \tag{3.8}$$

where

$$\frac{df(l_c')}{dx} = 0\tag{3.9}$$

and

$$\frac{df(0)}{dx} = 0, (3.10)$$

given that x' is the nondimensional length of the convergent subsection and $x' \in [-l'_c; 0]$. The effects of the nondimensional length have been in investigated by Ho and Emanuel (2000). The authors discovered that due to the design procedure an adverse pressure gradient exist close to the inlet. The gradient is smoothed for $l'_c \geq 5$. This being related to supersonic wall Mach numbers occurring before the throat. The selected ratio for the design is 5, resulting in

$$l_c = 5 \times 2 = 10[mm]. \tag{3.11}$$

For uniform velocity a set of derivatives at the nozzle throat are set to zero as defined by:

$$\frac{d^j f(0)}{dx} = 0 j = 1, 2, 3, \dots (3.12)$$

For smaller area ratios below 6 Ho and Emanuel (2000) deduced via the set of simulations that the third derivative provides satisfactory results with respect to the uniformity of the Mach number distribution at the exit and the displacement of the largest pressure gradient upstream.

Furthermore,

$$\frac{df(x')}{dx} \ge 0$$
 $x' \in [-l'_c; 0]$ (3.13)

The above resulting in an error function defines as

$$f(x) = a + b \cdot erf(\eta(z)), \tag{3.14}$$

where

$$z = x'/l_c', (3.15)$$

$$a = 1, (3.16)$$

$$b = (-1)^{l+1} \frac{y_i' - 1}{erf[1/(l+2)]},$$
(3.17)

$$\eta = \frac{z^{l+1}}{1 + (-1)^l (l+1)(x'/l'_c)^{l+2}}$$
(3.18)

The values for all control parameters, y'_i , land l'_c have been discussed previously. The resulting nozzle contour can be seen in Figure 3.6.

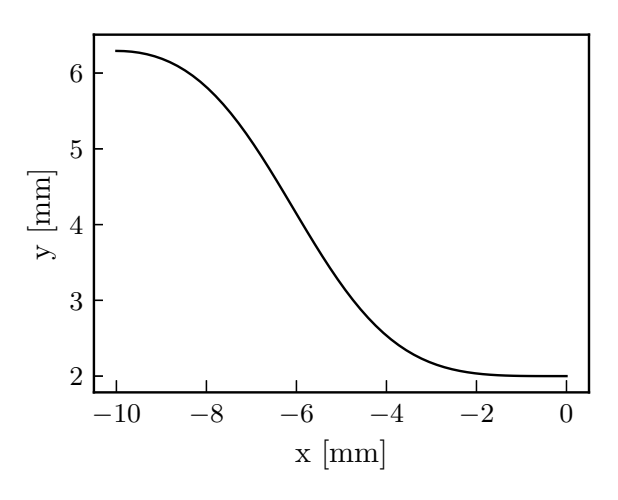


Figure 3.6: Nozzle contour

3.3.3 Nozzle dimensions

The leading dimensions for the sonic nozzle are presented in Table 3.10. For the details of the nozzle contour refer to Figure 3.6. The detailed drawings of the nozzle are presented in Appendix E.

Dimension	Value	Units
d_s	12.58	mm
t_s	1.50	mm
l_s	12.00	mm
d_e	4.00	mm
l_d	10.00	mm

Table 3.10: Summary of major sonic nozzle dimensions

3.4 Supersonic nozzle design

To accelerate the flow to supersonic velocities a divergent conical duct is added to the converging sonic nozzle. The schematic of the nomenclature for the nozzle is presented in the following rough sketch.

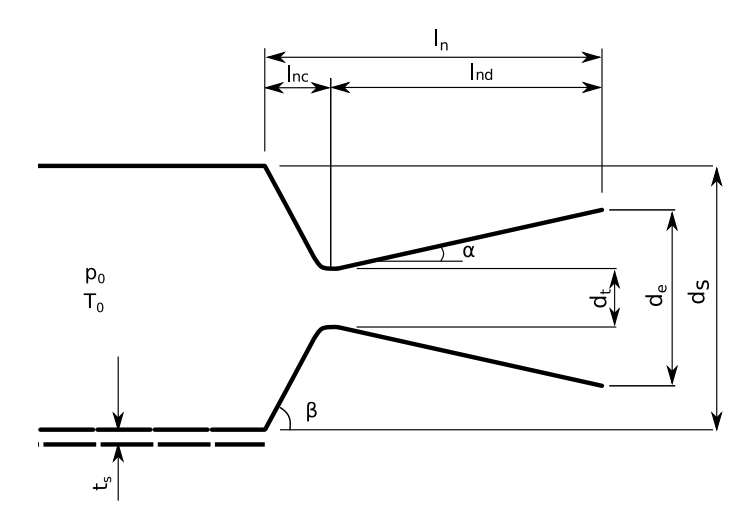


Figure 3.7: Nozzle schematic for general nozzle; flow left to right

The exit diameter is kept constant as it is directly related to the flow properties as explained by Portz and Segal (2006). Consequently the throat diameter can be estimated using the area Mach number relation as defined in Anderson Jr (1985).

A simple conical shape, the nozzle main dimensions that have to be determined are the throat diameter d_t , and the nozzle half angle, α . The exit diameter d_j is set previously to 0.004[m] or 4[mm] and the length l_{nd} of the divergent portion is related to the other parameters as

$$l_{nc} = \frac{\frac{d_e - d_t}{2}}{\tan(\alpha)}. (3.19)$$

3.4.1 Nozzle throat diameter

The nozzle throat diameter may be derived from inviscid theory for quasi 1-dimensional flow using the Mach-area relations from 3.2 together with the exit diameter $d_j = 4 \ mm$ and the design nozzle exit Mach number. This leads to the results presented in Table 3.11.

Table 3.11: Divergent subsection preliminary sizing

Parameter/M	1.0	1.5	2.0
$d_t[mm]$	4	3.69	3.08

3.4.2 Inviscid flow considerations

Looking from propulsion perspective, the conical nozzle half angle affects the divergence thrust losses defined by the divergent thrust loss coefficient

$$\lambda(\alpha) = \frac{P_{axial}}{P},\tag{3.20}$$

where P is the vacuum thrust and P_{axial} is the thrust aligned with the nozzle. Vlassov et al. (2007) This is, in fact, the geometrical efficiency of the nozzle, which is determined by the nozzle divergence factor correlation

$$\lambda(\alpha) = \frac{1 + \cos(\alpha)}{2}.\tag{3.21}$$

The correlation illustrates the deviation of the flow from the axial direction. Common angles used in rocket nozzle design vary between 12 and 18°.Östlund (2002)

As seen on Figure 3.8, already angles below 15° provide high geometrical efficiency. However, another driving factor for the nozzle performance is viscosity and boundary layer separation.

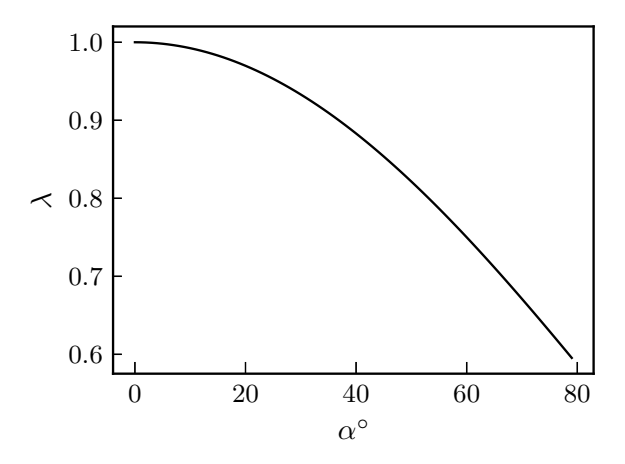


Figure 3.8: Nozzle geometrical efficiency

3.4.3 Friction losses

With respect to friction losses, a minimum α has been derived by Vlassov et al. (2007) based on compressible, viscous, quasi-1-dimensional flow equations as found in Leontiev (1997) and

Oosthuizen and Carscallen (1997). The expression can be defined as

$$\tan(\alpha_{min}) = \frac{f_D}{4} \frac{\gamma}{\gamma + 1} \frac{M}{\kappa(M)},\tag{3.22}$$

where

$$\kappa(M) = 1 - \frac{\gamma - 1}{\gamma + 1} M^2 \tag{3.23}$$

and the hydraulic friction coefficient, or Darcy friction factor is

$$f_D = 4f, (3.24)$$

with f being the nozzle internal surface friction factor.

The friction factor depends on the boundary layer state in the nozzle. For ducts the critical Reynolds number causing transition is generally accepted as 2300 and the fully turbulent Reynolds number is accepted to be around 4000. Based on the quasi-1 dimensional isentropic flow relations the Reynolds number for the core flow may be computed along the divergent duct. Kiijarvi (2011) The Reynolds number is based on the local diameter and can be expressed as

$$Re_d(x) = \frac{\rho u d}{\mu}. (3.25)$$

The Reynolds distribution along the nozzle in different flow cases is presented in Figure 3.9.

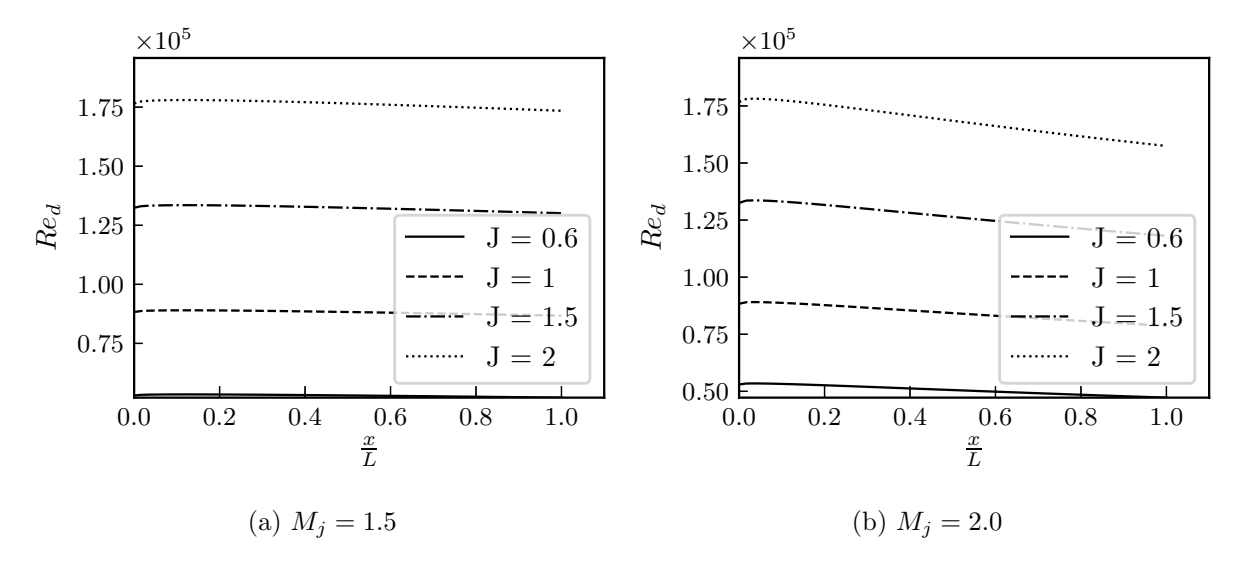


Figure 3.9: Local Reynolds number $Re_d(x)$ along the supersonic portion of the nozzle

As seen above, based on the criterion presented in Kiijarvi (2011), the flow in the duct may be considered turbulent. However, according to the conical nozzle data collected by Morrisette and Goldberg (1978), if no transition due to wall roughness or inflow instabilities occurs, the character of the boundary layer is either indeterminate or transitional for the nozzle dimensions under consideration. However, as the turbulent case is more critical with respect to wall shear stress, it has been used for a conservative calculation of the minimum angle.

To obtain the friction factor for turbulent ducts the Swamee-Jain non-iterative relation is used. It has been shown that the equation has an error of 0.05% error compared to the iterative Colebrook equation for a 6 [mm] pipe at Reynolds number of 1e5. Kiijarvi (2011) The equation has been also proposed for turbulent duct friction factor calculations by Oosthuizen and Carscallen (1997). The Swamee-Jain correlation can be defined as

$$f = 0.0625 \left[\log \left(\frac{e/D}{3.7} \frac{5.74}{Re^{0.9}} \right) \right]^{-2}.$$
 (3.26)

Here D is the local diameter and e is the wall roughness. The wall roughness for the most common materials has been summarized by Mcgovern (2011). For brass piping e = 0.0015[mm], for cast iron e = 0.26[mm]. The minimum angle α_{min} for the range of applicable wall roughness per Mach number and momentum ratio is presented on Figure 3.10. The minimum angle was thus found to be, with respect to this correlation, as big as possible, but preferably minimum of 4° .

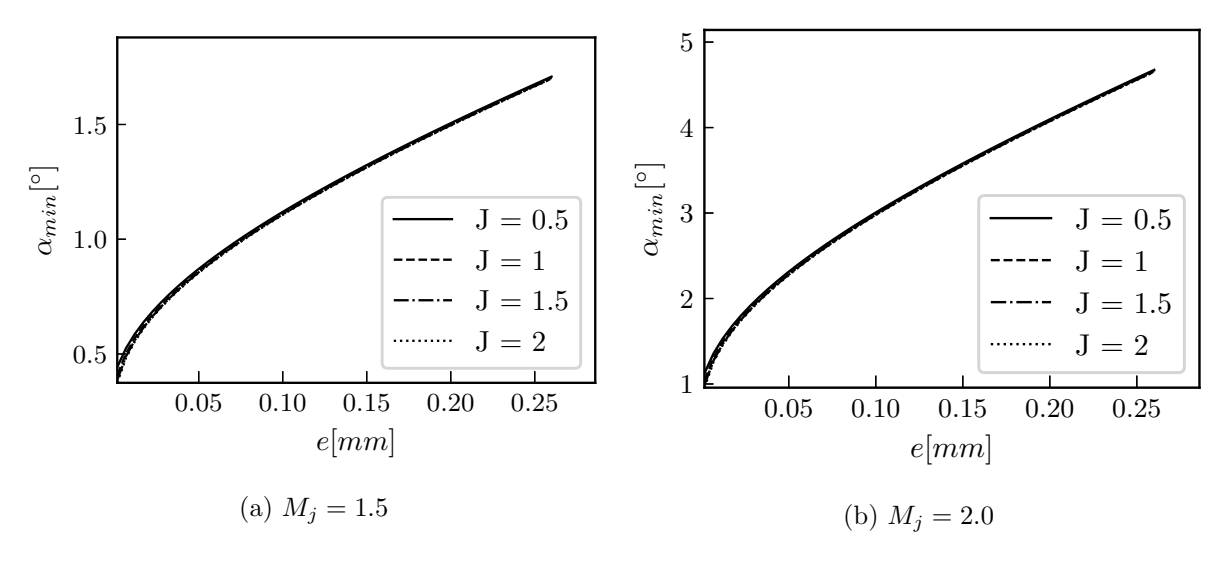


Figure 3.10: Minimum half angle α_{min} for given wall roughness

3.4.4 Flow separation

In the case of overexpanded operation of the nozzle the flow encounters adverse pressure gradient when approaching the exit of the orifice. Depending on the ratio between the wall exit pressure and the "equivalent backpressure", or ambient pressure, defined as

$$n = \frac{p_{e_w}}{pb} \tag{3.27}$$

the flow may separate from the wall, thus altering the desired flow discharge characteristics. Typically with ratios from 0.4 to 0.8 the gradient becomes too strong for the momentum in the boundary layer. Östlund (2002). Looking at the pressure matching presented in Table 3.7, one can immediately see that issues will arise due to the extremely low ratios, especially with the Mach 2 case, where the flow is highly overexpanded. Two major separation modes have been observed - free shock separation (FSS) and restricted shock separation (RSS).

Free shock separation

The most commonly observed type of separation is the free shock separation. The process is mainly guided by the mechanisms of conventional shock wave boundary layer interaction. A general schematic of the flow case and the related wall pressure distribution are presented in Figure 3.11.

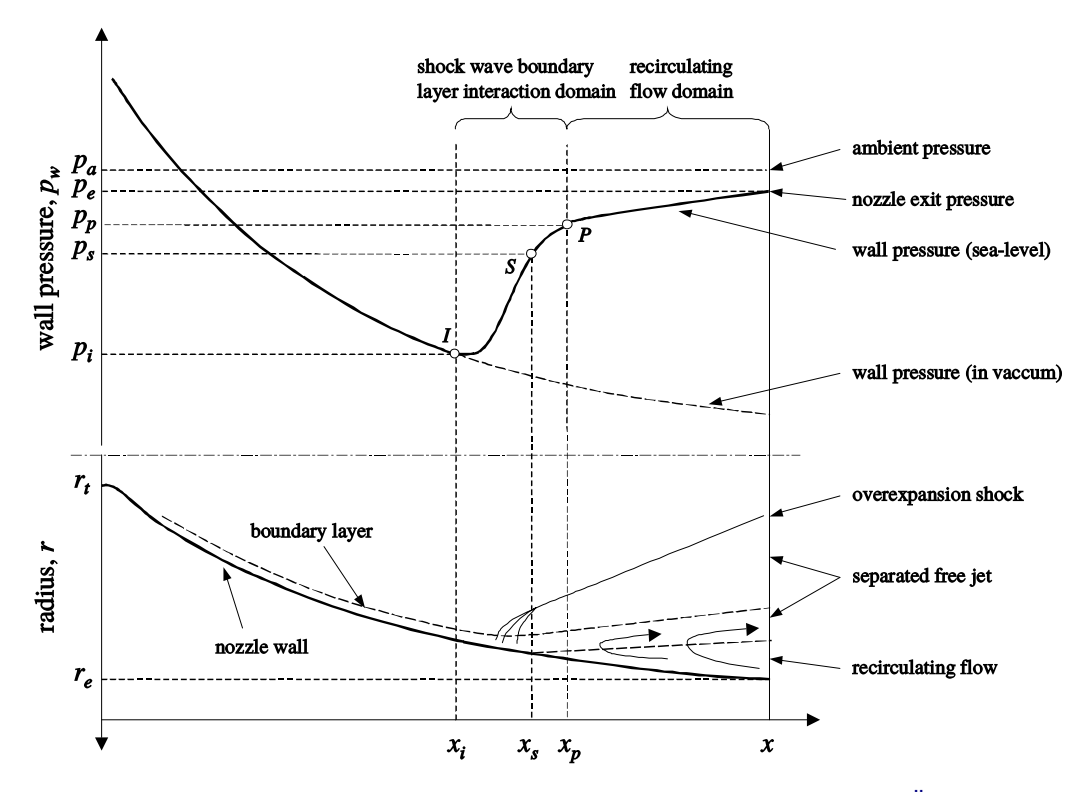


Figure 3.11: Free shock separation (FSS) schematics and pressure distribution Östlund (2002)

The interaction begins at a given incipient separation pressure, p_i , commonly referred in literature as p_{sep} . However, the actual flow separation pressure p_s is higher than the incipient pressure. Current studies have established that the separation location is not steady, as was previously considered in older research such as Schmucker (1984) and Romine (1998). Rather, It oscillates between the incipient pressure raise and a pressure raise plateau starting at p_p , which is below the ambient pressure. The ambient pressure in the figure is denoted as p_a . Ostlund (2002). In this study the concept of ambient pressure is replaced by the "equivalent back pressure" $p_{b_{eq}}$. In the analytical derivations performed by Romine (1998) the interaction between the separation shocks is further investigated. In order to adjust to the ambient pressure, the flow in the nozzle undergoes underexpansion and overexpansion, forming a Mach disc and triple points within the cells of the characteristic diamond shape exhaust, which would otherwise exist after the exit of the nozzle. In their analytical derivation of the separation location for steady flow, Romine (1998) theorized that above separation Mach number M_s of 2.254, M_3 in Figure 3.12, a triple point solution can be applied and below this value - a normal shock solution. At this low separation Mach number the Mach disc spans the entire diameter of the nozzle and the structures aft of it resemble the second half of the first cell in Figure 3.12. However viscous interaction and the formation of lambda pattern has to also be taken into account.

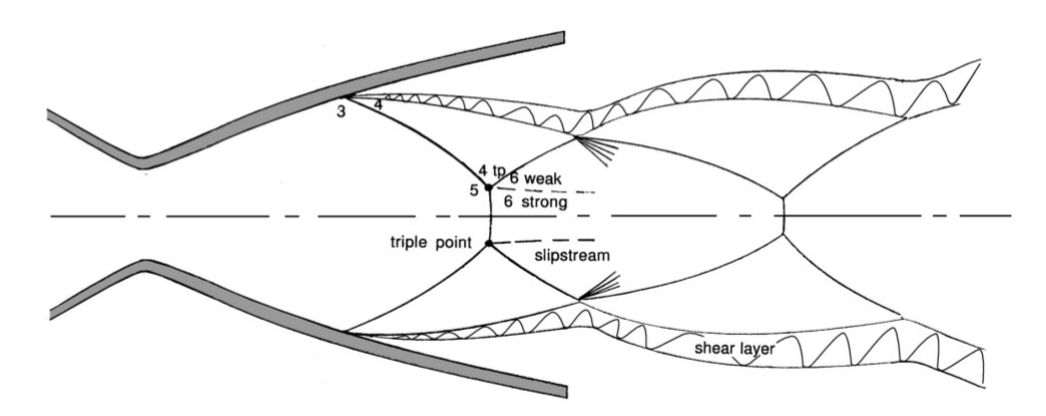


Figure 3.12: FSS Romine (1998)

An important correlation regarding the incipient pressure and, consequently, the onset of separation, is the variation of Mach number. As Mach number is increased, p_i/p_a decreases and the separation moves aft. However, around locations of about $A(x)/A^* = 0.8A_e/A^*$, the opposite behaviour is observed. Östlund (2002) This phenomenon can be traced back to the dependence of the flowfield on not only p_i/p_a , but on the combination of the ratio p_i/p_p and p_p/p_a . The first ratio can be related to the flow separation and the second one to the recirculation. As the separation shifts to the end of the nozzle the pressure plateau reaches ambient values for constant p_i/p_p , causing increase in p_i . When the plateau reaches the exit the flow is completely attached, yet p_i jumps. This phenomenon is referred to as incipient separation.

Prediction of incipient separation Initial studies into separation prediction took into account only the variation of p_i/p_a . The first simple empirical correlation formula considering the also the effect of Mach number is the one proposed by Schilling in 1962 and referred in Romine (1998) and Östlund (2002). The correlation is based on compendium of industrial data for different nozzle types, including conical. It can be defined as

$$\frac{p_i}{p_{b_{eff}}} = k_1 \left(\frac{p_{0_j}}{p_{b_{eff}}}\right)^{k_2},\tag{3.28}$$

where the quantities are expressed in terms of the transverse jet and the coefficients are defined as $k_1 = 0.541$, $k_2 = -0.136$ for conical nozzles.

Another empirical correlation which shows good fit with experimental data is the one developed by Schmucker in 1984 Schmucker (1984). It has been confirmed to fit well data for contoured nozzle at low Mach numbers. Östlund (2002) The correlation is also conservative as it gives higher p_i than other correlations. However, scarce data on low Mach number conical nozzles is available, even in the extensive compendium presented by Stark (2013), where data by Frey suggest a lower p_i . The Schmucker correlation can be defines as

$$\frac{p_i}{p_{b_{eff}}} = (1.88M_i - 1)^{-0.64}. (3.29)$$

Due to the large data scatter using correlation such as the above NASA proposed 20% margin on the calculations. Östlund (2002). A possible reason for this data scatter is the fact that, firstly,

none of the correlations take into account the effects of the shock separation and recirculation separately and, secondly, the correlations are based only on nozzles with turbulent flow. In addition, the incipient Mach number, as proposed by Morrisette and Goldberg (1978), is taken as the isentropic local value, if no numerical model is employed. All in all, this provides a relation which is independent on the nozzle half angle.

Several higher fidelity empirical and semi-empirical models taking into account the separate effects on the pressure rise caused by the shock-wave/boundary-layer interaction and recirculation have been developed. According Malik and Tagirov (1987), who developed experimentally validated semi-empirical model for the separation with low α conical nozzles, the pressure in the zone of interaction, bounded by points i and p in 3.11, rises due to the advent of the shock wave. The pressure in the recirculation zone, or pressure recovery zone, as referred to by the authors, remains constant for large half angles, yet positive pressure gradient develops for small angles. According to the model of Malik and Tagirov (1987), the flow in the nozzle is also partitioned vertically. It is divided into inviscid core, mixing zone, separation zone and boundary layer. Due to the separation air enters the nozzle and forms a reverse subsonic flow. The mixing zone is assumed to eject air from the separation zone at a constant rate, regardless of the half angle of the nozzle. However, as the half angle increases, the velocity of the reverse flow also decreases, effectively decreasing the pressure gradient. The theory was proved by experiments as seen by the case presented in Figure 3.13, where three nozzles of the same exit and throat diameters with varying half angles (15°,10°, 5°) were tested by wall pressure sensing.

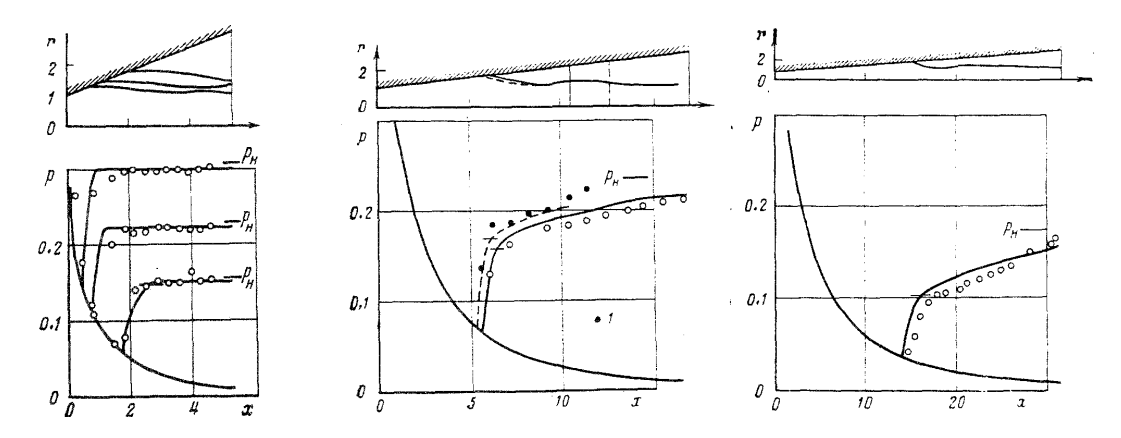


Figure 3.13: Nozzle wall pressure normalized with the ambient pressure for different half angles - 15° , 10° , 5° ; white circles denote wall static pressure measurements and the solid lines denote the semi-empirical model results Malik and Tagirov (1987)

A straightforward empirical correlation applicable for design purposes is developed by Kudryavtsev, as cited by Östlund (2002) and Stark (2013). According to Kudryavtsev the recirculation pressure rise can be defined as

$$\frac{p_p}{p_{b_{eff}}} = \left[1 + \left(\frac{0.192}{\sin(\alpha)} - 0.7\right) \left(1 - \frac{M_i}{M_j}\right)\right]^{-1}.$$
 (3.30)

Here M_a - the average exit Mach number, as defined as the nozzle expansion ratio, is replaced by the jet exit Mach number.

In the above relations the unknown quantities are the wall pressure distribution and Mach number. However, for conical nozzles with half angle less than 10° and large inlet diameter it has been shown that the isentropic values give good approximation of the wall values. Schmucker (1984), Fostrer and Cowles (1949) To exemplify, a plot of data collected by Fostrer and Cowles (1949) is presented in Figure 3.14¹. Therefore, in the absence of more relevant data, for the current nozzle design, the values from isentropic flow are used as input to the incipient values.

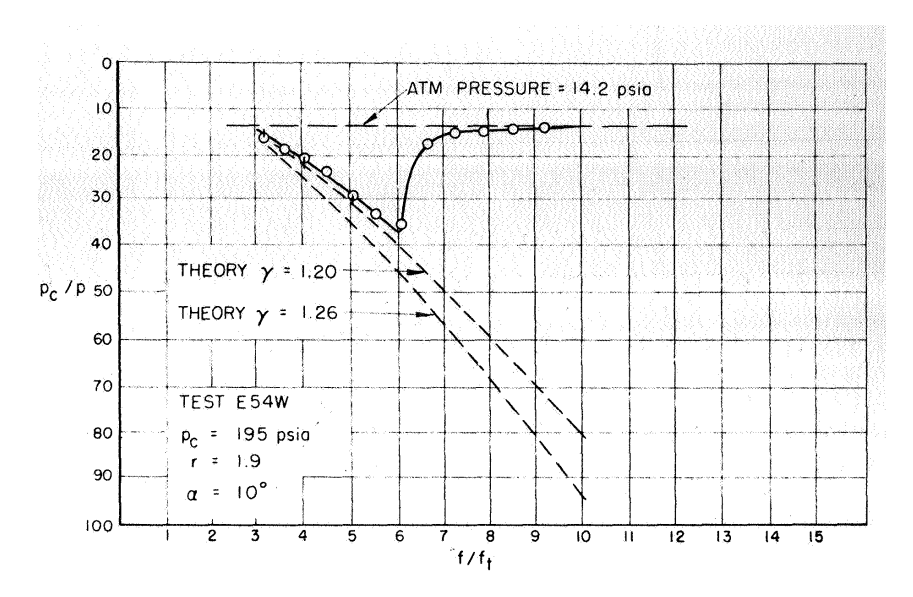


Figure 3.14: Pressure in overexpanded nozzle $A_e/A_t=10$, $\alpha=10^\circ$ Fostrer and Cowles (1949)

Plot of the variation of the jump in the separation zone as function of the local Mach number ratio for a selected range of possible half angles is presented in Figure 3.15.

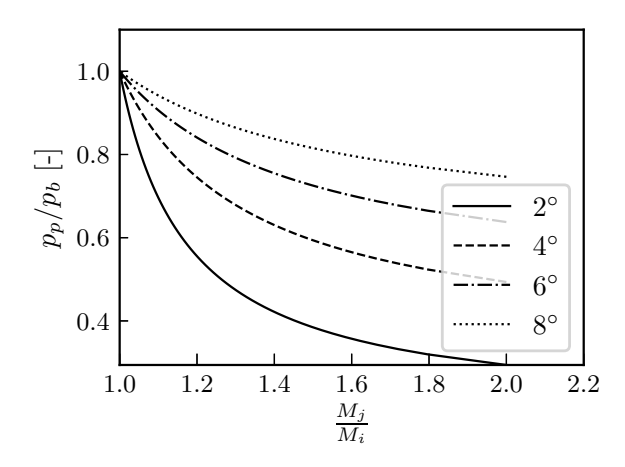


Figure 3.15: Pressure ratio over the separation zone as function of M_i for different half angle α

As can be seen in the figure above the $\frac{p_p}{p_b}$ trend for different half angles follows the conclusions of the semi-empirical model and experimental tests performed by Malik and Tagirov (1987). Namely, as the half angle decreases a pressure gradient is established in the separation zone.

¹For more experimental data confirming this statement please refer to the cited literature.

The pressure jump due to the shock separation can be approximated as

$$\frac{p_i}{p_p} = (1 + 0.5M_i)^{-1},\tag{3.31}$$

as proposed by Zukovsky and cited by Östlund (2002). However, the correlation has only been verified for conical nozzles with $M_i \in [2.0; 5.5]$.

However, another empirical model, based on experimental data by Summerfield and VOLVO, is presented by Östlund (2002). It uses oblique shock relations to take into account the change in shock wave and flow deflection angles and specific heats ratio. The relation can be expressed as

$$\frac{p_i}{p_p} = \left\{ 1 + \gamma M_i^2 \sin^2(\beta) \left[1 - \frac{\tan(\beta - \theta)}{\tan(\beta)} \right] \right\}^{-1},\tag{3.32}$$

The separation location along x/L for the correlations independent of the nozzle divergence are presented in the tables below. Here an indication of 1 means that the separation pressure is not reached in the nozzle. The location of separation is taken as the first value of local pressure which is below the incipient pressure threshold.

Table 3.12: Separation location according to Schilling Romine (1998) $\frac{x}{l_{n,j}}$

J/M	1.5	2.0
0.6	0.86	0.41
1.0	1.00	0.98
1.5	1.00	1.00
2.0	1.00	1.00

Table 3.13: Separation location according to Schmucker Schmucker (1984) $\frac{x}{l_{n_d}}$

J/M	1.5	2.0
0.6	0.00	0.05
1.0	1.00	0.76
1.5	1.00	1.00
2.0	1.00	1.00

The separation locations for different nozzle half angel according to the two-part models is presented in Tables 3.14 and 3.15.

Table 3.14: Separation location based on pressure raise in the separated zone predicted by Kudryavt-sev and pressure raise in the interaction zone predicted by Zukovsky. Information obtained from Östlund (2002).

(\mathbf{a})	$\alpha = 2$	0
J/M	1.5	2.0
0.6	0.85	0.69
1.0	1.00	0.95
1.5	1.00	1.00
2.0	1.00	1.00
(c)	$\alpha = 6$	0
J/M	1.5	2.0
$\frac{\mathrm{J/M}}{0.6}$	1.5 0.68	0.46
0.6	0.68	0.46

Table 3.15: Separation location based on pressure raise in the separated zone predicted by stlund and pressure raise in the interaction zone predicted by Zukovsky. Information obtained from Östlund (2002).

(a) $\alpha = 2^{\circ}$		0	(b	$\alpha = 4$
$\overline{ m J/M}$	1.5	2.0	m J/M	1.5
0.6	0.66	0.59	0.6	0.45
1.0	1.00	0.88	1.0	1.00
1.5	1.00	1.00	1.5	1.00
2.0	1.00	1.00	2.0	1.00
(c	$) \alpha = 6$	0	(d	$\alpha = 8$
J/M	1.5	2.0	m J/M	1.5
0.6	0.33	0.32	0.6	0.23
1.0	1.00	0.76	1.0	1.00
1.5	1.00	1.00	1.5	1.00

As seen by the separation location tables, the results of the correlations featuring only a single pressure ratio vary significantly. The one proposed Schilling relates more closely to the correlations based on two pressure ratios.

With respect to the correlations based on pressure jump over the interaction and separation zone it can be seen that the separation length increases with increasing nozzle half angle α . he equation derived stlund is more conservative, providing larger separation zone for a given nozzle divergence.

As seen above, according to the separation criterion, the nozzle half angle should be as small as possible in order to reduce the incipient separation inside the nozzle, yet it is not a sufficient parameter to prevent its onset. Given the result of the previous section, optimal half angle

selection falls on 4° degrees.

3.4.5 Nozzle contours

With the half angle set to four degrees and the jet exit diameter set to 4 millimetres the rest of the nozzle geometry for the supersonic nozzles is set. The conical section determines the new throat diameter and the uniform exit Mach number correlation determines the convergent section of the nozzle. The curves representing the nozzles are presented on Figure 3.16

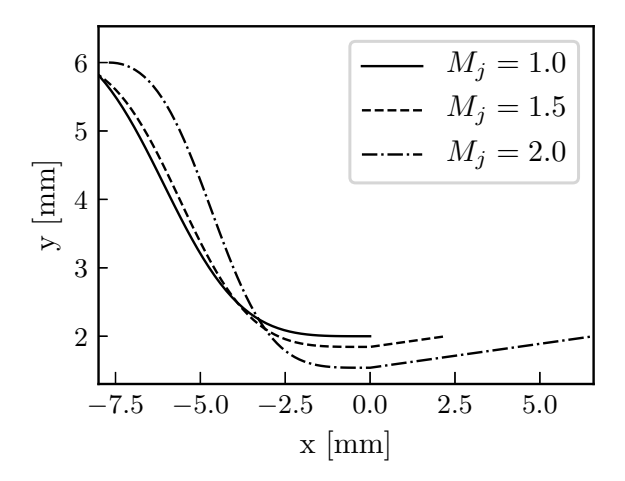


Figure 3.16: Nozzle contours

3.5 System concept and performance

3.5.1 System concept and implementation

To be able to span the test matrix presented in Table 3.2 the system has to be designed such that mechanisms for the variation of J and M_j in the defined ranges are considered. The jet-to-crossflow momentum flux ratio control for this system is achieved by varying the injection nozzle total pressure p_{0_j} . The jet exit Mach number is set geometrically - via exchanging the designed small sonic and conical nozzles.

Given a set jet Mach number M_j , free stream Mach number M_{∞} , free stream pressure p_{∞} and assuming constant specific heat ratios, the p_j can be calculated using the isentropic flow relationship.

The above-presented design considerations and constrains resulted in the development of the injection system concept seen in Figure 3.17. The system is comprised of two main assemblies. The schematic of the system is presented in Figure 3.17.

The air supply and seeding controller assembly is situated within the ST-15 control room and comprises of pressurised air feed from the ST-15 air feed, control valve, static pressure meter and a shut-off valve. Optionally, before the shut-off valve, a second air supply can be connected in parallel with the main air supply. The secondary supply is needed in order to seed the jet stream with atomised Di-Ethyl-Hexyl-Sebacat (DEHS) required for PIV experiments.

The second assembly located in the test section cavity is the Supersonic injector. It is fitted with exchangeable nozzles and a fitting for a Pitot tube and thermocouple connection used to measure the jet total conditions. The nozzles themselves are glued inside a pre-milled fitting, which can be screwed to the test section test plate and the injector. The final design of the assemblies from KIWI-grade components can be seen in the subsequent Figure 3.18. The component grade allows us to, theoretically, go to maximum pressures of 7 bar total pressure. Note that this is the critical pressure for the weakest link in the system.

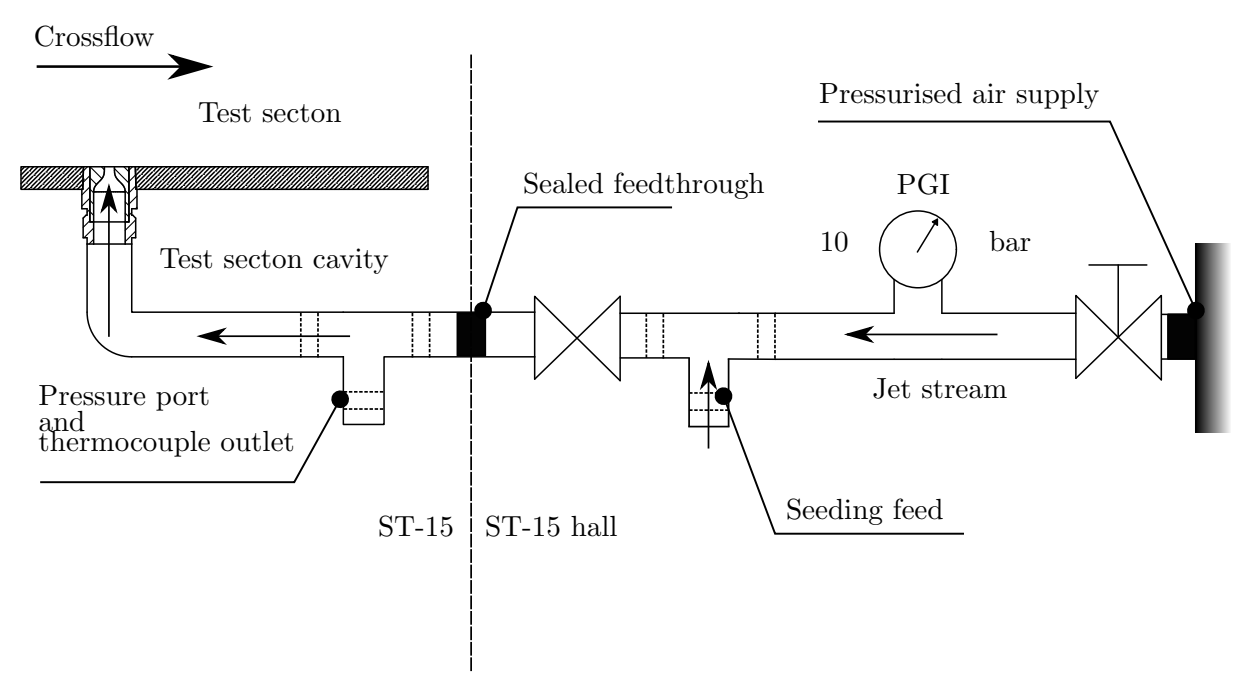
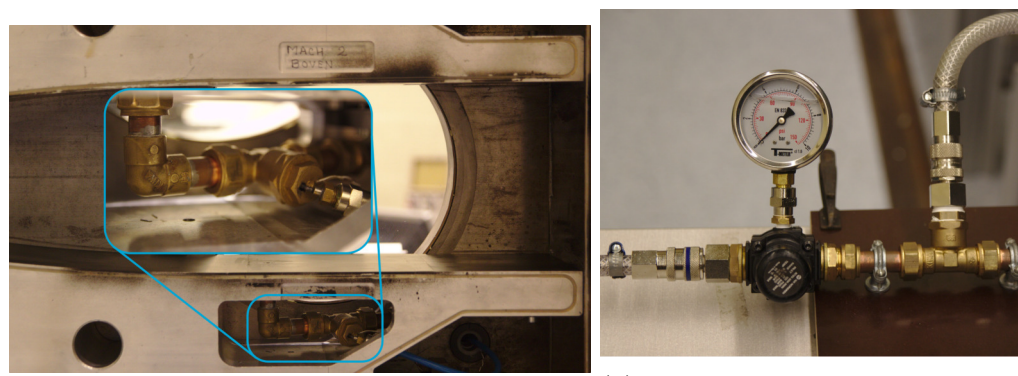


Figure 3.17: Injection system schematics



 ${
m (a)}$ Supersonic injector - located inside ST-15

(b) Air supply and seeding controller - located outside of ST-15

Figure 3.18: Injection system

Drawings of the system are presented in Appendix E.

3.5.2 System performance

Finally, prior to beginning of the experiments, the performance do the system is determined. The performance estimate provides the relation between the set gauge control pressure and the actual total pressure measured prior to injection. The measurement tables are presented in Appendix C. The pressure drop is based on the delta between the static pressure gauge reading with the shut-off valve succeeding it closed with the total sensor pressure measured at the pressure port located prior to jet injection. The pressure drop over the system for two different jet injection nozzles can be found on Figure 3.19.

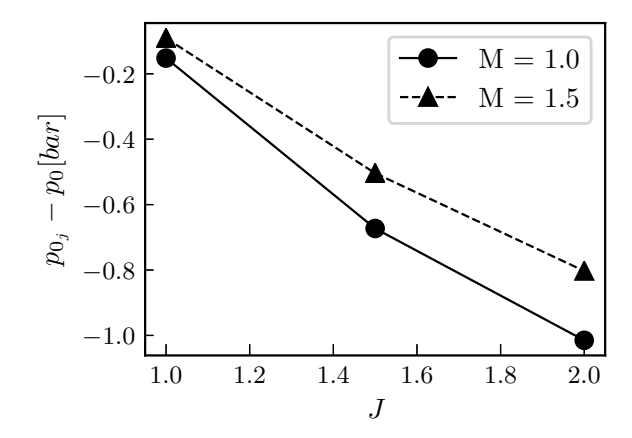


Figure 3.19: Pressure drop over the system for two injection Mach numbers

As seen above, with increasing J, and thus increasing the total pressure of the jet, the pressure losses in the system increase significantly, up to 1 bar for the case of sonic injection. At this jet-to-crossflow momentum flux ratio the total pressure of the $p_{0_j} = 3.8$ bar and $p_0 = 4.9$ bar. As the tendency is rather linear we can see that the losses over J of one are about 0.8 bar of total pressure. For the sonic injection the required total pressure increase per J has been also found to be a bar. Consequently, it is suspected that the maximum obtainable sonic injection for this system with the current parameters would be about J = 4. The jet Mach number reduces the losses due to the reduced injection nozzle throat diameter.

Experimental Techniques

After the wind tunnel cut-out and system design was completed, the experimental design of the flowfield qualitative and quantitative visualisation in the mid-field of jet injection was initiated. The latter comprises of Schlieren imaging and 2-dimensional PIV. The basic theory of the techniques, related set-up and required post-processing are discussed in this chapter.

4.1 Schlieren imaging

Schlieren imaging is a full-field non-intrusive flow visualization technique which provides visual information regarding the variation of density within the investigated FOV. This is achieved by translating the density gradients into light intensity and projecting the latter on an image capturing device sensor. Due to the high density gradients associated with the supersonic flow regime it has been established as a standard technique in the field. The use of Schlieren imaging for this research is based on two considerations. First and foremost, as it is very straightforward to set-up and well established it is very suitable for initial investigation of the flow domain and the newly-developed jet injection system.

4.1.1 Governing principle

A short, yet complete description of the essence of the Schlieren technique was presented by Hubert Schardin and quoted by Settles and Covert (2002), namely:

The basic principle of the Schlieren technique is the combination of the optical projection of an object with an indication of its light deflection.

In the general case of the application of Schlieren the optical projection of an object would be the model shadow and the test section walls. In the current set of experiments only the bottom wall of the wind tunnel test section is visible as a solid projection. The indication of the light deflection as used in fluid flow research is tied to the propagation properties of light through a medium different than vacuum. Neglecting quantum effects and relativistic effects on the light propagation, the ray approximation is been a model consistent both with the wave and particle theory. According to the ray approximation, absent disturbances, light propagates along straight lines - rays. Following this, as per physical optics, light would be comprised of planar, parallel wave fronts, perpendicular to the rays, or propagation directions. The planes of constant phase ϕ are separated by a wavelength λ . According to Maxwell's equations for electromagnetic fields, the wave, or phase, velocity can be defined as

$$c = \frac{2\pi\omega}{\lambda}. (4.1)$$

The velocity of the phase propagation of light waves in vacuum is the well-known speed of light, $2.998 \times 10^8 [m/s]$. Let us from now on denote this velocity as c_0 . However, the speed of light is lower in matter. The relationship can be defined as

$$c = \frac{c_0}{n},\tag{4.2}$$

where c is the speed of light in the material and n is the material refractive coefficient. The refractive coefficient in vacuum is, of course, 1.

The effect of refraction on the light propagation can be explained through Snell's law, after Willebrod Snellus. Detailed derivation, no matter the geometrical simplicity of the law, is left outside this discussion but can be found in the notes of Steeneken (2019). Snell's law states that upon passing to a region with different coefficient of refraction, the ratio of the light deflection and incidence angle will change in proportion to the ratio of the ratio of the refractive coefficients of the two media, or, in mathematical terms

$$n_1 \sin \theta_1 = n_2 \sin \theta_2,\tag{4.3}$$

where θ_1 and n_1 are the incidence angle and refractive coefficient of the media where the light comes from and θ_2 and n_2 are the deflection angle and the refraction coefficient of the medium where the light travels into, respectively. Consequently the effect of change of the refractive index on the wave front or ray propagation bending of the ray in direction of the increasing refractive index. Such discontinuities in the reflective index cause, due to the perpendicularity of the light rays and wave fronts, a wrinkling of the wave front itself and effective delta in the phase velocity.

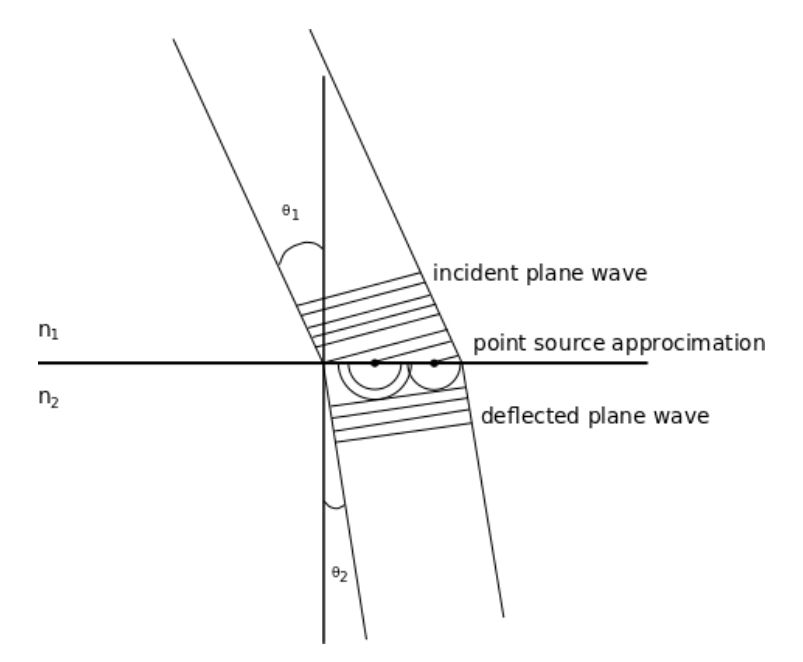


Figure 4.1: Visual interpretation of light deflection according to Snell's Law. The incoming light is approximated to consist of plain waves. Using point-source approximation the deflected light ray can be constructed with by parallel waves formed tangent to the point source waves.

Settles and Covert (2002), however, provide a more dedicated derivation for the deflection of light based on the curvature equations presented in Equation 4.4. Here the light ray is pointed in the z-direction and the gradients in refractive index are in the x-y plane.

$$\frac{\partial^2 x}{\partial z^2} = \frac{1}{n} \frac{\partial n}{\partial x}, \quad \frac{\partial^2 y}{\partial z^2} = \frac{1}{n} \frac{\partial n}{\partial y}$$
(4.4)

The components of the light ray deflection in a direction perpendicular to the propagation direction, z, can be obtained via integration of the above relations, resulting in

$$\varepsilon_x = \frac{1}{n} \int \frac{\partial n}{\partial x} \partial z$$
 and $\varepsilon_y = \frac{1}{n} \int \frac{\partial n}{\partial y} \partial z$. (4.5)

The boundaries of integration can be set to 0 and L - the optical path length in z direction, resulting in

$$\varepsilon_x = \frac{L}{n_0} \frac{\partial n}{\partial x}$$
 and $\varepsilon_y = \frac{L}{n_0} \frac{\partial n}{\partial y}$, (4.6)

where n_0 is the local refractive index of the medium. As seen by this relation, changes in the refractive index spanning longer distance parallel to the optical path will will have much larger influence on the angular ray deflection. Furthermore, refraction of the light rays is directly related to the derivative of the refractive incex, rather than magnitude of n itself. For air, the refractivity, n-1 can be linearly related to the density of the gas ρ as

$$n - 1 = K\rho, \tag{4.7}$$

where K is the Gladstone-Dale constant, being around $0.23cm^3/g$. As observed by Settles and Covert (2002), the refractivity depends on gas composition, wavelength of the illumination and temperature and density of the medium.

The name of the Schlieren method comes from the German word for streak - schliere. In the framework of fluid dynamics, as elaborated on by Settles and Covert (2002), schliere are refractive index gradients (disturbances) present in inhomogeneous transparent media. through the above observations and by the definition of Equations 4.6 and 4.7, schliere will result in bending of the light rays and wrinkling of the wave fronts. As seen by this, interestingly enough the name of the resultant observable phenomena has been used for the definition of the disturbances causing them.

A basic schlieren arrangement with an extended light source is presented in Figure 4.2. The extended source can be considered as an area of unit point sources. As a result, the test section is illuminated by light-ray bundles from all those sources in a cone. Consequently, every point in the test section is illuminated by each and every point on the extended source. Furthermore, a collimation lens is used in order to create planar wave fronts. However, collimation of light from extended sources results in a depth-of-focus of the schlieren system as a multitude of point sources illuminate the section from different location on the emitting surface. To exemplify extremities of the source light rays passing through the lens system are also presented in the Figure 4.2. The knife edge located at the focal point of the second lens is a spacial filter. In essence, it is nothing more than a plate with a sharp edge blocking part of the light of what we can call the composite source. This filter is pivotal for the implementation of Schlieren. Before proceeding into the explanation of the use of this filter we should note that the last behind the knife edge is not essential, but it can be used to control the focal point location of the resulting image so the focus on the imaging sensor or surface can be manipulated.

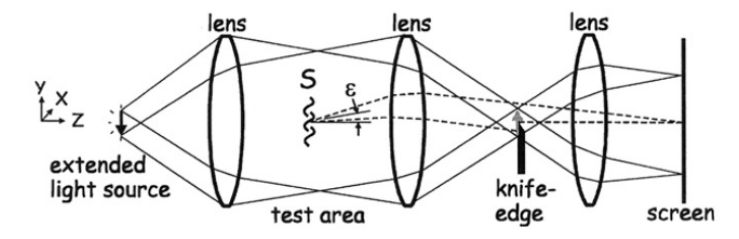


Figure 4.2: Basic system schematics of a Schlieren arrangement with extended light source, lenses and no collimator lens and pinhole at the source. Taken from Settles and Covert (2002)

Returning to the functional discussion of Schlieren, the simplified explanation for the way-of-working of the system is quite straightforward. Absent schliere object in the test section, the light from the source is collimated and passes through the test plane undisturbed, unless there is a physical model in the test section. In such a case, the model will leave a nearly exact geometrical shadow of its shape at the focal point of the system on the knife edge. At the knife-edge plane where the system is focused the filter can be moved - blocking different blocking different amount of light based on its spacial position and orientation. This reduces the total illuminate of the image captured by the sensor.

However, if a schliere is present at the test section plane, as derived from Equations 4.6 and 4.7, the light rays will be bent in direction of the increasing refractive index or, equivalently,

the increase in air density. This deflection of incoming light can be seen as the dotted lines in Figure 4.2, where S is the schliere and ϵ is the light ray deflection. Part of the light rays that are deflected in negative y direction are blocked by the knife edge filter. This results in a dark region on the imaging surface. The differences in the intensity distribution in the Schlieren image thus signify the change of density in the flow due to the presence of the schliere, this is Schlieren reacts to $(\partial n/\partial x)$ instead of to the Laplacian, as in Shadowgraphy.

To fully grasp the formation of Schlieren images needed both for understanding of the set-up and for their interpretation, a few extra words on the scientific background behind the technique will be presented. One thing that is fundamental for proper understanding of Schlieren imaging is that the source and knife edge and test section and imaging plane are conjugate optical planes. As a result an exact image of the source is focused on the knife edge and an the same follows for the test section and imaging plane. returning to the approximation of the source as a combination of point sources, the existence of the conjugation between its plane and the knife edge plane means that a composite image of it is projected accurately on the latter. Consequently, as observed by Settles and Covert (2002), each point of the test section plane contributes an entire elemental source image to the composite source image on the knife edge plane. Thus, when one blocks part of the light with the filter, light for several of the elemental sources is blocked but not all. This means that the imaging plane still receives illumination at the schliere position from all other but the blocked sources. Consequently a grey-scale image is formed rather than binary black and white. Absent schliere increasing the filter blockage will dim the entire image plane equally if the optics are well aligned.

Furthermore, due to the intrinsic properties of the filtering, the simple knife edge filter is only sensitive for the density gradients in one direction. It can either be horizontal or vertical. More elaborated filters as pinholes and colour filters have also been developed but the latter are outside of the scope of this study. The sensitivity of the schlieren system for density gradients can be improved by filtering more light with the knife edge, however, this reduces the illumination of the image. Should camera be used as image-capturing device, the sensitivity can also be increased by reducing the exposure time for transient effects. This however also reduces the amount of illumination.

Talking about transient effects, a final topic relevant for this experimental investigation has to be discussed. As the time-scale of the experiments is significantly small due to the supersonic velocities present in the flowfield, conventional Schlieren with continuous light source continuous Schlieren - even in its instantaneous" images - hereby from now on called pseudo -instantaneous - captures only a local average of the flowfield during the exposure time. More accurate instantaneous representation of the flowfield can be achieved with Spark Schlieren. Here the light source is a spark light that provided high levels of illumination for only a fraction of the exposure times encountered with Continuous Schlieren. The latter can be coupled and co-triggered for acquisition through a personal computer with a normal CCD or SCIMOS camera, providing more sensitive instantaneous images where shear layers and their interaction with the shock systems are much more easy to distinguish. This is associated with the fact that the time-scale related to the convection of the large-scale structures and the fluctuation of the shock system are very small. Combined with high-speed cameras high-speed Schlieren set-up can be used. However, for this research due to the limitations of the PIV system with respect to time resolution with supersonic flow - as will be discussed later. Only the average flow fields will be analysed. Subsequently it has been chosen to implement the continuous schlieren set-up. As a side note, several Spark Schlieren tests to visualise the jet shear layer with a CCD camera were also performed.

4.1.2 Schlieren configuration for transverse injection into supersonic cross-flow

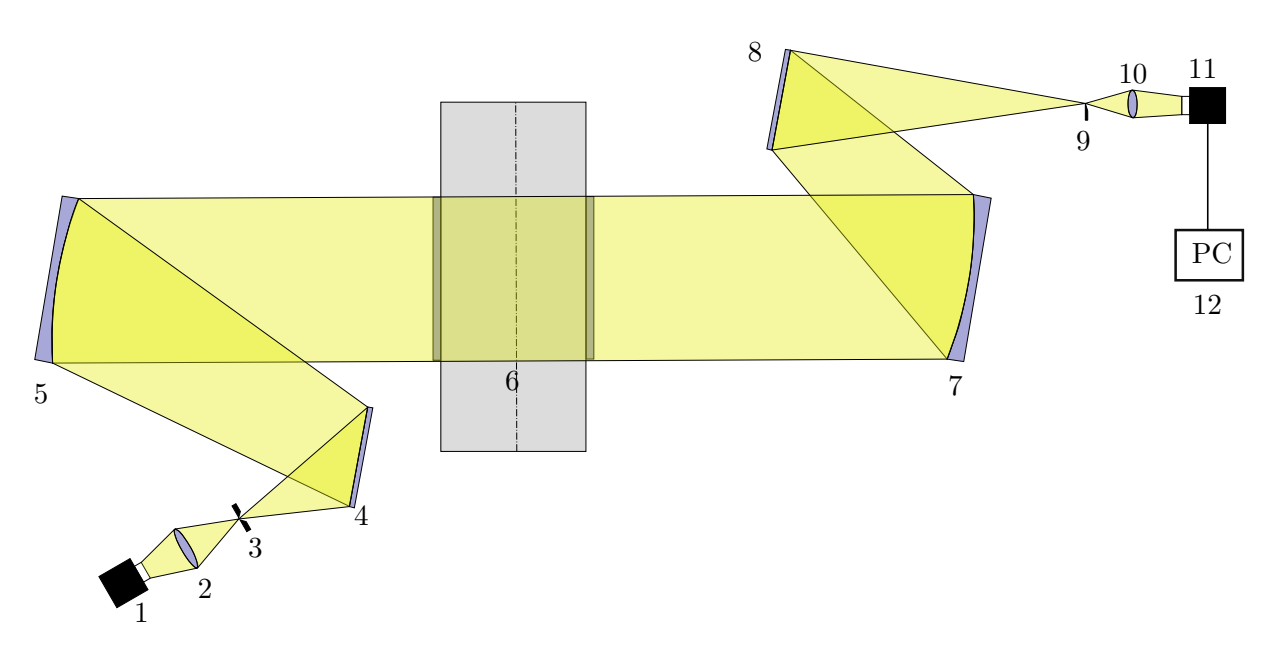


Figure 4.3: Schlieren configuration for transverse injection into supersonic crossflow

The schlieren configuration used in the ST-15 wind tunnel test-hall is mirror-based Z-Schlieren configuration, presented in Figure 4.3.As described earlier, a continuous source has been selected for the experimental campaign as average flow fields are to be investigated. This is the Solarc Lighting Technology short-arc Xenon lamp (1). The light of the lamp passes through a condenser lens (2), which focuses the light rays at a pin hole (3) of about 1 millimetre. The pinhole allows for a more uniform effective source without intensity drop at its edges. The light is then reflected by a mirror (4) and onto the parabolic mirror (5). The parabolic mirror acts as a lens, collimating the light beam. The collimated beam passes through a set of optical windows and into the test section (6). The beam is then sent to the second parabolic mirror (7) and into the second mirror(8) and then onto the knife-edge (9). As explained previously, the beam is focused at the filter where the cut-off is determined based on the required sensitivity and available light intensity. After the knife edge the beam passes through a second lens (10) of focal length f = 180 millimetres, which focuses the light onto the detector of the LaVision Imager LX 2MP interframe CCD (11) camera. The data is subsequently sent to the acquisition PC (11) for collection and processing.

To be able to capture the entirety of the jet flow topology in the near and mid-field of the interaction whilst retaining sufficient resolution given the sensor size of the LaVision Imager LX 2MP interframe CCD (11), a field of view of approximately 81by62[mm] is imaged. In terms of jet diameters this is 20by $15[d_j]$. That provides an imaging resolution of 20[pix/mm]. To achieve statistical convergence a sufficiently large dataset is required. For this reason 250 samples per test case are obtained. The images are images are captured at an acquisition frequency of 16[Hz]

with exposure time of $400[\mu s]$. The exposure time, together with the cut-off of the knife edge are optimised visually for sensitivity and illumination. The resulting acquisition time is 15.63[s]

The obtained images are then further post-processed in order to reduce background noise and sharpen the intensity gradients prior to statistical analysis.

4.2 Particle Image Velocimetry

PIV is a quantitative flow measurement technique which has, in the recent years, gained much attention in the field of experimental fluid dynamics. This comes from the fact that, unlike conventional quantitative velocity measurement techniques such as Hot Wire Anemometry (HWA) and LDV it is a non-intrusive, full-field method. Consequently, PIV will yield full-field flow velocity vector maps (u, v). The capability of providing information for both velocity distributions and turbulent characteristics over the entire FOV makes PIV the selected technique for the core of this research. Finally, as this research also aims to establish the feasibility of using PIV in the near-field of the injection through dual seeding, the domain of interest has been limited to the centreline of the jet in the near- and mid-field of the interaction. Therefore, given the large FOV, planar interrogation domain and the pilot status of the study, planar (2-dimensional) configuration selected for the experiments.

4.2.1 Governing principle

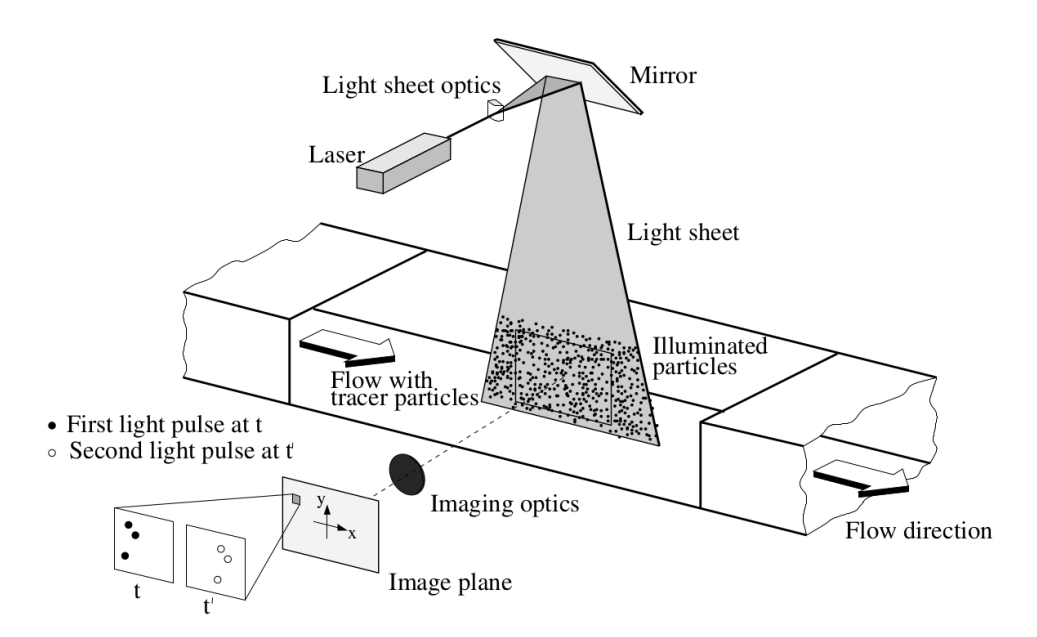


Figure 4.4: Basic PIV measurement system. Obtained from Raffel et al. (2007)

The governing principle of PIV is the measurement of the displacement of tracer particles over a pre-defined time interval. The combination of those two parameters can then be used to determine the flow velocity. The basic planar PIV measurement system can be seen in Figure 4.4. The latter consists of three distinct components - the source and light-sheet optics, the particle

seeding, and the imaging optics and image acquisition device. In order to trace the velocity of the flow, flow tracer particles that are capable to follow the fluid motion are introduced in the free stream. The experimental domain is then illuminated by a thin light sheet, which is shaped from a laser beam through the laser sheet optics. The light for the illumination is provided by a pulsed laser source that allows for the generation of pulses in pairs separated by Δt . The pulses within a pair are separated by a smaller interval, δt , over which the particle displacement is measured. Imaging optics then project the light scattered by the flow tracers in the selected FOV onto a digital camera. The camera is positioned at a right angle to the imaged plane. Furthermore, the image acquisition is synced with the laser, such that the device captures one image at each laser pulse, providing sets of image pairs for processing.

The generic PIV processing algorithm starts with splitting the image plane projected on the image sensor, in small sub domains called interrogation windows, as seen in 4.2. The typical interrogation window varies from 16x16 to 128x128 pixels of the sensor array. The two interrogation window pairs at time t and t' pass through statistical cross-correlation which uses the movement of the uniformly seeded particles to calculate the a cross-correlation map such as the one seen on 4.5. The correlation peak indicates the most-probable displacement in x and y coordinate of the set of the entirety particles imaged in the interrogation window, thus, the uniform seeding. When the calculated displacement is divided by the δt the velocity vector is for this interrogation window is obtained as per Equation 4.8. The interrogation window grid thus becomes the velocity map grid. Note this is the simplest form of the processing algorithm and overlap, multiple passes and image pre-processing as well as vector validation and other options are also possible depending on the obtained data and experimental requirements. The latter shall be discussed in the subsequent chapter in more detail. In the following sections focus will be put on the three main components of the system as implemented per the requirements of this research.

$$\mathbf{U} = \left(\frac{dx}{\delta t}\right)_i + \left(\frac{dy}{\delta t}\right)_i \tag{4.8}$$

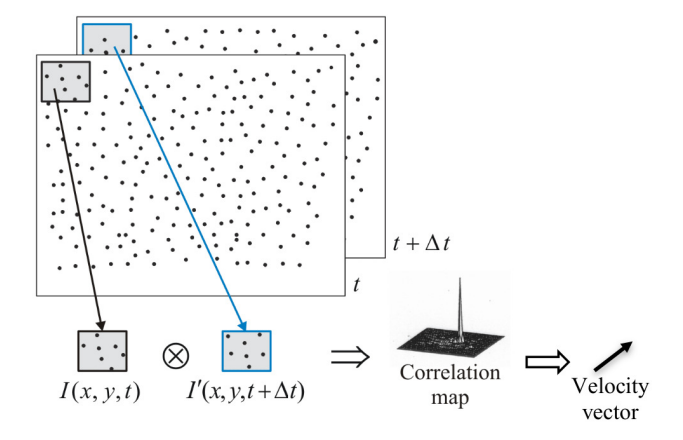


Figure 4.5: Schematic of the generic PIV processing routine. Obtained from Scarano (2013)

4.2.2 Flow seeding

Flow seeding with tracer particles is a critical aspect of PIV. As seen above, in order for the cross-correlation algorithm to work particle concentration should be sufficiently large in order to correlate and not track individual particles, yet small enough so that no multi-phase flow effects are encountered. The latter has to be determined during the experimental campaign. Furthermore flow seeding particles themselves also have to satisfy two conflicting requirements - light scattering and fluid tracing.

To faithfully trace the flow a particle should follow the same trajectory as the stream. As discussed by Raffel et al. (2007), this is affected by the particle fluid mechanical properties, among which Stokes drag - a quasi-steady viscous force - has the highest contribution. Based on the quasi-steady viscous force, the velocity lag of a particle can be defined as

$$\mathbf{U}_{s} = \mathbf{U}_{p} - \mathbf{U} = d_{p}^{2} \frac{(\rho_{p} - \rho)}{18\mu} \frac{d\mathbf{U}_{p}}{dt}, \tag{4.9}$$

where $\mathbf{U}_{\rm p}$ is the particle velocity, \mathbf{U} is the flow velocity, $d_{\rm p}$ is the particle diameter and $\rho_{\rm p}$ is the particle density. As for gases the particle density is generally much larger than the gas density one can simplify and solve this ordinary differential equation, derivation being outside of the scope of this work, obtaining the particle relaxation time constant

$$\tau_{\rm s} = d_{\rm p}^2 \frac{\rho_{\rm p}}{18\mu}.\tag{4.10}$$

The fidelity of the flow tracers in turbulent flows can now be quantified by the particles Stokes number

$$S_k = \frac{\tau_s}{\tau_f},\tag{4.11}$$

where τ_f is a characteristic time scale of the flow. As stated in Scarano (2013), given a step change in flow velocity $\Delta U_{1-2} = U_1 - U_2 \tau_s$ can be defined as can be defined as the time a particle reaches $1 - e^{-1} = 63\%$ of ΔU_{1-2} . From practical considerations faithful tracing of turbulent flow would result in $S_k < 0.1$ giving 10% accuracy. However, for regions where shock waves are present $S_k >> 1$. This results in the fact that the flower time response always tends to smear the discontinuity. Returning to turbulent flows, the time-scale of the flow can be determined through dimensional analysis. The latter can then be also expressed for the turbulent boundary layer, resulting in:

$$\tau_f \approx \frac{L_f}{\Delta U} \approx \frac{\delta_{99}}{U_{\infty}}.$$
(4.12)

Due to their tracing properties the most-commonly used tracer particles for PIV in high-speed flows are DEHS oil and TiO₂ particles. Due to health and safety concerns with the use of the TiO₂, DEHS oil is the selected seeding method for this study. Its properties are summarised in Table 4.1. DEHS provides acceptable particle response times for the study.

Table 4.1: Properties of PIV seeding used in supersonic flows based on Ragni et al. (2011) and Scarano (2013). The S_k is estimated based on the τ_s results presented by Ragni et al. (2011) and the τ_f based on the boundary layer thickness as seen in Equation 4.12 and the date presented in Table 3.1.

Material	$d_p[\mu m]$	$\rho[kg_m^3]$	$\tau_s[\mu s]$ Ragni et al. (2011)	Estimated $S_k[-]$
DEHS	1.0	10^{3}	1.92 to 2.02	0.201

Important for the scattering properties of the seeding is the normalized diameter of the particles. The parameter is obtained from Mie's Scattering theory and it characterizes the light scattering cross-section of the particles. It is defined as

$$q = \frac{\pi d_p}{\lambda},\tag{4.13}$$

where λ is the illumination wavelength, which, as will be explained in the following section, is 532[nm] for the experiments performed in this study. As a result, we see that the scattering and tracing requirement are indeed conflicting. Given that the parameters other than the seeding diameter are going to be the same for the experiments, it can be seen that the DEHS would, in general, be expected to have slightly better scattering properties than the TiO_2 .

The DEHS oil droplet seeding is produced through atomisation. For this purpose the *PIVTEC Aerosol Generator PivPart45 serial number 100* is used. This is a Laskin-nozzle based seeding generator. The generic schematic of oil seeding generator can be seen on Figure 4.6. With such generators, pressurised air is injected in several tubes. The tubes are immersed in DEHS oil. Each one of them has four entraining orifices - the Laskin nozzle. As the air exits through the large opening it draws oil through the small opening at the top of the contraption. In this manner small oil droplets are trapped in air bubbles. The bubbles then raise to the surface where they are ruptured. Upon rupturing, the small oil particles are release. This would, of course, produce particles of various sizes. To provide seeding particles of uniform proportions an impactor plate effectively filters out the large particles.

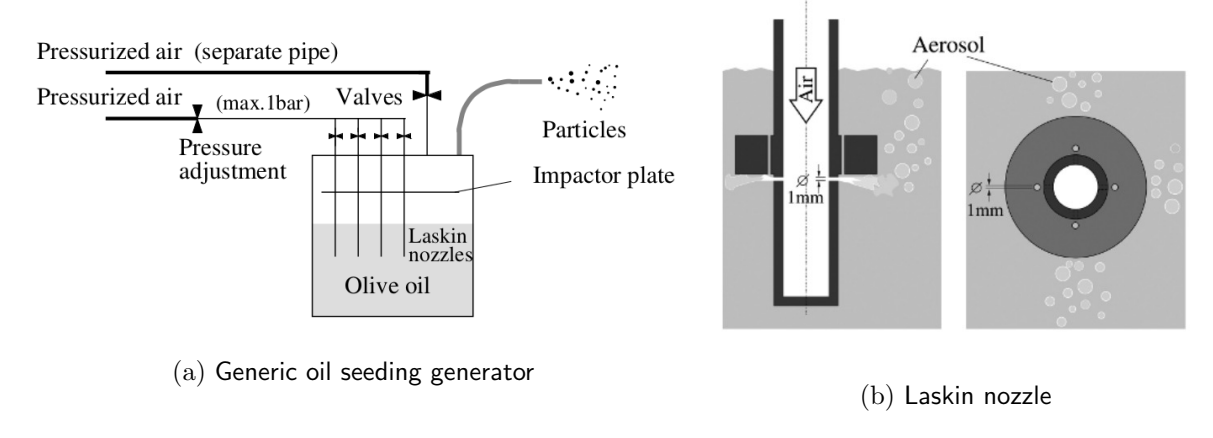


Figure 4.6: Laskin-nozzle based seeding generator Raffel et al. (2007)

The combination of primary jet flow and secondary crossflow (free stream) brings about the requirement for seeding both streams in order to obtain valid vector-fields in the areas near

injection orifice. The latter is achieved by seeding the free stream of the ST-15 through the in-build PIV seeding rake and the jet itself via the pressure feed system. Therefore, two seeding generators are used. The jet seeding generator is the above mentioned *PivPart45* and the second one is a generator build within TU delft. It was observed that, besides the fact different control settings were needed for the seeding, similar seeding was provided by both units. As discussed earlier the PIV seeding can be connected in parallel to the main jet flow in the injection system. The connection is marked in Figure 4.13.

An important note which was mentioned earlier in this report is the limitation of the system due to teh seeding generators. The PivPart45 can only withstand 5[bar] pressure. Given that 1[bar] overpressure is required for seeding only 4[bar] is left as margin. Therefore, the maximum jet total pressure was limited to 4[bar], reducing the maximum attainable J.

4.2.3 Illumination and light-sheet optics

The illumination for the experiments is provided by the double-pulsed solid-state frequency-doubled Neodymium-Doped Yttrium Aluminium Garnet laser (Nd:YAG) Quantel Evergreen 200. Such lasers are a common choice for PIV measurements. The Evergreen provides powerful laser pulses (200[mJ]) with short pulse duration (<10[ns]). However, its low repetition rate does not allow for time-resolved measurements(15[Hz]). Provided time-resolved measurements are out of scope for this research, however, this is not considered an important factor. The light emission for the unit is provided by two separate laser heads. The initially emitted light has wavelength of $\lambda = 1064[nm]$. Subsequently a polarised beam combiner combines the two beams and a frequency doubler decreases the output wavelength to $\lambda = 532[nm]$. The laser pulse separation for this experiment is set to $\delta t = 0.75\mu s$, which can be seen in Figure 4.7. This results in particle displacement of approximately 14 pixels in the free stream, setting limit to the minimum interrogation window size. The equations related to this calculation will be presented in the following section.

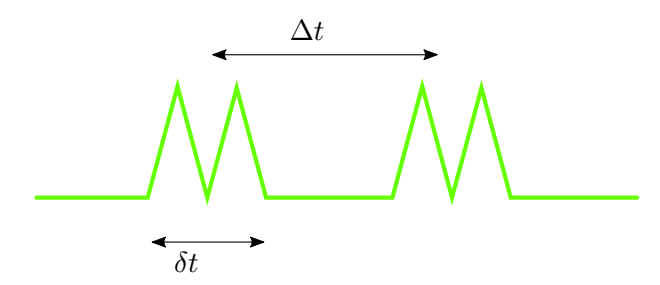
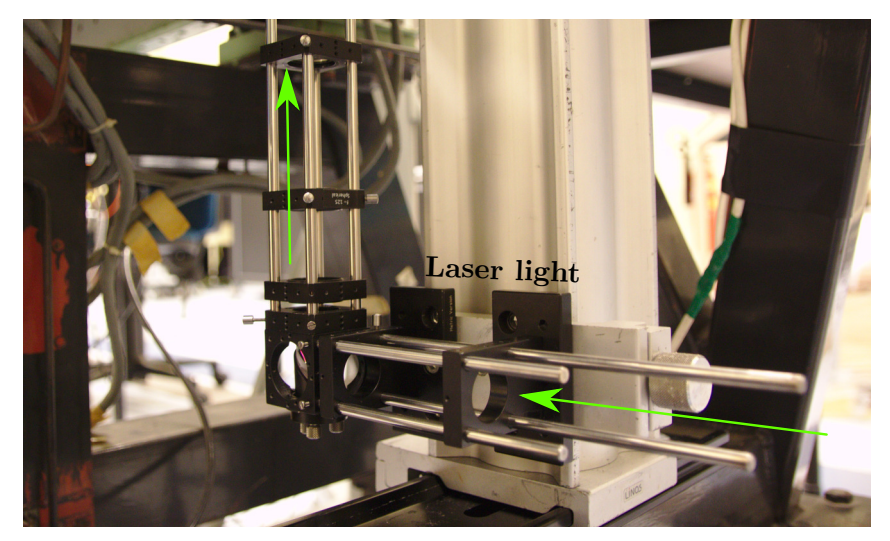


Figure 4.7: Laser pulse separation and and pulse pair separation

To deliver the light to the laser light to the test section a set of cylindrical lenses in combination with two mirrors is used. The system components can be seen on Figure 4.8. The system expands the beam into a narrow sheet of 2[mm] and directs it into the test section. The light enters in the wind tunnel from a mirror attached to a flange at the bottom of the tunnel. The laser shines from the aft of the test section, or in other words, against the free stream direction. The full configuration with laser light shining in the test section can be seen in Figure 4.9.



(a) Light sheet formation optics with adjustable 45° directing the light into the optical window attached below the wind tunnel





 $(b) \ \, \mbox{Optical window located at the bottom of ST-15,} \ \, (c) \ \, \mbox{Adjustable mirror directing the laser sheet within below the ineluctable mirror} \qquad \qquad \mbox{the ST-15}$

Figure 4.8: Components of the laser sheet formation optics used for the experiments

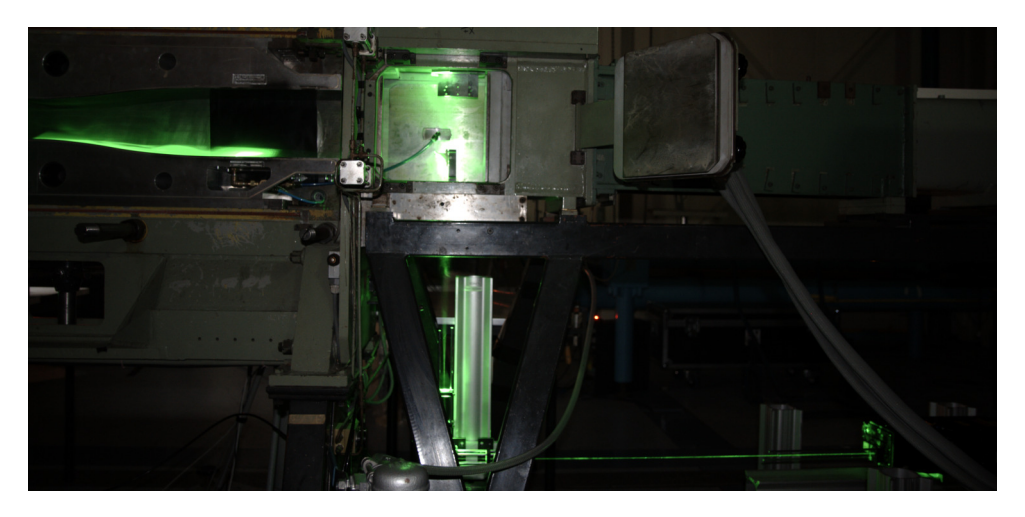


Figure 4.9: Image of the laser optics of the PIV set-up with laser light on

4.2.4 Acquisition and imaging optics

The imaging optics and acquisition configuration is critical for providing properly focused particles with sufficient illumination and with acceptable particle exposure and image displacement, such that there are neither streaks on the images, nor do a significant amount of the particles exit the interrogation window domain. The general configuration of the set-up is presented in Figure 4.10.

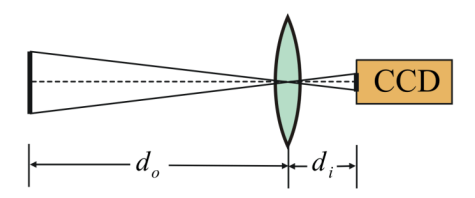


Figure 4.10: Generic PIV imaging optics. Taken from Scarano (2013)

With respect to the acquisition hardware, due to the fact that no time-resolved are to be performed e the La Vision Imager LX 2MP interframe CCD. The Charge Coupled Device (CCD) is a sensor that converts light into free electrons. When discharged, current and voltage proportional to the charge accumulated are produced. The sensor array performing the conversion has a size of 1620×1236 pixels. The size of each pixel is $4.40 [\mu m]$ The standard camera frame rate is 17 frames per second. The data was obtained at 7.5 [Hz] due to the need to synchronize the camera triggering with the laser. The optimal response for the camera sensor is achieved with light wavelength of about 500[nm], as it is optimized to work with the generic Nd:YAG PIV lasers.

The PIV acquisition device has to then be fitted with the respective imaging optics in order to provide optimum projection of the particles in the FOV onto the camera sensor. The optics consist of a single objective. As observed by Scarano (2013), the main parameters driving its selection are the focal length and the magnification defined by thin lens formula as:

$$\frac{1}{f} = \frac{1}{d_i} + \frac{1}{d_o}$$
 and (4.14)

$$M = \frac{d_i}{d_o} = \frac{\text{sensor size}}{\text{imaged object size}} = \frac{\text{pixel size} \times \text{number of pixels in the sensor}}{\text{FOV}}, \quad (4.15)$$

where d_i and d_o are the distances from the lens to the object of observation and from the lens to the imaging sensor respectively. Furthermore, the magnification is directly related to the scaling of the object with respect to its projection onto the CCD sensor surface. An actual working control parameter in photography is the so-called f-stop

$$f_{\#} = \frac{f}{D},\tag{4.16}$$

where D is the lens aperture diameter. The effective f-number controls the pupil diameter, thus the illumination, and the depth of focus, or focal depth of the FOV

$$\delta z = 4.88\lambda f_{\#}^2 \left(\frac{M+1}{M}\right)^2.$$
 (4.17)

The δz is important as it determines the range in which the particles are in focus. Should the laser sheet thickness be smaller than the depth of focus then the particle imaged diameter on the sensor can be calculated as a combination of the geometrical projection of the diameter plus the diameter change due to diffraction effects caused by the finite resolution of the imaging system, namely

$$d_{\tau} = \sqrt{\left(d_{geom}\right)^2 + \left(d_{diff}\right)^2} \text{ where}$$
(4.18)

$$d_{\text{geom}} = M d_p \text{ and} (4.19)$$

$$d_{diff} = 2.44\lambda(1+M)f_a. (4.20)$$

As per the research goals presented in Chapter 1, the near and mid-field of the jet-crossflow comprise the target instigation region. This constitutes a region of at least about 20 jet diameters. Furthermore, the jet shock structure should also be clearly visible, requiring several jet diameters in the negative direction, considering the origin as the jet exit. As a result, the defined FOV for the measurements is $\mathbf{x}:(-5:20[x/d_j]);\ \mathbf{y}:(-1:19[x/d_j])$. Where the y-coordinate is related to the sensor width to height ratio. (This results in a physical imaging area of 100:80[mm]. To be able to capture the required FOV, two LaVision Imager LX 2MP interframe CCD cameras are positioned side by side and fitted with f=60[mm] Nikkor objectives at $f_{\#}=8$, yielding a magnification M=0.16. The camera overlap for this dual-PIV arrangement is about 10% of the sensor size. The latter is required for stitching the two FOVs together. The configuration is presented in Figure 4.11. The configuration can also be seen in the subsequent Figure 4.12.

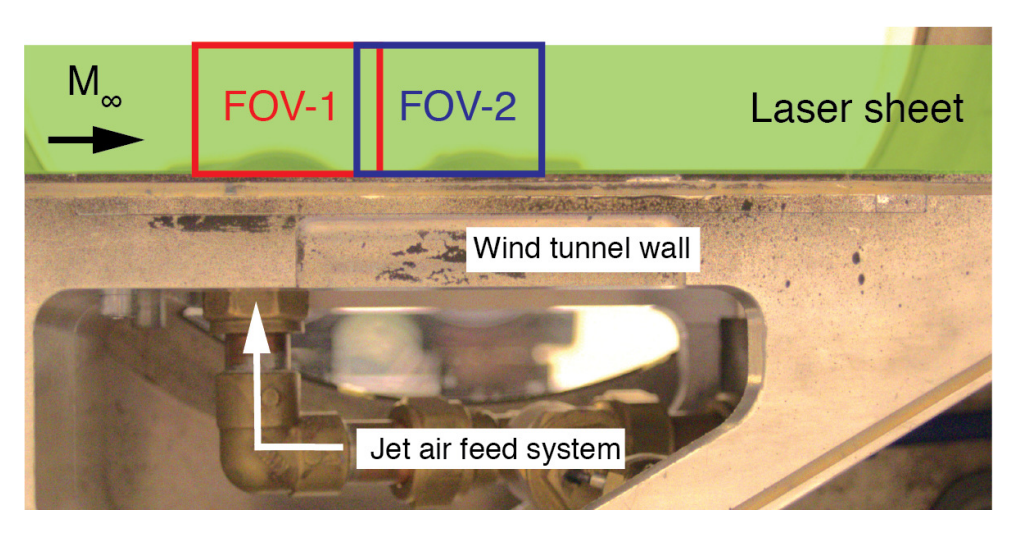


Figure 4.11: FOV for PIV with camera overlap Pazhev et al. (2019)



Figure 4.12: Dual PIV camera configuration

The above configuration leads to $\delta z = 8.73 [mm]$ which is much larger than the laser sheet thickness. Consequently the particle imaged diameter is $d_{\tau} = 12 [\mu m]$. The latter is about three times the pixel size. This is around the optimum particle size according to sampling theory. According to it, sub-pixel sized particles would cause pixel locking - locking the position of the particle to the pixel integer value. Oversized particles, on the other hand, would lead to overlap decreasing the contrast of the image.

Finally an note for the image acquisition. Due to the large gradients of the flow and especially in the vicinity aft of the injection point caused by suction of the particles inwards toward the jet centreline and up into the jet core or CVP, sufficient sample size is required for performing the statistical averaging. As a result, per test case, three sets of 150 images are taken at the frequency of 15[Hz], leading to total acquisition time per case of 20[s]. Furthermore, since the height of the laser sheet is smaller than the field of view of the cameras, the top part of the images will be cropped which results in a combined effective field of view of $83 \times 34mm$ or $21.8 \times 8.5[d_j]$ at a resolution of 36[pix/mm].

4.2.5 PIV configuration for transverse injection into supersonic crossflow

The above observations lead to the PIV configuration presented in Figure 4.13. All the seeding and jet feed pressure are supplied from the ST-15 pressure system outlets, connected to the large pressurized air tank that also feeds the ST-15. PTU, seed valve control, LaVision acquisition PC and sensor data pc are all located at the control room of the wind tunnel.

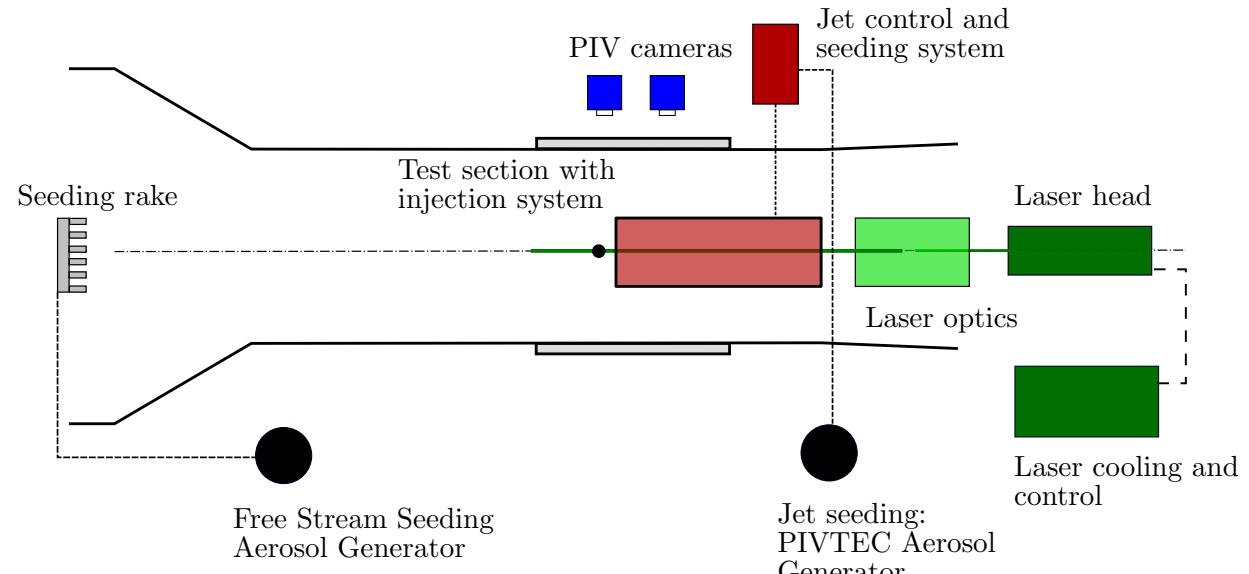


Figure 4.13: Experimental set-up for the \overrightarrow{PIV} experiments

Table 4.2: Particle image velocimetry experimental parameters summary

Parameter	Value	Units
Cam	ieras	
# Cameras	2	-
X pixels	1638	-
Y pixels	1236	-
Pixel Size	4.4e-6	m
Ler	ises	
f	60	mm
D_{max}	f/2.8	-
D_{min}	f/22	
Illumination	Parame	eters
Sheet thickness	2	mm
dt	7,5e-7	\mathbf{S}
Seed	ding	
$\overline{ au_s}$	2	μs
Seeding type	DEHS	-
FOV and	d Optics	5
FOV Total	85	mm
FOV Camera	44.7	mm
M	0.16	-
d_i	69	mm
d_o	435	mm
$f_{\#}$	8	-
focal depth	10	mm

4.2.6 PIV data processing

To obtain the mid-plane velocity flow fields and their statistics PIV data processing was performed using the DaVis 8.4.0 software. The software offers wide range of possibilities for image enhancement, cross-correlation parameters control and vector field enhancement, such that the optimal information is extracted form the data. To provide a general overview, the list of the main processing steps and the parameters optimized in the processing necessary for this study are listed as follows:

- Image pre-processing Enhance particle visibility for the cross-correlation algorithm and reduce background reflections:
 - Time filter Subtract a minimum found on a subset of image: Optimize for filer length in [# images];
 - Space filter (non-linear) Subtract a sliding minimum found on a squared pixel window per image: Optimize for filer length in [# pixels]. The filter length should be such that it is larger than the average particle diameter in pixels so it does not erode it, yet smaller than the interrogation window and kept minimal to avoid producing non-physical intensity distributions in areas of high seeding at the jet exit.
- Masking Areas with reflections and lack of seeding are masked: No particular parameter to optimize;
- Vector calculation parameter Perform iterative multi-grid cross-correlation to obtain the particle displacement of each images pair. Several passes over the image with decreasing window size and changing shape of the interrogation window aid in obtaining the maximum possible concentration of vectors for the given data. Parameters to optimize:
 - Window size [# pixels] for the first and the second window
 - Window shape for the first and the second window
 - Number of passes for the first and the second window
 - Window overlap [%]
- Vector field post-processing Process outliers and fields devoid of vectors
 - Outlier filter type
 - Number of passes for the filtering
 - Filter size [# vectors]
 - Filter thresholds
 - Remove groups below certain number of vectors

After investigation into the effects if the above parameters, the following processing routine was selected:

- 1. Image pre-processing:
 - Time filter Subtract a minimum Filter length: 3 images
 - Space filter (non-linear) Subtract a sliding minimum Filter length: 5 pixel (particle diameter is 3 to 4 pix)
- 2. Masking Masking of top and bottom of the field for reflections and laser sheet height being smaller than the imaging size
- 3. Vector calculation parameter:

- Multiple passes of decreasing size sets of 2 and 3
- Window sizes 64x64 (2 passes), 32x32 (3 passes)
- Window shape Round (all passes)
- Number of passes for the first and the second window
- Window overlap 50 % (2 passes), 75 % (3 passes) resulting in a vector pitch of 0.22 mm (0.055 jet diameters)
- High accuracy mode enabled for the final passes
- 4. Vector field post-processing Process outliers and fields devoid of vectors
 - Median filter: Universal outlier detection (2 passes)
 - Number of passes for the filtering
 - Remove if residual > 2, filter region: 7x7
 - (Re)insert if residual < 3 minimum number of vectors 1
 - Remove groups with < 5 vectors

To exemplify the steps of the algorithm, Figure 4.14 presents a sample of raw data and its conversion to instantaneous velocity field.

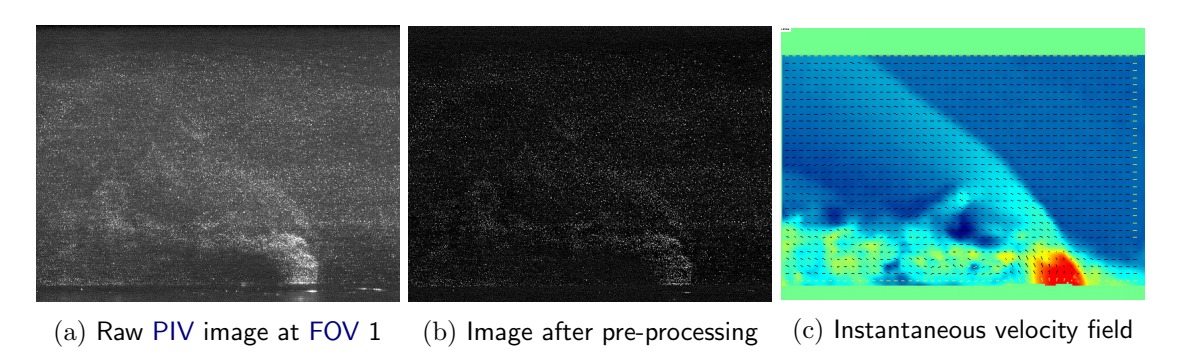


Figure 4.14: Visualisation of the PIV image processing algorithm

Finally, based on 600 image pairs which, the velocity statistics such as the mean and rms were computed. The resulting flow fields can be found in Chapter 5 and Appendix D.

4.3 Conclusions

In this chapter the experimental set-ups for the two parallel investigation techniques were presented, alongside with the relevant background theory needed for understanding of the experiments and the derivation of the test parameters. For more details regarding the use of the set-up and the measured and averaged pressures and temperatures used for executing the test matrices please refer to Appendix C and Appendix .

Chapter 5

Results And Discussion

As seen previously, the jet-in-crossflow flowfield is characterised by turbulence and compressibility effects. In order to be able to address the research questions posed in Chapter 1 four issues are addressed in the subsequent analysis. First of all, the effects of the variation of the flow control parameters on the internal jet shock structures and the interaction shock structures between the crossflow and the jet are analysed. After the gas-dynamic characterisation, observations on the behaviour of the velocity field surrounding the flow discontinues is to be performed. This analysis is conducted by derivation of mean velocity contours in the midplane of the region from PIV data. Besides this, profiles of the velocity deficit in the jet wake and the vertical velocity are also extracted. This will provide better insight into the development of the velocity field and the location and size of the jet core and the CVP structures. The knowledge of the strength and the size of the CVP has been found to be fundamental for the near-field mixing potential of the transverse jet, as discussed in 2.5. From the velocity profiles' loci of maximum magnitudes, jet trajectories are extracted. The latter are analysed with respect to their dependence on the control parameters J and M_i , and compared to empirical correlations discussed in Chapter 2.4. Finally, the turbulent velocity fluctuations around the mean are characterised via TI and nondimensionalised Reynolds shear stress, R_{xy} , contours.

5.1 Shock structure analysis

The conducted Schlieren imaging experiments reveal similar shock structures, as observed in the consulted literature. Time-averaged flow field visualisations for different values of the control parameters based on 250 Schlieren images are presented in Figure 5.1.

Concerning the interaction shock structure, a bow shock is observed on all images in Figure 5.1. The structure is indicated on Figure 5.1d. As previously discussed, the origin of this discontinuity is the blockage of the crossflow introduced by the transverse jet. The overall shape of the shock is similar for different jet Mach numbers. However, upon detailed observations, it can be seen that increasing J leads to an increase in the bow shock angle. This increase can be related to jet

blockage. Besides this, as discussed in Chapter 2, the impediment presented by the jet further causes boundary layer thickening and possible flow reversal. This results in the generation of 3-dimensional horseshoe vortex systems and what-will-be-referred-to as a separation shock. The separation shock materializes at the advent of the horseshoe vortex system. The last is clearly visible for the $M_j=2$ injection cases such as the one shown in Figure 5.1f. At lower Mach numbers, the waves remind more of a compression fan. Note that compression waves caused by model seams are integrated over the length of the test section and are also visualised in the presented images.

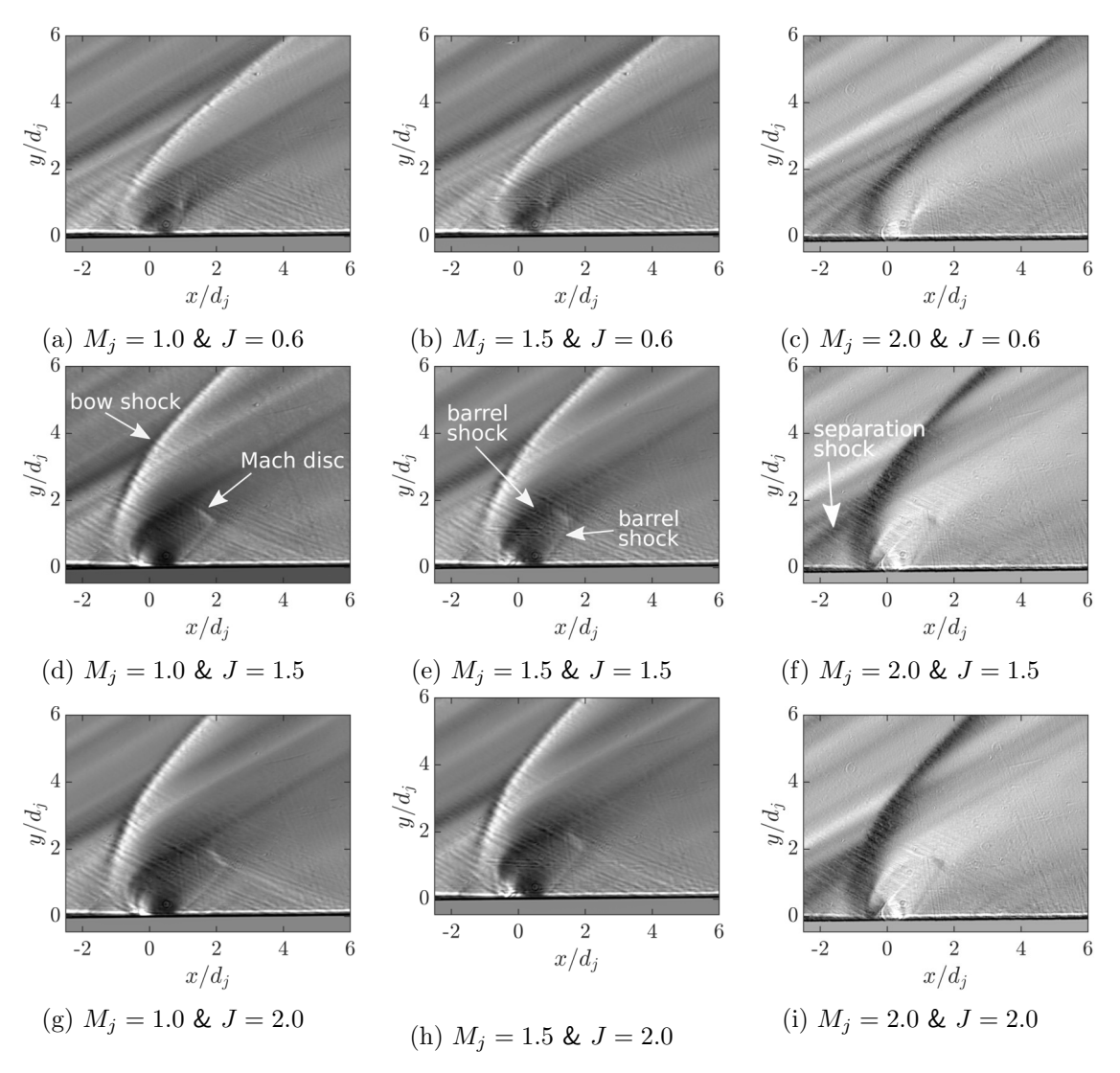


Figure 5.1: Schlieren imaging of the jet in supersonic crossflow

To estimate the oblique shock wave inclination an approximation based on the information from the averaged images such as ones presented in Figure 5.1 is made. The mean angle of the bow shock is taken between two lines. The first one is the line drawn through the intercept of the separation shock and the bow shock, b/d_j and the shock location at $d_j = 4.0$. The second line is the test section floor. The result is presented in Figure 5.2. On the plot, the standard deviation is also presented as error bars of $1 \times \sigma$. The value is obtained from at least 15 manual

measurements of the shock edge. As previously observed, an increase in the momentum flux ratio leads to increased blockage and larger shock angle β . The delta between the different injection Mach numbers is small. The obtained data will be used later for additional calculations.

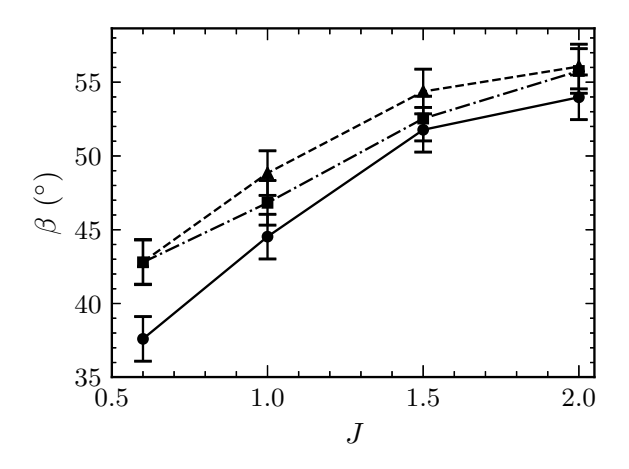


Figure 5.2: Variation of the mean oblique shock wave angle approximation β with J and M_j . Lines are plotted for $M_j=1$ (\bullet), $M_j=1.5$ (\blacktriangle) and $M_j=2$ (\blacksquare). Error bars representing measurement standard deviation of $1\times\sigma$ are also included.

Besides the interaction shocks, the jet shock system is also observable on all images presented in Figure 5.1. Under or overexpansion of the jet leads to the formation of a barrel shock and a Mach disc, which are indicated on Figure 5.1e and Figure 5.1d, respectively. On all obtained images the barrel shock and Mach disc are tilted in the crossflow direction. This tilt can be related to the ratio between the jet exit pressure and the ambient pressure field surrounding the jet. It can be seen that the structures are scaled-up when the momentum ratio is increased. It must be noted that the $M_j = 2$ cases appear to display a slight increase in the curvature of the windward side of the barrel shock and a reduced length of the quasi-normal Mach disc. It is expected from theory that reflected shock waves should occur at triple points formed between the barrel shock and the Mach disc. However, no clear shock wave is seen in the direction of the wall. The latter would normally be expected to engulf the secondary separation after the jet.

The shock systems' main geometric characteristics are measured and plotted in Figure 5.3. Similarly to Figure 5.2, the data is obtained through manual measurements. The standard deviation shown on the plots is calculated in the same manner. It must be noted that the model seams and the materialization of compression fans instead of separation shock increased the difficulty of obtaining some of the data.

Supplementing the observations on the bow shock inclination, Figure 5.3a further confirms that the bow shock stand-off distance, x_{sf} , is directly proportional to the momentum flux ratio and inversely proportional to the jet Mach number. Theoretically, increased J would increase jet penetration into the crossflow and create a more extensive effective flow blockage. Assuming we can model the jet as a solid body, the effective increase in the nose radius is indeed expected to result in a larger shock stand-off and a larger mean angle between the shock and the test section wall. To elaborate on this, we note that in previous studies, such as the one performed by Orth et al. (1969), the Mach disc height has been commonly used as a penetration estimate in Schlieren measurements of jets in crossflow. This approximation assumes that the jet loses

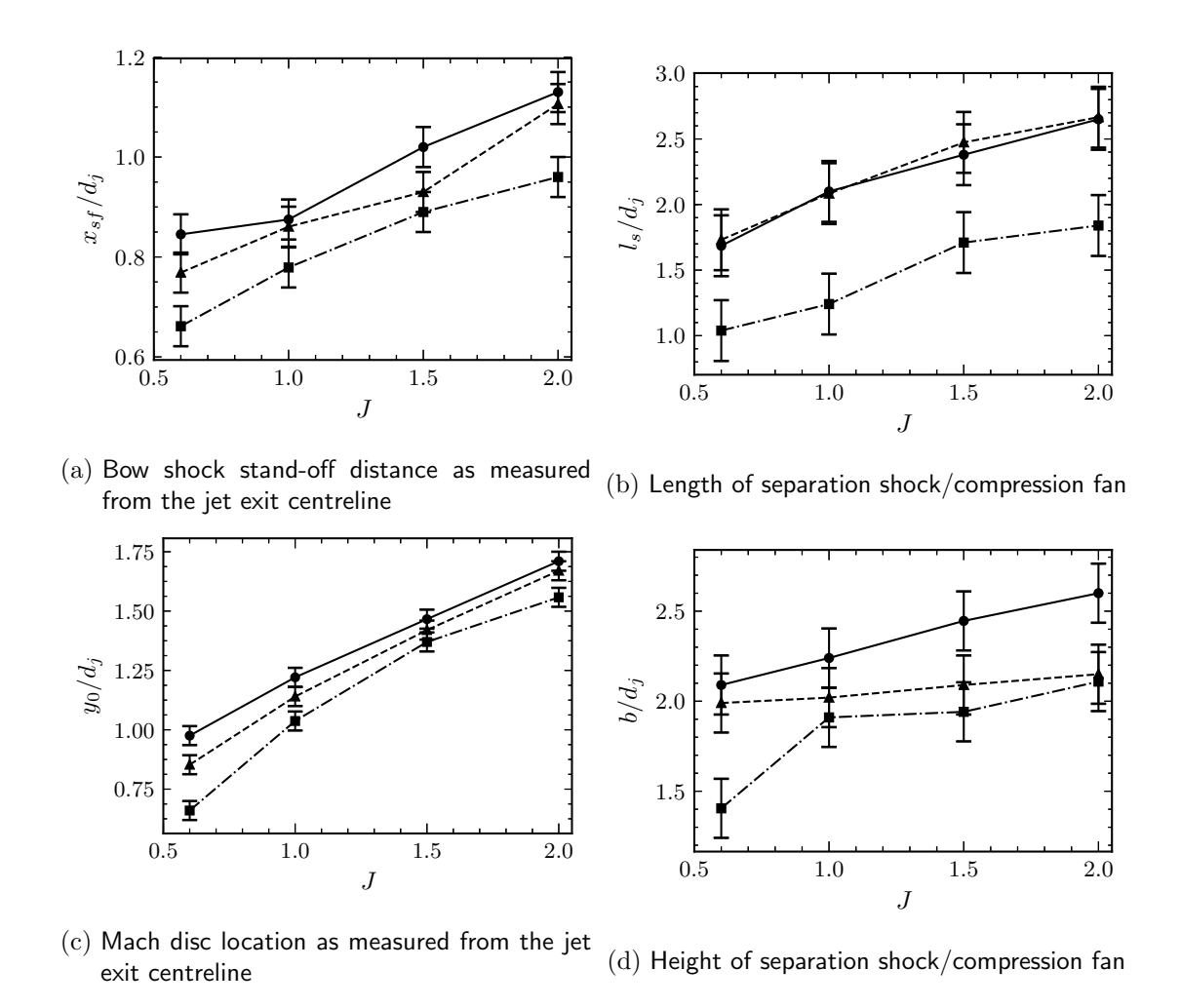


Figure 5.3: Shock system geometric characteristics as measured from averaged Schlieren images. Lines are plotted for $M_j=1$ (\bullet), $M_j=1.5$ (\blacktriangle) and $M_j=2$ (\blacksquare). Error bars representing measurement standard deviation of $1\times\sigma$ are also included.

momentum quickly after the Mach disc and turns sharply in the direction of the crossflow. From Figure 5.3c, it can be seen that the height of the Mach disc does increase with the momentum ratio. The combination of those results supports the relationship between the jet-to-crossflow momentum flux ratio, Mach disc height, transverse jet penetration and the resulting effective flow blockage. With respect to the variation of M_j , the inverse relationship is seen. As the jet Mach number increases, there is a reduction of the Mach disc height.

Figures 5.3b and 5.3d show the dimensions of the area beneath the separation shock or compression fan windward of the jet. It is seen that the region increases with the jet-to-crossflow momentum flux ratio as the effective blockage increases. This observation is consistent with the fact that the shock stand-off distance increases with J, and thus the effective obstruction is larger. The inverse relationship is found with respect to the variation of M_i .

In many of the cases in Figure 5.3, and, in particular in Figure 5.3b, the data points for jet Mach numbers of $M_j = 1$ and $M_j = 1.5$ are quite close. This may be caused by both measurement error and manufacturing tolerances due to the small delta between the dimensions of the $M_j = 1$

and $M_j = 1.5$ nozzle.

To summarise, as seen above, all major shock structures besides the reflection shocks described in the literature were observed. The jet Mach disc is always strongly tilted in the crossflow direction. The increase of J seems to pose a larger obstruction to the flow. The near-field penetration is higher based on the Mach disc location. This increases the bows shock angle, stand-off and the area under the separation shock or compression fan structures. Supersonic injection, on the other hand, displays a slight decrease in the Mach disc height. This leads to reduced bow shock stand-off and a decreased length of the area under the separation shock. A clear separation shock wave was only observed for $M_j = 2$. This may be related to the shorter separation length and thus steeper flow turning angle, providing a stronger compression.

The previous discussion and results reveal that the current study deals with an injection topology case that is not described in Figure 2.7. With the current injection case, there is indeed a thick boundary layer compared to the Mach disc height. The jet boundary layer is of the order of 1.25 jet diameters, and the Mach disc height can reach $2d_i$. However, the Mach disc is tilted in the crossflow direction. Returning to figure 5.1, it can be seen that for all cases the bow shock penetrates into the boundary layer itself, well beyond the height of the separation shock. This can be related to the magnitude of the inflow Mach number and the large thickness of the boundary layer, in combination with the selected values of the jet control parameters. It seems part of the boundary layer is supersonic, and the bow shock thus spreads deeper into it. In this area, the bow shock has a substantial angle. As a result of this, a much larger compression is expected as compared to the case where the crossflow boundary layer does not undergo additional compression. Consequently, for jets at $M_{\infty}=2$ and higher with thick boundary layer and the range of selected J, this study proposes the flow regime schematic presented in Figure 5.4. Here we see a lambda shock structure at the interaction. We should additionally note that the separation shock may manifest as compression fans. The jet chock structures themselves are curved on the windward side due to the adverse pressure gradient of the bow shock. Finally, the Mach disc has a somewhat limited diameter, and a large portion of the jet stream is expected to pass through the barrel shock.

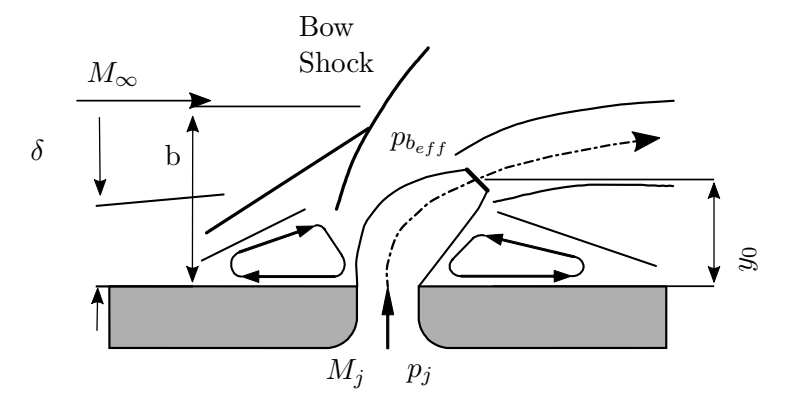


Figure 5.4: Schematic of the proposed operational regime for a compressible jet in crossflow with thick boundary layer δ penetrated by the bow shock. It should be noted that, depending on the injection parameters, the separation shock may be replaced by a compression fan. Indicated are the free stream Mach number M_{∞} , the separation shock height b an the Mach disc height y_0 , and the jet exit properties, M_j and p_j .

To supplement the previous discussion, sensor data combined with the semi-analytical method-

ology from the correlations of Orth et al. (1969) and the results of Heister and Karagozian (1990) presented in Chapter 2.3 is used to calculate the effective backpressure pressure ratio at the jet exit. The ratio can be defined as $p_j/p_{b_{eff}}$. The variables are also shown in Figure 5.4. The approximation for the static pressure jump over the shock system is based on either normal or approximated oblique shock wave beyond the separation height b. For the latter the data from Figure 5.2. The significance of this ratio for the strength and formation of the jet shock structures and the jet penetration was discussed in Chapter 2.3. The results for both cases are presented in Figure 5.1.

Table 5.1: Pressure matching $p_j/p_{b_{eff}}$ for the jet plume at the jet exit and after the Mach disc for the case of NS and OS approximation based on sensor data and information extracted from Schlieren images.

(a) $(p$	$_{j}/p_{b_{eff}}$	$)_{exit}$ aft	er NS
J/M	1.0	1.5	2.0
0.6	1.07	0.50	0.27
1.0	1.79	0.81	0.44
1.5	2.74	1.16	0.71
2.0	3.64	1.65	0.89

As seen in Table 3.7, both the conditions of over- and underexpanded jet manifest themselves with the current experimental matrix. Depending on the approximation used for the interaction shock system, for the $M_j = 2$ injection, either all or half of the cases are overexpanded. Furthermore, depending on the approximation, the $M_j = 1.5$ injection can be composed of either a full set of underexpanded cases or a combined set of over-and underexpanded cases. Given the previously seen downscaling of the parameters with supersonic injection, this shift to over-expanded jet could possibly be related to the effective drop in the Mach disc height and thus, reduced near-field penetration. As discussed previously, this is also reflected in all the other shock structure characteristics.

5.2 Mean velocity field analysis

To characterise the mean flow filed and obtain information on the jet location and wake profile for different values of the control parameters and a qualitative indication of the vortical strength, the PIV mean flowfield in the centreline of jet injection is analysed in this section. The latter is combined with a more qualitative visualisation based on the velocity deficit and vertical velocity profiles. The analysis focuses on the characterisation of the effect of the control parameters and their effect of the velocities fields and the imprint of the 3-dimensional large-scale structures in the midplane y/h=0 of the interaction. As discussed previously, the strength and location of the large-scale structures are essential for both the near-field bulk mixing related to the application as fuel nozzles and for the prospective jet-body interaction, as related to reaction attitude control jets. The jets in this study, however, replicate more closely the injection conditions for supersonic combustion fuel injectors.

Due to the similarity of the velocity fields, it has been decided to present only a subset of the data in the main report. Based on the observations from Schlieren imaging and PIV only the cases with $M_j \in [1, 2]$ and $J \in [1, 1.5]$ are discussed. Additional material is present in Appendix D.

Before the beginning of the discussion, it must be noted that the J=2 case was not selected due to both similarities of the flowfield and seeding issues behind the jet. The combination of high particle Stokes number and the pressure gradients caused by the expansion of the crossflow around the jet, high centrifugal forces are encountered, and the aerosol is ejected out of the wake, effectively starving the region of seed particles. To avoid such issues, velocity profiles were also not obtained from the region, for all cases and masking was applied to the data in the problematic region.

5.2.1 Velocity contours

The streamwise velocity flowfield provide insight into the flow acceleration, CVP and wake strength location and extend of the latter. As explained in Chapter 2.5, the CVP, combined with the impingement of freestream on both sides of the jet and the formation of wake vortices, plays important role in the near- and mid-field mixing potential of the injection. The flow fields for variable momentum flux ratio and jet Mach number for the two are presented Figures 5.5 and 5.6, and 5.7 and 5.8, respectively.

At all injection conditions, both the interaction shock structures, and in particular the bow shock, and the transverse jet are visible. As seen in Figure 5.5, due to the perpendicularity of the jet to the incoming crossflow the u-component of the velocity is zero inside the jet and increases as it turns and eventually becomes aligned to the crossflow. This is also reflected by the v-component of the velocity seen in Figure 5.6. It reaches a maximum as the jet is expelled into the crossflow and is terminated by the barrel shock, decreasing rapidly as the jet is turned and passes through the discontinuity. As it was also observed from the analysis on the Schlieren data, immediately upstream of the jet exit, thickening and possible separation of the boundary layer can be seen. In the PIV flow fields, this is manifested as a decrease in the u-and an increase in the v-component. However, the resolution of the measurement is insufficient to detect any flow reversal and analyse the formation of horseshoe and shear layer vortices. The relative thickness of the 5mm boundary layer compared to the jet flow structures is also immediately visible. The relative thickness of the layer can be correlated with the previously observed formation of compression waves rather than a single separation shock wave.

As seen in Figure 5.5, a velocity deficit is observed in the u-component downstream of the jet. This deficit is caused by the jet core blockage, which leads to the formation of a jet wake. When increasing the momentum flux ratio for the injection at $M_j = 1$, the wake becomes stronger, penetrates deeper into the flow and its vertical spread also increases. For the lower J cases, it is observed that the latter interacts with the wall-bound flow. The strength of the wake seems to diminish with the downstream distance of the injection. Additionally, a downward tilt of the location of the wake is observed directly after the jet, which subsequently has an inflexion point and penetrates upwards into the crossflow.

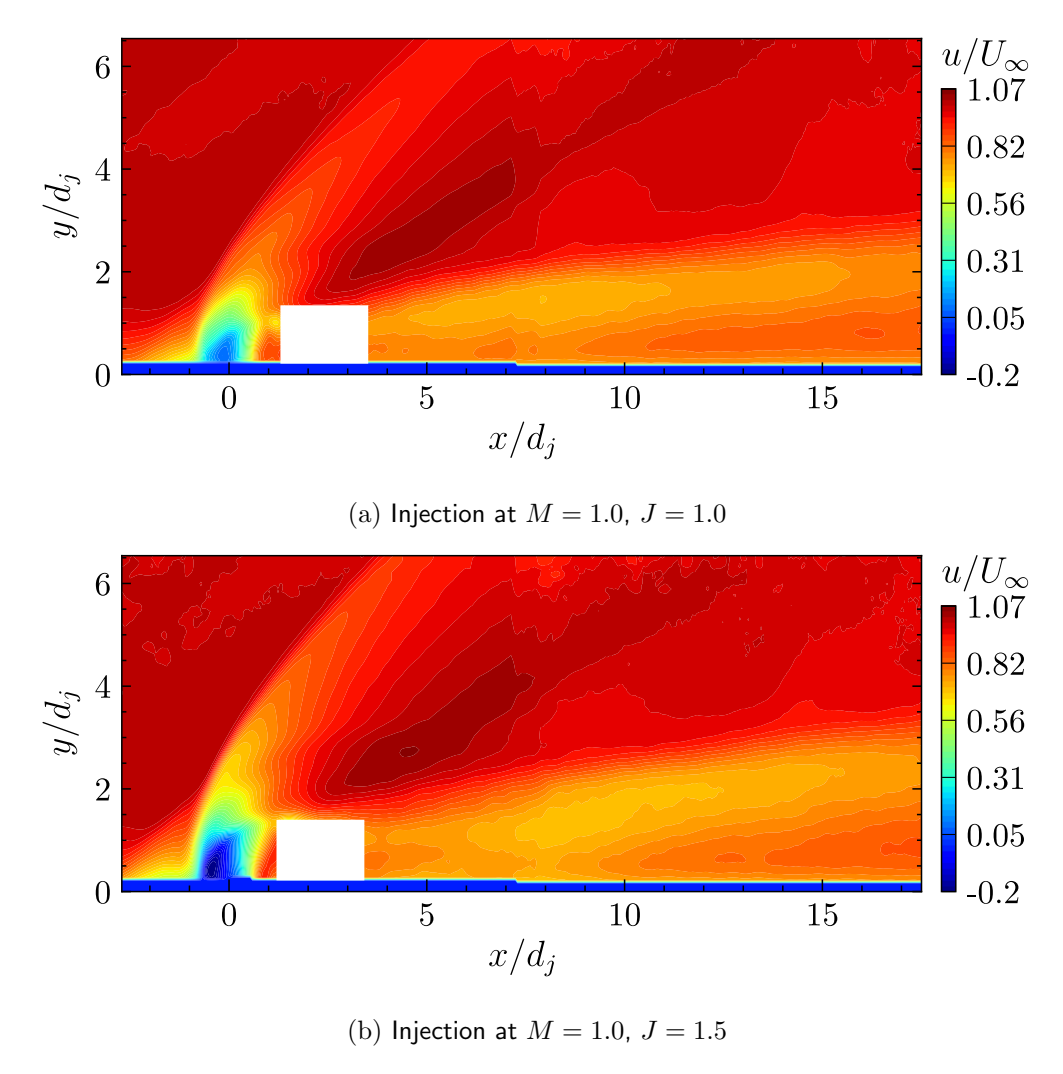


Figure 5.5: Streamwise horizontal velocity contours for variable momentum flux ratio for the Mach 1 injection at the midplane y/h=0 of the test section, designated as $z/d_j=0$

Concerning the vertical velocity contours, which are presented in Figure 5.6, several flow structures are observed. Firstly, the acceleration of the jet within the area engulfed by the barrel shock is visible. Based on the jet-to-crossflow momentum flux ratio, the vertical velocity increases due to the expansion of the jet. Sharp termination of this acceleration is seen at the perceived shock location. Behind the jet chock structures, upwash is observed in the wake. This upwash is in the midplane y/h=0 is caused by the CVP. The jet location based on this upwash is not identical to the location based on the streamwise velocity contours. When the jet-to-crossflow momentum flux ratio increases, the intensity of the upwash and its spread increase as well. It further seems to also penetrate higher into the crossflow, indicating the vortex pair should also be lifting higher away from the wall. Finally, at distances far downstream of the injection, a decrease of the CVP upwash is observed. The latter can be related to decay in the CVP strength as well as an increase of the distance between the two vortex cores. Finally, it can be seen that the near field penetration of the jet is rapid. Subsequently, a gradual increase in penetration depth is observed downstream.

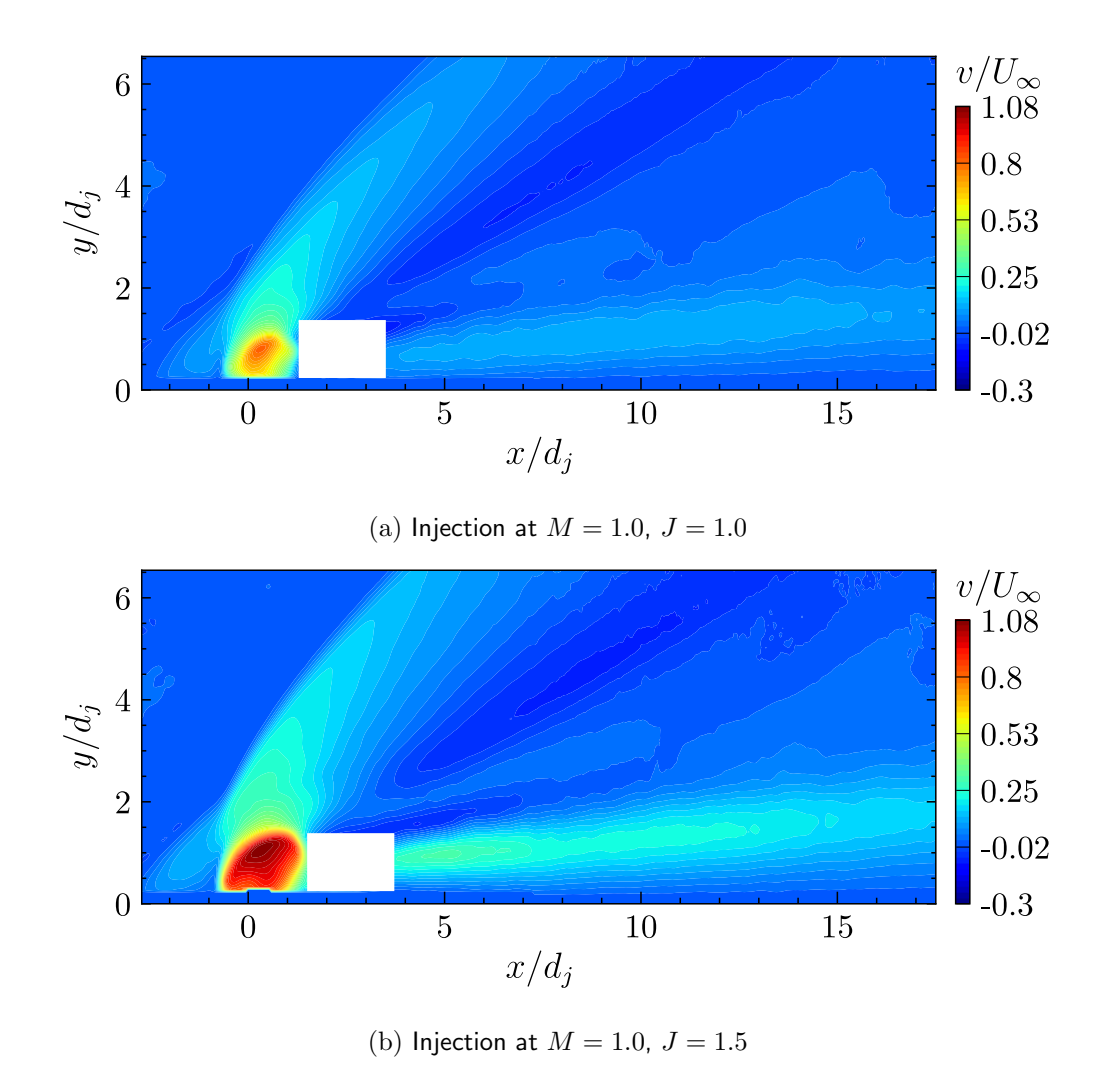


Figure 5.6: Vertical velocity contours for variable momentum flux ratio for the Mach 1 injection at the midplane y/h=0 of the test section, designated as $z/d_j=0$

The streamwise velocity contours for variable jet Mach number are presented in Figure 5.7. Variation of J for $M_j = 2$ leads to increased wake penetration and width. However, the wake strength does not seem to increase significantly. The last shows a decrease for the case of supersonic injection at J = 1, as compared to the sonic injection. Furthermore, the retardation area at the jet exit is much smaller, which can be related to lower blockage.

Figure 5.8 reveals that the increase in the M_j leads to a reduction of the area of jet acceleration at the jet exit. For the J=1 case shown in Figure 5.8b the structures are not visible. Furthermore, for supersonic injection, the upwash related to the CVP is visible only after $x/d_j=10$. The decrease in strength of the upwash as compared to sonic injection is significant. This is expected to have a negative impact on the mixing capabilities of the jet. Before the upwash materializes a region of downwash is visible. Comparison between Figures 5.8b and 5.8c reveals that with increasing J, the downwash zone remains of similar size and the upwash zone seems to penetrate below the downwash. Upwash can also be seen with sonic injection; for example, Figure 5.8a, but its extent is limited. The extend of the downwash for the sonic injection cases is around five

injection diameters and for the one of supersonic injection around ten injection diameters.

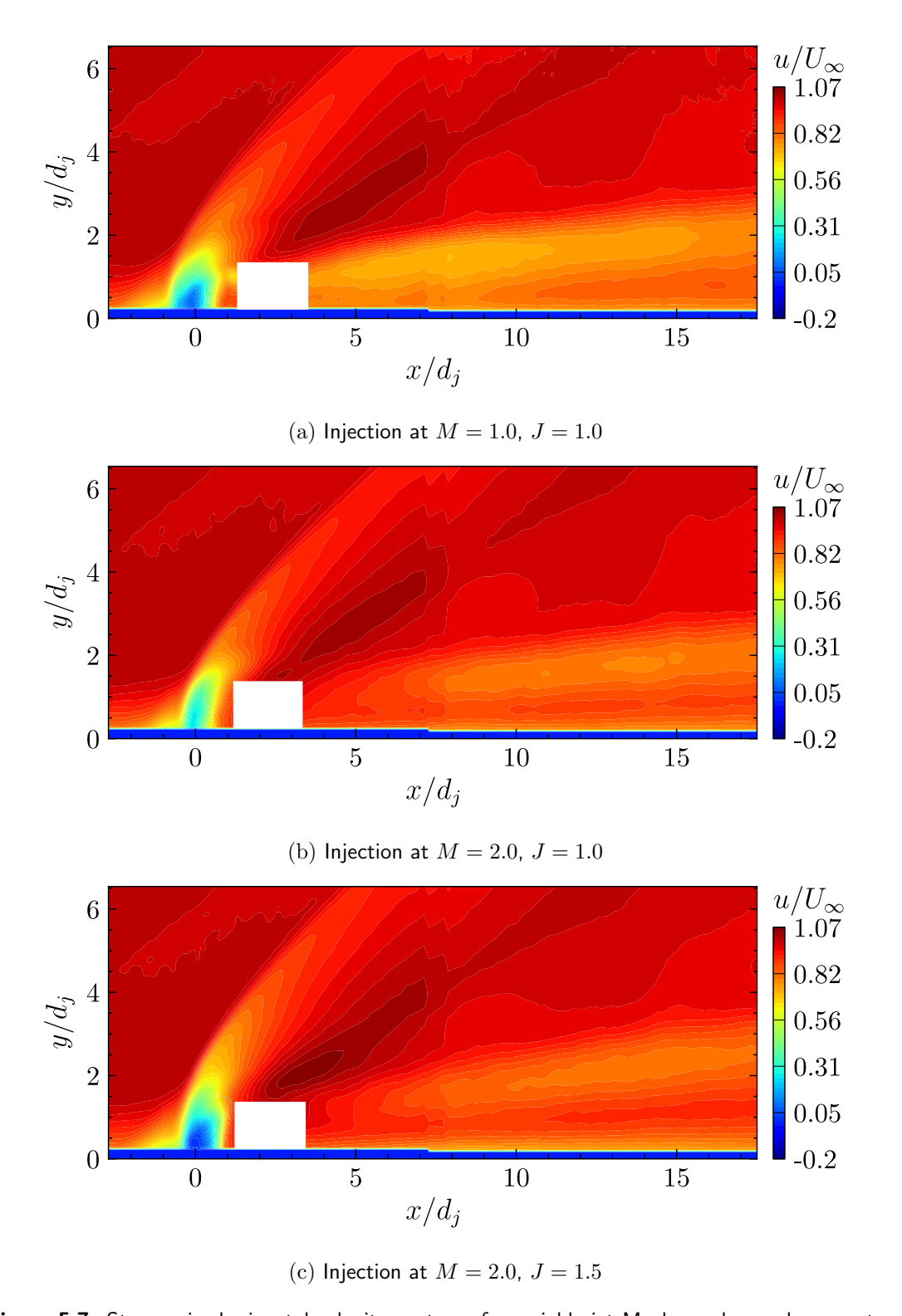


Figure 5.7: Streamwise horizontal velocity contours for variable jet Mach number and momentum flux ratio injection at the midplane y/h=0 of the test section, designated as $z/d_j=0$

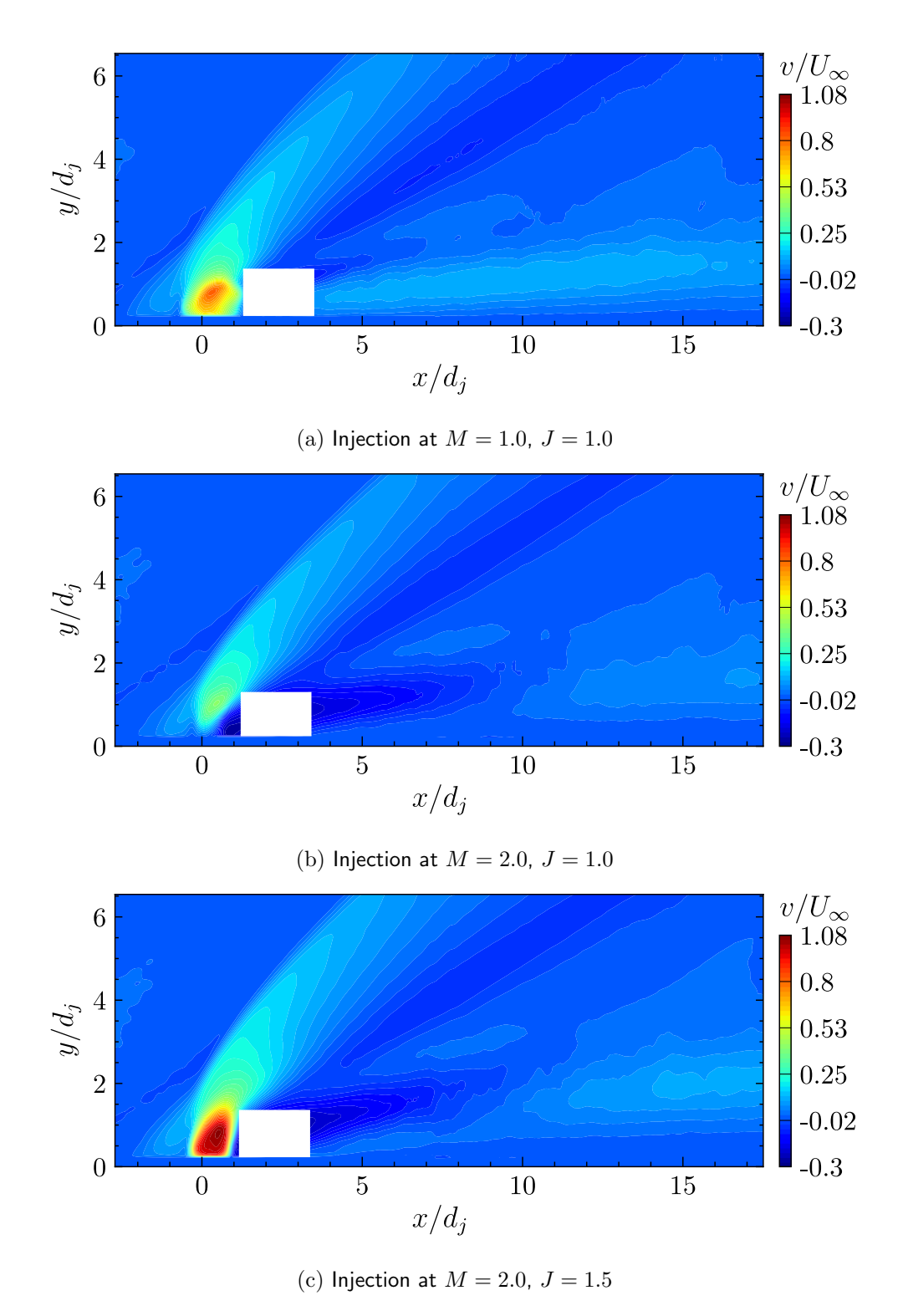


Figure 5.8: Vertical velocity contours for variable jet Mach number and momentum flux ratio injection at the midplane y/h=0 of the test section, designated as $z/d_j=0$

Although the figures are omitted from the main body of the report, it must be mentioned that for J=0.6 for both cases that upwash and the downwash zone are parallel with the downwash preceding the upwash. To complement this, it can be seen that the downwash area appears when the flow exits the almost-vertical aft wall of the barrel shock in Figure 5.8a, and the Mach disc with the cases in 5.8.

Additionally, with the case of J=1 and $M_j=2$, presented in Figure 5.8b, the acceleration of the flow due to jet shock structures and its compression over the jet shock system is not apparent. Likely the barrel shock is collapsed close to or inside the nozzle, causing separation, yet, this cannot be said with certainty. In addition, however, returning to Table 5.1 the injection cases with $M_j=2$ and J=[0.6,1] display a different operational regime than the rest of the cases for both pressure matching after NS and OS.

5.2.2 Velocity profiles

More quantitative information for all cases of the test matrix in a compact way can be obtained by extracting representative velocity profiles at a selected set of representative streamwise locations aft of the jet exit. The latter provides a better overview of the profile development and penetration and span of both the horizontal and vertical velocity. Furthermore, in order to limit the streamwise velocity to profiles to only the local variation, instead of actual velocity, the streamwise velocity deficit is plotted. The latter is defined as

$$u_{deff} = \frac{U_{\infty} - u}{U_{\infty}}. (5.1)$$

The profiles presented in this section are obtained for the following locations: $x/d_j = [0, 1, 5, 10, 15]$. Here we have avoided the region without seeding that spans one to four jet diameters.

Velocity deficit profiles for all cases within the PIV experimental matrix are presented in Figure 5.9. For the profiles located further than five jet diameters away from the jet, the same trends are observed as in the previously-discussed velocity contours. The wake, presented by the rise in u_{deff} , penetrates deeper into the crossflow and increases in width with increasing distance away from the injector for both $M_j = 1$ and $M_j = 2$ cases. The same up-scaling is also observed with the increase of the jet-to-crossflow momentum flux ratio. It can also be seen in Figure 5.9a the sonic injection cases at low momentum flux and close to the wall seem to interact with the wall-bounded flow. Furthermore, interestingly, the J = 0.6 profiles do not show the same scaling as the profiles at a higher J. The deficit of this profile is larger than expected. That may be related to the different operational regime at the $M_j = 1$ J = 0.6 injection case, which, in the mid-field above $d_j = 5$, is similar to that of the low momentum flux $M_j = 2$ cases.

Proceeding with the analysis of the $M_j = 2$ injection profiles, Figure 5.10a is analysed. Similarly to what can be seen on Figure 5.8, the jet caused by injection at the same momentum flux ratio and higher jet Mach number causes a lower blockage, which is observed as lower velocity deficit in the wake.

At and just behind the injector location, the effect of both the jet located close to the wall and the bow shock are seen. This causes the existence of two inflexion points on the curves. The deficit caused by the jet is not clearly seen at one jet diameter for $M_j = 2$ injection, which corresponds to the previous observations.

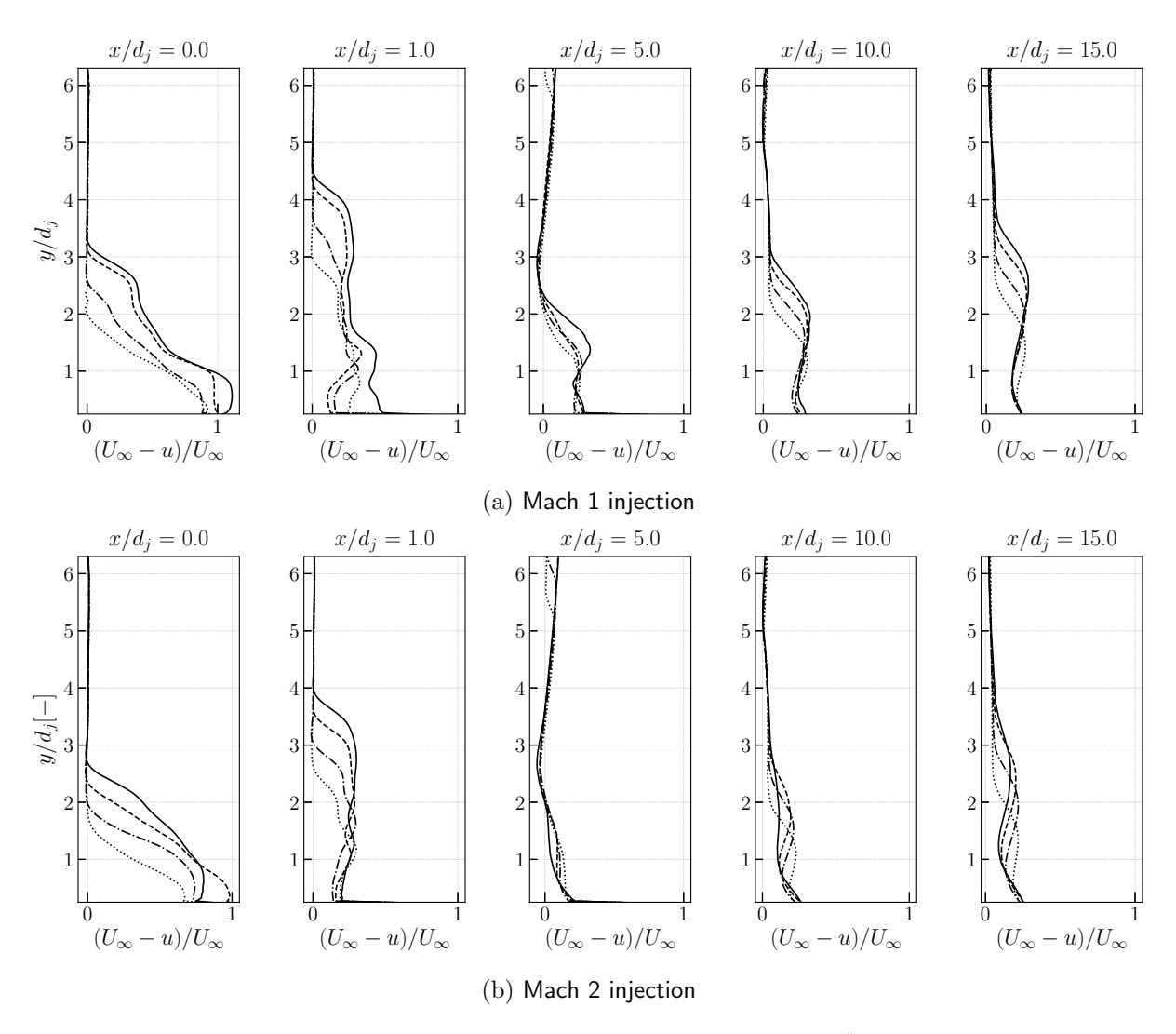


Figure 5.9: Streamwise velocity deficit, u_{deff} , profiles at the midplane y/h = 0. Lines are plotted for J = 0.6 (·····), J = 1 (-·-·), J = 1.5 (-···), J = 2 (——).

With respect to the vertical velocity profiles, similar trends are observed with the plots for $x/d_j = [10, 15]$ as compared to the velocity deficit profiles. Namely, increased penetration and width with increasing J and downstream distance from the injector, and reduced upwash with for the $M_j = 2$ injection. A significant conclusion of the study, for the given experimental conditions, M_j reduces both vortical pair upwash imprint and width. This can be related to either a reduction of strength and/or increased separation distance between the cores of the CVP. Due to the decreased wake strength, and the previous observations on the flowfield, however, most likely the actual strength of the pair is reduced. Therefore, the increase in jet Mach number at constant J would be decremental for the near-field mixing properties of the jet based on the entrainment of crossflow fluid due to the advent of wake vortices. To determine the source of this effect and the validity of this statement, however, cross-plane or 3-dimensional velocity data is required. Preforming a cross-plane PIV could yield the required data. At this point, however, it is also important to note that the effect of the shear layer vortices is also critical for the mixing process.

Besides the upwash, at $x/d_j = [5, 10]$ for injection at $M_j = 2$, the previously-observed downwash can also be seen from the profiles. It is located exactly above the upwash region and decreases in strength downstream and with jet-to crossflow momentum flux ratio. The latter is also observed to a much smaller extent with the cases of sonic injection.

Finally, the profiles close to the jet exit display high transverse penetration of the jet compared to the ones in the mid-field. Consequently it seems that the jet penetration based on this parameter reduces between those two locations.

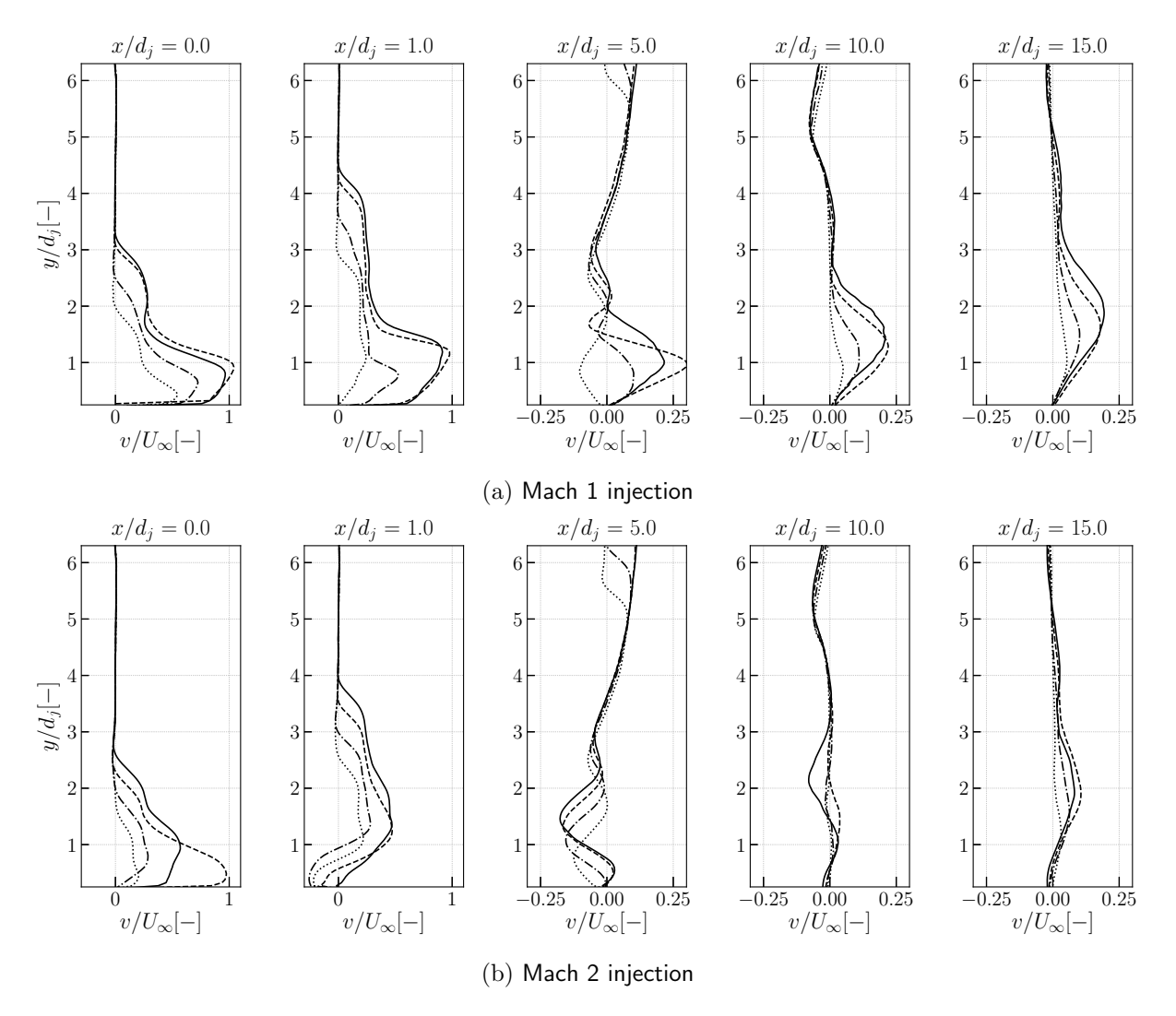


Figure 5.10: Vertical velocity profiles at the midplane y/h = 0.Lines are plotted for J = 0.6 (·····), J = 1 (---), J = 1.5 (-···), J = 2 (—).

In conclusion, the major flows structures' imprint on the midplane y/h = 0 flowfield has been observed. Up-scaling of the structures and their strength has been seen with momentum ratio. With the $M_j = 2$ cases visible reduction of the strength of the imprint of the CVP in the midfield, having a negative effect on the mixing capabilities of the jet. Furthermore, at supersonic injection, due to the over-pressurization of the nozzle, different operational regimes were observed with distinctly different vertical velocity contours in the midplane y/h = 0 of the injection. The

latter seems to be correlated with the lee-side of the barrel shock and the Mach disc for supersonic and sonic injection, respectively. Based on the consulted literature, this has not been observed. The velocity profiles based on streamwise velocity deficit displayed rapid initial penetration followed by a reduction of penetration until $x/d_i > 5$.

5.3 Turbulence analysis

Characterisation of the turbulent velocity field is performed by obtaining contours of TI and nondimensionalised Reynolds shear stress $R_{xy}/[U_{\infty}^2]$. The turbulence intensity can be defined as

$$TI[\%] = \frac{\sqrt{\frac{1}{2}u'^2 + \frac{1}{2}v'^2}}{\bar{U}} \times 100.$$
 (5.2)

Due to the manipulation of the data, increased noise is seen on all plots.

The turbulence intensity contours of selected test cases for variable J and M_j are shown on Figure 5.11. Three areas of high TI are observed in the images. The first area is located at the location of the barrel shock. This could be related to shear between the jet core and the crossflow and SWBLI. The exact magnitude of the turbulence intensity in the area, however, is affected by the low resolution, differential particle slip due to the high-pressure gradient over the shock wave and optical aberrations. The second area is located at the bow shock. The third and last area is a band of high turbulence stemming from behind the Mach disc and extending further into the flowfield. This third area can be related to the generation of the CVP structures and to their subsequent propagation through the flowfield. Due to seeding issues, the intensity in and at the masking region cannot be obtained. Maximum intensity is contained within the region between 1 and 5 or 7 jet diameters, signifying the importance of this region for rapid mixing of the fluids. Gradual dissipation of the TI related to the CVP can be seen downstream.

Increase of J seems to increase the strength and spread of the high TI zone behind the injection. Similarly to the observations for the vertical velocity contours, the increase in M_j leads to a later formation of the band of high TI that can be related to the CVP. It also seems to form lower, as compared to the sonic injection case, which can be correlated to the locations of the maximum vertical velocities observed previously. The near-field turbulence intensity area also seems significantly reduced.

The R_{xy} contours are presented on Figure 5.12. The same three zones can be observed as in the TI contours. Similarly to the turbulence intensity, the Reynolds shear stress related to the CVP also increases with J. The latter decreases with M_j . On the windward side of the barrel shock regions of Reynolds stresses with opposite sign are observed. Keeping in mind the previously discussed limitations, those stresses could be related to SWBLI and the formation of shear layer vortices. To elaborate the unstable region of interaction between the two flows creates opposite signed stresses that bear stimulate the generation of shear layer vortices. This has also been observed by Kawai and Lele (2009). The positive shear stress zone seems to increase with J and decrease with M_j .

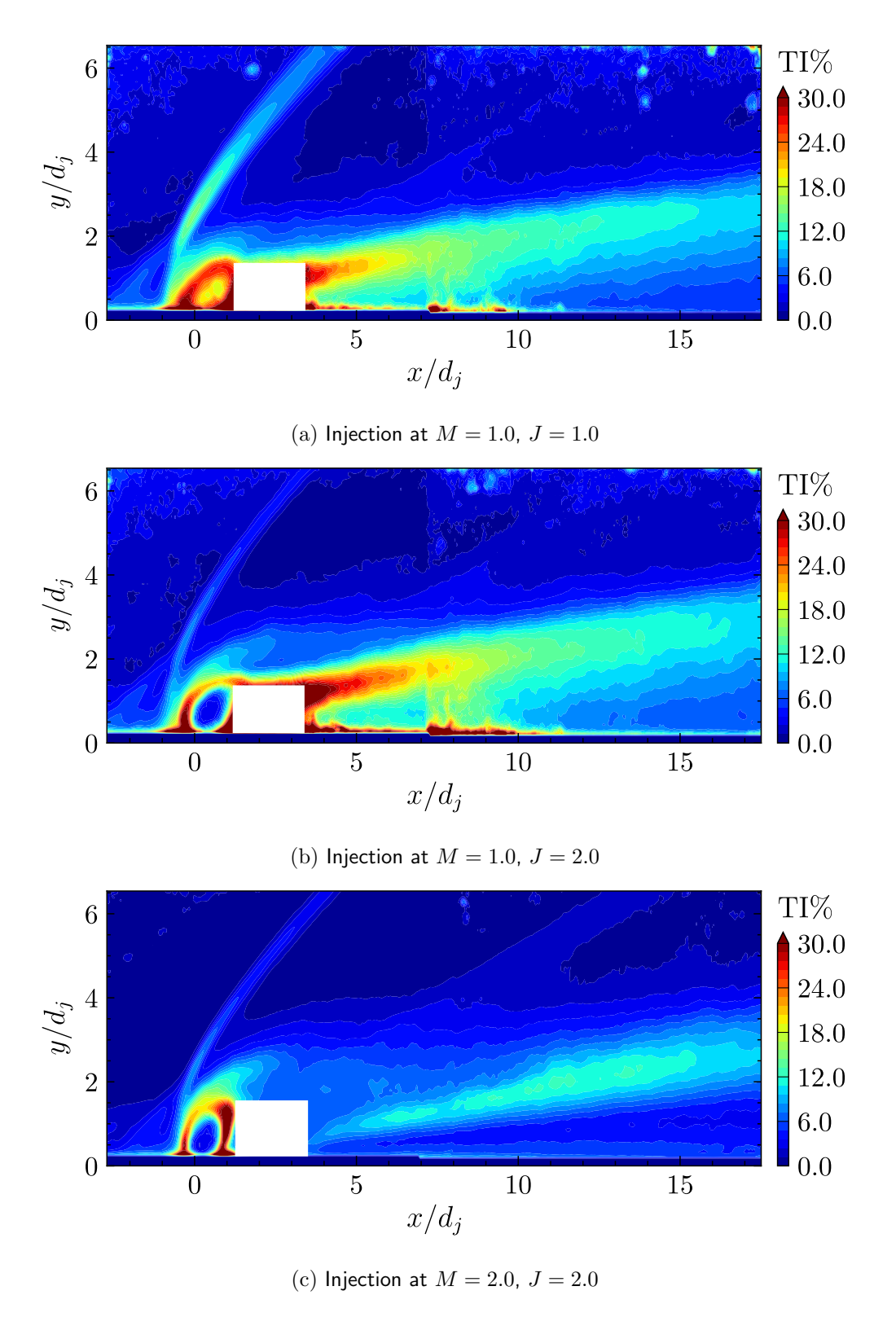


Figure 5.11: TI contours for variable jet Mach number and momentum flux ratio injection at the midplane y/h=0 of the test section, designated as $z/d_j=0$

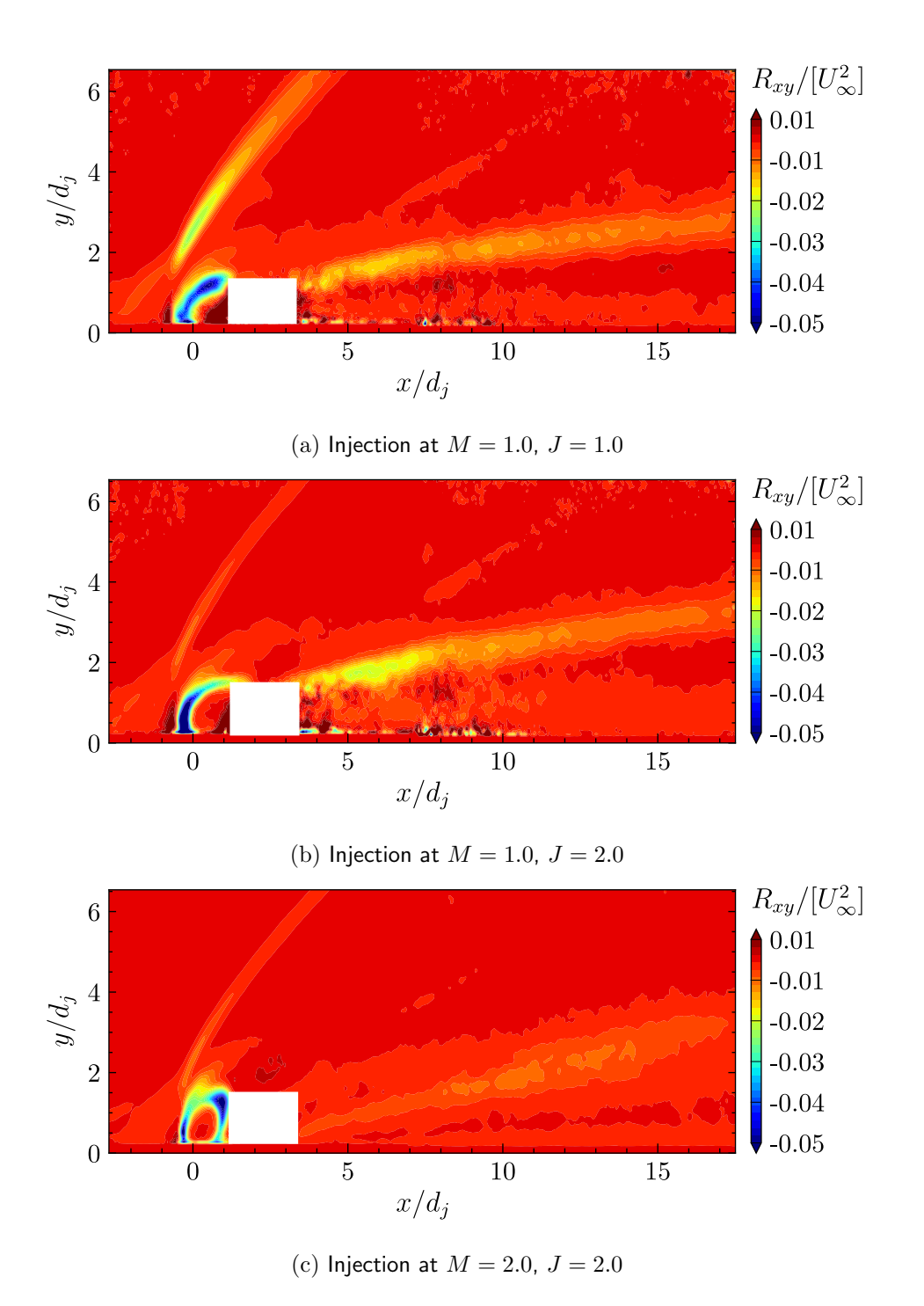
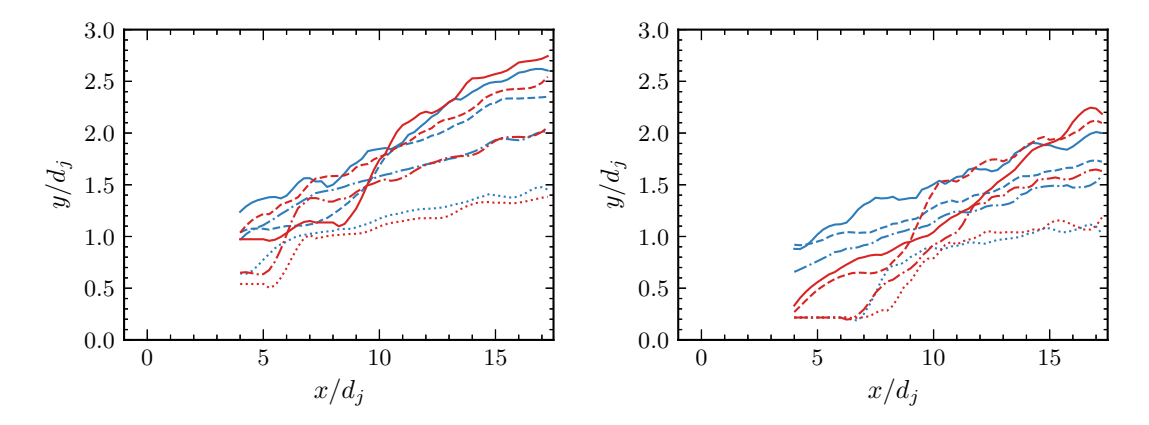


Figure 5.12: Reynolds shear stress R_{xy} contours for variable jet Mach number and momentum flux ratio injection at the midplane y/h=0 of the test section, designated as $z/d_j=0$

5.4 Jet trajectory analysis

5.4.1 Experimental trajectory fits

Experimental trajectory fits based on maxima for extended sets of velocity profiles for the streamwise velocity deficit u_{deff} and the vertical flow velocity were generated in order to evaluate the jet penetration. Due to the strong gradients in the vicinity of the jet and the region devoid of velocity vectors just aft of the injector port, it has been decided to obtain trajectories in the near field after four jet diameters. The spacing of the data points is $\delta x/d_j = 0.25$. Windowing was used for different areas of the injection in order to avoid flow outside of the jet core and aft of the shock, as well as values at the wall, to provide a false maximum. Subsequently, quadratic least-squares fitting of using six points surrounding the initially found maximum location is performed, and the maximum of that curve is used to increase accuracy. The generated curves were still noisy and additional smoothing using Savgol filter from the Scipy signal processing library. The smoothed curves were observed to present the same trajectory, yet the noise that made it difficult to read the curves was reduced sufficiently. The curves for all PIV test cases are presented in Figure 5.13.



(a) Trajectories based on streamwise velocity (b) Trajectories based on maximum vertical vedeficit u_{deff} locity $(v)_{max}$

Figure 5.13: Experimental trajectories based on velocity maxima for variable momentum flux ratio J at jet Mach number M_j . $(M_j=1:\ J=0.6\ (\cdots\cdot\cdot),\ J=1\ (-\cdot\cdot\cdot),\ J=1.5\ (-\cdot\cdot\cdot),\ J=2\ (-\cdot\cdot\cdot),\ J=2\ (-\cdot\cdot\cdot),\ J=1.5\ (-\cdot\cdot\cdot),\ J=2\ (-\cdot\cdot),\ J=2\ (-\cdot\cdot)$

For almost all plotted trajectories, in the second half of the mid-field, after about ten jet diameters, a trend of increased wake and CVP penetration with increasing J is seen. Furthermore, supersonic injection achieves similar penetration for the wake and the CVP as compared to sonic injection. In some cases, it may be argued that supersonic injection penetrates slightly higher, but the difference is very small. The case of injection at M_2 and J=1.5 shows, surprisingly, higher penetration of the trajectory based on the maximum vertical velocity that the J=2 injection.

Below $x/d_j = 10$ the situation looks more complicated. Some of the trajectories, both based on velocity deficit maxima and vertical velocity maxima, show flattened trend and then sharp increase, whilst others are represented by a continuous curve.

For the u_{deff} -based plots this can be related to the observed initial high penetration and then deflection of the flow downwards from one to five-six jet diameters for the $M_j=1$ cases. For the $M_j=2$ cases this, however, is more apparent since, as observed from Figure , the acceleration area behind the bow shock penetrates deeper into the jet core and behind the barrels shock, and thus the deficit in the wake is not seen clearly before six to eight jet exit diameters. Therefore, the maxima search ends up at the lower side of the selected sampling window as the wake is not present.

For the vertical velocity-based trajectories the same snapping to the bottom of the sampling region is seen for the cases of supersonic injection at J = [0.6, 1.5] and sonic injection with J = 0.6. These have all been observed to be cases with a regime where the downwash area is parallel to the upwash and extends for a long distance behind the jet.

Finally, a small jump to the subsequent section is made due to the useful presentation of bot the trajectories based on maximum deficit and vertical velocity in one image for a sing J setting. The plots can be found on Figure 5.14. It can be seen from all the figures that for both sonic and supersonic injection the trajectory based on maximum streamwise velocity deficit in the wake is located higher than the trajectory based on maximum wall normal velocity.

5.4.2 Comparison with empirical trajectory correlations

On Figure 5.14 a comparison is made between four selected empirically developed trajectories and the trajectories for the current experimental conditions and the trajectories obtained from this study. Clearly, the empirical trajectories all show much higher penetration of the jet as compared to the maximum velocity deficit and the maximum wall-normal velocity trajectories. To understand this, it has to be noted how the latter is established. The trajectories of Gruber et al. (1994) and Sun et al. (2013) are based on the detected upper edge of the jet with 90% and 99% concentration, respectively. The latter were obtained from Mie scattering images or NPLS. The trajectories of Papamoschou and Hubbard (1993) and Portz and Segal (2006) were also based on upper edge detection, but this time from Schlieren imaging. The upper edge is expected, indeed to be much higher than the maximum upwash of the CVP and here is seen it also seems to be higher than the centre of the wake, based on those correlations. The upper edge trajectory is important for mixing studies due to the mixing potential of the jet shear layer vortices. However, the second contributor to bulk mixing in the near field has been shown to be the CVP, which also makes it important to understand its penetration in the near-field.

The different studies, including the formula by Portz (2005) that takes into account the boundary layer thickness, lead to very high penetration compared to the current data. The trajectory equation of Gruber et al. (1997) is closest to the current plots. However, it is unclear if this is an artefact of the way the trajectory is defined.

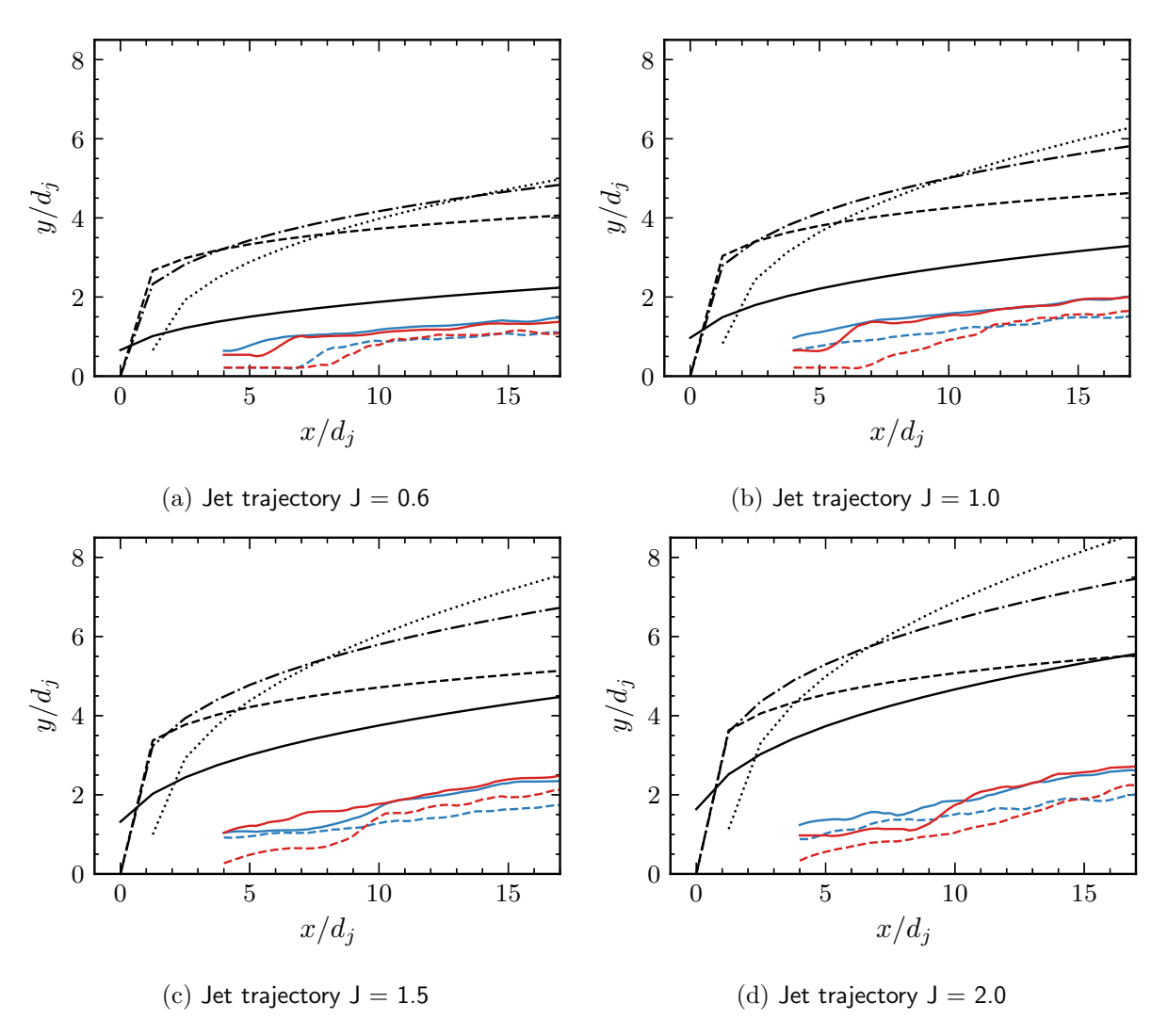


Figure 5.14: Comparison between the trajectories based on velocity loci - $((U_{inf}-u)/U_{inf})_{max}$ sonic (—), v_{max} sonic (---), $((U_{inf}-u)/U_{inf})_{max}$ supersonic (—), v_{max} supersonic (---) and fits based on the experimental studies by Gruber et al. (1994) (—),Sun et al. (2013) (---), Papamoschou and Hubbard (1993) (----) and Portz (2005) (----)

5.4.3 Approximate momentum flux

To supplement the observations of this section an approximate estimate of what will be defined as the effective momentum flux ratio are made. The effective momentum flux is defined as the approximate J after the flow discontinuities. The ratios are computed through the same methodology as the pressure matching values in Tables 5.1 and 5.2. In Table 5.2 a set of approximations are made to supplement the discussion. Namely, the pressure ratio between the flow exiting the Mach disc based on the derivations of Schetz et al. (1990) is divided by the ambient pressure of the free stream passing either a normal or an approximated oblique shock wave.

(a) $(p_j/p_{b_{eff}})_{MD}$ after NS

Table 5.2: Pressure matching for the jet plume at the jet exit and after the Mach disc for the case of NS and OS approximation based on sensor data and information extracted from Schlieren images.

(b) $(p_j/p_{b_{eff}})_{MD}$ after OS

	(**) (F.	(a) (FJ/Foeff) MD area in			(*) (FJ/F0eff)MD							
	$\overline{ m J/M}$	1.0	1.5	2.0	-	-	J/M	1.0	1.5	2.0		
	0.6	0.34	0.42	0.67			0.6	0.97	0.95	1.51		
	1.0	0.36	0.47	0.82			1.0	0.77	0.85	1.60		
	1.5	0.39	0.54	0.84			1.5	0.64	0.84	1.36		
	2.0	0.42	0.54	0.95			2.0	0.65	0.80	1.41		
$ \begin{array}{c c} 10 \\ & \\ & \\ 8 \\ & \\ 6 \\ & \\ 0.5 \end{array} $	1.0	J	1.5		2.0	J_{eff}	3 2	1.		1.5		2.0
(a)) J_{eff} at the	jet exit	behind	a NS			(b) J_{e_j}	$_{ff}$ at th	ie jet ex	it behin	d an OS	
0.5 0.4					· · · · · · · · · · · · · · · · · · ·	J_{eff}).20		, .≡· ·-			
0.3	1.(J[-	1.5		2.0	(0.5		1.0	1.! J	5	2.0
(c)	J_{eff} at the N	∕lach dis	sc behin	d a NS			(d) J_{eff}	at the	Mach o	lisc behi	nd an OS	

Figure 5.15: Estimated effective momentum flux ratios at two flow positions behind a normal and oblique shock wave for $M_j = 1$ (\bullet), $M_j = 1.5$ (\blacktriangle) and $M_j = 2$ (\blacksquare).

Looking at the data presented in Table 5.2, for the case of normal shock wave the pressure of the jet drops significantly for $M_j = 1$ and remains very similar for $M_j = 2$. A weaker Mach disc will have implication for the leftover momentum and can be related to an effective momentum ratio for the jet behind the discontinuity.

Based on the derived pressure ratios, two effective momentum flux ratios at two locations are estimated - J_{eff} at the jet exit and after the Mach disc behind both a normal and an oblique shock wave. The results are presented in Figure 5.15.

First of all, on all observable curves in Figure 5.15 an increase of the approximated effective momentum flux ratio with respect to the increase of the conventional momentum flux J can be seen. Furthermore, the effective momentum flux ratio shows little theoretical variation at the injection point with respect to M_i . This could be related to the similar penetration of the jets.

behind the Mach disc there is a visible increase of the theoretical effective J with jet Mach number. This can be attributed to the presence of a normal shock wave, affecting the jet momentum after the discontinuity. At those low momentum flux ratios in the decelerated flow it can be seen that M_j has a positive impact. However, at this point the jet is already tilted in direction of the crossflow.

A distinct difference between the J_{eff} absolute values can be observed between Figures 5.15a and 5.15b, and the one observed in Figures 5.15c and 5.15d. The decreased gradient in the cases where the J_{eff} is calculated behind the Mach disc are due to the loss of total pressure and slow-down of the jet after the Mach the structure. Returning to the trajectory discussion, it can be seen that, indeed, the rapid transverse penetration prior to the compression of the jet by the Mach disc can be expressed the high J_{eff} , using both normal and oblique shock wave approximation. Additionally, the observed reduced penetration after the discontinuity can also be related to the low J_{eff} after the Mach disc. However, it must be noted that in this gas-dynamic analysis the viscous interactions and the effective displacement of the bow shock by the boundary layer thickening and possible separation are not taken into consideration. Furthermore, it was observed that the Mach disc size, although playing important role in the flowfield, is relatively small and, especially for the $M_j = 2$ cases, large portion of the jet passes through the barrel shock.

5.5 Summary

Within the scope of the current study averaged Schlieren images and mid-plane two-dimensional PIV were used to obtain visualisations and quantitative data on the discontinuities in the flow, as well as the velocity contours and the related streamwise velocity deficit and wall-normal velocity profiles behind the injection point. Full-field turbulence intensity and Reynolds shear stress data were also generated form the instantaneous velocities. Trajectory plots were obtained, analysed and compared to current empirical correlations. Sensor data was used for the generation of the empirical plot and for the supplementary analysis of the nozzle operational regime.

It has been found that all structures, both discontinuities, trajectories, CVP and wake height, strength and spread scale up with the jet-to-crossflow momentum flux ratio.

Schlieren data analysis displayed reduced blockage for the same J with supersonic as compared to sonic injection. This resulted in decreased Mach disc height, separation zone size under the separation shocks and lower stand-off distance. It has been found that for $M_j = 1$ injection, the separation shock resembled more a compression fan. For all configuration, the Mach disc was already tilted streamwise, despite the thick boundary layer. This was found to be related to the deep penetration of the bow shock into the boundary layer due to its high velocity. The proposed

5.5 Summary 117

gas-dynamic flow topology was schematised. Pressure measurements and approximated pressure ratios over the discontinuities suggested overexpanded operational regime for the $M_j=2$ injection cases.

The PIV indicated the position, extend and strength of the jet wake through velocity deficit measurements. The wake strength was found to increase with J and decrease with M_j The wake was formed later for supersonic injection.

Velocimetry data displayed the existence of a pronounced downwash zone for the supersonic injection cases. The latter is also observed with the sonic injection cases but only after the Mach disc. For the supersonic case, it is observed aft of the leeward side of the barrel shock directly. The zone spans around five diameters for the sonic and ten diameters for supersonic injection. With increasing momentum flux ration, the upwash is formed preceding this zone and increases in strength and seems to penetrate inwards and below the downwash zone.

Besides bringing this downwash structure in existence the increase of the jet Mac number has been shown to have a negative effect on the strength of the CVP shown as an imprint on the vertical velocity in the mid-field. This is of negative consequence for any mixing implications but a good result for thrust vectoring applications. To elaborate, the increased strength and height of the large scale structures is beneficial for the rapid bulk mixing in the near field due to the possibility to entrain larger quantities of uncreated fluid surrounding the jet. This has been shown to be critical due to the short residence time of the air in the combustor. Secondly, the strength of the CVP, if its trajectory hits a fin or if the jets remain low such that it can interact with the body, has a negative effect on the jet effectiveness and attitude control of the vehicle.

Analysis of the TI and Reynolds shear stress R_{xy} revealed three zones. The first is the bow shock. The second is the zone around the barrel shock, and the third is the band created after the barrel shock and extending far downstream, related to the CVP. Increase in J showed an increase in the extend of the TI and R_{xy} zones related to the vortex pair. The increase of M_j had the opposite effect, confirming the above observations on the vertical velocities. Additionally, an area of shear stresses of the opposite sign was indicated windward of the jet. This area could possibly be related to the generation of the shear layer vortices responsible for rapid near-field mixing. This area seems to reduce in size with J and increase in size with an increase of M_j .

Mach disc height showed grater initial penetration for the sonic injection cases. Trajectory plots showed similar penetration for sonic and supersonic injection at the end of the near-field. The velocity deficit has been shown to penetrate higher than the maximum wall-normal velocity. Empirical correlations over predict the penetration as they are mostly based on upper edge detection of shear layer vortices via concentration or Schlieren measurements. The trajectory of Gruber et al. (1994) seems closest to the current case. Approximations of the pressure matching were made, which are in line with most of the observations, but they are incomplete for the understanding of the flow as large part passes through the large barrel shocks compared to the small Mach disc.

Conclusions and Recommendations

In this last chapter of the MSc Thesis the research conclusions and contribution, as well as a short discussion on the recommendations for future research and system improvement are presented.

6.1 Conclusions and Contribution

6.1.1 Engineering contribution

As pilot research of the HSL of the Aerodynamics group at the TU Delft Aerospace engineering faculty on the topic of compressible jet-in-crossflow, this thesis required the development of the required facilities to start this research.

In order to house the parts of the injection system located inside the wind tunnel, a cut-out was made in the bottom aluminium Mach block, part of the set of Mach blocks forming the $M_{\infty}=2$ de Laval nozzle. The cut-out has approximate dimensions of $143 \times 110 \times 80.6$ millimetres. It was designed to allow housing of various experimental equipment below the bottom wall of the test section. When not using specific experimental equipment, the cavity is closed by a cap plate.

Secondly, a jet injection system allowing for introducing jets transversely from the wind tunnel bottom wall was developed. The system is capable of producing jets with a variable momentum-flux ratio by altering the total pressure of the injection nozzle. The system is fed through the facility's pressurized air delivery system and has acceptable system losses, allowing it to even deliver above the current experimental envelope maximum of J=2, given limiting safety total pressure is 7 bars.

Variable jet injection Mach number capability is delivered via an exchange of the end-piece injectors connected to the delivery system and the wind tunnel bottom wall. The sonic nozzle contour was designed for uniform jet exit Mach number. The supersonic nozzles were an extension of the sonic nozzle designed as a conical nozzle with half angle of 4°, taking into consideration friction losses and free shock separation. The nozzles were designed with the same jet exit diameter in

order to retain the scaling with respect to the boundary layer thickness. The settling chamber was designed based on Mach number considerations from literature. All the nozzles were metal 3D printed based on powder bed technology and post-processed to reduce surface roughness. Nozzles for $M_i = [1, 1.5, 2]$ were manufactured.

The system was further fitted with a connection point for measurement of total conditions just before the jet exit and a second connection point for connecting PIV DEHS seeding. The seeding was designed to be connected right after the manual pressure control as part of the air supply and seeding controller located outside of the wind tunnel. Finally, one of the wind tunnel flanges was also modified with a fitting for the entry hose of the system.

6.1.2 Scientific contribution

For this study, instantaneous Schlieren imaging and PIV velocity fields for the mid-plane of the near and mid-field of the interaction were obtained and processed. Experimental design was performed for a test matrix consisting for variable J = [0.6, 1, 1.5, 2] and, jet Mach number $M_j = [1, 1.5, 2]$ for Schlieren and $M_j = [1, 2]$ for the PIV measurements. The Schlieren visualisation was achieved through a single campaign using a single camera and providing FOV or 70×60 mm (17.5 × 15 jet diameters). For PIV a single campaign with dual camera configuration yielding FOV of 83×34 mm (21.8 × 8.5 jet diameters) was performed. A secondary zoomed-in PIV campaign with a single camera was also performed related to this research. This campaign provides additional validation data and can be used for future work but is deemed out of scope for this research as it does not add to the answer of the main research questions.

Schlieren results

The Schlieren dataset was obtained to answer the first sub-question posed in Chapter 1: How are internal jet shock structures and interaction shock structures affected by the jet control parameter variation?

The imaging data from the Schlieren campaign was processed in order to obtain time-averaged images of the wave structures in the flow field. The shock structures formed upon the interaction between the two jet and the crossflow, as well as the internal jet shock structures, materializing upon exiting a different ambient pressure, have been successfully visualized. The structures have been found to scale-up in size with increasing J and scale-down with increasing M_j . Besides imaging, this was also expressed in a quantitative manner via the measurement of the Mach disc height, bow shock stand-off distance and separation height and length. This suggests higher blockage of the incoming crossflow by the jet at higher momentum-flux-ratios and lower jet Mach number.

Despite the change of the ratio between the jet static pressure and the ambient pressure at the jet exit, the topology of the discontinuities remains relatively unchanged. For sonic injection, the separation shock resembled more a compression fan. This was not the case for supersonic injection, likely due to the fact that the shorter and steeper separation would cause a stronger pressure jump. The barrel shock was found to be turned in a streamwise direction even for this relatively thick boundary layer. This could be related to the penetration of the bow shock into the boundary layer and the consequent pressure rise. This did not directly correlate with the four operational regimes proposed in the literature, although it matched some results from the oldest

experimental and newer numerical research. Consequently, jet operational regime schematic has been proposed for the jet wave structures for similar low-momentum-flux compressible jets, in order to supplement the previously proposed four regimes.

PIV results

Through the conducted 2-dimensional PIV measurements, mean velocity contours were obtained. Those contours were further used to extract profiles of vertical velocity and streamwise velocity deficit. The analysis of the velocity profiles and contours provides the answer of the following sub-question:

How do the jet-to-crossflow momentum flux ratio and jet Mach number affect the flow mean velocities in the near and mid-field?

Analysis of the velocimetry data shows that the jet turns sharply after injection. Upon turning, a characteristic wake and a counter-rotating vortex pair are formed. Those phenomena are observed as streamwise velocity deficit and the advent of upwash in the centreline, respectively. It has been found that downstream from the injection point both the upwash and streamwise velocity deficit magnitude, penetration into the crossflow and width scale proportionally with the increase in J. The area directly after the jet injection did not provide good vector cross-correlation due to lack of sufficient particles.

Increasing M_j at constant J has been found to decrease the magnitude of the streamwise velocity deficit and vertical velocity in the mid-field. This is critical as it implies deterioration of the mixing capabilities of the jet and is also important for jet iteration with solid surfaces. Furthermore, besides the upwash resulting from the imprint of the CVP, a downwash zone is formed downstream of the jet. To elaborate, it has been observed with the cases of supersonic injection that the downwash zone precedes the upwash zone for low momentum-flux ratios. Upon increasing J the upwash band extends upstream and seems to penetrate below the downwash, which also reduces in size. Upon closer observation, those structures have also been found for the $M_j = 1$ cases but with a smaller extent and magnitude of the downwash. Finally, the location after which the imprint of the CVP is observed for the cases of supersonic injection is shifted backwards to around $10d_j$. The jet wake appears clearly only after five jet diameters.

Besides the averaged flow fields, contours of turbulence intensity and Reynolds shear stress R_{xy} were also obtained. The analysis of these turbulence characteristics give an answer to the next research question:

textbfHow do the jet-to-crossflow momentum flux ratio and jet Mach number affect the turbulent characteristics in the near and mid-field of the injection?

Both R_{xy} and TI contours display three zones of high turbulence intensity and shear stress magnitude. Those consist of the barrel shock, bow shock and a third area manifesting just aft of the barrel shock and extending deep into the mid-field. This area can be related to the CVP.

The high magnitudes of turbulence intensity and shear stress were found to be contained within the near field. Increase in J was found to extend the span of the area of high turbulence magnitudes associated with the CVP from between one and five jet diameters to between one and seven jet diameters. The change from sonic to supersonic injection caused a decrease of R_{xy} and TI for the CVP-related area. Similarly to the observations on the upwash in the same area, the CVP is not observed until about five jet diameters.

Analysis of the R_{xy} contours at the windward side of the barrels shock revealed an area containing shear stress of opposite sign. This area can be related to SWBLI and to the generation of shear layer vortices, which are paramount for near field mixing. Although difficult to analyse due to particle slip caused by the shocks and aberration, the data suggested that the area increases in size when J is increased. The area seemed to be smaller for supersonic injection.

Based on the previous observations the next research question can be answered. It is defined as: What is the implication control parameters variation on the vortical strength and mixing potential of the jet in the near and mid-field?

It is clearly seen from the preceding paragraphs that the increase in J leads to a larger penetration and increased magnitude of the deficit caused by the jet wake and the upwash caused by the CVP. The turbulent shear stress R_{xy} and the TI also increase proportionally. Besides this, increase of the size of the area with R_{xy} with opposite sign windward from the jet has also been observed. All this points towards an increase of the strength of the large-scale vortical structures and the mixing potential of the flowfield. With respect to M_j , the opposite effect is observed. This can however, be beneficial for applications such as side thrust attitude control.

The final research question answered in this section is:

Does the approximated ratio between the jet exit pressure and the ambient backpressure show any relation to flowfield structures observed in the experiments?

To answer this question, semi-empirical calculations were performed in order to obtain the nozzle operational regimes based on ratios between the jet exit pressure and the approximated ambient backpressure. All approximations point to a different operational regime for the supersonic nozzle, suggesting high overexpansion, compared to the underexpansion observed with the sonic nozzles. It was also seen from PIV and schlieren images, that the jet shock structures collapse towards the jet exit. Those two observations, combined with the discussion in the preceding paragraphs provide evidence that the jet pressurization, expressed as jet Mach number, has a significant effect on the velocity fields in the near-and midfield and strong impact on the strength and spread of both the jet wake and large-scale structures.

Trajectory and penetration of the mean flow field structures

This section provides the answer to the last sub-question:

How is the jet trajectory based on the averaged velocity field affected by the variation of the jet control parameters?

Penetration based on Mach disc heigh and velocity maxima at injection was found to be higher than the velocity maxima trajectory penetration close to the jet, suggesting the jet is turned downwards by the pressure jump over the bow shock before it recovers. Furthermore, the increase of jet Mach number decreases the Mach disc height and thus the penetration at the injection location.

Jet trajectories have also been constructed for streamwise sections above 4 jet diameters based on the streamwise deficit and vertical velocity maxima. Data directly behind the jet has been found to not be trustworthy in many of the injection cases due to centrifugal effect shooting PIV seeding particles outside the sampling domain. To obtain the trajectories windowing of valid data, least-squares fit around the maxima for sub-sampling interpolation of the peaks and smoothing of the curves has been implemented.

The results confirmed the increased jet penetration with J. The effect of the jet Mach number has been shown to be very small. The velocity deficit trajectory has further been found to be generally higher than the vertical velocity one. From contour plot data, it has been seen that the jet initially penetrates higher than the predicted trajectories after $d_j = 4$. The current data available points that at low momentum-flux ratios, the jet tends to bend downwards after the rapid initial penetration and subsequently goes on to recover and continue spreading upwards after the formation of the CVP. This effect is further amplified by the increased size and strength of the downwash and increase in the magnitude of the upwash zone in the $M_j = 2$ cases.

Comparison of the experimental velocity profiles with those obtained from semi-empirical and analytical correlations for the same magnitude of the flow field scaling and thermodynamics properties was also performed. The latter showed that the experimental correlations could not be directly used in the trajectory prediction of jet wake and CVP as they severely over-predict the transverse penetration. This has been found to be related to the fact that the latter correlations are based mostly on upper shear layer boundary, which is expected to be located much higher than the CVP core and the wake centreline. However, the closest correlation found is the one proposed by Gruber et al. (1994).

6.1.3 Main question

The main question posed for this study was:

How are the averaged flow field and jet trajectory in the near and mid-field of a jet injected transversely into supersonic crossflow affected by the jet control parameters?

The results of the current study show that the increase of the jet-to-crossflow momentum flux ratio leads to an up-scaling of the jet shock structures, penetration of the jet trajectory based on velocity maxima and increase of the strength, width and penetration of both the jet wake, CVP and possibly the shear layer vortices. Furthermore, for supersonic injection a qualitatively and quantitatively different flow field is observed in the mid-plane. A clear and large area of downwash precedes the upwash zone. The upwash is more pronounced at higher momentum flux ratios. Furthermore, the penetration of the jet trajectory remains the same, whilst both the wake and CVP strength reduce in magnitude and width. Due to the large importance of this structure in mixing, it is found as a negative impact on the mixing properties of the jet in the near-field due to the reduced vortical strength. Finally, trajectory of the jet displays sharp penetration at injection and then a downward deflection and subsequent recovery.

6.2 Recommendations

Based on the system design, operational experience and scientific observations, several recommendations were drawn from this research:

1. It has been seen from instantaneous images that the system shows some intermittent behaviour. Furthermore, control of the jet was quite elaborate as the simple pressure regulating system was located within the wind tunnel hall itself. This way of controlling the jet was simple end fit well this pilot study but is not optimal. Consequently, it is

- proposed that a system update is done. An automatic flow control valve, for example, would to maintain constant mass-flow and ease the operation of the system. This will also require a one-way flow valve to prevent backflow of seeding in the flow control valve and damage of its components.
- 2. This study focused on mean velocity field analysis. However, to obtain complete data with respect to the turbulent characteristics, a higher resolution 3-dimensional measurements are needed, especially in the near field of the injection. This could be obtained through tomographic PIV at the jet exit. Although there is an issue with insufficient seeding directly behind the jet, the large scale structures forming on the windward side and just behind the Mach disc could be visualised.
- 3. To better understand the effect of the jet Mach number on the large-scale structure formation in the near field, cross-plane velocity fields are needed. This can be obtained through cross-plane PIV. Furthermore, experimental data of cross-plane PIV for this region has not been found in the literature.
- 4. Finally, a long term outlook, a scale-up investigation with respect to practical application such as fuel injectors and effect of shock interaction is recommended. It would also provide an experimental dataset for validation of numerical simulations.

References

- Krishnan Mahesh. The interaction of jets with crossflow. Annual Review of Fluid Mechanics, 45 (1):379-407, 2013. ISSN 0066-4189. doi: 10.1146/annurev-fluid-120710-101115. URL http://www.annualreviews.org/doi/10.1146/annurev-fluid-120710-101115.
- Jd Anderson Jr. Fundamentals of Aerodynamics. McGraw-Hill, New York, second edi edition, 1991. ISBN 0-07-001679-8.
- R.D. Zucker and O. Biblarz. Fundamentals of gas dynamics. John Whiley \$ Sons, Inc., Monterey, California JOHNWILEY, second edi edition, 2012. ISBN 0471059676.
- Dan Wang and Yong Yu. Shock wave configurations and reflection hysteresis outside a planar Laval nozzle. *Chinese Journal of Aeronautics*, 28(5):1362–1371, 2015. ISSN 10009361. doi: 10.1016/j.cja.2015.07.010. URL http://dx.doi.org/10.1016/j.cja.2015.07.010.
- A. Hadjadj, A. N. Kudryavtsev, and M. S. Ivanov. Numerical investigation of shock-reflection phenomena in overexpanded supersonic jets. *AIAA Journal*, 42(3):570–577, 2004. ISSN 0001-1452. doi: 10.2514/1.989. URL http://arc.aiaa.org/doi/10.2514/1.989.
- Gabi Ben-Dor. Shock wave reflection phenomena. Springer, Berlin Heidelberg New York, second edi edition, 2007. ISBN 9783540713814.
- Werner Kieffer. Fluid dynamics of the May 18 blast at mount St. Hellens. In P.W. Lipman and D.R. Mullineaux, editors, *The 1980 Eruptions of mount St. Hellens, Washington*, pages 379–400. United States Government Printing Office, Washington, D.C, 1981.
- M.V. Morkovin, C.A. Pierce Jr, and C.E. Craven. Interaction of a side jet with a supersonic main stream. Technical report, University of Michigan, 1952.
- Ron Portz. Transverse jet penetration in supersonic flows with variable boundary layer thickness. PhD thesis, University of Florida, 2005.
- R.C. Orth, J.A. Schetz, and F.S. Billig. The interaction and penetration of gaseous jets in supersonic flow. Technical Report NASA-CR-1386, John Hopkins University, Silver Spring, 1969.

D. Papamoschou and D. G. Hubbard. Visual observations of supersonic transverse jets. Experiments in Fluids: Experimental Methods and their Applications to Fluid Flow, 14(6):468–476, 1993. ISSN 14321114. doi: 10.1007/BF00190201.

- Edward E Zukoski and Frank W Spaid. Secondary Injection of Gases into a Supersonic Flow. *AIAA Journal*, 2(10):1689–1696, 1964. ISSN 0001-1452. doi: 10.2514/3.2653.
- M. R. Gruber, A. S. Nejad, T. H. Chen, and J. C. Dutton. Compressibility effects in supersonic transverse injection flowfields. *Physics of Fluids*, 9(5):1448–1461, 1997. ISSN 10706631. doi: 10.1063/1.869257.
- A. Ben-Yakar, M. G. Mungal, and R. K. Hanson. Time evolution and mixing characteristics of hydrogen and ethylene transverse jets in supersonic crossflows. *Physics of Fluids*, 18(2), 2006. ISSN 10706631. doi: 10.1063/1.2139684.
- Mingbo Sun, Shunping Zhang, Yanhui Zhao, Yuxin Zhao, and Jianhan Liang. Experimental investigation on transverse jet penetration into a supersonic turbulent crossflow. *Science China Technological Sciences*, 56(8):1989–1998, 2013. ISSN 16747321. doi: 10.1007/s11431-013-5265-7.
- A. Rothstein and P. Wantuck. A study of the normal injection of hydrogen into a heated supersonic flow using planar laser-induced fluorescence. 28th Joint Propulsion Conference and Exhibit, 1992. doi: 10.2514/6.1992-3423. URL http://arc.aiaa.org/doi/10.2514/6.1992-3423.
- Xiaochuan Chai, Prahladh S. Iyer, and Krishnan Mahesh. Numerical study of high speed jets in crossflow. *Journal of Fluid Mechanics*, 785:152–188, 2015. ISSN 14697645. doi: 10.1017/jfm.2015.612.
- Steven J. Beresh, John F. Henfling, Rocky J. Erven, and Russell W. Spillers. Penetration of a Transverse Supersonic Jet into a Subsonic Compressible Crossflow. *AIAA Journal*, 43(2): 379–389, 2005a. ISSN 0001-1452. doi: 10.2514/1.9919. URL http://arc.aiaa.org/doi/10.2514/1.9919.
- M. R. Gruber, A. S. Nejad, T. H. Chen, and J. C. Dutton. Transverse injection from circular and elliptic nozzles into a supersonic crossflow. *Journal of Propulsion and Power*, 16(3):449–457, 2000. ISSN 0748-4658. doi: 10.2514/2.5609. URL http://arc.aiaa.org/doi/10.2514/2.5609.
- M. Sun and Z. Hu. Generation of upper trailing counter rotating vortices of transverse sonic jet in a supersonic crossflow at Ma = 2.7. AIAA Journal, 56(3), 2018. doi: https://doi.org/10.2514/1.J056442.
- Rajes Sau and Krishnan Mahesh. Dynamics and mixing of vortex rings in crossflow. *Journal of Fluid Mechanics*, 604:389–409, 2008. ISSN 00221120. doi: 10.1017/S0022112008001328.
- Yancheng You, Heinrich Luedeke, and Klaus Hannemann. Injection and mixing in a scramjet combustor: DES and RANS studies. *Proceedings of the Combustion Institute*, 34(2):2083–2092, 2013. ISSN 15407489. doi: 10.1016/j.proci.2012.10.001. URL http://dx.doi.org/10.1016/j.proci.2012.10.001.

J. Warnatz, U. Maas, and R. W. Dibble. Combustion: Physical and chemical fundamentals, modeling and simulation, experiments, pollutant formation. 2006. ISBN 3540259929. doi: 10.1007/978-3-540-45363-5.

- Zhengzhong Sun. Micro Ramps in Supersonic Turbulent Boundary Layers. Thesis, Delft University of Technology, 2014.
- Jan Östlund. Flow processes in rocket engine nozzles with focus on flow separation and sideloads. Licentiate thesis, Royal Institute of Technology, 2002. URL http://kth.diva-portal. org/smash/record.jsf?pid=diva2:7328.
- G. L. Romine. Nozzle Flow Separation. *AIAA Journal*, 36(9):1618–1625, 1998. ISSN 0001-1452. doi: 10.2514/2.588. URL http://arc.aiaa.org/doi/10.2514/2.588.
- T.I. Malik and R.K. Tagirov. Semiempirical Method of Calculating Overexpanded Turbuilent Separated Flow in a Cobical Laval Nozzle. *Mehanika Zhidkosti i Gaza*, (6):851–856, 1987.
- Charles R. Fostrer and Frederick B. Cowles. Experimental study of gas-flow separation in overexpanded exhaust nozzles for rocket motors. Technical report, California Institute of Technology, Pasadena, 1949.
- GS Settles and EE Covert. Schlieren and Shadowgraph Techniques: Visualizing Phenomena in Transport Media. *Applied Mechanics Reviews*, 2002. ISSN 0003-6900. doi: 10.1115/1.1483362.
- Markus Raffel, Christian E Willert, Steve T Wereley, Jürgen Kompenhans, Markus Raffel, Christian E Willert, Steve T Wereley, and Jürgen Kompenhans. *Particle Image Velocimetry: a practical guide*. Springer, Berlin Heidelberg New York, second edition, 2007. ISBN 9783540723073.
- F Scarano. Experimental Aerodynamics. Technical Report February, Delft University of Technology, Delft, The Netherlands, 2013.
- Ventsislav Pazhev, Ferdinand Schrijer, and Bas van Oudheusden. Experimental Investigation of Jet in Supersonic Cross-flow by Means of PIV. FAR Conference, 2019.
- M. R. Gruber, A. S. Nejadt, T. H. Chen, and J. C. Dutton. Mixing and penetration studies of sonic jets in a mach 2 freestream. *Journal of Propulsion and Power*, 11(2):315–323, 1994. ISSN 0748-4658. doi: 10.2514/3.51427. URL http://arc.aiaa.org/doi/10.2514/3.51427.
- S D Heister and A R Karagozian. Gaseous jet in supersonic crossflow. *AIAA Journal*, 28(5): 819–827, 1990. ISSN 00011452. doi: 10.2514/3.25125. URL https://arc.aiaa.org/doi/abs/10.2514/3.25125.
- Robert H Schmucker. Flow Processes in Overexpanded Chemical Rocket Nozzles. Part 1: Flow Separation. Technical report, NASA, 1984.
- D. Ragni, F. Schrijer, B. W. Van Oudheusden, and F. Scarano. Particle tracer response across shocks measured by PIV. *Experiments in Fluids*, 2011. ISSN 07234864. doi: 10.1007/s00348-010-0892-2.
- S. Hills. Inland voyage of discovery: Unique photos capture last generation to work Britain's industrial canals, oct 2012. URL https://www.dailymail.co.uk/news/article-2213750/.

Corin Segal. The scramjet engine: processes and characteristics. 2009. ISBN 9780511627019. doi: 10.1017/CBO9780511627019.

- NASA. Simplified graphic of SCRamjet engine, 2006. URL https://www.nasa.gov/centers/langley/images/content/142861main_x43a_intscramjet_550.gif.
- Ron Portz and Corin Segal. Penetration of gaseous jets in supersonic flows. AIAA Journal, 44 (10):2426-2429, 2006. ISSN 0001-1452. doi: 10.2514/1.23541. URL http://arc.aiaa.org/doi/10.2514/1.23541.
- Steven J. Beresh, Justin L. Wagner, John Henfling, Russell Spillers, and Brian Pruett. Turbulent characteristics of a transverse supersonic jet in a subsonic compressible crossflow. 45th AIAA Fluid Dynamics Conference, (June):1–19, 2005b. doi: 10.2514/6.2015-2481. URL http://arc.aiaa.org/doi/10.2514/6.2015-2481.
- Steven J. Beresh, John F. Henfling, Rocky J. Erven, and Russell W. Spillers. Crossplane velocimetry of a transverse supersonic jet in a transonic crossflow. *AIAA Journal*, 44(12): 3051–3061, 2006. ISSN 0001-1452. doi: 10.2514/1.22311. URL http://arc.aiaa.org/doi/10.2514/1.22311.
- S. Eberhardt and S. Hickel. Comparative numerical investigation of a sonic jet in a supersonic turbulent wrossflow. High Performance Computing in Science and Engineering '14: Transactions of the High Performance Computing Center, Stuttgart (HLRS) 2014, pages v-viii, 2015. doi: 10.1007/978-3-319-10810-0.
- S. Kawai and S. K. Lele. Dynamics and mixing of a sonic jet in a supersonic turbulent crossflow. *Annual Research Briefs* 2009, Center for Turbulence Research, (Lele 1992):285–298, 2009.
- Juan Gabriel Santiago and J. Craig Dutton. Velocity measurements of a jet injected into a supersonic crossflow. *Journal of Propulsion and Power*, 13(2):264–273, 1997. ISSN 0748-4658. doi: 10.2514/2.5158.
- Suman Muppidi and Krishnan Mahesh. Direct numerical simulation of round turbulent jets in crossflow. *Journal of Fluid Mechanics*, 574:59–84, 2007. ISSN 00221120. doi: 10.1017/S0022112006004034.
- Wei Huang. Transverse jet in supersonic crossflows. Aerospace Science and Technology, 50: 183-195, 2016. ISSN 12709638. doi: 10.1016/j.ast.2016.01.001. URL http://dx.doi.org/10.1016/j.ast.2016.01.001.
- T. Fric. Structure in the near field of the transverse jet. PhD thesis, California Institute of Technology, 1963.
- R. M. Kelso and A. J. Smits. Horseshoe vortex systems resulting from the interaction between a laminar boundary layer and a transverse jet. *Physics of Fluids*, 7(1):153–158, 1995. ISSN 10706631. doi: 10.1063/1.868736.
- R. M. Kelso, T.T. Lim, and A.E. Perry. An experimental study of rpund jets in cross-flow. pages 111–144, 1996.

S. J. Beresh, J. F. Henfling, and R. J. Erven. Flow Separation Inside a Supersonic nozzle exhausting into a subsonic compressible crossflow. *Journal of Propulsion and Power*, 19(4): 655–662, 2003. ISSN 0748-4658. doi: 10.2514/2.6154. URL http://arc.aiaa.org/doi/10.2514/2.6154.

- M. R. Gruber, A. S. Nejad, T. H. Chen, and J. C. Dutton. Bow shock/jet interaction in compressible transverse injection flowfields. *AIAA Journal*, 34(10):2191–2193, 1996. ISSN 0001-1452. doi: 10.2514/3.13372.
- United States Air Force. Underexpaned plume of the Saturn V during the launch of the Apollo 11 mission, 1969. URL https://www.flickr.com/photos/gsfc/4812876740.
- C.E. Peters and W.J. Phares. An approximate analysis of the shock structure in underexpanded plumes. Technical report, Arnold Engineering Development Center, Tennessie, 1976.
- Erwin Franquet, Vincent Perrier, Stéphane Gibout, and Pascal Bruel. Review on the underexpanded jets. (September), 2015. doi: 10.13140/RG.2.1.2640.6883.
- P. F. Hawkins, H. Lehman, and J. A. Schetz. Structure of highly underexpanded transverse jets in a supersonic stream. *AIAA Journal*, 1967. ISSN 0001-1452. doi: 10.2514/3.4095.
- Jd Anderson Jr. Hypersonic and high temerature gas dynamics, volume 134. AIAA, Blacksburg, Virginia, second edition, 2007. ISBN 9781563477805.
- Valerio Viti, Reece Neel, and Joseph A. Schetz. Detailed flow physics of the supersonic jet interaction flow field. *Physics of Fluids*, 21(4), 2009. ISSN 10706631. doi: 10.1063/1.3112736.
- Sergei K. Godunov, A. V. Zabrodin, and G. P. Prokopov. A computational scheme for twodimensional non stationary problems of gas dynamics and calculation of the flow from a shock wave approaching a stationary state. *Zh. vych. mat.*, 1(6):1020–1050, 1961.
- S.F. Horner. Fluid-dynamic drag. Horner Fluid Dynamics, Bakersfield, CA, 1965.
- J. McDaniel and J. Graves. A laser-induced-fluorescence visualization study of transverse, sonic fuel injection in a nonreacting supersonic combustor. AIAA 24th Perospace Sciences Meeting, 1986. doi: 10.2514/6.1986-507.
- R Clayton Rogers. A study of the mixing of hydrogen injected normal to a supersonic airstream. Technical report, NASA Langley Research Center, Hampton, Va., 1971.
- Kuo-Cheng Lin, Michael Ryan, Mark Gruber, Campbell Carter, and Charbel Raffoul. Raman scattering measurements of gaseous ethylene jets in a Mach 2 supersonic crossflow. *Journal of Propulsion and Power*, 26(3):503–513, 2010. ISSN 0748-4658. doi: 10.2514/1.43757.
- Wayne M. VanLerberghe, Juan G. Santiago, J. Craig Dutton, and Robert P. Lucht. Mixing of a Sonic Transverse Jet Injected into a Supersonic Flow. *AIAA Journal*, 38(3):470–479, 2000. ISSN 0001-1452. doi: 10.2514/2.984. URL http://arc.aiaa.org/doi/10.2514/2.984.
- T.F. Fric. Structure in the near field of the transverse jet. Doctoral thesis, California Institute of Technology, 1990.
- T F Fric and A Roshko. Vortical structure in the wake of a turbulent jet. *Journal of Fluid Mechanics*, 279:1–47, 1994.

Suman Muppidi and Krishnan Mahesh. Two-dimensional model problem to explain counterrotating vortex pair formation in a transverse jet. *Physics of Fluids*, 18(8), 2006. ISSN 10706631. doi: 10.1063/1.2236304.

- Steven Hollo, James Mcdaniel, and Roy Hartfield, jr. Characterization of supersonic mixing in a nonreacting Mach 2 combustor. 30th Aerospace Sciences Meeting and Exhibit, 1992. doi: 10.2514/6.1992-93. URL http://arc.aiaa.org/doi/10.2514/6.1992-93.
- Sebastian Eberhardt and Stefan Hickel. Large-eddy simulation of a strut injector with perpendicular jet injection into a supersonic flow. AIAA Journal, pages 1–24, 2013.
- E. Eberhardt and S. Hickel. Large-Eddy simulation of a scramjet strut injector with pilot injection. High Performance Computing in Science and Engineering '15: Transactions of the High Performance Computing Center, Stuttgart (HLRS) 2015, pages 591–592, 2016. doi: 10.1007/978-3-319-24633-8.
- Z. A. Rana, B. Thornber, and D. Drikakis. Dynamics of sonic hydrogen jet injection and mixing inside scramjet combustor. *Engineering Applications of Computational Fluid Mechanics*, 7 (1):13–39, 2013. ISSN 1997003X. doi: 10.1080/19942060.2013.11015451.
- Rogier Giepman. Flow Control for Obluique Shock Wave Reflections. Thesis, Delft University of Technology, 2016.
- Jd Anderson Jr. Fundamentals of Aerodynamics, volume Third Edit. McGraw-Hill, 1985. ISBN 0073398101. doi: 10.1036/0072373350. URL http://scholar.google.com/scholar?hl=en{&}btnG=Search{&}q=intitle:Fundamentals+of+Aerodynamics{#}0.
- Alan Pope and Kennith L. Goin. *High-speed wind tunnel testing*. John Wiley & Sons, New York, 1965.
- T.-L. Ho and G Emanuel. Design of a Nozzle Contraction for Uniform Sonic Throat Flow. AIAA Journal, 38(4):720–723, 2000. ISSN 0001-1452. doi: 10.2514/2.1019. URL http://dx.doi.org/10.2514/2.1019.
- Lee M Ahlstrom and B Jan. Pressure Vessels. Technical Report June 1989, 1992.
- D. Vlassov, J. V.C. Vargas, and J. C. Ordonez. The optimization of rough surface supersonic nozzles. *Acta Astronautica*, 61(10):866–872, 2007. ISSN 00945765. doi: 10.1016/j.actaastro. 2007.01.068.
- A I Leontiev. Gas Dynamics. MHTS Publishers, Moscow, 1997.
- P. H Oosthuizen and William Carscallen. *Compressible fluid flow*. McGraw-Hill, first edition, 1997. ISBN 978-0070481978.
- Jukka Kiijarvi. Darcy Friction Factor Formulae in Turbulent Pipe Flow. Lunowa Fluid Mechanics Paper, pages 1-11, 2011. URL http://www.kolumbus.fi/jukka.kiijarvi/clunowa/fluid{_}mechanics/pdf{_}articles/darcy{_}friction{_}factor.pdf.
- EL Morrisette and TJ Goldberg. Turbulent-flow separation criteria for overexpanded supersonic nozzles. Technical report, 1978. URL http://adsabs.harvard.edu/abs/1978STIN... 7830554M.

Jim Mcgovern. Technical Note: Friction Factor Diagrams for Pipe Flow Technical Note: Friction Factor Diagrams for Pipe Flow. pages 0–15, 2011.

- Ralf H. Stark. Flow Separation in Rocket Nozzles An Overview. 49th AIAA/ASME/SAE/ASEE Joint Propulsion Conference, pages 1-8, 2013. doi: 10.2514/6. 2013-3840. URL http://arc.aiaa.org/doi/10.2514/6.2013-3840.
- Peter Steeneken. ME46005 PHYSICS AND MEASUREMENTS Optics I Properties of light. Technical report, Delft University of Technology, Delft, 2019.
- J.A. Schetz, R. H. Thomas, and F.S. Billig. Mixing of transverse jets and wall jets in supersonic flow. In *IUATM Symposium*, Novosibirsk, USSR, 1990. doi: 10.1007/978-3-642-84447-8_101.
- Ernst Mach. Uber den verlauf von funkenwellen in der ebene und im raume. Sitzungsbr. Akad. Wiss., Wien, 1878.
- Luis Laguarda Sanchez. Bi-directional transition between regular and Mach reflections in asymmetric shock interactions. Master of science thesis, Fachhochschule Wiener Neustadt, 2017.
- John von Neumann. Oblique reflection of shocks. Technical report, Navy Department Bureau of Ordinance, Washington, D.C, 1943.

Appendix A

Supplementary Equations and Theory

A.1 General relations

The Isentropic relations are thoroughly derived and presented by Anderson Jr (1991) as

$$\frac{T_{0_j}}{T} = 1 + \frac{\gamma - 1}{2}M^2,\tag{A.1}$$

$$\frac{p_{0_j}}{p} = \left(1 + \frac{\gamma - 1}{2}M^2\right)^{\frac{\gamma_j}{\gamma_j - 1}} and \tag{A.2}$$

$$\frac{\rho_{0_j}}{\rho} = \left(1 + \frac{\gamma - 1}{2}M^2\right)^{\frac{1}{\gamma_j - 1}}.$$
(A.3)

where M is the local Mach number and T, p and ρ are the local static pressure, temperature and density, respectively.

The Mach number is defined as

$$M = \frac{U}{a},\tag{A.4}$$

where the speed of sound is defined as

$$a = \sqrt{\left(\frac{dp}{d\rho}\right)_{ise}} \tag{A.5}$$

Assuming isentropic flow, the latter can be re-expressed as

$$a = \sqrt{\gamma \frac{p}{\rho}},\tag{A.6}$$

where γ is the specific heats ratio of the fluid $\gamma = \frac{Cp}{Cv}.$

A.1.1 Nozzle operational regimes

In this section, a more detailed introduction on the nozzle operational regimes is provided.

Assuming steady, inviscid, quasi one-dimensional flow, the operational regime of the nozzle with fully isentropic flow development can be determined via the mass conservation laws and the well-known isentropic relations derived in Anderson Jr (1985) and presented in Appendix A. Introducing the sonic conditions Anderson Jr (1985) presented the Mach-area relation

$$\left(\frac{A}{A^*}\right)^2 = \frac{1}{M^2} \left[\frac{2}{\gamma_j + 1} \left(1 + \frac{\gamma_j - 1}{2} M^2 \right) \right]^{\frac{\gamma_j + 1}{\gamma_j - 1}},\tag{A.7}$$

where A is the area of the selected station within the nozzle and A^* is the sonic throat area. This allows to calculate the local Mach number at a selected station of a supersonic nozzle given a-priory knowledge of its geometry. Furthermore, knowing the Mach number Equations A.1, A.2 and A.3 can be used to obtain a relationship between the static conditions at the given station and the total conditions at the settling chamber. In the context of this discussion a specific interest is put on the jet total pressure, p_{0_j} as a flow control variable as, assuming isentropic flow through the nozzle, it can be directly related to the jet exit pressure p_j , which is one of the two leading parameters defining the state of the jet exhaust plume.

Before proceeding with the discussion a note should be made to the applicability of the derived relations. The calculated properties are so-called station properties as the quasi-one-dimensional assumption restricts the model to a uniform flow within the nozzle. This assumption is backed further by the inviscid flow assumption. Given a steady, but viscous and 3-dimensional flow, the Mach distribution will be altered due to the presence and growth of the boundary layer. Such effects add additional complications to the analysis. Boundary layer growth effectively changes the cross-section of the nozzle, which can be compensated for during nozzle design. Viscous shear causes frictional losses, which, as discussed in the case of conical nozzles by Vlassov et al. (2007), may cause the nozzle flow to stop accelerating depending on the diverging geometry. Finally, at low p_j as compared to the ambient pressure, the relation which will be discussed in the following paragraphs, separation can occur at the exit or within the nozzle itself, as discussed by Östlund (2002) and observed by Beresh et al. (2003), in the case of transverse injection.

Returning to the discussion of the free jet exhaust state and flow topology, the exiting plume have to satisfy two major boundary conditions. The first condition, as defined by Zucker and Biblarz (2012), is the pressure equilibrium across the jet boundary. This condition implies that the flow exiting the nozzle should be expanded or compressed to match the nozzle backpressure p_b . As stated by Anderson Jr (1991), the nozzle operational regime itself depends on the ratio of the nozzle exit static pressure to the ambient pressure $\frac{p_j}{p_b}$. A schematic of a general supersonic nozzle with denoting the respective pressures can be seen in Figure 2.3. Although the pressure ratio completes the picture for the initial wave formation, the secondary and subsequent wave structures in the jet plume obey a second condition - the flow tangency at the centre streamline.

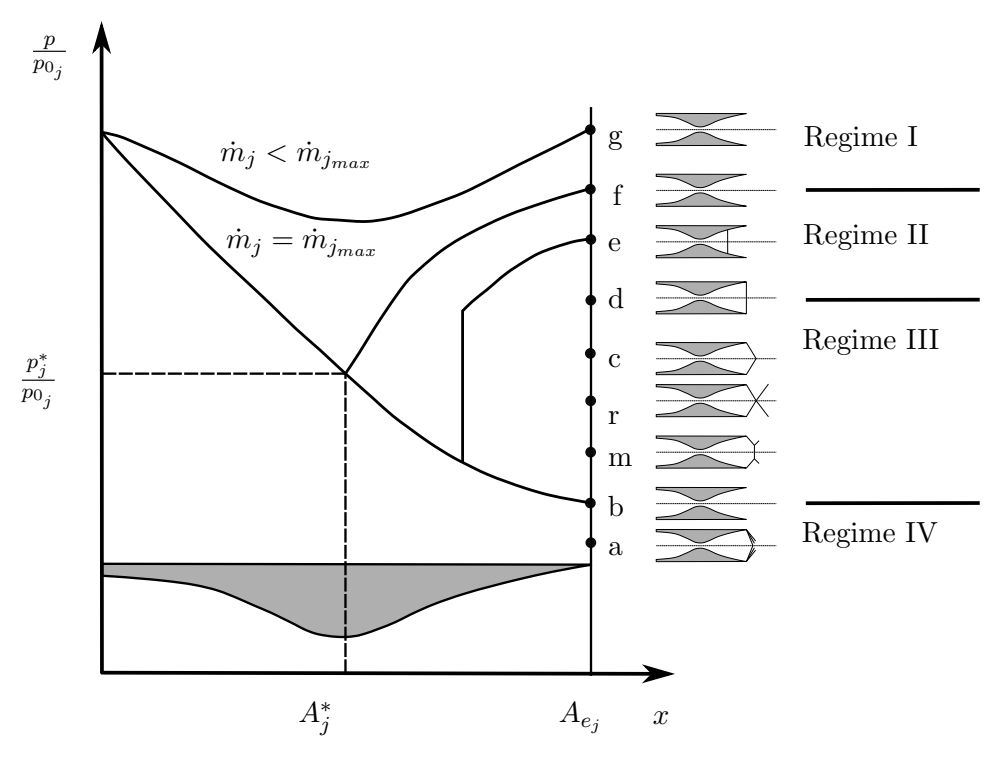


Figure A.1: Operational conditions and regimes for de Laval nozzle. Adapted from Wang and Yu (2015)

Focusing on the first boundary condition and the nozzle flow regimes, as discussed by Wang and Yu (2015), 4 operational regimes and 9 conditions can be encountered for exhaust plume of a de Laval nozzle. The operating conditions are presented in Figure A.1.

If backpressure of a de Laval nozzle is lowered below the total pressure, or the total pressure is increased, Regime I occurs, where subsonic flow is established in the nozzle. The limiting situation for this regime is operational condition f, where the maximum mass flow is achieved and the flow at the nozzle throat is sonic. If the backpressure is lowered further, a supersonic flow is established in the divergent section of the nozzle and a normal shock is formed, as seen in flow condition e in Figure A.1. As the backpressure decreases the limiting condition where the shock is located at the nozzle exit is achieved.

Further lowering the pressure of the de Laval nozzle leads to Regime 3 - overexpanded flow. The overexpanded flow condition is characterised by the formation of two oblique shocks that compress the flow to the nozzle backpressure p_b . However, within this regime, three flow conditions can be encountered. If the nozzle exit pressure ratio is sufficiently high, as observed by Zucker and Biblarz (2012) and Wang and Yu (2015), then the strong oblique shock solution will be encountered. The strong shock solution will bring the flow to subsonic velocity. Thus, as noted by Zucker and Biblarz (2012), the flow can turn and satisfy the centreline tangency condition without the formation of additional waves.

If the backpressure is lowered further, however, the weak shock solution is encountered. The flow is not decelerated sufficiently to become subsonic and, in order to turn away from the centreline, it has to be compressed through reflected shock waves. During his early research, Mach (1878) observed two shock wave reflection configurations - the Mach reflection and regular reflection.

The regular reflection consists of two shock waves - incident (IW) and reflected shock wave (RW) - which meet at a reflection point R. The configuration can be seen between in area 1, 2 and 3 in Figure 2.4. The Mach reflection, as seen between areas 1, 2 and 3 in Figure 2.4 consists of three waves - the incident wave (IW), the reflected wave (RW) and the Mach disc, which is referred to as meniscus by Morkovin et al. (1952). The three shock structures meet at the triple point, T, where a fourth discontinuity is initiated - a slip line between the subsonic flow that passes through the Mach disc and the supersonic flow that passes through the reflected shock wave.

Returning to Figure A.1, as stated by Wang and Yu (2015), in the region c-r only regular reflections are possible. If the pressure is lowered further, a dual solution is encountered in the region from r to m. In other words, both regular and Mach reflections may occur. As noted by Sanchez (2017) and Wang and Yu (2015), von Neumann (1943) defined the transition limits for RR-MR and MR-RR, the so called detachment condition and von Neumann criterion, respectively. Furthermore, von Neumann (1943) proposed the concept of the double solution domain (r-m) whose existence has been proven by later experimental and numerical studies.

As the backpressure is further decreased an optimal nozzle operation condition of perfect expansion is reached at point b. No wave structures are formed behind the nozzle. After this critical condition Regime IV is encountered. The nozzle exit pressure is larger than the ambient pressure and the flow has to be further expanded through a set of Prandtl-Meyer expansion waves.

A.2 Heister and Karagozian summarized backpressure prediction

Following Heister and Karagozian (1990) and using the normal shock relations, the equivalent Mach number is defined as:

$$M_{eq} = \frac{(\gamma - 1)(M_{\infty}\sin\theta_j)^2 + 2}{2\gamma(M_{\infty}\sin\theta_j)^2 - (\gamma - 1)},$$
(A.8)

for $M_{\infty} \sin \theta_j \in (1; 5]$ and

$$M_{eq} = M_{\infty} \sin \theta_j, \tag{A.9}$$

for $M_{\infty} \sin \theta_i \in (0.8; 1]$.

Subsequently, after performing the numerical solutions, curve fit for an equivalent static pressure is plotted as a function of $M_{\infty} \sin \theta_j$. The equivalent pressure is defined as the average pressure surrounding the jet. For the purpose of this research this equivalent backpressure will be referred to as $p_{b_{eff_{HK}}}$ The curve fit formulas are defined as follows:

$$p_{b_{eff_{HK}}} = p_{\infty} [0.405 + 0.426(M_{\infty} \sin \theta_j)^2], \tag{A.10}$$

for $M_{\infty} \sin \theta_i \in [1.5; 5]$,

$$p_{b_{eff_{HK}}} = p_{\infty} [0.861 + 0.217(M_{\infty} \sin \theta_j)^2], \tag{A.11}$$

for $M_{\infty} \sin \theta_i \in (0.8; 1.5)$ and

$$p_{b_{eff_{HK}}} = p_{\infty}, \tag{A.12}$$

for $M_{\infty} \sin \theta_i \leq 0.8$.

The above expressions were used to approximate the effective backpressure and jet plume regime for the set-up of the Schlieren experiments performed by Papamoschou and Hubbard (1993).

A.3 Analytical interaction shock shape prediction

In order to predict the interaction shock system geometry, Orth et al. (1969) developed a model based on shock shapes around blunt solid bodies. To achieve that, an "equivalent solid body" is defined as a measure of the crossflow obstruction is needed. To model the jet the nose radius of this solid body has to be defined. One of the possible approximations for this parameter is the equivalent nose radius based on blast wave theory(See Anderson Jr (2007) or Orth et al. (1969)):

$$R_{B_1} = \sqrt{\frac{\dot{m}_j}{\rho_\infty u_\infty}}. (A.13)$$

A second manner in which the obstruction can be determined is by approximating the height of the Mach disc within the jet shock system. For the cases where $\gamma = 1.4$ Orth et al. (1969) proposes the following formula for the Mach disc height, y_0 :

$$y_0 = R_{B_2} = 2r_j K M_j \sqrt{\frac{p_j}{p_{b_{eff}}}},$$
 (A.14)

where r_j is the injection orifice radius and K = 1 for $M_j = 1$.

Orth et al. (1969) then determined the shock shape using the following formula:

$$\frac{x_s}{r_i} = \frac{R_B}{r_i} + \frac{\Delta}{R_B} \frac{R_B}{r_i} - \frac{R}{R_B} \frac{R_b}{r_i} \cot^2 \theta, \tag{A.15}$$

where $\frac{\Delta}{R_B}$ is the shock stand-off distance, defined as:

$$\frac{\Delta}{R_B} = 0.143e^{\frac{3.24}{M_\infty^2}} \,, \tag{A.16}$$

 $\frac{R}{R_B}$ is the nondimensionalised radius of curvature of the shock at the equivalent body nose, defined as:

$$\frac{R}{R_B} = 0.143e^{\frac{0.54}{(M_{\infty}^2 - 1)^{1.2}}} and \tag{A.17}$$

 θ is the bluff body station flow incidence angle, with respect to the crossflow.

When Equation A.15 is rewritten in terms of the shock disc height the final relation for the shock shape is obtained:

$$\frac{x_s}{r_j} = \sqrt{1 + \left(\frac{y_s}{r_j}\right)^2 \left(\frac{r_j}{R_B}\right)^2 \left(\frac{R_B}{R}\right)^2 \tan^2 \theta} - 1. \tag{A.18}$$

Schlieren measurements, however showed inflection point of the detached shock located above the surface. As a result a displaced model with the solid body above the surface is proposed by Orth et al. (1969). Correlation for this height, as well as results for the shock shape prediction are shown in the Figure A.2b.

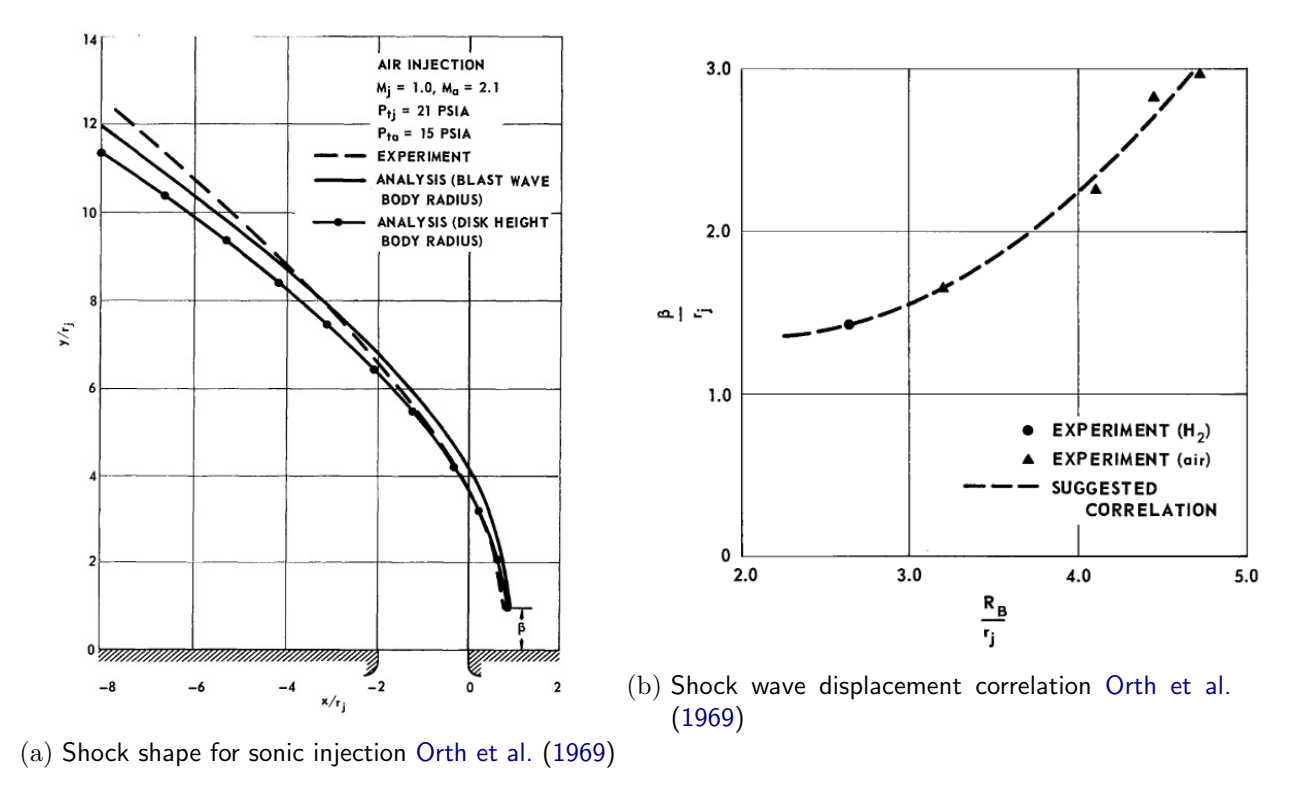


Figure A.2: Characteristic shock shape and displacement correlation. As presented by Orth et al. (1969)

Schlieren results for underexpanded sonic jets reported by Orth et al. (1969) showed good correlation with the above model when the Mach disc height is used to compute the equivalent body radius. The model has two major limitations. Firstly, it is only applicable for underexpanded sonic jets where the Mach disc is much higher than the incoming boundary layer thickness. Secondly, it only predicts the platform of the interaction shock system.

Another prediction for the interaction shock system is proposed by Heister and Karagozian (1990). The prediction is based on curve-fitting results for the shock stand-off distance D_{bs} , form their numerical calculation method. The stand-off distance, nondimensionalised by the

models vortex pair half spacing is defined as:

$$D_{bs} = 1.162 + \frac{3.5}{(M_{\infty}\sin\theta_j - 1)},\tag{A.19}$$

for $M_{\infty} \sin \theta_i > 1.1$.

The x_s and y_s coordinates of the bow shock per jet cross-section slice are then defined as:

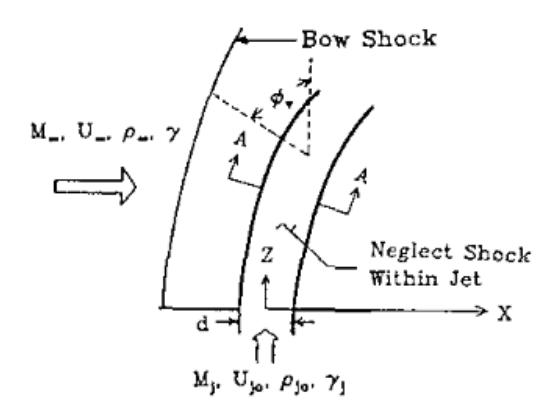
$$x_s = X - D_{bs}h\sin\theta_i \ and \tag{A.20}$$

$$y_s = Y - D_{bs}h\cos\theta_j,\tag{A.21}$$

where h is the dimensionless vortex pair half spacing used in the model and X and Z are the jet centreline coordinates. Fore more information reference should be made to Heister and Karagozian (1990). To the knowledge of the author, model has not been validated with respect to other studies with respect to the shock shape as mainly the penetration profile has been compared.

A.4 Heister and Karagozian Compressible vortex pair trajectory model

To solve the two-dimensional Euler equations and find the pressure distribution surrounding the vortex pair, a first order method developed by Godunov et al. (1961) is used for the outer flow solution. The grid is generated using the elliptic nature of the vortex pair. According to Heister and Karagozian (1990), the numerical method gives very good results compared to experimental and numerical data of compressible flows along ellipses and circles. The model also permits computation of the wave drag on the jet. The numerical model approximates the crossflow as inviscid and uses the method developed by Godunov et al. (1961). It determines the stand-off distance of the bow shock and the properties surrounding the jet.



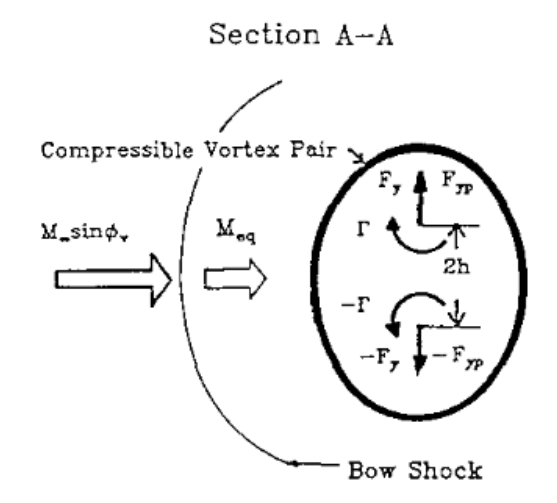


Figure A.3: Schematic of the perfectly expanded jet in inviscid supersonic crossflow model developed by Heister and Karagozian (1990)

The coupling between the numerical and analytical model consists in converting the non-uniform, rotational flow behind the bow shock into an equivalent uniform upstream flow, which is used as an input to the compressible vortex pair model. The aim of this coupling is the calculation of the equivalent properties after the shock. Given an equivalent Mach number M_{eq} , the jet cross-section is derived. This Mach number is approximated as the Mach number behind a normal shock with freestream Mach number:

$$M_{eq} = \left[\frac{(\gamma - 1) \left(M_{\infty} \sin \theta_j \right)^2 + 2}{2\gamma \left(M_{\infty} \sin \theta_j \right)^2 - (\gamma - 1)} \right]$$
(A.22)

for $M_{\infty} \sin \theta_j > 1$ and

$$M_{eq} = M_{\infty} \sin \theta_j \tag{A.23}$$

for $M_{\infty} \sin \theta_j \leq 1$.

When the cross-section is known, the outer flow can be calculated using the scheme by Godunov. To accelerate the calculations, Heister and Karagozian (1990) defined curve fits for the model results for the drag experienced by the jet, C_D , the shock stand-off distance, D_{bs} and the equivalent properties behind the shock wave, p_{eq} and ρ_{eq} , where the values are nondimensionalised with the vortex half spacing h. ¹ From the obtained values the equivalent velocity seen by the vortex pair is calculated as:

$$U_{\rm eq} = M_{\rm eq} \sqrt{\gamma p_{\rm eq}/\rho_{\rm eq}}.$$
 (A.24)

The vortex pair model is based on adapted fully-analytical and locally two-dimensional derivations for incompressible injection. The incompressible model is also developed by Karagozian. It implements the observation that the incompressible jet plume is dominated by a CVP. To calculate the vortex pair deflection angle, its relation to the vortex pair circulation is established. For the incompressible case, the two main vorticity sources - the viscous forces and the jet impulse. However, for the compressible vortex pair the non-uniform crossflow conditions after the bow shock and the wave drag have to be accounted for. As a result the local jet angle is expressed as:

$$\frac{d\theta_j}{dt} = \left(\frac{d\theta}{dt}\right)_{\text{circ}} + \left(\frac{d\theta}{dt}\right)_{drag} \tag{A.25}$$

The change in angle due to the change in local crossflow conditions, and thus, circulation is defined as

$$\left(\frac{d\theta_j}{dt}\right)_{circ} = \frac{-U_{eq}(8\pi h - 2)dh/dt}{\lambda \sin\theta_j + hU_{eq}(4\pi h - 2)\left(\tilde{M}'_{eq} + \frac{1}{2}\left(\tilde{p}'_{eq} - \tilde{\rho}'_{eq}\right)\right)},\tag{A.26}$$

where

$$\tilde{M}'_{eq} \equiv \frac{dM_{eq}/dt}{M_{eq}d\theta_i/dt} \tag{A.27}$$

and analogous definitions hold for \tilde{p}'_{eq} and the $\tilde{\rho}'_{eq}$.

The above relations are developed taking intro account the jet thrust and crossflow equivalent velocity U_{eq} . The term h denotes the half spacing of the vortex pair, as seen ion Figure A.3.

The expression for the change of the jet angle due to the wave drag is based on a balance between the drag and the jet centripetal force. The relation is thus defined as:

$$\left(\frac{d\phi}{dt}\right)_{drag} = \frac{-C_D \sin^2 \theta_j}{\rho_j U_j \frac{\pi^3}{2} h},$$
(A.28)

where $\frac{\pi^3}{2}$ is related to the dimensionless cross-sectional area of the jet.

¹The full correlations can be found in Heister and Karagozian (1990).

The vortex half spacing is calculated via momentum balance along the trajectory. The forces are determined via the pressure force acting on a compressible vortex closed streamline, F_y streamline and an additional term for slight underexpansion of the jet F_{yp} , as seen in Figure A.3. The differential equation for the vortex half spacing can then be defined as 2 :

$$\frac{d^2h}{dt^2} = \frac{F_y + F_{yp}}{w_i} - \left(\frac{1}{\rho_i} \frac{d\rho_j}{dt} + \frac{2}{h} \frac{dh}{dt}\right) \frac{dh}{dt},\tag{A.29}$$

where w_j is defined by Heister and Karagozian (1990) as a dimensionless mass per unit length in the upper half of the recirculation cell.

Finally, applying momentum balance along the trajectory of the jet the local jet velocity can is defined as:

$$\frac{dU_j}{dt} = \frac{\left[\frac{1}{\rho} \frac{dp_j}{dt} (U_{eq} \cot \theta_j - U_j - \frac{y_j p_j}{\rho U}) + (U_{eq} \cot \theta_j - U_j) \frac{2}{h} \frac{dh}{dt}\right]}{\left(2 - \frac{U_{eq} \cot \theta_j}{U_j}\right)}$$
(A.30)

The jet centreline coordinates are then defined as:

$$X = \int_{t_0}^{t} U_j \cos \theta_j dt \tag{A.31}$$

and

$$Y = \int_{t_0}^{t} U_j \sin \theta_j dt \tag{A.32}$$

A.5 Parametric analysis of compressible jet in crossflow

The first dimensional analysis of the problem of transverse injection in supersonic crossflow was performed by Morkovin et al. (1952). The analysis took into account the conservation of mass, momentum and energy equations, together with the equation of state for an ideal gas. However, the analysis used static pressure as the principal dependant variable. Without going into detail, advising the reader to turn to Morkovin et al. (1952) and Anderson Jr (1991) for the derails of the dimensional analysis process, the set of 12 dependant variables is converted to 9 nondimensional parameters. The relation is shown in Equation A.33.

$$\frac{p}{p_{\infty}} = f\left(\frac{p_{0_j}}{p_{\infty}}, \frac{\rho_{0_j}}{\rho_{\infty}}, M_{\infty}, Re_{\infty}, \frac{d_j}{D}, \frac{\mu_j}{\mu_{\infty}}, \gamma_{\infty}, \gamma_j\right), \tag{A.33}$$

where D is a physical quantity related to the boundary condition of zero vertical velocity over the body surface.

²For full derivation and definition of the force terms and initial conditions please refer to Heister and Karagozian (1990).

The semi-analytical and numerical correlations discussed above can also be used to determine, what is considered as, the driving parameters for jet trajectory. According to the correlation by Zukoski and Spaid (1964) for sonic jet injected into supersonic crossflow without boundary layer, one can say that:

$$\frac{y}{d_j} = f\left(\frac{p_{0_j}}{p_{\infty}}, M_{\infty}, \gamma_j, \gamma_{\infty},\right),\tag{A.34}$$

where, reminding, $\frac{y}{d_j}$ is the nondimensional jet penetration. Recognizing the effect of J on the penetration, Orth et al. (1969) formed a functional relationship described as:

$$\frac{y_{pe}}{d_j} = f(J, M_{\infty}) \tag{A.35}$$

for the perfectly expanded part of the plume and

$$\frac{y_{Md}}{d_i} = g(M_j, \gamma_j) \tag{A.36}$$

for the Mach disc height.

Papamoschou and Hubbard (1993) performed parametric analysis related directly to the jet penetration, noting the previously established strong dependence between the trajectory and the jet-to-crossflow momentum flux ratio and noting the importance of the effective backpressure concept developed by Orth et al. (1969). Their parametric statement builds on previous research and can be defined as:

$$\frac{y}{d_j} = f\left(J, M_{\infty}, M_j, \frac{p_j}{p_{b_{eff}}}, \frac{\rho_j}{\rho_{b_{eff}}}\right). \tag{A.37}$$

However, Papamoschou and Hubbard (1993) went a step further, taking into account the definition of J as seen in Equation 2.2 and the normal shock relation for pressure as seen in Equation 2.3. After approximating the shock relation for $M_{\infty} \geq 2$ with:

$$p_{b_{eff}} \approx p_{\infty} \frac{2\gamma_{\infty} M_{\infty}^2}{\gamma_{\infty} + 1}$$
 (A.38)

a relation between J and the nozzle backpressure is formulated. With this relation Equation A.37 can be rewritten as:

$$\frac{y}{d_j} = f\left(J = \frac{2\gamma_j}{\gamma_{\infty} + 1} \frac{p_j}{p_{b_{eff}}} M_j^2, M_{\infty}, M_j, \frac{p_j}{p_{b_{eff}}}, \frac{\rho_j}{\rho_{b_{eff}}}\right). \tag{A.39}$$

The authors note the strong dependence of the jet-to-crossflow momentum flux ratio on the jet Mach number. Therefore, noting the freedom of altering the crossflow Mach number without altering J, whilst both the nozzle exit pressure ratio, or pressure matching, and M_j being both linked to the momentum flux ratio.

Appendix B

Sensor Data

In this Appendix section the sensor data for the averaged temperatures and pressures per experiment per test case per wind tunnel run are presented. The latter complement the presentation of the experimental conditions and the experimental results analysis discussed in the main body of the report.

B.1 Section Schlieren test matrix and control settings

Figure B.1, presented below, summarises the test matrix and the applicable experimental conditions. The target pressure is pre-calculated. The gauge pressures are the pressures read from the gage of the control system. During the experiment, on-line monitoring of the temperature and pressure sensors located at direct vicinity of the nozzle was also possible. Due to the proximity of these sensors to the nozzle and the cross-sectional area of the pipe compared to the nozzle throat, assuming no significant losses are encountered, the sensor readouts may be considered to be representative of the total pressure and temperature. Consequently, the valve settings were adapted to better match those readings. The gauge pressures could then be used as reference if subsequent runs are needed.

Sensor Data

Table B.1: Test matrix and injection parameters for the Schlieren campaign

#	J	$p_{0_{j_{calc}}}[bar]$	$p_{gauge}[bar]$	$p_{gauge_{closed}}[bar]$	$\bar{p}_{j_{sens}} \pm \sigma[bar]$	$p_{sens_{med}}[-]$	$\bar{T}_{sens} \pm \sigma[K]$
	Mach 1 Nozzle						
1	0.6	1.16	NA	NA	1.169 ± 0.0010	1.169	293.46 ± 0.140
2	1.0	1.93	1.8	2.1	1.948 ± 0.0021	1.948	293.87 ± 0.083
3	1.5	2.90	3.2	3.6	2.937 ± 0.0011	2.926	293.75 ± 0.305
4	2.0	3.87	4.6	4.9	3.885 ± 0.0013	3.885	294.09 ± 0.245
	Mach 1.5 Nozzle						
5	0.6	1.00	NA	NA	1.059 ± 0.0004	1.059	294.72 ± 0.039
6	1.0	1.67	1.4	1.8	1.689 ± 0.0005	1.689	294.50 ± 0.078
7	1.5	2.50	2.6	3.0	2.496 ± 0.0011	2.496	294.40 ± 0.349
8	2.0	3.34	3.8	4.2	3.397 ± 0.0009	3.397	294.87 ± 0.269
	Mach 2 Nozzle						
9	0.6	1.200	NA	NA	1.265 ± 0.0007	1.266	293.83 ± 0.145
10	1.0	2.000	1.4	1.8	2.013 ± 0.0008	2.013	294.07 ± 0.124
11	1.5	3.000	2.8	3.2	3.220 ± 0.0008	3.220	294.09 ± 0.267
12	2.0	4.000	3.9	4.4	4.057 ± 0.0014	4.057	294.50 ± 0.206

Table B.2: Free stream (crossflow) parameters for the Schlieren campaign

#	J	$p_{0_{sc}} \pm \sigma[bar]$	$\bar{p}_{ts} \pm \sigma[bar]$	$\bar{T}_{sc} \pm \sigma[K]$				
Mach 1 Nozzle								
1	0.6	$2.002 \pm 5e-4$	$0.256 \pm 2e-4$	285.03 ± 0.120				
2	1.0	$1.991 \pm 3e-4$	$0.255 \pm 3e-4$	285.51 ± 0.161				
3	1.5	1.964 ± 0.06	$0.251\pm1\text{e-}4$	287.19 ± 0.848				
4	2.0	1.960 ± 0.05	0.250 ± 0.006	287.10 ± 1.022				
	Mach 1.5 Nozzle							
5	0.6	$1.990 \pm 4e-4$	$0.253 \pm 3e-4$	285.29 ± 0.10				
6	1.0	$1.985 \pm 4e-4$	$0.252\pm2\text{e-}4$	286.01 ± 0.15				
7	1.5	1.981 ± 0.01	0.259 ± 0.006	288.59 ± 1.26				
8	2.0	1.951 ± 0.05	0.249 ± 0.006	289.34 ± 1.26				
Mach 2 Nozzle								
9	0.6	$2.009 \pm 5e-4$	$0.257 \pm 3e-4$	290.17 ± 0.09				
10	1.0	$2.007\pm5\text{e-}4$	$0.257\pm3\text{e-}4$	290.59 ± 0.14				
11	1.5	1.976 ± 0.08	0.257 ± 0.033	291.57 ± 0.47				
12	2.0	1.954 ± 0.14	0.257 ± 0.086	292.45 ± 0.95				

B.2 PIV test matrix and control settings

 $\textbf{Table B.3:} \ \, \textbf{Test matrix and injection parameters for the PIV campaign}$

#	J	$p_{0_{j_{calc}}}[bar]$	$p_{gauge}[bar]$	$p_{gauge_{closed}}[bar]$	$\bar{p}_{j_{sens}} \pm \sigma[bar]$	$p_{sens_{med}}[-]$	$\bar{T}_{sens} \pm \sigma[K]$	
	Mach 1 Nozzle							
1	0.6	1.16	NA	NA	$1.12 \pm 4e-4$	1.13	294 ± 0.36	
2	0.6	1.16	NA	NA	1.17 ± 0.001	1.20	291 ± 0.14	
3	0.6	1.16	NA	NA	1.19 ± 0.008	1.18	292 ± 0.15	
4	1.0	1.93	1.8	2.1	$1.91\pm7\mathrm{e}\text{-}4$	1.91	293 ± 0.23	
5	1.0	1.93	1.8	2.1	$1.93\pm9\mathrm{e}\text{-}4$	1.93	292 ± 0.23	
6	1.0	1.93	1.8	2.1	1.95 ± 0.002	1.94	293 ± 0.30	
7	1.5	2.90	3.2	3.6	2.88 ± 0.001	2.88	292 ± 0.22	
8	1.5	2.90	3.2	3.6	2.91 ± 0.002	2.91	292 ± 0.20	
9	1.5	2.90	3.2	3.6	$2.94 \pm 6\text{e-}4$	2.94	293 ± 0.25	
10	2.0	3.87	4.6	4.9	3.83 ± 0.001	3.83	293 ± 0.18	
11	2.0	3.87	4.6	4.9	3.83 ± 0.001	3.83	293 ± 0.14	
12	2.0	3.87	4.6	4.9	3.80 ± 0.006	3.80	293 ± 0.15	
				Mach 2 No	zzle			
13	0.6	1.20	NA	NA	$1.23 \pm 5e-4$	1.23	294 ± 0.45	
14	0.6	1.20	NA	NA	$1.23 \pm 3e-4$	1.23	292 ± 0.66	
15	0.6	1.20	NA	NA	$1.23\pm3\text{e-}4$	1.23	293 ± 0.44	
16	1.0	2.00	1.4	1.8	1.94 ± 0.0021	1.94	293 ± 0.27	
17	1.0	2.00	1.4	1.8	1.94 ± 0.001	1.94	294 ± 0.40	
18	1.0	2.00	1.4	1.8	1.94 ± 0.001	1.94	293 ± 0.20	
19	1.5	3.00	2.8	3.2	$3.17 \pm 5\text{e-}4$	3.17	292 ± 0.30	
20	1.5	3.00	2.8	3.2	$3.17\pm5\text{e-}4$	3.17	293 ± 0.41	
21	1.5	3.00	2.8	3.2	$3.16 \pm 5\text{e-}4$	3.16	293 ± 0.40	
22	2.0	4.00	3.9	4.4	$4.04\pm6\mathrm{e}\text{-}7$	4.03	292 ± 0.24	
23	2.0	4.00	3.9	4.4	$4.03 \pm 6e-7$	4.03	293 ± 0.26	
24	2.0	4.00	3.9	4.4	$4.03\pm6\mathrm{e}\text{-}7$	4.03	293 ± 0.26	

148 Sensor Data

Table B.4: Free stream (crossflow) parameters for the PIV campaign

#	J	$p_{0_{sc}} \pm \sigma[bar]$	$\bar{p}_{ts} \pm \sigma[bar]$	$\bar{T}_{sc} \pm \sigma[K]$			
Mach 1 Nozzle							
1	0.6	2.01 ± 0.0053	$0.254 \pm 6e-4$	286 ± 0.17			
2	0.6	$2.01\pm9\text{e-}4$	$0.256\pm3\text{e-}4$	288 ± 0.12			
3	0.6	$2.01\pm9\mathrm{e}\text{-}4$	$0.255\pm3\text{e-}4$	289 ± 0.44			
4	1.0	$2.03\pm7\text{e-}4$	$0.253\pm3\text{e-}4$	289 ± 0.42			
5	1.0	2.03 ± 0.001	$0.252 \pm 3e-4$	289 ± 0.38			
6	1.0	$2.03\pm8\text{e-}4$	$0.247\pm3\text{e-}4$	285 ± 0.54			
7	1.5	2.01 ± 0.011	$0.249 \pm 3e-4$	284 ± 0.71			
8	1.5	2.01 ± 0.001	$0.251\pm1\text{e}4$	285 ± 0.65			
9	1.5	$1.95\pm7\text{e-}4$	$0.249\pm1\text{e-}4$	289 ± 0.30			
10	2.0	$1.95 \pm 7e-4$	0.249 ± 0.006	289 ± 0.40			
11	2.0	2.01 ± 0.001	$0.253\pm4\text{e-}4$	284 ± 0.40			
12	2.0	2.01 ± 0.001	$0.252 \pm 3e-4$	284 ± 0.40			
Mach 2 Nozzle							
13	0.6	2.01 ± 0.005	$0.259 \pm 6e-4$	290 ± 0.37			
14	0.6	$2.01\pm9\mathrm{e}\text{-}4$	$0.259 \pm 3e-4$	291 ± 0.48			
15	0.6	2.01 ± 0.049	$0.256\pm6\text{e}4$	291 ± 0.48			
16	1.0	$2.02 \pm 5\text{e-}4$	$0.257\pm3\text{e-}4$	290 ± 0.42			
17	1.0	2.02 ± 0.001	$0.258\pm3\text{e-}4$	$290 \!\pm 0.48$			
18	1.0	2.02 ± 0.002	$0.258\pm4\mathrm{e}\text{-}4$	290 ± 0.42			
19	1.5	1.99 ± 0.08	$0.257\pm7\text{e}4$	$285 \!\pm 0.58$			
20	1.5	1.98 ± 0.08	$0.259 \pm 3e-4$	285 ± 0.59			
21	1.5	2.00 ± 0.08	$0.259\pm7\text{e-}4$	285 ± 0.59			
22	2.0	2.03 ± 0.005	$0.260\pm3\text{e-}4$	286 ± 0.34			
23	2.0	2.02 ± 0.002	$0.262\pm3\text{e-}4$	286 ± 0.30			
24	2.0	2.02 ± 0.002	$0.262\pm3\text{e-}4$	286 ± 0.30			

Appendix C

Experimental Procedures

C.1 Run procedures PIV

- 1. Set the recording equipment Experimentalist Control room
- 2. Set desired total pressure Experimentalist Hall ST-15
- 3. Start the jet Experimentalist Hall ST-15
- 4. Main valve on seeder Assistant Control room
- 5. Regulate to desired seeder pressure - Experimentalist Hall ST-15
- 6. Main valve off/on seeder Assistant Hall ST-15
- 7. Check jet pressure Experimentalist Control room
- 8. Main valve off seeder Experimentalist Control room
- 9. Begin recording sensor data Experimentalist Control room
- 10. Start viewing images Experimentalist Control room
- 11. Run wind tunnel 25 seconds Assistant Control room
- 12. Turn on jet seeder with wind tunnel Experimentalist Control room
- 13. Open maximum the seeding of the crossflow Experimentalist Control room
- 14. Switch to recording Experimentalist Control room
- 15. Stop wind tunnel and sensors Assistant
- 16. Stop the seeding a bit after wind tunnel Experimentalist Control room
- 17. Stop Laser Experimentalist Control room
- 18. Close the jet valve Experimentalist Hall-ST15

C.2 Nozzle exchange procedure

- 1. Close wall valve
- 2. Discharge pressure
- 3. Close the system valve
- 4. Disconnect the PVC hose to the control system
- 5. Loosen the sealing connection for the sensors

- 6. Open the starboard side of the wind tunnel (with caution)
- 7. Disconnect the PVC hose of the injector system
- 8. Open the diffuser
- 9. Dismount the injector system and lay it on the table next to the door
- 10. Mount the new nozzle and tighten it
- 11. Mount the system
- 12. Connect all couplings
- 13. Tighten the sensor sealing
- 14. Paint the surface
- 15. Close the tunnel and open the wall valve

Appendix D

Supplementary Figures

D.1 PIV velocity fields

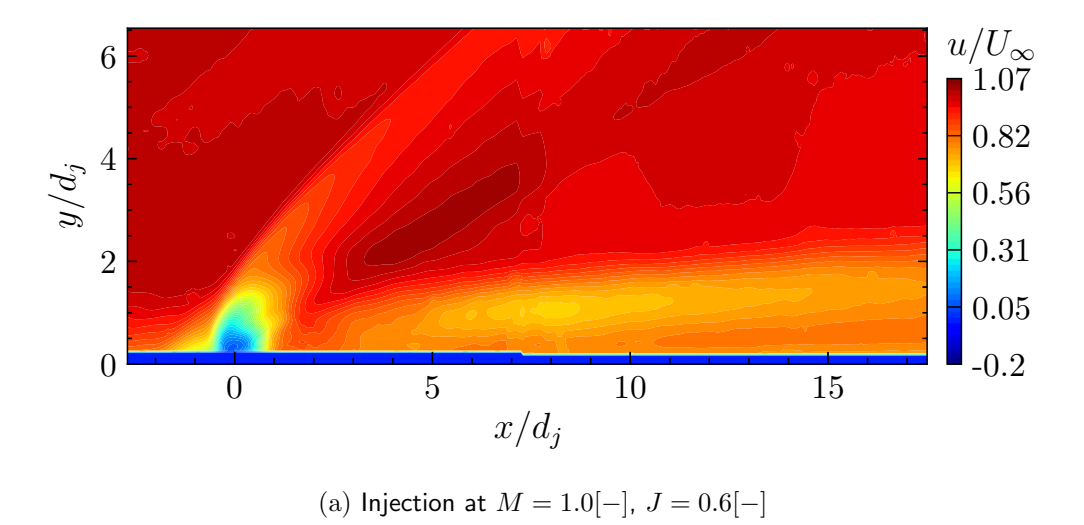


Figure D.1: Streamwise velocity contours

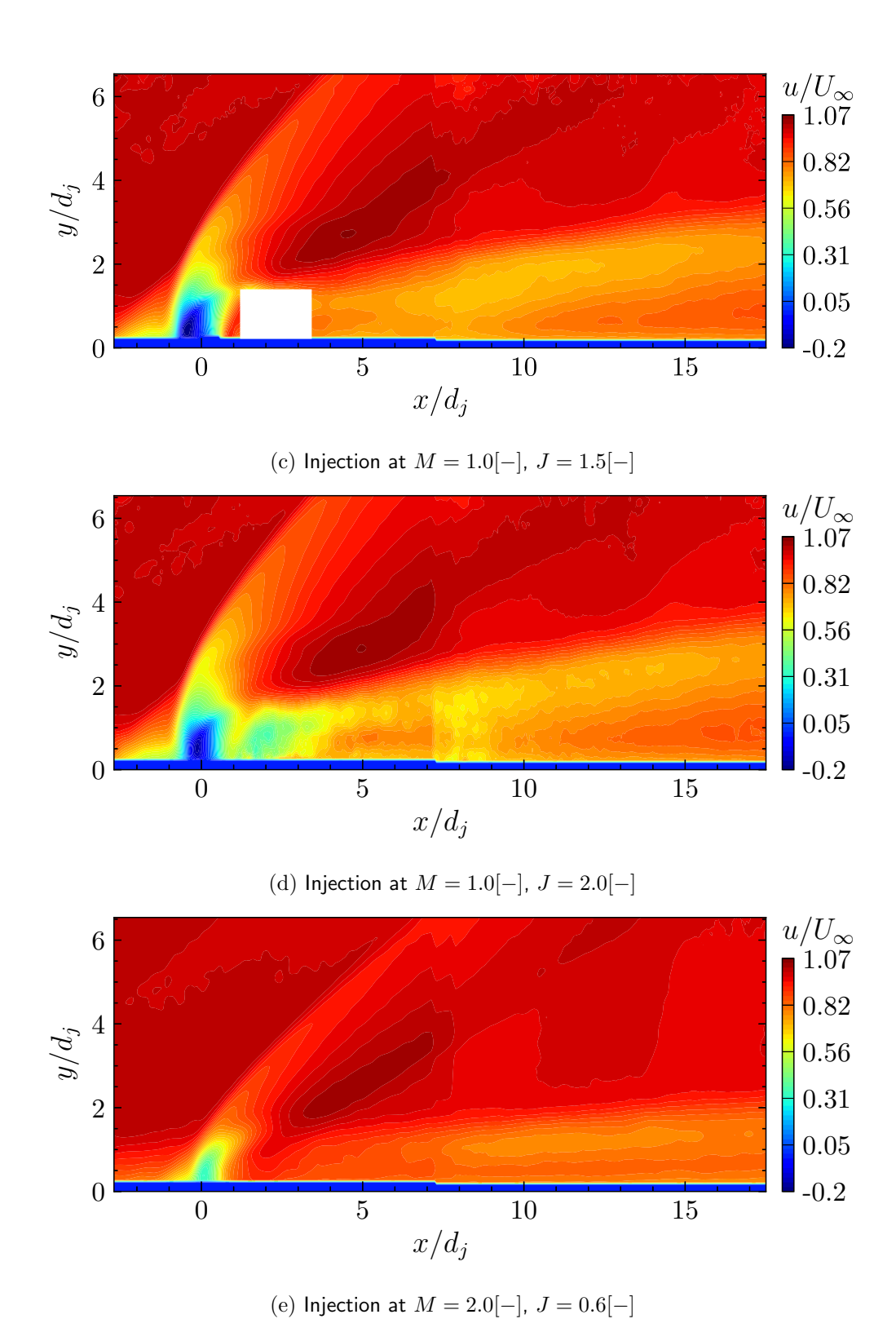


Figure D.1: Streamwise velocity contours

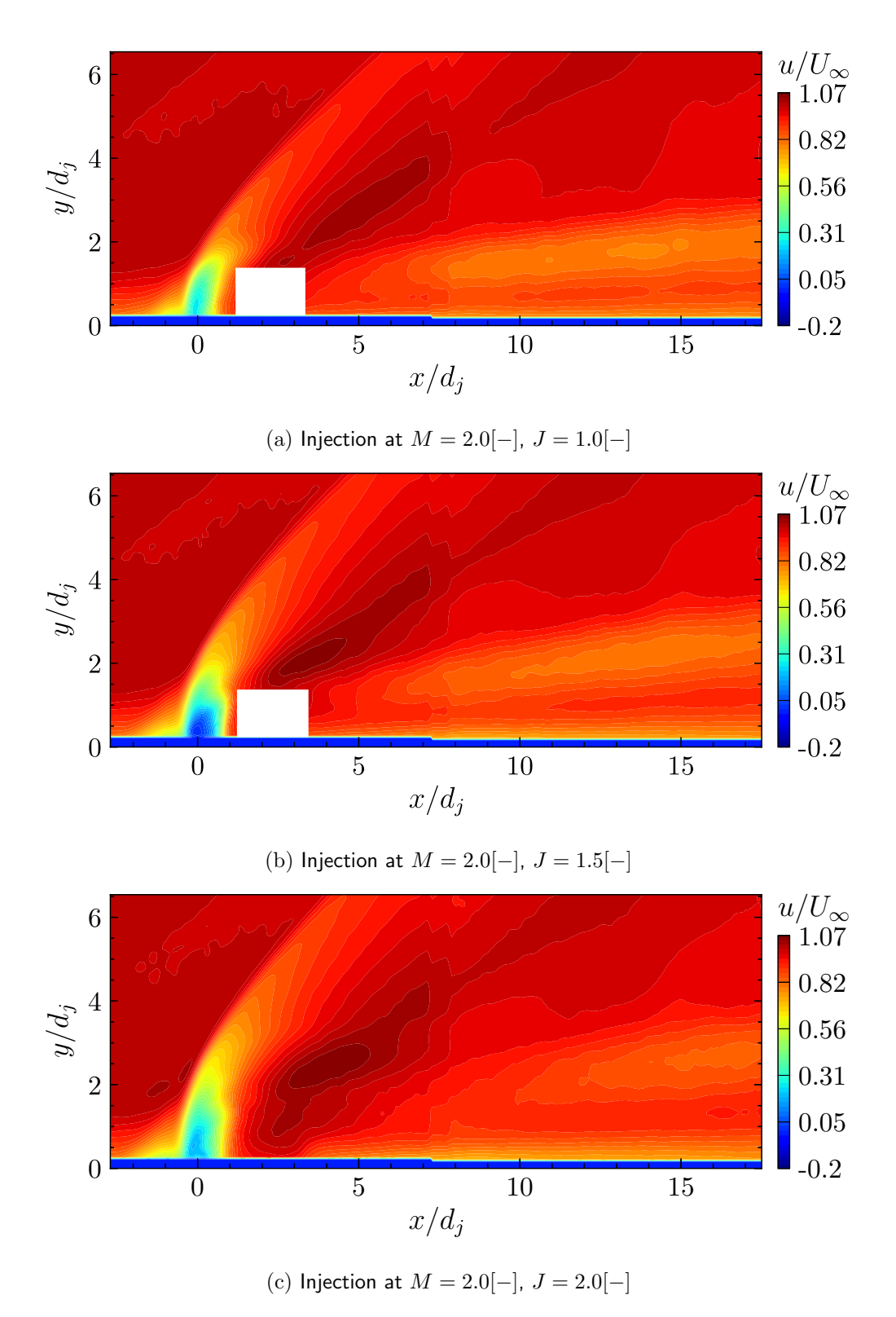


Figure D.2: Streamwise velocity contours

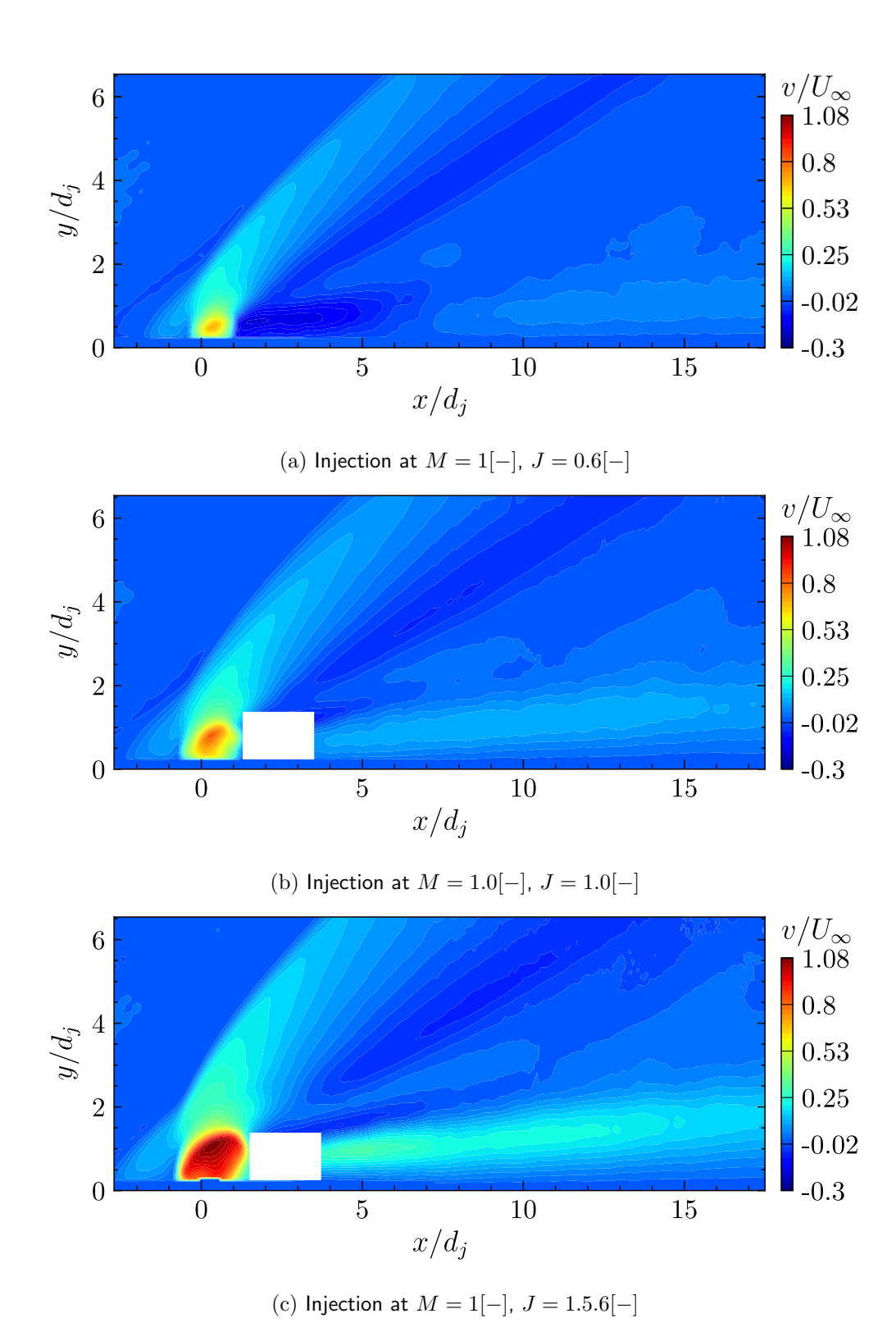


Figure D.3: Vertical velocity contours

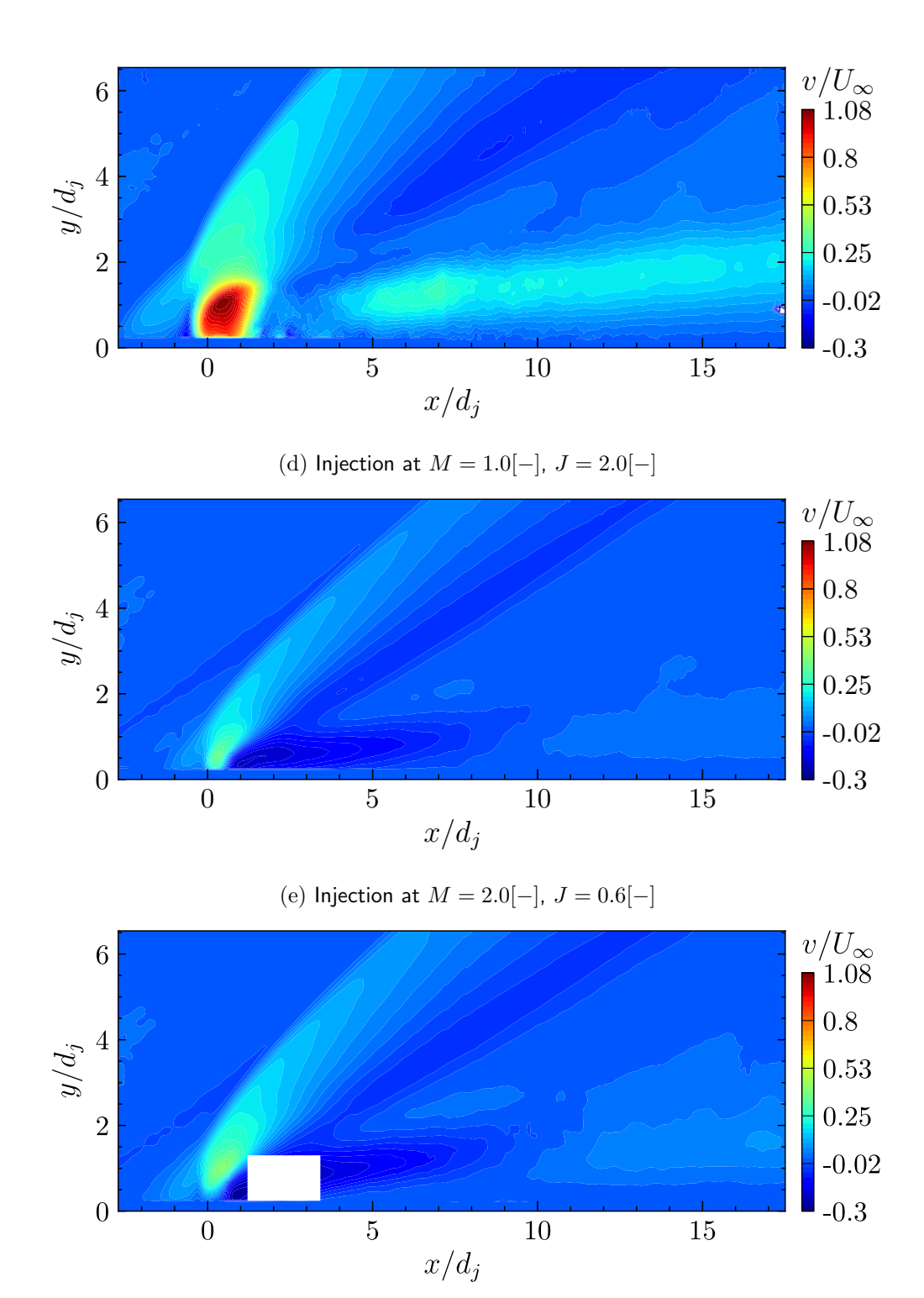


Figure D.3: Vertical velocity contours

 $({\rm f)\ Injection\ at}\ M=2.0[-],\ J=1.0[-]$

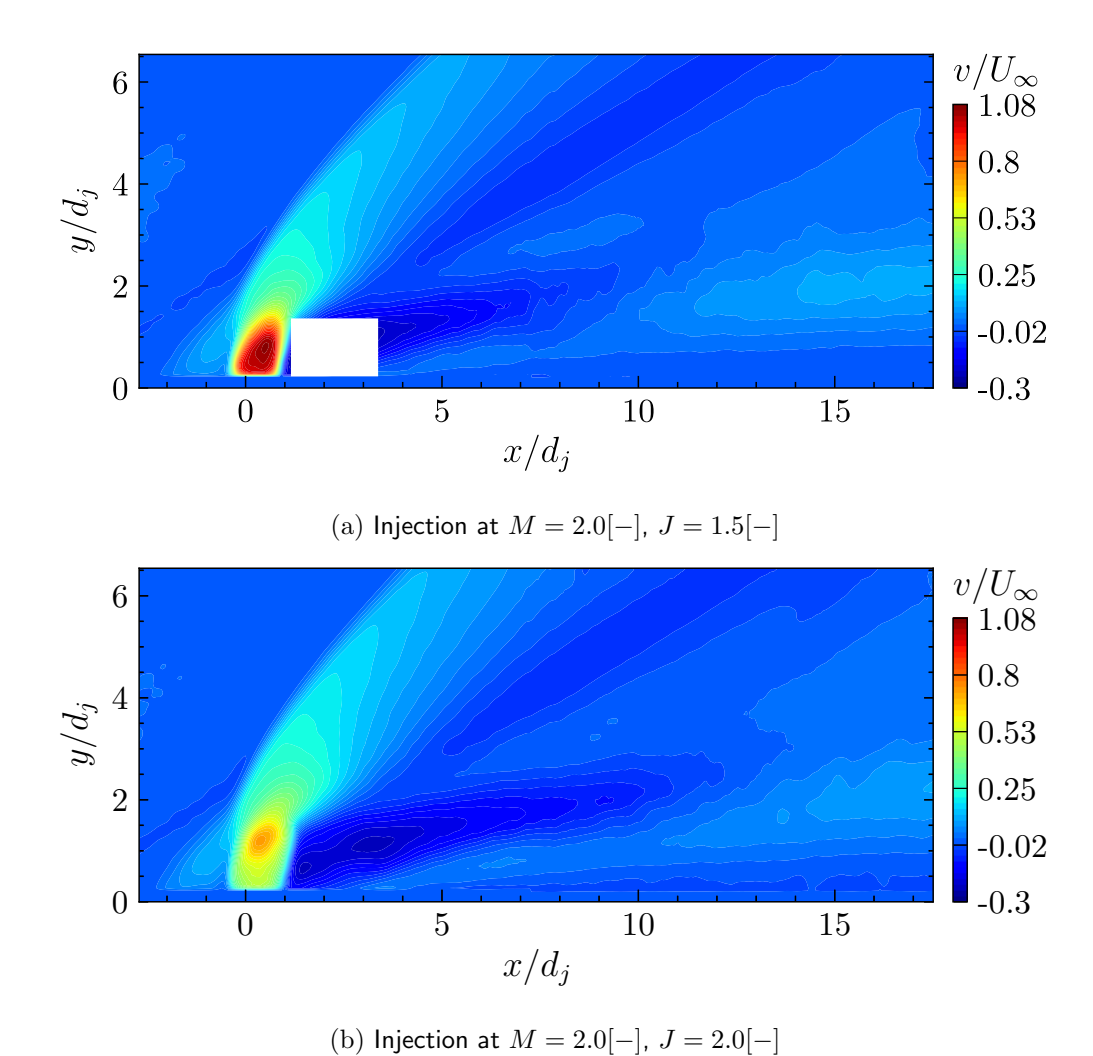
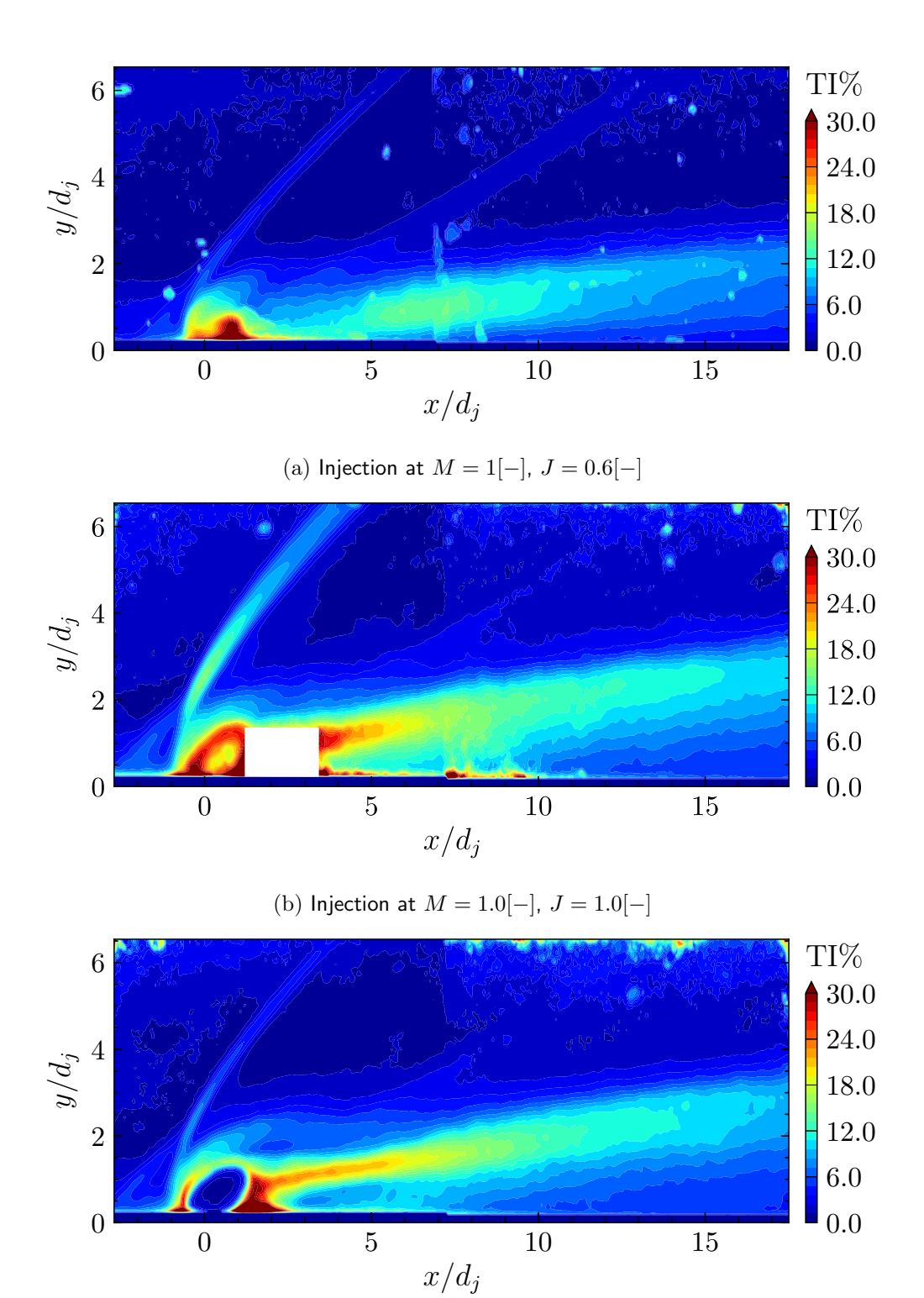
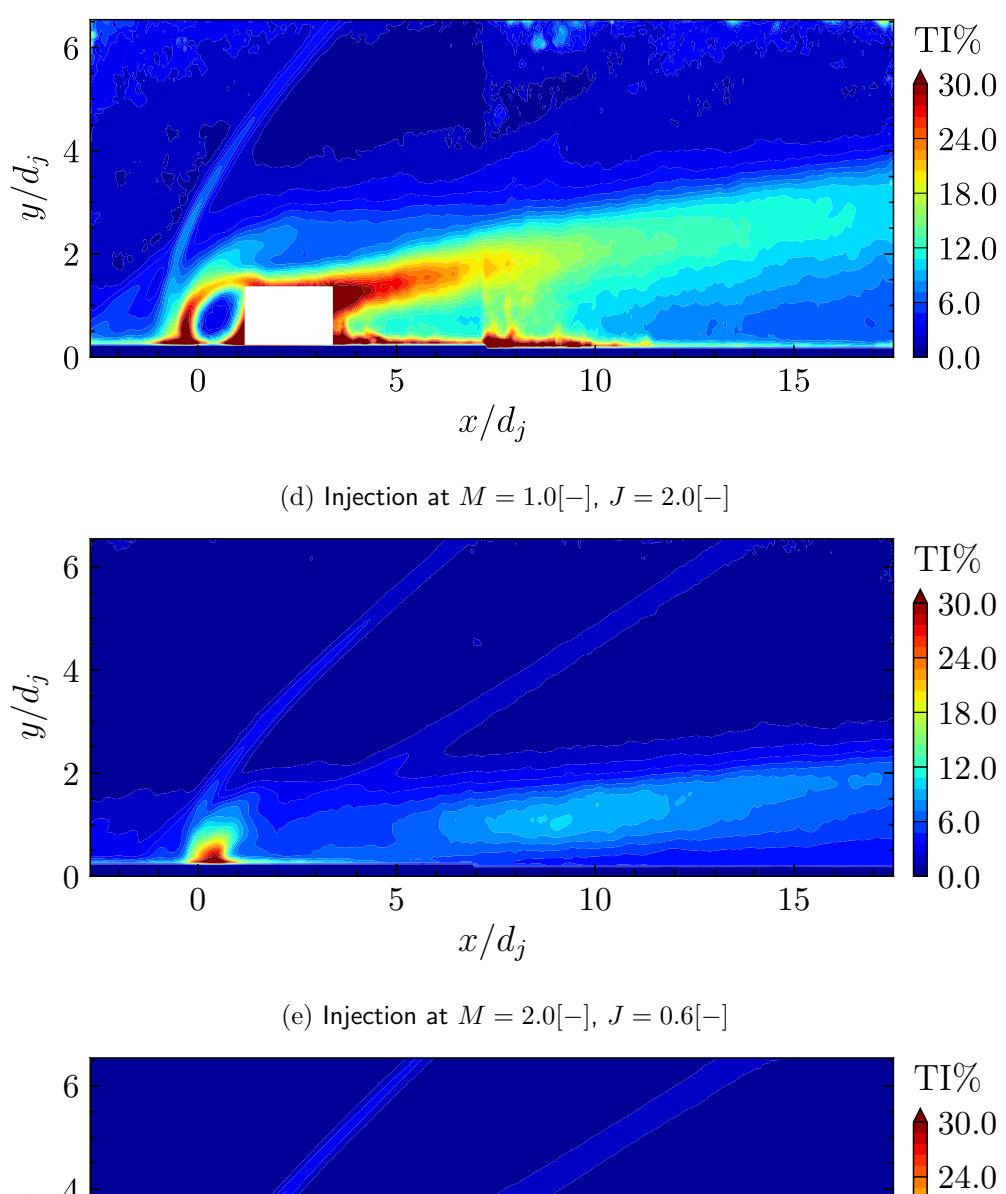


Figure D.4: Vertical velocity contours



(c) Injection at M=1[-], J=1.5[-]

Figure D.5: TI contours



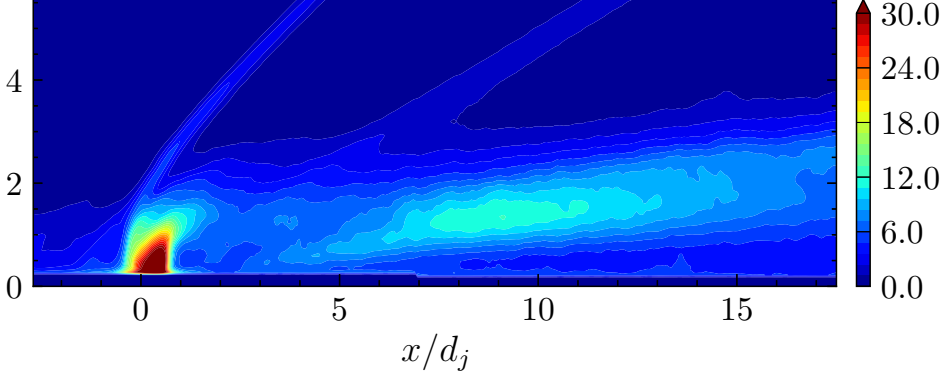
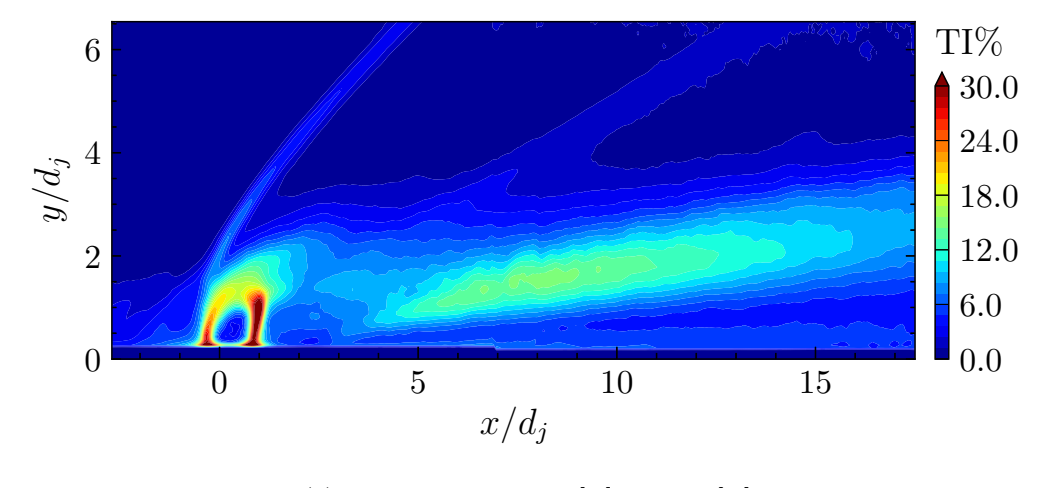
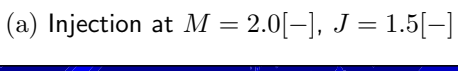
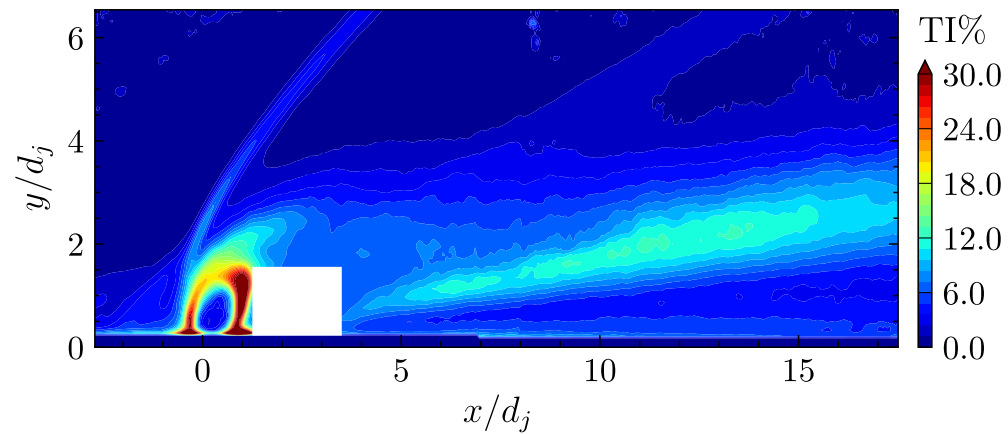


Figure D.5: TI contours

 $({\rm f)\ Injection\ at}\ M=2.0[-],\ J=1.0[-]$







(b) Injection at M=2.0[-], J=2.0[-]

Figure D.6: TI contours

D.2 Schlieren images

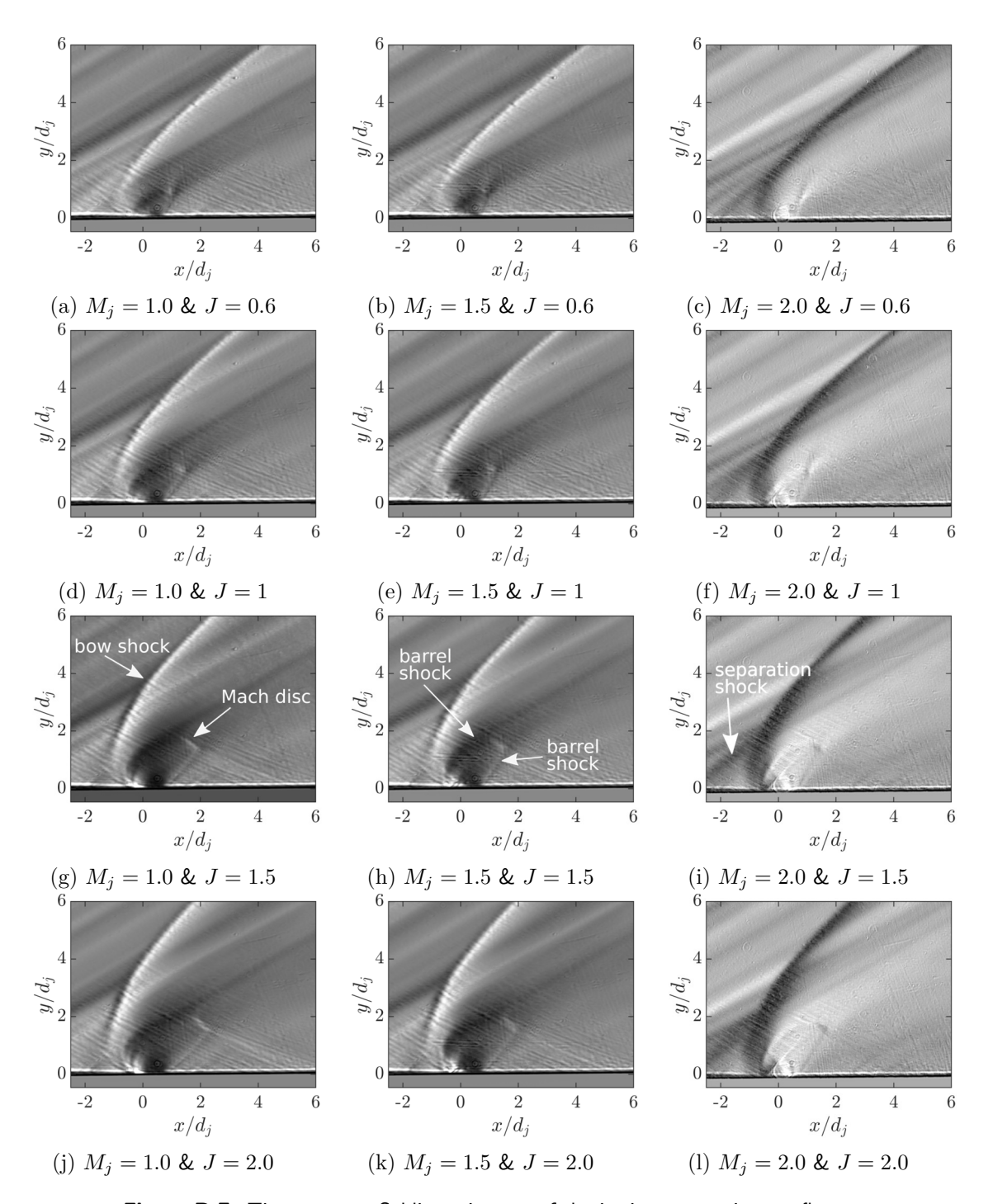


Figure D.7: Time average Schlieren images of the jet in supersonic crossflow

Appendix E

Drawings

E.1 Wind tunnel Mach 2 nozzle block cut-out drawings

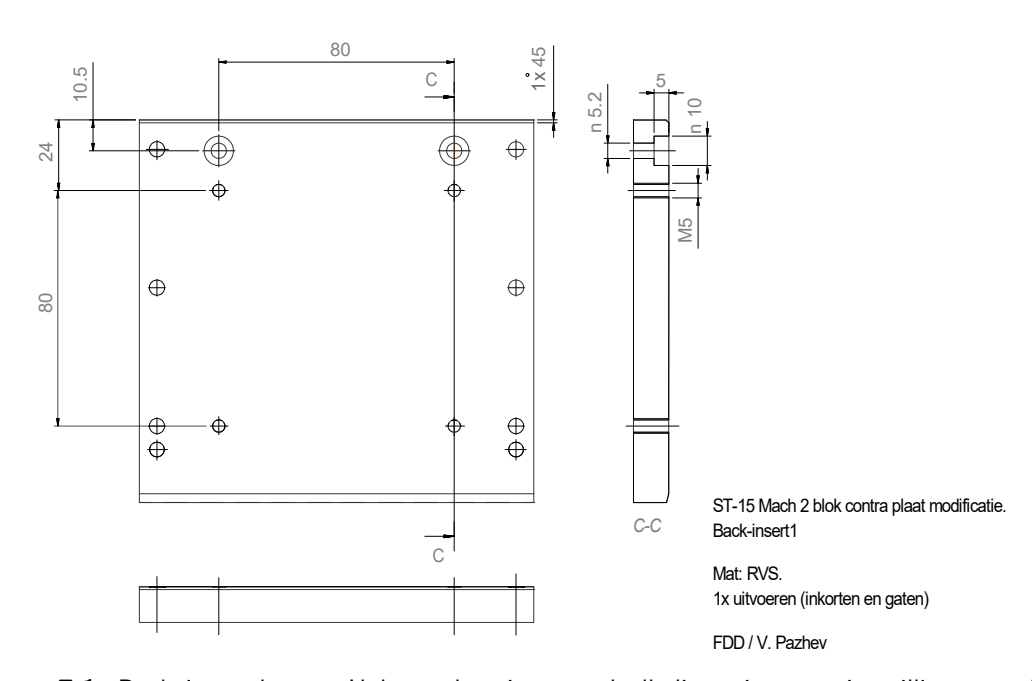


Figure E.1: Back insert lower. Unless otherwise stated all dimensions are in millimetres. The drawing Title block was omitted per request from the technical personnel. Author: FDD/V.Pazhev

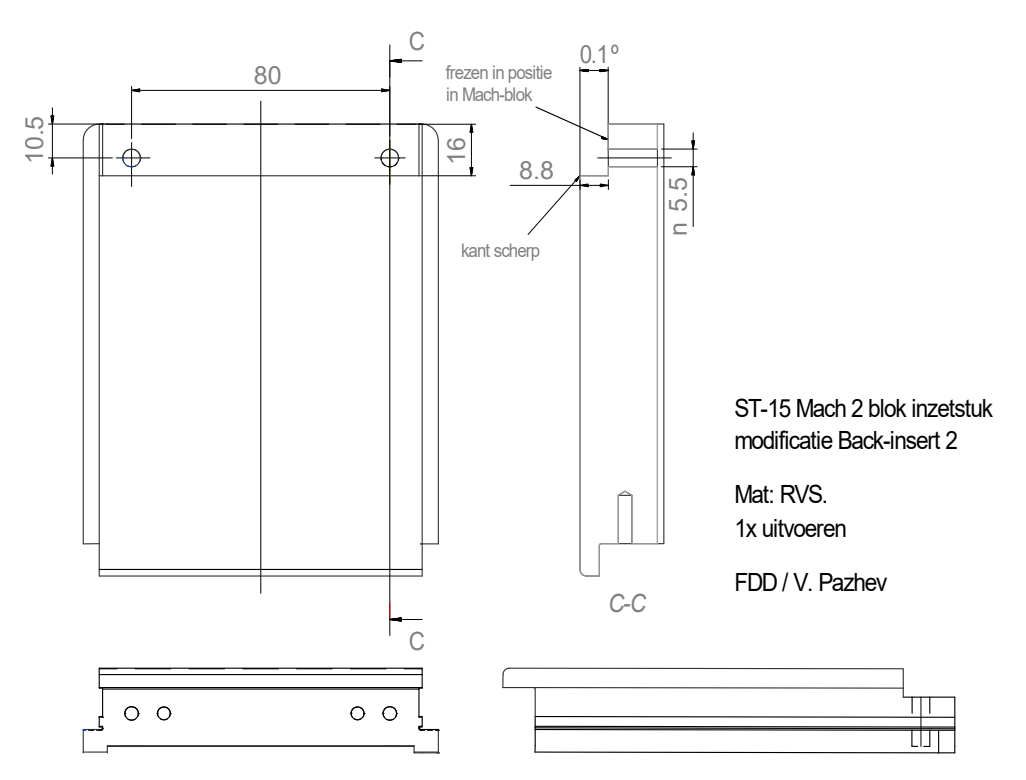


Figure E.2: Back insert upper. Unless otherwise stated all dimensions are in millimetres. The drawing Title block was omitted per request from the technical personnel. Author: FDD/ V.Pazhev

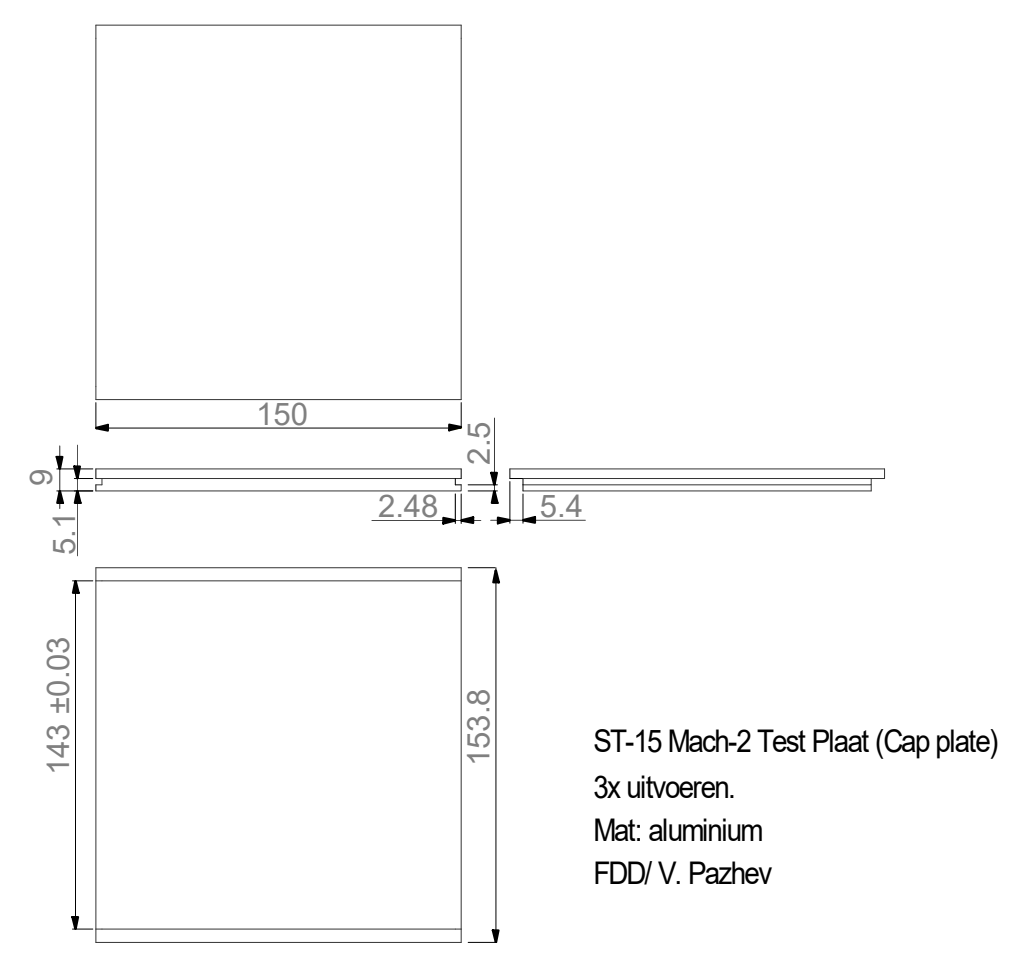


Figure E.3: Cap plate. Unless otherwise stated all dimensions are in millimetres. The drawing Title block was omitted per request from the technical personnel. Author: FDD/ V.Pazhev

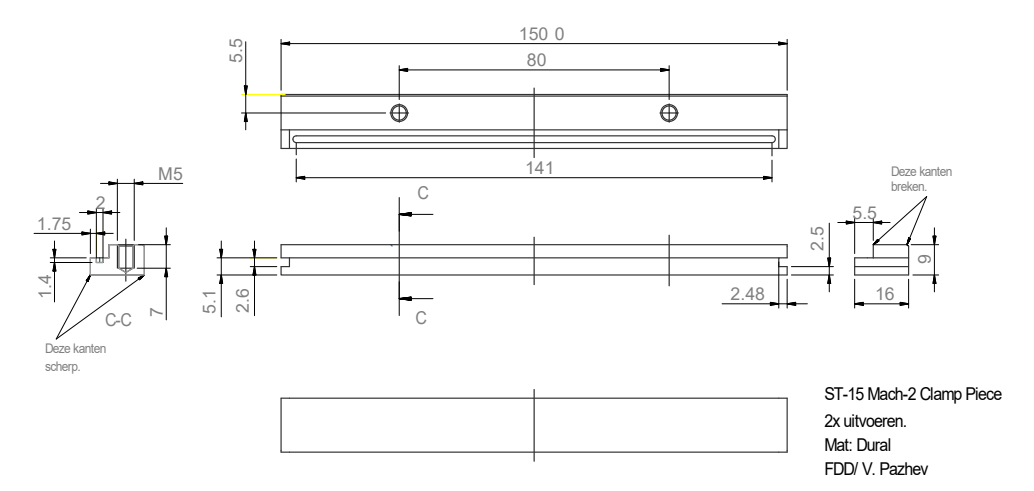
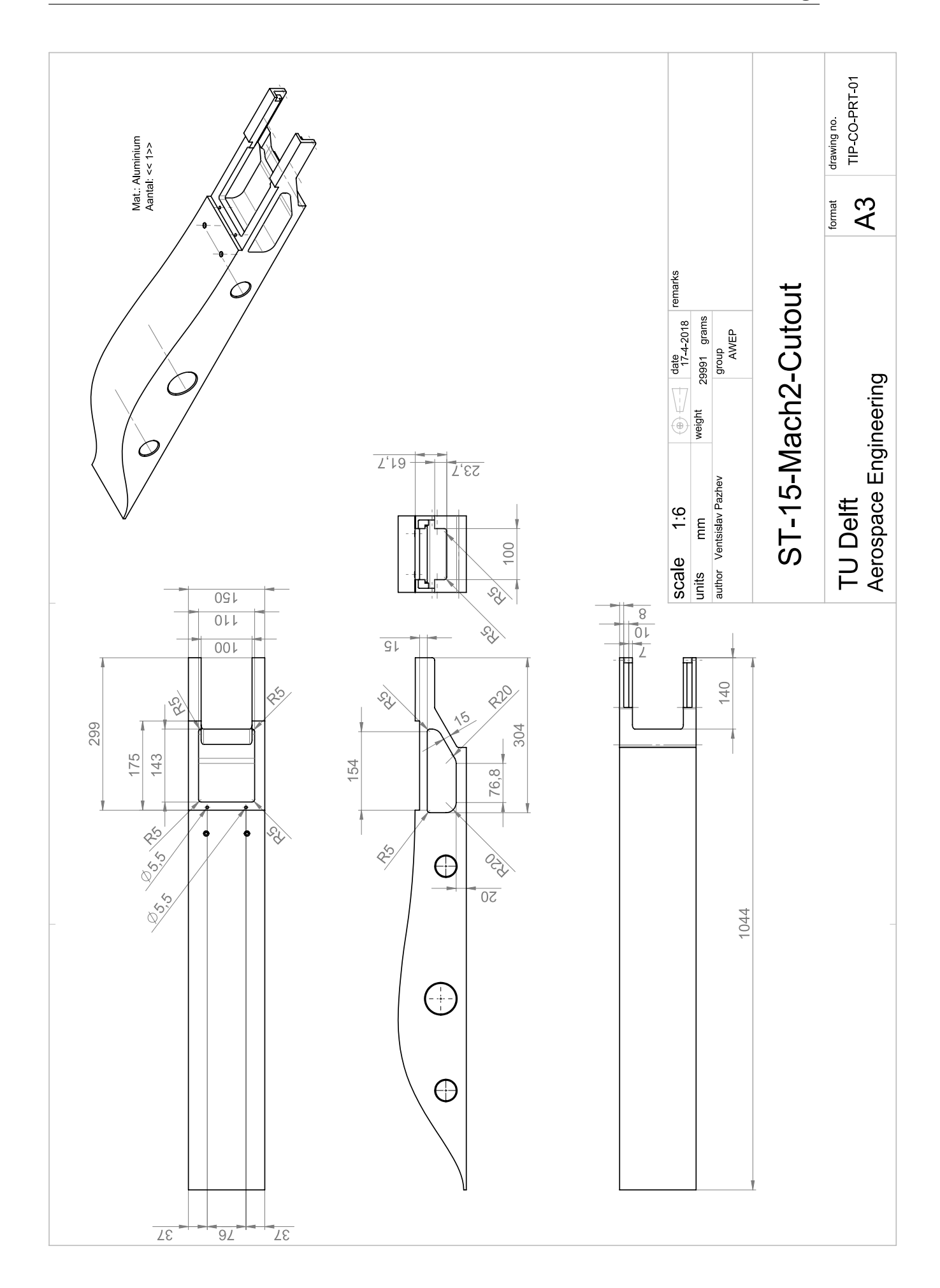


Figure E.4: Clamp piece. Unless otherwise stated all dimensions are in millimetres. The drawing Title block was omitted per request from the technical personnel. Author: FDD/V.Pazhev



E.2 Injection system drawings

Uploaded are the original manufacturing drawings. After the Green Light it will be decided if changes to the format are necessary. Additional drawings are currently exported to PDF to fit document.

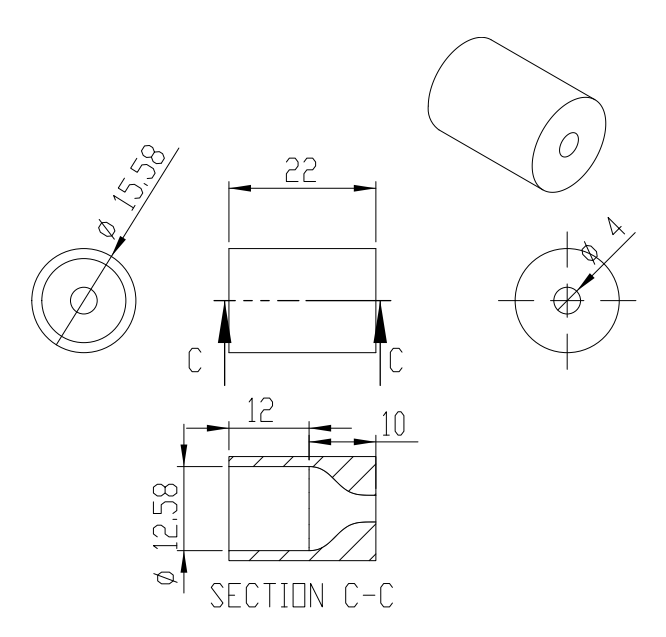


Figure E.5: $M_j=1.0$ injection nozzle. Unless otherwise stated all dimensions are in millimetres. The drawing Title block was omitted per request from the technical personnel. Author: V.Pazhev

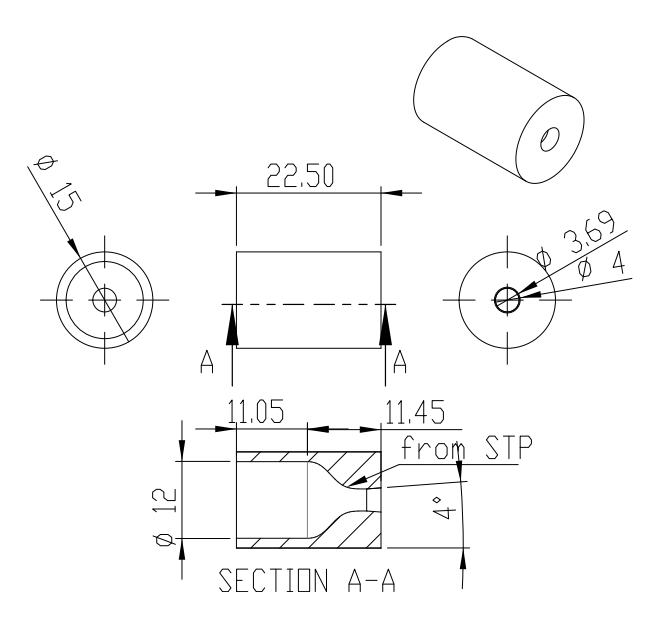


Figure E.6: $M_j=1.5$ injection nozzle. Unless otherwise stated all dimensions are in millimetres. The drawing Title block was omitted per request from the technical personnel. Author: V.Pazhev

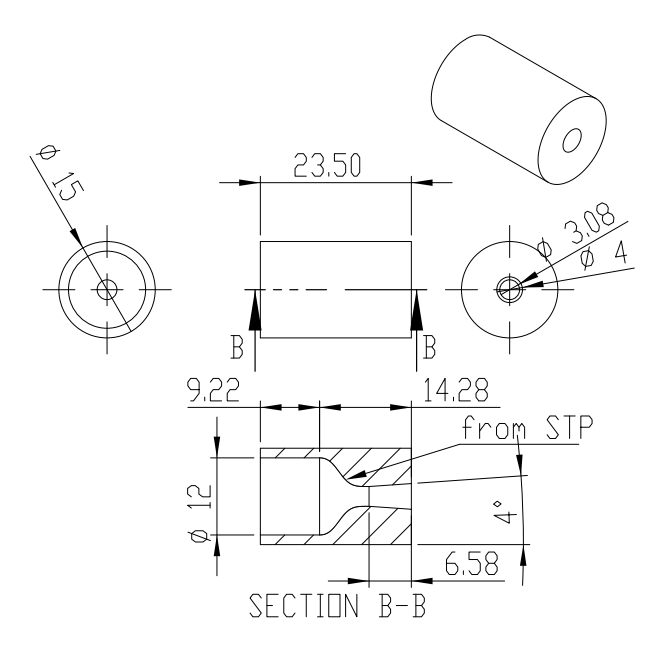


Figure E.7: $M_j=2.0$ injection nozzle. Unless otherwise stated all dimensions are in millimetres. The drawing Title block was omitted per request from the technical personnel. Author: V.Pazhev

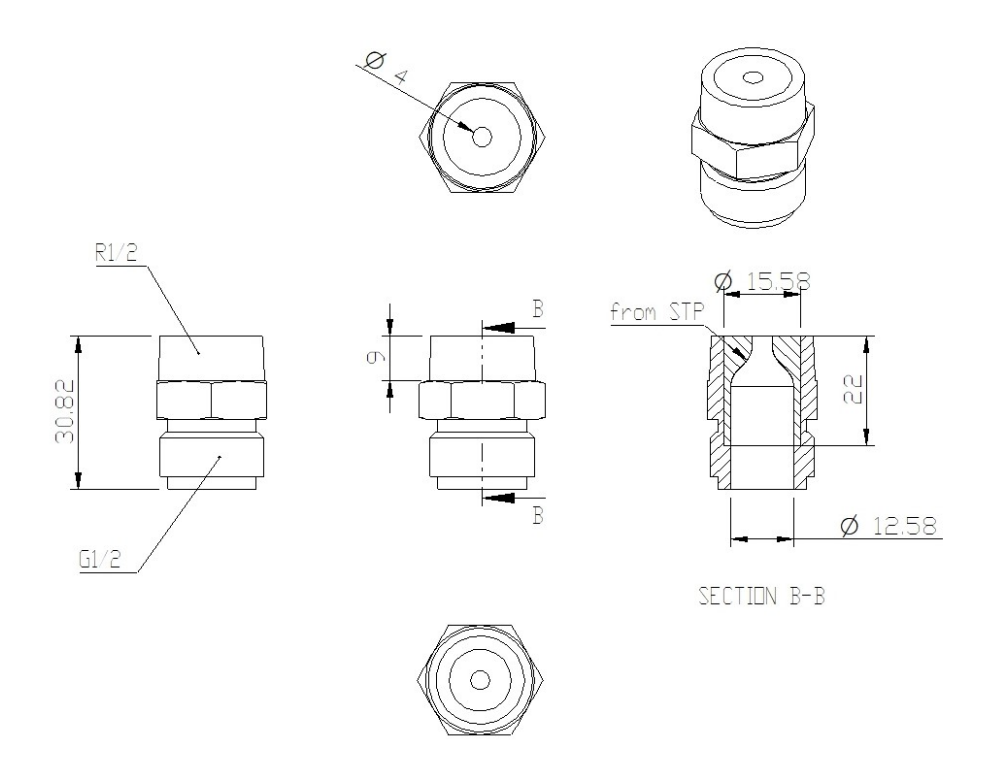


Figure E.8: $M_j=1.0$ injection assembly. Nozzle and fitting. Unless otherwise stated all dimensions are in millimetres. The drawing Title block was omitted per request from the technical personnel. Author: V.Pazhev

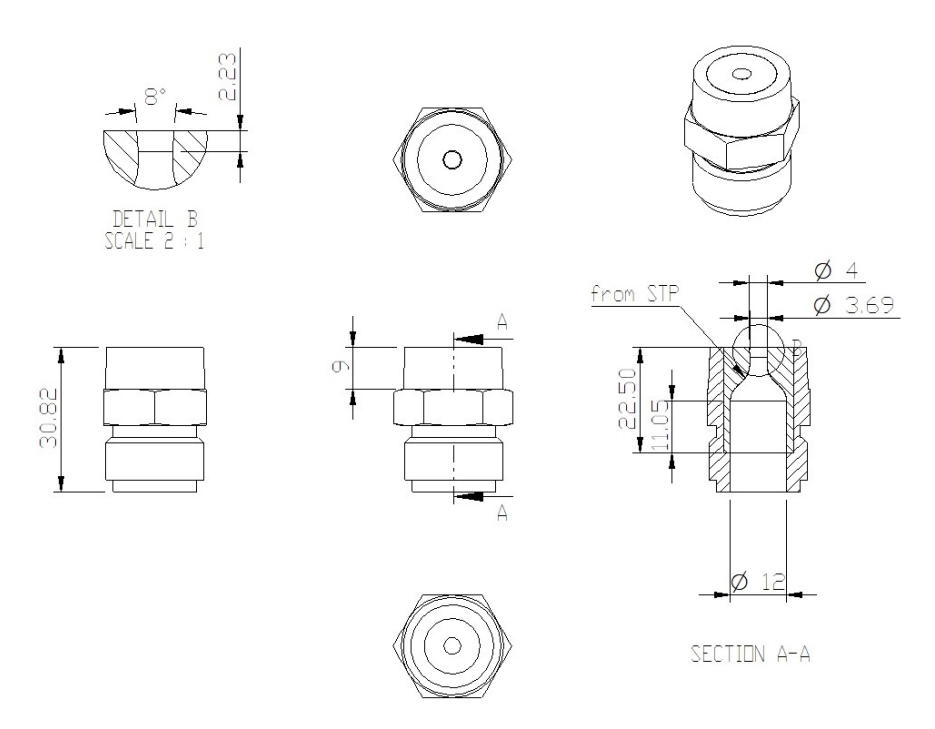


Figure E.9: $M_j=1.5$ injection assembly. Nozzle and fitting. Unless otherwise stated all dimensions are in millimetres. The drawing Title block was omitted per request from the technical personnel. Author: V.Pazhev

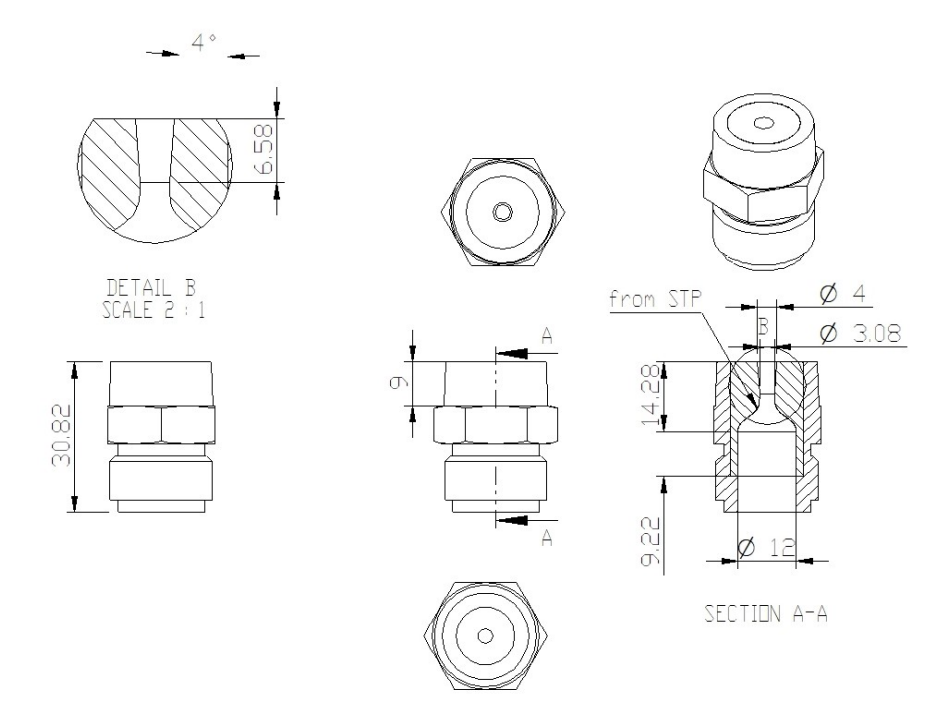


Figure E.10: $M_j=2.0$ injection assembly. Nozzle and fitting. Unless otherwise stated all dimensions are in millimetres. The drawing Title block was omitted per request from the technical personnel. Author: V.Pazhev